Investigations on bottom-up and top-down processing in early visual cortex with high-resolution fMRI

Investigations on bottom-up and top-down processing in early visual cortex with high-resolution fMRI

Ingo Marquardt

Propositions of the thesis

Investigations on bottom-up and top-down processing in early visual cortex with high-resolution fMRI

Ingo Marquardt

1. Visual perception arises from an interplay of bottom-up and top-down processes. Cortical depth-specific fMRI has the potential to afford deeper insights into the interplay of bottom-up and top-down signals in visual cortex.

2. High-resolution fMRI can measure the neuronal processes underlying perception in the human brain at an unprecedented level of spatial detail. However, vascular artefacts pose a great challenge to this line of research.

3. Even though it is difficult to model and remove signal bias due to draining veins from the cortical depth-specific fMRI signal, it is better to model the bias with some degree of uncertainty than to ignore it.

4. Even though primary visual cortex is one of the best-studied cortical areas in humans, much remains unknown about its function. Simple experimental stimuli can reveal surprising response patterns.

5. Cognitive neuroscience should attempt to bridge the gap between cognitive science and 'classical' neuroscience. In particular, the long-term goal of fMRI research should be to integrate functional and structural levels of description.

6. The processing and analysis of fMRI data requires substantial amounts of computer code. Computer code should not only be machine-readable, but also human-readable.

7. Like natural languages, computer languages require adherence to grammatical and stylistic rules for clear and efficient communication.

8. Sharing of data, metadata, and analysis code increases transparency, facilitates the efficient use of resources, and has the potential to increase the trust in science.

9. The responses to surfaces and edges in early visual cortex are modulated by the background. The response to the background has a complex temporal pattern.

10. More research will be needed.

Doctoral thesis

INVESTIGATIONS ON BOTTOM-UP AND TOP-DOWN PROCESSING IN EARLY VISUAL CORTEX WITH HIGH-RESOLUTION FMRI

Ingo Marquardt

2019

Cover	Ingo Marquardt, 2019
Production	proefschriftmaken.nl
ISBN	978-94-6380-472-1

INVESTIGATIONS ON BOTTOM-UP AND TOP-DOWN PROCESSING IN EARLY VISUAL CORTEX WITH HIGH-RESOLUTION FMRI

Dissertation

To obtain the degree of Doctor at Maastricht University,
on the authority of the Rector Magnificus,
Prof. Dr. Rianne M. Letschert,
in accordance with the decision of the Board of Deans,
to be defended in public
on Thursday, 29th of August 2019, at 10.00 hours

by

Ingo Marquardt

Supervisor
Prof. Dr. Rainer Goebel

Co-supervisor
Prof. Dr. Kâmil Uludağ, University of Toronto

Assessment Committee
Prof. Dr. Elia Formisano (Chair)
Prof. Dr. Bernadette M. Jansma
Prof. Dr. Serge O. Dumoulin, Spinoza Centre for Neuroimaging
Dr. Peter J. Koopmans, University of Duisburg-Essen
Dr. Laurentius Huber

The research presented in this thesis was supported by the Netherlands Organisation for Scientific Research (NWO) grants VIDI 452-11-002 to Kâmil Uludağ and Research Talent 406-14-085 to Kâmil Uludağ and Ingo Marquardt.

Contents

1
General Introduction

1.1 Cognitive neuroscience

What is – or should be – the purpose of cognitive neuroscience? The objective of 'classical' neuroscience is to study the anatomy and physiology of the nervous system. On the other hand, the study of cognition has traditionally been within the realm of psychology. In its most general sense, the term 'cognition' refers to the processing of information by animals and humans. Animals process sensory information in order to guide their behaviour. In fact, the presence of a nervous system that enables an organism to respond to environmental stimuli in an adaptive and flexible way is a feature that distinguishes most animals from other organisms. It is instructive to consider that the study of mind, brain, and behaviour can be divided into three aspects: the functional, the structural, and the phenomenal (Chalmers, 2007). This division is not an ontological one, but purely epistemological; psychology deals with the functional, neuroscience with the structural and physiological basis of cognition, and philosophy of mind is concerned with the phenomenal and its relation to the other two aspects.

Attempts to bridge the explanatory gap between the functional and the structural realms have been made from both sides. In addition to studying the anatomy and physiology of the nervous system, neuroscientists have investigated the neural correlates of perception in non-human animals, and psychologists have employed non-invasive methods to record brain activity in humans. Invasive electrophysiological research, conducted mostly in anaesthetised rodents, cats and monkeys, has produced a detailed picture of the workings of the visual system (see, for example, Albrecht & Hamilton, 1982; Felleman & Van Essen, 1991; Hubel & Wiesel, 1968; Maunsell & Newsome, 1987). Interestingly, insights from electrophysiological studies had a great impact on human cognitive science. It is hard to overestimate the importance of the realisation that neurons in the visual system are feature detectors in a hierarchical system of progressively more abstract representations. These 'cognitive' ideas have even had a huge impact on another discipline that deals with information processing – i.e. computer science and particularly neural network modelling (Buduma & Locascio, 2017). At the same time, psychologists were able to constrain cognitive theories based on electroencephalographic recordings (for example, Cheour, Shestakova, Alku, Ceponiene, & Näätänen, 2002; Libet, Gleason, Wright, & Pearl,

1983; VanRullen & Thorpe, 2001; Winkler et al., 1999). In the 1990s, another tool became available to measure brain activity non-invasively – functional magnetic resonance imaging (fMRI) (Ogawa et al., 1992).

Critics have argued that simply mapping brain activity during a variety of tasks does not yield any deep neuroscientific insight (Coltheart, 2006; Page, 2006; Van Orden & Paap, 1997). Some have even gone so far as to denounce fMRI mapping studies as a modern form of phrenology (Uttal, 2001). I would like to argue that, on the contrary, fMRI has revolutionised the study of human brain function, and strengthened the bridge between the functional and structural levels of description. Functional MRI opened up the possibility to measure human brain activity over large areas at a spatial scale of less than one cubic millimetre. For the first time, the organisation of human visual cortex into several retinotopic maps could be demonstrated *in vivo* (Engel, Glover, & Wandell, 1997). Other examples of fMRI studies with both cognitive and neuroscientific implications are the discovery of distributed object representations in human ventral temporal cortex (O'Toole, Jiang, Abdi, & Haxby, 2005), the reconstruction of visual experiences from fMRI data (Nishimoto et al., 2011), and the mapping of increasingly complex receptive field properties along the visual hierarchy (Güçlü & van Gerven, 2015).

However, linking theory and observation can be difficult. Much research in cognitive neuroscience is necessarily exploratory. Like other disciplines before it, cognitive neuroscience may be at risk of accumulating huge amounts of data, while neglecting theory building. The goal of academic research should not be limited to the description of observable phenomena, but to explain and understand them. To this end, quantitative models that identify causal mechanisms and allow predictions about future observations are necessary.

Whereas psychologically inspired cognitive models were typically abstracted away from their biological implementation (for example, Bower, Clark, Lesgold, & Winzenz, 1969; Phillips, 1974; Pylyshyn, 1973; Sternberg, 1966), modern cognitive theory can take the form of computational models at the microscopic, neuronal scale (for example, Durbin & Rumelhart, 1989; Itti, Koch, & Niebur, 1998; Izhikevich, 2004; Mazzoni, Andersen, & Jordan, 1991; Von Neumann & Churchland, 2000). Because fMRI data could until recently only be acquired at the macroscopic scale (i.e. at the level of brain areas), it was difficult

to bridge empirical data and theory. With recent increases in spatial resolution, fMRI became able to map brain function at the so-called mesoscopic scale, i.e. at different cortical depths, and possibly at the level of columns, or otherwise computationally relevant clusters. Differences in thalamic input between cortical layers, together with differences in their functional properties (Hubel & Livingstone, 1990; Tootell, Hamilton, & Switkes, 1988), have led to the insight that cortical layers can be understood as interconnected but separate neuronal networks (Callaway, 1998; Lund, 1988). By mapping functional differences between cortical depth levels, high-resolution fMRI research might help to lessen the gap between data and theory, and thereby aid the development of mechanistic physiological models of cognition.

1.2 Mapping visual cortex with high-resolution fMRI

While others have set out to functionally map columnar structures with fMRI (Cheng, Waggoner, & Tanaka, 2001; Goncalves et al., 2015; Nasr, Polimeni, & Tootell, 2016; Tootell & Nasr, 2017; Zimmermann et al., 2011), this thesis provides a contribution to the study of laminar function in the human visual cortex. It is important to note, however, that the term 'laminar' in the context of current high-resolution fMRI is not synonymous with the terminology used in histological research. At the currently achievable spatial resolution, individual histological layers cannot be directly resolved with fMRI (but for current attempts to directly resolve laminar activation when measuring from a relatively flat section of cortex using highly anisotropic voxels, see Kashyap et al., 2018). Thus, in the context of fMRI, as an alternative to 'cortical layers', the term 'cortical depth levels' may avoid confusion and misinterpretations, especially with respect to readers who have a background in fundamental neuroscience. Even though individual, histologically defined layers cannot currently be resolved, responses at different cortical depth levels (e.g. deep, middle, and superficial) are in reach of high-resolution fMRI (Koopmans, Barth, & Norris, 2010; Polimeni, Fischl, Greve, & Wald, 2010)(De Martino et al., 2017; Polimeni, Renvall, Zaretskaya, & Fischl, 2017; Uludağ & Blinder, 2017).

Although invasive electrophysiological recordings afford consider-

ably higher spatial and temporal resolution, fMRI offers a distinct set of advantages for studying certain aspects of visual processing. Perhaps most importantly, current high-resolution fMRI allows measuring activity over comparatively large areas of cortex. A 'functional' (i.e. T2*-weighted) image covering early visual areas V1, V2, and V3 at sub-millimetre resolution (e.g. 0.8^3 mm^3) can be acquired in about two seconds (Marquardt, Schneider, Gulban, Ivanov, & Uludağ, 2018; Poser, Koopmans, Witzel, Wald, & Barth, 2010).

Another obvious advantage of fMRI is that it is non-invasive, so that data can be acquired from awake human volunteers. This is in contrast with invasive electrophysiological research, which is often conducted in anaesthetised animals and, in exceptional cases, in patients. In studies on awake animals, extensive training on the experimental task is necessary. Both of these factors – anaesthesia and very prolonged training – can have an impact on the ecological validity of the results. To be sure, electrophysiological research did and does play a paramount role in neuroscience. Nevertheless, fMRI can and should contribute to the advance of neuroscience by leveraging its specific advantages.

Even though the spatial and temporal resolution of fMRI is lower than that of invasive methods, the unique combination of good coverage with reasonably high spatial and temporal resolution makes high-resolution fMRI very well suited for studying visual perception. One interesting aspect of visual perception that can be addressed with high-resolution fMRI is the constructive nature of vision, and the corresponding interplay between feedforward and feedback processing. The microcircuit model (Douglas, Martin, & Whitteridge, 1989) postulates that feedforward and feedback processing engage neuronal networks at different cortical depths (Callaway, 1998; Rockland, 2017; Rockland & Pandya, 1979). High-resolution fMRI may, therefore, help to map the neural correlates of feedforward and feedback effects at different cortical depths. By providing a more fine-grained mapping of both processing streams, human neuroimaging may thus become increasingly capable of constraining and even inspiring novel cognitive theories of perception.

1.3 Feedforward & feedback processing

The transmission of information from a sensory organ through a hierarchy of subcortical and cortical areas is referred to as feedforward

processing (Hochstein & Ahissar, 2002). Feedforward processing is accompanied by information flow in the opposite direction down the hierarchy of visual areas, known as feedback processing (Felleman & Van Essen, 1991; Maunsell & Newsome, 1987; Rockland & Pandya, 1979), and lateral connections within a level of the hierarchy (Gilbert & Wiesel, 1983; McGuire, Gilbert, Rivlin, & Wiesel, 1991).

Visual illusions illustrate the role of prior assumptions about the world in perception (Kleffner & Ramachandran, 1992), presumably implemented by feedback processing (Hochstein & Ahissar, 2002). Feedback mechanisms are involved in the selective gating of information flow depending on expectancy and behavioural relevance (Lamme & Roelfsema, 2000), by selectively enhancing the responses to relevant stimuli. For instance, invasive electrophysiological research in monkeys has demonstrated selective synchronisation of activity between higher-order parietal cortex and visual cortex during selective spatial attention (Saalmann, Pigarev, & Vidyasagar, 2007). Feedback to visual cortex was found to correlate with an enhanced response to the attended stimulus (Saalmann et al., 2007). Direct evidence for a role of top-down feedback in the selection of relevant information comes from a study, in which localised microstimulation was applied at a specific retinotopic location in monkeys' frontal eye fields (Moore & Armstrong, 2003; Moore & Fallah, 2004). Microstimulation in the frontal eye fields was found to modulate activity in visual cortex, as does selective spatial attention (Moore & Armstrong, 2003), leading to improved target detection at the corresponding retinotopic location (Moore & Fallah, 2004). Optogenetic inactivation of feedback connections in monkey early visual cortex revealed an effect of top-down feedback on receptive field size, surround suppression, and response amplitude (Nurminen, Merlin, Bijanzadeh, Federer, & Angelucci, 2018). Taken together, these findings illustrate the importance of feedback processing in visual perception.

Evidence for top-down attention effects in human visual cortex came from early fMRI studies, which indicated that attention causes both a response enhancement for attended stimuli/locations and a suppression of surrounding, unattended stimuli/locations (Müller & Kleinschmidt, 2004; Silver, Ress, & Heeger, 2007; Slotnick, Schwarzbach, & Yantis, 2003; Somers, Dale, Seiffert, & Tootell, 1999; Tootell et al., 1998). These results were corroborated by a study that employed EEG and fMRI in humans (Grent-'t-Jong & Woldorff, 2007), suggesting that attention

effects in visual cortex are initiated by top-down signals from frontal and parietal cortex. Neuronal activity in human early visual cortex was found to be modulated by stimulus context and attention in a case study in an epileptic patient, providing support for the generalisability of conclusions drawn from electrophysiological studies in monkeys (Self et al., 2016).

1.4 Laminar feedforward & feedback modules

The distinction between feedforward and feedback modules has been related to the laminar structure of the cortex, which can be visualized using histological methods. Electrophysiological experiments (Hubel & Livingstone, 1990; Hubel & Wiesel, 1972) and tracer studies (Blasdel & Lund, 1983; Henderickson, Wilson, & Ogren, 1978; Rockland & Pandya, 1979; Tootell et al., 1988) have shown that feedforward projections terminate mostly in layers 4 and 6. The notion that the first feedforward sweep of visual input arrives in layers 4 and 6 is corroborated by the observation that response latencies are shortest in these thalamo-recipient layers (Constantinople & Bruno, 2013; Maunsell & Gibson, 1992).

In primary visual cortex, cortico-cortical feedback connections predominantly target layers 1, 2, and 5 (Anderson & Martin, 2009; Rockland & Pandya, 1979; Rockland & Virga, 1989). However, this picture is complicated by the fact that indirect, cortico-thalamo-cortical connections are probably involved in feedback processing as well. For example, the pulvinar has been termed a 'higher-order relay' because of its role in cortico-cortical communication (Sherman, 2005; Sherman & Guillery, 2002). In extrastriate cortex, the middle layers receive projections from the pulvinar (Benevento & Rezak, 1976; Benevento, Rezak, & Bos, 1975; Ogren & Hendrickson, 1977; Rezak & Benevento, 1979), in addition to cortico-cortical feedback projections towards deep and superficial layers. Moreover, although the LGN is *driven* by direct retinal input, its activity is *modulated* by cortico-thalamic projections, which actually make up a substantial share of all geniculate synapses (Sherman, 2005; Sherman & Koch, 1986). Thus, when interpreting activation maps of top-down effects, one has to consider several possible

routes of information flow.

Although cortical layers are thought to be differentially involved in feedforward and feedback processing, it should not be forgotten that cortical layers form a highly connected network (Callaway, 1998; Douglas et al., 1989; Rockland & Pandya, 1979). The initial sweep of stimulus-induced activity spreads across all layers in primary visual cortex (Schroeder, Mehta, & Givre, 1998), irrespective of stimulus condition (Self, van Kerkoerle, Supèr, & Roelfsema, 2013). Nevertheless, distinct laminar profiles of feedforward and feedback activity have been observed in spiking rates and postsynaptic activity. Especially in the later phase of the stimulus evoked response (>100 ms), the relative distribution of activity across layers was found to be modulated by stimulus conditions related to feedback effects (Self et al., 2013). Furthermore, deep/superficial and middle layers were reported to evoke oscillatory neuronal activity at different frequencies (van Kerkoerle et al., 2014). Hence, even if a stimulus activates all cortical layers, the relative contributions of the layers can differ, and can be modulated by stimulus conditions.

Attentional selection of relevant stimuli or stimulus features is a classic example of a feedback mechanism that has inspired research both from the cognitive (Posner, Snyder, & Davidson, 1980) and from the neuroscientific perspective (Moran & Desimone, 1985). The laminar profile of attentional modulation was studied in monkey visual cortex using multi-contact electrodes (Mehta, Ulbert, & Schroeder, 2000; Nandy, Nassi, & Reynolds, 2017; van Kerkoerle, Self, & Roelfsema, 2017). Mehta et al. (2000) found attention effects in superficial and deep layers in V4, and in superficial layers in V2, but not in V1. Using a different task, van Kerkoerle et al. (2017) did report attentional modulation of neuronal activity in superficial and deep layers of V1. An attention effect was also present in layer 4, but this was weaker and at a greater latency compared to superficial and deep layers (van Kerkoerle et al., 2017). Another recent study (Nandy et al., 2017) also observed attention effects in monkey V4. Firing rates were elevated across all cortical layers, but the increase in spiking and higher correlations between spikes were maximal in layer 4 (Nandy et al., 2017). Thus, the evidence on the laminar profile of attentional modulation is mixed. A possible explanation that could consolidate diverging findings is that feedback may target deep and superficial layers in the receiving area, and subsequently up-regulate

activity of feedforward projects (Edelman & Gally, 2013; Supèr & Romeo, 2011). Such re-entrant feedback could result in enhanced activity in the input layer of higher-level receiving areas. For example, if re-entrant feedback arrives in primary visual cortex, it may result in elevated activity in middle layers in extrastriate cortex (Nandy et al., 2017).

1.5 Cortical-depth dependent fMRI

In one of the first human fMRI studies that investigated responses at different cortical depths, Koopmans et al. (2010) presented participants with a simple flickering checkerboard stimulus (for further pioneering cortical-depth-specific fMRI studies, see Koopmans, Barth, Orzada, & Norris, 2011; Polimeni, Witzel, Fischl, Greve, & Wald, 2010; Ress, Glover, Liu, & Wandell, 2007). Because of the effective lack of high-level perceptual qualities (such as perceptual grouping, depth, semantic content, etc.), a stimulus of this kind is supposed to preferentially evoke bottom-up, feedforward processing. In addition to a general signal increase towards the cortical surface due to ascending draining veins, Koopmans et al. (2010) observed a slight local maximum at mid-cortical depth, presumably reflecting neuronal processing of feedforward thalamic input to layer 4.

Recently, attempts have been made to investigate the profile of top-down feedback across cortical depths in humans, using high-resolution fMRI. To this end, Muckli et al. (2015) presented participants with photographs of natural scenes, in which one quadrant was occluded by a mask. They trained a pattern classifier to predict which stimulus had been presented (one out of three photographs) based on the fMRI signal from the region of V1 representing the mask. Prediction accuracy was highest at superficial cortical depth levels, suggesting that information about stimulus context is projected to superficial levels of V1 by means of a top-down mechanism (Muckli et al., 2015).

In the only other depth-specific human fMRI study on top-down feedback known to us to date, Kok et al. (2016) presented participants with stimuli containing illusory contours. The illusory contours caused a response at deep cortical depths in V1. In the context of earlier studies in monkeys, there has been disagreement as to whether the processing of illusory contours involves top-down mechanisms, or lateral connections. Illusory contours were found to cause neuronal activity in V2 (von der

Heydt, Peterhans, & Baumgartner, 1984) and in V1 (Grosof, Shapley, & Hawken, 1993), but the investigators attributed this effect to horizontal connections, and not to top-down feedback. A later electrophysiological study confirmed responses to illusory contours in V1 and V2 (Lee & Nguyen, 2001). The authors do not rule out the possibility that the response to illusory contours is caused by horizontal interactions, but they regard feedback mechanisms as the more likely explanation (because the response to illusory contours in V2 precedes that in V1) (Lee & Nguyen, 2001). Thus, it can be argued that top-down feedback is the most probable explanation of the activation in deep grey matter observed by Kok et al. (2016).

In summary, previous fMRI studies have found evidence for feedforward processing at mid-cortical depths (Koopmans et al., 2010) in human primary visual cortex, and for feedback effects in deep (Kok et al., 2016) and superficial layers (Muckli et al., 2015). The discrepancy regarding the latter observations (i.e. deep vs. superficial feedback effects) is not necessarily surprising, because the respective studies differed widely in their experimental design and consequently may have recruited different feedback mechanisms. For instance, short range vs. long range feedback projections (Barone, Batardiere, Knoblauch, & Kennedy, 2000) and cortical-cortical vs. cortical-subcortical-cortical pathways may result in distinct laminar activation profiles. In addition, disparities regarding analysis methods between studies may have exacerbated differences in the resulting laminar profiles.

1.6 Thesis outline

This thesis comprises three empirical studies, all of which employed high-resolution fMRI at sub-millimetre resolution to study the processing of sensory signals in the early visual cortex. Chapter 2 features a study on feedforward processing in early visual cortex (Marquardt et al., 2018). We measured the response to stimuli at parametrically varied levels of luminance contrast, since luminance contrast is one of the most prevailing stimulus feature in early visual cortex (Albrecht, Geisler, Frazor, & Crane, 2002; Albrecht & Hamilton, 1982), and thus constitutes an ideal test case for feedforward processing. Because ascending draining veins introduce a spatial bias into the cortical-depth dependent fMRI signal, we employed, for the first time in a human fMRI study, a spatial deconvolution model,

whose parameters were derived from simulation results by Markuerkiaga et al. (2016). This approach allowed us to estimate and remove the venous bias, and thus approximate the local neuronal contribution to the fMRI signal at different cortical depths. After accounting for the venous bias, we found the response to peak at deep and mid cortical depths in V1 and V2. There was no evidence for a difference in contrast sensitivity between cortical depths. In line with previous research (Avidan et al., 2002; Buracas & Boynton, 2007; Levitt, Kiper, & Movshon, 1994; Sclar, Maunsell, & Lennie, 1990), contrast sensitivity was higher in V2 than in V1.

The study on feedforward processing (Marquardt et al., 2018) was followed-up by a complementary study on feedback effects in early visual cortex, presented in Chapter 3. In this study, we presented stimuli that were retinotopically identical in one visual hemifield, but varied in their global perceptual qualities. By focusing our analysis on the cortical hemisphere representing the retinotopically constant hemifield, we were able to investigate the cortical depth-profile of top-down feedback effects in early visual cortex. The top-down effect was found to be most pronounced at mid-cortical depths in V2 and V3, and slightly more superficial inV1. Since cortico-cortical feedback connections preferentially target superficial and deep layers (Benevento & Rezak, 1976; Benevento et al., 1975; Ogren & Hendrickson, 1977; Rezak & Benevento, 1979), the observed activation pattern is in accordance with feedback from a higher cortical area re-entering at the level of V1, followed by a feedforward sweep through V2 and V3. Alternatively, our result may be caused by an indirect, cortico-thalamic-cortical feedback effect (Standage & Benevento, 1983; Trojanowski & Jacobson, 1977).

When investigating the cortical depth-profiles of top-down feedback, we observed a strong negative response to our luminance-defined surface stimuli. This negative response occurred at a high latency, and was accompanied by a faster, transient, positive response to the edges of the stimuli. The negative response to a luminance-defined surface, and especially the temporal dynamics of the response, were unexpected for a stimulus characterised by a luminance increment. Thus, we conducted a control experiment, in which we discovered that the negative surface response only occurs when a uniform surface stimulus is presented on a texture pattern background, irrespective of the shape of the stimulus. The decision to present the stimuli on a texture pattern had originally

been motivated by an earlier study (Akin et al., 2014), which used the texture background as a means to improve perceptual figure-ground segregation.

Based on the data acquired for our study on feedback effects (Chapter 3), we estimated the point spread functions of the fMRI signal (Chapter 4). More specifically, we determined the width both of a cortical depth dependent and of a cortical depth independent point spread function. The parameters of the point spread function indicate the level of spatial detail that can be resolved with an imaging system, an aspect that is particularly relevant in the context of sub-millimetre fMRI research.

We continued our investigation of surface perception with a study on the spatial and temporal dynamics of responses to real and illusory contours and surfaces in early visual cortex (Chapter 5). Although this work is still under way, preliminary findings indicate that there was no activation specific to the processing of an illusory surface in V1 and V2. Instead, we observed a slight trend towards a negative response at the retinotopic representation of the illusory surface relative to rest. Because a similar response pattern also occurred in a control condition, it may be explained by a general background suppression that was unrelated to the illusory surface. Moreover, peripheral regions of V2 that did not receive direct bottom-up stimulus input exhibited strong background suppression under a variety of stimulus conditions. For V1, background suppression or a transient, positive background response was observed under different stimulus conditions. However, more data will be needed before any definite conclusions can be drawn.

In summary, this thesis presents investigations into the detailed spatial profile of bottom-up and top-down processing in early visual cortex. We have explored activation profiles of stimuli that were designed to preferentially engage bottom-up or top-down perceptual mechanisms, and have employed a new technique to account for known biases in the cortical-depth dependent fMRI signal. Innovative visualisation methods enabled us to better understand the spatio-temporal patterns of activation in early visual cortex.

1.7 References

Akin, B., Ozdem, C., Eroglu, S., Keskin, D. T., Fang, F., Doerschner, K.,

... Boyaci, H. (2014). Attention modulates neuronal correlates of interhemispheric integration and global motion perception. *Journal of Vision*, 14(12). https://doi.org/10.1167/14.12.30

Albrecht, D. G., Geisler, W. S., Frazor, R. A., & Crane, A. M. (2002). Visual cortex neurons of monkeys and cats: temporal dynamics of the contrast response function. *Journal of Neurophysiology*, 88(2), 888–913.

Albrecht, D. G., & Hamilton, D. B. (1982). Striate cortex of monkey and cat: contrast response function. *Journal of Neurophysiology*, 48(1), 217–237.

Anderson, J. C., & Martin, K. A. C. (2009). The synaptic connections between cortical areas V1 and V2 in macaque monkey. *The Journal of Neuroscience: The Official Journal of the Society for Neuroscience*, 29(36), 11283–11293. https://doi.org/10.1523/JNEUROSCI.5757-08.2009

Avidan, G., Harel, M., Hendler, T., Ben-Bashat, D., Zohary, E., & Malach, R. (2002). Contrast sensitivity in human visual areas and its relationship to object recognition. *Journal of Neurophysiology*, 87(6), 3102–3116.

Barone, P., Batardiere, A., Knoblauch, K., & Kennedy, H. (2000). Laminar distribution of neurons in extrastriate areas projecting to visual areas V1 and V4 correlates with the hierarchical rank and indicates the operation of a distance rule. *The Journal of Neuroscience: The Official Journal of the Society for Neuroscience*, 20(9), 3263–3281.

Benevento, L. A., & Rezak, M. (1976). The cortical projections of the inferior pulvinar and adjacent lateral pulvinar in the rhesus monkey (Macaca mulatta): an autoradiographic study. *Brain Research*, 108(1), 1–24.

Benevento, L. A., Rezak, M., & Bos, J. (1975). Extrageniculate projections to layers VI and I of striate cortex (area 17) in the rhesus monkey (Macaca mulatta). *Brain Research*, 96(1), 51–55.

Blasdel, G. G., & Lund, J. S. (1983). Termination of afferent axons in macaque striate cortex. *The Journal of Neuroscience: The Official Journal of the Society for Neuroscience*, 3(7), 1389–1413.

Bower, G. H., Clark, M. C., Lesgold, A. M., & Winzenz, D. (1969). Hierarchical retrieval schemes in recall of categorized word lists. *Journal of Verbal Learning and Verbal Behavior*, 8(3), 323–343. https://doi.org/10.1016/S0022-5371(69)80124-6

Buduma, N., & Locascio, N. (2017). Fundamentals of deep learning: designing next-generation machine intelligence algorithms.

Buracas, G. T., & Boynton, G. M. (2007). The effect of spatial attention on contrast response functions in human visual cortex. *The Journal of Neuroscience: The Official Journal of the Society for Neuroscience*, 27(1), 93–97. https://doi.org/10.1523/JNEUROSCI.3162-06.2007

Callaway, E. M. (1998). Local circuits in primary visual cortex of the macaque monkey. *Annual Review of Neuroscience*, 21(1), 47–74. https://doi.org/10.1146/annurev.neuro.21.1.47

Chalmers, D. J. (2007). Consciousness and its Place in Nature. In S. P. Stich & T. A. Warfield (Eds.), *The Blackwell Guide to Philosophy of Mind* (pp. 102–142). https://doi.org/10.1002/9780470998762.ch5

Cheng, K., Waggoner, R. A., & Tanaka, K. (2001). Human ocular dominance columns as revealed by high-field functional magnetic resonance imaging. *Neuron*, 32(2), 359–374.

Cheour, M., Shestakova, A., Alku, P., Ceponiene, R., & Näätänen, R. (2002). Mismatch negativity shows that 3-6-year-old children can learn to discriminate non-native speech sounds within two months. *Neuroscience Letters*, 325(3), 187–190.

Coltheart, M. (2006). What has functional neuroimaging told us about the mind (so far)? *Cortex; a Journal Devoted to the Study of the Nervous System and Behavior*, 42(3), 323–331.

Constantinople, C. M., & Bruno, R. M. (2013). Deep cortical layers are activated directly by thalamus. *Science* (New York, N.Y.), 340(6140), 1591–1594. https://doi.org/10.1126/science.1236425

De Martino, F., Yacoub, E., Kemper, V., Moerel, M., Uludag, K., De Weerd, P., ... Formisano, E. (2017). The impact of ultra-high field MRI on cognitive and computational neuroimaging. *NeuroImage*. https://doi.org/10.1016/j.neuroimage.2017.03.060

Douglas, R. J., Martin, K. A. C., & Whitteridge, D. (1989). A Canonical Microcircuit for Neocortex. *Neural Computation*, 1(4), 480–488. https://doi.org/10.1162/neco.1989.1.4.480

Durbin, R., & Rumelhart, D. E. (1989). Product Units: A Computationally Powerful and Biologically Plausible Extension to Backpropagation Networks. *Neural Computation*, 1(1), 133–142. https://doi.org/10.1162/neco.1989.1.1.133

Edelman, G. M., & Gally, J. A. (2013). Reentry: a key mechanism for integration of brain function. *Frontiers in Integrative Neuroscience*, 7, 63. https://doi.org/10.3389/fnint.2013.00063

Engel, S. A., Glover, G. H., & Wandell, B. A. (1997). Retinotopic organization in human visual cortex and the spatial precision of functional MRI. *Cerebral Cortex* (New York, N.Y.: 1991), 7(2), 181–192.

Felleman, D. J., & Van Essen, D. C. (1991). Distributed hierarchical processing in the primate cerebral cortex. *Cerebral Cortex* (New York, N.Y.: 1991), 1(1), 1–47.

Gilbert, C. D., & Wiesel, T. N. (1983). Clustered intrinsic connections in cat visual cortex. *The Journal of Neuroscience: The Official Journal of the Society for Neuroscience*, 3(5), 1116–1133.

Goncalves, N. R., Ban, H., Sánchez-Panchuelo, R. M., Francis, S. T., Schluppeck, D., & Welchman, A. E. (2015). 7 tesla FMRI reveals systematic functional organization for binocular disparity in dorsal visual cortex.

The Journal of Neuroscience: The Official Journal of the Society for Neuroscience, 35(7), 3056–3072. https://doi.org/10.1523/JNEUROSCI.3047-14.2015

Grent-'t-Jong, T., & Woldorff, M. G. (2007). Timing and sequence of brain activity in top-down control of visual-spatial attention. *PLoS Biology*, 5(1), e12. https://doi.org/10.1371/journal.pbio.0050012

Grosof, D. H., Shapley, R. M., & Hawken, M. J. (1993). Macaque V1 neurons can signal 'illusory' contours. *Nature*, 365(6446), 550–552. https://doi.org/10.1038/365550a0

Güçlü, U., & van Gerven, M. A. J. (2015). Deep Neural Networks Reveal a Gradient in the Complexity of Neural Representations across the Ventral Stream. *The Journal of Neuroscience: The Official Journal of the Society for Neuroscience*, 35(27), 10005–10014. https://doi.org/10.1523/JNEUROSCI.5023-14.2015

Henderickson, A. E., Wilson, J. R., & Ogren, M. P. (1978). The neurological organization of pathways between the dorsal lateral geniculate nucleus and visual cortex in old world and new world primates. *The Journal of Comparative Neurology*, 182(1), 123–136. https://doi.org/10.1002/cne.901820108

Hochstein, S., & Ahissar, M. (2002). View from the top: hierarchies and reverse hierarchies in the visual system. *Neuron*, 36(5), 791–804.

Hubel, D. H., & Livingstone, M. S. (1990). Color and contrast sensitivity in the lateral geniculate body and primary visual cortex of the macaque monkey. *The Journal of Neuroscience: The Official Journal of the Society for Neuroscience*, 10(7), 2223–2237.

Hubel, D. H., & Wiesel, T. N. (1968). Receptive fields and functional architecture of monkey striate cortex. *The Journal of Physiology*, 195(1), 215–243. https://doi.org/10.1113/jphysiol.1968.sp008455

Hubel, D. H., & Wiesel, T. N. (1972). Laminar and columnar distribution of geniculo-cortical fibers in the macaque monkey. *The Journal of Comparative Neurology*, 146(4), 421–450. https://doi.org/10.1002/cne.901460402

Itti, L., Koch, C., & Niebur, E. (1998). A model of saliency-based visual attention for rapid scene analysis. *IEEE Transactions on Pattern Analysis and Machine Intelligence*, 20(11), 1254–1259. https://doi.org/10.1109/34.730558

Izhikevich, E. M. (2004). Which Model to Use for Cortical Spiking Neurons? *IEEE Transactions on Neural Networks*, 15(5), 1063–1070. https://doi.org/10.1109/TNN.2004.832719

Kashyap, S., Ivanov, D., Havlicek, M., Sengupta, S., Poser, B. A., & Uludağ, K. (2018). Resolving laminar activation in human V1 using ultra-high spatial resolution fMRI at 7T. *Scientific Reports*, 8(1), 17063. https://doi.org/10.1038/s41598-018-35333-3

Kleffner, D. A., & Ramachandran, V. S. (1992). On the perception of shape from shading. *Perception & Psychophysics*, 52(1), 18–36.

Kok, P., Bains, L. J., van Mourik, T., Norris, D. G., & de Lange, F. P. (2016). Selective Activation of the Deep Layers of the Human Primary Visual Cortex by Top-Down Feedback. *Current Biology*, 26(3), 371–376. https://doi.org/10.1016/j.cub.2015.12.038

Koopmans, P. J., Barth, M., & Norris, D. G. (2010). Layer-specific BOLD activation in human V1. *Human Brain Mapping*, 31(9), 1297–1304. https://doi.org/10.1002/hbm.20936

Koopmans, P. J., Barth, M., Orzada, S., & Norris, D. G. (2011). Multi-echo fMRI of the cortical laminae in humans at 7T. *NeuroImage*, 56(3), 1276–1285. https://doi.org/10.1016/j.neuroimage.2011.02.042

Lamme, V. A., & Roelfsema, P. R. (2000). The distinct modes of vision offered by feedforward and recurrent processing. *Trends in Neurosciences*, 23(11), 571–579.

Lee, T. S., & Nguyen, M. (2001). Dynamics of subjective contour formation in the early visual cortex. *Proceedings of the National Academy of Sciences of the United States of America*, 98(4), 1907–1911. https://doi.org/10.1073/pnas.031579998

Levitt, J. B., Kiper, D. C., & Movshon, J. A. (1994). Receptive fields and functional architecture of macaque V2. *Journal of Neurophysiology*, 71(6), 2517–2542.

Libet, B., Gleason, C. A., Wright, E. W., & Pearl, D. K. (1983). Time of conscious intention to act in relation to onset of cerebral activity (readiness-potential). The unconscious initiation of a freely voluntary act. *Brain: A Journal of Neurology*, 106 (Pt 3), 623–642.

Lund, J. S. (1988). Anatomical Organization of Macaque Monkey Striate Visual Cortex. *Annual Review of Neuroscience*, 11(1), 253–288. https://doi.org/10.1146/annurev.ne.11.030188.001345

Markuerkiaga, I., Barth, M., & Norris, D. G. (2016). A cortical vascular model for examining the specificity of the laminar BOLD signal. *NeuroImage*, 132, 491–498. https://doi.org/10.1016/j.neuroimage.2016.02.073

Marquardt, I., Schneider, M., Gulban, O. F., Ivanov, D., & Uludağ, K. (2018). Cortical depth profiles of luminance contrast responses in human V1 and V2 using 7 T fMRI. *Human Brain Mapping*. https://doi.org/10.1002/hbm.24042

Maunsell, J. H., & Gibson, J. R. (1992). Visual response latencies in striate cortex of the macaque monkey. *Journal of Neurophysiology*, 68(4), 1332–1344. https://doi.org/10.1152/jn.1992.68.4.1332

Maunsell, J. H., & Newsome, W. T. (1987). Visual processing in monkey extrastriate cortex. *Annual Review of Neuroscience*, 10, 363–401. https://doi.org/10.1146/annurev.ne.10.030187.002051

Mazzoni, P., Andersen, R. A., & Jordan, M. I. (1991). A more biologically plausible learning rule for neural networks. *Proceedings of the National Academy of Sciences of the United States of America*, 88(10), 4433–4437.

McGuire, B. A., Gilbert, C. D., Rivlin, P. K., & Wiesel, T. N. (1991). Targets of horizontal connections in macaque primary visual cortex. *The Journal of Comparative Neurology*, 305(3), 370–392. https://doi.org/10.1002/cne.903050303

Mehta, A. D., Ulbert, I., & Schroeder, C. E. (2000). Intermodal selective attention in monkeys. II: physiological mechanisms of modulation. *Cerebral Cortex* (New York, N.Y.: 1991), 10(4), 359–370.

Moore, T., & Armstrong, K. M. (2003). Selective gating of visual signals by microstimulation of frontal cortex. *Nature*, 421(6921), 370–373. https://doi.org/10.1038/nature01341

Moore, T., & Fallah, M. (2004). Microstimulation of the frontal eye field and its effects on covert spatial attention. *Journal of Neurophysiology*, 91(1), 152–162. https://doi.org/10.1152/jn.00741.2002

Moran, J., & Desimone, R. (1985). Selective attention gates visual processing in the extrastriate cortex. *Science* (New York, N.Y.), 229(4715), 782–784.

Muckli, L., De Martino, F., Vizioli, L., Petro, L. S., Smith, F. W., Ugurbil, K., ... Yacoub, E. (2015). Contextual Feedback to Superficial Layers of V1. *Current Biology*: CB, 25(20), 2690–2695. https://doi.org/10.1016/j.cub.2015.08.057

Müller, N. G., & Kleinschmidt, A. (2004). The attentional 'spotlight's' penumbra: center-surround modulation in striate cortex. *Neuroreport*, 15(6), 977–980.

Nandy, A. S., Nassi, J. J., & Reynolds, J. H. (2017). Laminar Organization of Attentional Modulation in Macaque Visual Area V4. *Neuron*, 93(1), 235–246. https://doi.org/10.1016/j.neuron.2016.11.029

Nasr, S., Polimeni, J. R., & Tootell, R. B. H. (2016). Interdigitated Color- and Disparity-Selective Columns within Human Visual Cortical Areas V2 and V3. *The Journal of Neuroscience: The Official Journal of the Society for Neuroscience*, 36(6), 1841–1857. https://doi.org/10.1523/JNEUROSCI.3518-15.2016

Nishimoto, S., Vu, A. T., Naselaris, T., Benjamini, Y., Yu, B., & Gallant, J. L. (2011). Reconstructing visual experiences from brain activity evoked by natural movies. *Current Biology*: CB, 21(19), 1641–1646. https://doi.org/10.1016/j.cub.2011.08.031

Nurminen, L., Merlin, S., Bijanzadeh, M., Federer, F., & Angelucci, A. (2018). Top-down feedback controls spatial summation and response amplitude in primate visual cortex. *Nature Communications*, 9(1), 2281. https://doi.org/10.1038/s41467-018-04500-5

Ogawa, S., Tank, D. W., Menon, R., Ellermann, J. M., Kim, S. G., Merkle,

H., & Ugurbil, K. (1992). Intrinsic signal changes accompanying sensory stimulation: functional brain mapping with magnetic resonance imaging. *Proceedings of the National Academy of Sciences of the United States of America*, 89(13), 5951–5955.

Ogren, M. P., & Hendrickson, A. E. (1977). The distribution of pulvinar terminals in visual areas 17 and 18 of the monkey. *Brain Research*, 137(2), 343–350.

O'Toole, A. J., Jiang, F., Abdi, H., & Haxby, J. V. (2005). Partially distributed representations of objects and faces in ventral temporal cortex. *Journal of Cognitive Neuroscience*, 17(4), 580–590. https://doi.org/10.1162/0898929053467550

Page, M. P. A. (2006). What can't functional neuroimaging tell the cognitive psychologist? *Cortex; a Journal Devoted to the Study of the Nervous System and Behavior*, 42(3), 428–443.

Phillips, W. A. (1974). On the distinction between sensory storage and short-term visual memory. *Perception & Psychophysics*, 16(2), 283–290. https://doi.org/10.3758/BF03203943

Polimeni, J. R., Fischl, B., Greve, D. N., & Wald, L. L. (2010). Laminar analysis of 7T BOLD using an imposed spatial activation pattern in human V1. *NeuroImage*, 52(4), 1334–1346. https://doi.org/10.1016/j.neuroimage.2010.05.005

Polimeni, J. R., Renvall, V., Zaretskaya, N., & Fischl, B. (2017). Analysis strategies for high-resolution UHF-fMRI data. *NeuroImage*. https://doi.org/10.1016/j.neuroimage.2017.04.053

Polimeni, J. R., Witzel, T., Fischl, B., Greve, D. N., & Wald, L. L. (2010). Identifying common-source driven correlations in resting-state fMRI via laminar-specific analysis in the human visual cortex. *Proc. Intl. Soc. Mag. Reson. Med.*, 18, 353.

Poser, B. A., Koopmans, P. J., Witzel, T., Wald, L. L., & Barth, M. (2010). Three dimensional echo-planar imaging at 7 Tesla. *NeuroImage*, 51(1), 261–266. https://doi.org/10.1016/j.neuroimage.2010.01.108

Posner, M. I., Snyder, C. R., & Davidson, B. J. (1980). Attention and the detection of signals. *Journal of Experimental Psychology*, 109(2), 160–174.

Pylyshyn, Z. W. (1973). What the mind's eye tells the mind's brain: A critique of mental imagery. *Psychological Bulletin*, 80(1), 1–24. https://doi.org/10.1037/h0034650

Ress, D., Glover, G. H., Liu, J., & Wandell, B. (2007). Laminar profiles of functional activity in the human brain. *NeuroImage*, 34(1), 74–84. https://doi.org/10.1016/j.neuroimage.2006.08.020

Rezak, M., & Benevento, L. A. (1979). A comparison of the organization of the projections of the dorsal lateral geniculate nucleus, the inferior pulvinar and adjacent lateral pulvinar to primary visual cortex (area 17) in the

macaque monkey. *Brain Research*, 167(1), 19–40.
Rockland, K. S. (2017). What do we know about laminar connectivity? *NeuroImage*. https://doi.org/10.1016/j.neuroimage.2017.07.032
Rockland, K. S., & Pandya, D. N. (1979). Laminar origins and terminations of cortical connections of the occipital lobe in the rhesus monkey. *Brain Research*, 179(1), 3–20. https://doi.org/10.1016/0006-8993(79)90485-2
Rockland, K. S., & Virga, A. (1989). Terminal arbors of individual 'feedback' axons projecting from area V2 to V1 in the macaque monkey: a study using immunohistochemistry of anterogradely transported Phaseolus vulgaris-leucoagglutinin. *The Journal of Comparative Neurology*, 285(1), 54–72. https://doi.org/10.1002/cne.902850106
Saalmann, Y. B., Pigarev, I. N., & Vidyasagar, T. R. (2007). Neural mechanisms of visual attention: how top-down feedback highlights relevant locations. *Science* (New York, N.Y.), 316(5831), 1612–1615. https://doi.org/10.1126/science.1139140
Schroeder, C. E., Mehta, A. D., & Givre, S. J. (1998). A spatiotemporal profile of visual system activation revealed by current source density analysis in the awake macaque. *Cerebral Cortex* (New York, N.Y.: 1991), 8(7), 575–592.
Sclar, G., Maunsell, J. H., & Lennie, P. (1990). Coding of image contrast in central visual pathways of the macaque monkey. *Vision Research*, 30(1), 1–10.
Self, M. W., Peters, J. C., Possel, J. K., Reithler, J., Goebel, R., Ris, P., ... Roelfsema, P. R. (2016). The Effects of Context and Attention on Spiking Activity in Human Early Visual Cortex. *PLoS Biology*, 14(3), e1002420. https://doi.org/10.1371/journal.pbio.1002420
Self, M. W., van Kerkoerle, T., Supèr, H., & Roelfsema, P. R. (2013). Distinct roles of the cortical layers of area V1 in figure-ground segregation. *Current Biology*: CB, 23(21), 2121–2129. https://doi.org/10.1016/j.cub.2013.09.013
Sherman, S. M. (2005). Thalamic relays and cortical functioning. *Progress in Brain Research*, 149, 107–126. https://doi.org/10.1016/S0079-6123(05)49009-3
Sherman, S. M., & Guillery, R. W. (2002). The role of the thalamus in the flow of information to the cortex. *Philosophical Transactions of the Royal Society of London. Series B, Biological Sciences*, 357(1428), 1695–1708. https://doi.org/10.1098/rstb.2002.1161
Sherman, S. M., & Koch, C. (1986). The control of retinogeniculate transmission in the mammalian lateral geniculate nucleus. *Experimental Brain Research*, 63(1), 1–20.
Silver, M. A., Ress, D., & Heeger, D. J. (2007). Neural correlates of sustained spatial attention in human early visual cortex. *Journal of Neurophysiol-*

ogy, 97(1), 229–237. https://doi.org/10.1152/jn.00677.2006

Slotnick, S. D., Schwarzbach, J., & Yantis, S. (2003). Attentional inhibition of visual processing in human striate and extrastriate cortex. *NeuroImage*, 19(4), 1602–1611.

Somers, D. C., Dale, A. M., Seiffert, A. E., & Tootell, R. B. (1999). Functional MRI reveals spatially specific attentional modulation in human primary visual cortex. *Proceedings of the National Academy of Sciences of the United States of America*, 96(4), 1663–1668.

Standage, G. P., & Benevento, L. A. (1983). The organization of connections between the pulvinar and visual area MT in the macaque monkey. *Brain Research*, 262(2), 288–294.

Sternberg, S. (1966). High-speed scanning in human memory. *Science* (New York, N.Y.), 153(3736), 652–654.

Supèr, H., & Romeo, A. (2011). Feedback enhances feedforward figure-ground segmentation by changing firing mode. *PloS One*, 6(6), e21641. https://doi.org/10.1371/journal.pone.0021641

Tootell, R. B., Hadjikhani, N., Hall, E. K., Marrett, S., Vanduffel, W., Vaughan, J. T., & Dale, A. M. (1998). The retinotopy of visual spatial attention. *Neuron*, 21(6), 1409–1422.

Tootell, R. B., Hamilton, S. L., & Switkes, E. (1988). Functional anatomy of macaque striate cortex. IV. Contrast and magno-parvo streams. *The Journal of Neuroscience: The Official Journal of the Society for Neuroscience*, 8(5), 1594–1609.

Tootell, R. B., & Nasr, S. (2017). Columnar Segregation of Magnocellular and Parvocellular Streams in Human Extrastriate Cortex. *The Journal of Neuroscience: The Official Journal of the Society for Neuroscience*. https://doi.org/10.1523/JNEUROSCI.0690-17.2017

Trojanowski, J. Q., & Jacobson, S. (1977). The morphology and laminar distribution of cortico-pulvinar neurons in the rhesus monkey. *Experimental Brain Research*, 28(1–2), 51–62.

Uludağ, K., & Blinder, P. (2017). Linking brain vascular physiology to hemodynamic response in ultra-high field MRI. *NeuroImage*. https://doi.org/10.1016/j.neuroimage.2017.02.063

Uttal, W. R. (2001). The new phrenology: the limits of localizing cognitive processes in the brain. In Life and Mind: Philosophical Issues in Biology and Psychology. Cambridge, Mass: MIT Press.

van Kerkoerle, T., Self, M. W., Dagnino, B., Gariel-Mathis, M.-A., Poort, J., van der Togt, C., & Roelfsema, P. R. (2014). Alpha and gamma oscillations characterize feedback and feedforward processing in monkey visual cortex. *Proceedings of the National Academy of Sciences*, 111(40), 14332–14341. https://doi.org/10.1073/pnas.1402773111

van Kerkoerle, T., Self, M. W., & Roelfsema, P. R. (2017). Layer-specificity

in the effects of attention and working memory on activity in primary visual cortex. *Nature Communications*, 8, 13804. https://doi.org/10.1038/ncomms13804

Van Orden, G. C., & Paap, K. R. (1997). Functional Neuroimages Fail to Discover Pieces of Mind in the Parts of the Brain. *Philosophy of Science*, 64, S85–S94. https://doi.org/10.1086/392589

VanRullen, R., & Thorpe, S. J. (2001). The time course of visual processing: from early perception to decision-making. *Journal of Cognitive Neuroscience*, 13(4), 454–461.

von der Heydt, R., Peterhans, E., & Baumgartner, G. (1984). Illusory contours and cortical neuron responses. *Science* (New York, N.Y.), 224(4654), 1260–1262.

Von Neumann, J., & Churchland, P. M. (2000). The computer and the brain (2. ed). In Mrs. Hepsa Ely Silliman Memorial Lectures (2. ed). New Haven, Conn.: Yale Nota Bene.

Winkler, I., Kujala, T., Tiitinen, H., Sivonen, P., Alku, P., Lehtokoski, A., ... Näätänen, R. (1999). Brain responses reveal the learning of foreign language phonemes. *Psychophysiology*, 36(5), 638–642.

Zimmermann, J., Goebel, R., De Martino, F., van de Moortele, P.-F., Feinberg, D., Adriany, G., ... Yacoub, E. (2011). Mapping the organization of axis of motion selective features in human area MT using high-field fMRI. *PloS One*, 6(12), e28716. https://doi.org/10.1371/journal.pone.0028716

2

Cortical depth profiles of luminance contrast responses in V1 and V2

Corresponding publication:

Marquardt, I., Schneider, M., Gulban, O. F., Ivanov, D., & Uludağ, K. (2018). Cortical depth profiles of luminance contrast responses in human V1 and V2 using 7 T fMRI. *Human Brain Mapping*. https://doi.org/10.1002/hbm.24042

2.1 Abstract

Neural activity in early visual cortex is modulated by luminance contrast. Cortical depth (i.e. laminar) contrast responses have been studied in monkey early visual cortex, but not in humans. In addition to the high spatial resolution needed and the ensuing low signal-to-noise ratio, laminar studies in humans using fMRI are hampered by the strong venous vascular weighting of the fMRI signal. In this study, we measured luminance contrast responses in human V1 and V2 with high-resolution fMRI at 7 T. In order to account for the effect of intra-cortical ascending veins, we applied a novel spatial deconvolution model to the fMRI depth profiles. Before spatial deconvolution, the contrast response in V1 showed a slight local maximum at mid cortical depth, whereas V2 exhibited a monotonic signal increase towards the cortical surface. After applying the deconvolution method, both V1 and V2 showed a pronounced local maximum at mid cortical depth, with an additional peak in deep grey matter, especially in V1. Moreover, we found a difference in contrast sensitivity between V1 and V2, but no evidence for variations in contrast sensitivity as a function of cortical depth. These findings are in agreement with results obtained in non-human primates, but further research will be needed to validate the spatial deconvolution approach.

2.2 Introduction

The visual system is conceptualised as a hierarchical structure, in which information is conveyed from the eye, through the lateral geniculate nucleus (LGN) of the thalamus, the primary visual cortex (V1), on to extrastriate cortical areas (Felleman & Van Essen, 1991). This feedforward sweep carries incoming sensory information and is complemented by feedback mechanisms related to higher cognitive processes, such as attention. The feedback mechanisms control the flow of sensory information and modify its content according to cognition and behavioural needs (Lamme & Roelfsema, 2000).

As information is processed along the visual hierarchy, neurons become selective for increasingly complex stimulus features – i.e., their preferred stimuli evolve from simple spots of light to more elaborate stimulus properties (Maunsell & Newsome, 1987). Neurons in the early

stages of the visual system are particularly sensitive to luminance contrast (Albrecht, Geisler, Frazor, & Crane, 2002; Albrecht & Hamilton, 1982). For most neurons in early visual areas, the relationship between stimulus contrast and neuronal response is not linear, but can be modeled by a power function or a combination of power functions (Albrecht et al., 2002; Albrecht & Hamilton, 1982; Boynton, Demb, Glover, & Heeger, 1999; Sclar, Maunsell, & Lennie, 1990). Within the hierarchy of early visual areas, there is a gradient of contrast response properties: The responses of LGN, V1, V2, and progressively higher visual areas are successively less modulated by luminance contrast – the contrast response function becomes steeper, and the response saturates at a lower contrast (Avidan et al., 2002; Buracas & Boynton, 2007; Levitt, Kiper, & Movshon, 1994; Sclar et al., 1990).

Tootell et al. (1995) presented drifting square wave gratings at various luminance contrasts and compared the contrast sensitivity in V1 and MT. In accordance with electrophysiological findings in monkeys (Sclar et al., 1990), fMRI contrast sensitivity in humans was found to be considerably higher in MT than in V1, but only slightly higher in V2 compared to V1. The respective fMRI data were acquired at voxel sizes of $3 \times 3 \times 5$ to 6 mm^3 or $1.6 \times 1.6 \times 4$ mm^3 (Tootell et al., 1995). Another early fMRI study (Boynton et al., 1999) used contrast-reversing sine wave gratings at six contrast levels to study contrast response properties in early visual cortex of two human observers, at an anisotropic voxel size of $1.02 \times 1.02 \times 4$ mm^3. For contrast levels well above the perceptual threshold, the contrast discrimination function (relating the minimum detectable contrast increment to the absolute contrast of the reference stimulus) can be modelled with a power function (Legge, 1981), and, if the range of contrast levels is very broad, a combination of power functions can be used (Boynton et al., 1999). In the study by Boynton et al. (1999), the same function yielded a good fit for both the behavioural and the fMRI data for V1, V2, and V3, suggesting that contrast discrimination judgements are instantiated by neuronal processing in these areas. A significant difference in contrast sensitivity between these early visual areas was not reported (Boynton et al., 1999). Using a similar experimental design, Buracas et al. (2005) presented further evidence for a link between behavioural performance on a contrast discrimination task and the fMRI response in early visual cortex. Moreover, although not explicitly stated, their data (Buracas

et al., 2005) and a follow-up study (Buracas & Boynton, 2007) support an increase of contrast sensitivity along the visual hierarchy in V1, V2, V3, and MT+. These two studies were conducted at an isotropic spatial resolution of $3 \times 3 \times 3$ mm^3. A more recent fMRI study (Yan et al., 2014) confirmed these earlier findings, and presented evidence for higher contrast sensitivity for peripheral than for central vision, at a voxel size of $2 \times 2 \times 2$ mm^3. All these fMRI studies were performed at 1.5 and 3 Tesla (T). Tootell & Nasr (2017) studied response properties of extrastriate visual cortex at 7T with a voxel size of $1 \times 1 \times 1$ mm^3. In accordance with previous low-resolution fMRI experiments and animal studies, they found differences in the contrast response between lower and higher extrastriate visual areas. In addition, they found clusters of response variation along the cortical surface, which may correspond to functional subdivisions previously only reported in macaque (Tootell & Nasr, 2017).

With the exception of Tootell & Nasr (2017), previous fMRI studies in humans averaged the signal over entire cortical areas, such as V1 and V2, thereby treating these areas as homogeneous structures and disregarding potential variability in the contrast response properties within each area. However, cortical areas are not homogeneous structures (Lund, 1988): Instead, cortical areas can be divided into cortical columns (orthogonal to the surface of the cortex) and layers (across the cortical depth, i.e. orthogonal to the columns). Most cortical areas are divided into six main layers based on microstructural features (Douglas & Martin, 2004; Fitzpatrick, Itoh, & Diamond, 1983; Kleinnijenhuis et al., 2013; Lund, 1973, 1988). Layers 3 and 4 of the primate visual cortex are further divided into sub-layers (Lund, 1988). Electrophysiological (Hubel & Livingstone, 1990; Hubel & Wiesel, 1972) and tracer (Blasdel & Lund, 1983; Henderickson, Wilson, & Ogren, 1978; Rockland & Pandya, 1979; Tootell, Hamilton, & Switkes, 1988) studies in V1 have shown that thalamocortical projections primarily target layers 4C and 6, whereas projections from V2 to V1 terminate in layers 1, 2, and 5 (Anderson & Martin, 2009; Rockland & Pandya, 1979; Rockland & Virga, 1989). Based on this evidence, Callaway (1998) proposed a two-stage model of information processing in V1. According to the model, thalamorecipient layer 4C constitutes the first cortical feedforward module. It projects feedforward connections to the second-level feedforward module located in the supragranular layers. Layer 6 acts as the first-level feedback

module, receiving collaterals of the thalamic feedforward input to layer 4C as well as the output from layer 4C. In other words, this feedback module is characterised by sampling both the feedforward module's input and output (Callaway, 1998).

In recent years, high-resolution fMRI studies at ultra-high field strength (7 T and above) have demonstrated the feasibility of sampling functional signals at different cortical depth levels in humans (for recent reviews, see De Martino et al., 2017; Dumoulin, Fracasso, van der Zwaag, Siero, & Petridou, 2017; Polimeni, Renvall, Zaretskaya, & Fischl, 2017; Uludağ & Blinder, 2018). Two recurrent findings from fMRI studies investigating the cortical-depth-dependent responses in humans sensory cortices are: (1) a signal increase towards the cortical surface and (2) an increased signal around mid-level grey matter, which is detected in some studies but not in others.

The first finding is attributed to the fact that the laminar specificity of the fMRI signal is degraded by the properties of the vascular system, in particular when gradient-echo (GE) fMRI sequences are used (see Uludağ & Blinder, 2018, for an overview). After having passed the capillaries and venules, blood drains through ascending veins of increasing diameter towards the cortical surface. Because GE fMRI sequences have a strong weighting towards the signal originating from veins (Uludağ, Müller-Bierl, & Uğurbil, 2009), the reported signal increases towards the cortical surface are thought to originate from an increasingly larger contribution from draining veins (Koopmans, Barth, Orzada, & Norris, 2011; Markuerkiaga, Barth, & Norris, 2016).

The cause of the (elusive) second finding is less clear. One possible explanation suggests a neuronal origin. The thalamic input to primary visual cortex terminates mainly in layer 4 and 6 (Blasdel & Lund, 1983; Henderickson et al., 1978; Hubel & Livingstone, 1990; Hubel & Wiesel, 1972; Rockland & Pandya, 1979; Tootell et al., 1988). Thus, increased metabolic demand due to local processing of incoming signals at mid-cortical depth may explain a peak in the amplitude of the haemodynamic response. However, an alternative explanation is offered by the differences in vascular density at different cortical depths (Uludağ & Blinder, 2018; Weber, Keller, Reichold, & Logothetis, 2008). In addition to the six cortical layers that are distinguished with respect to cytoarchitectonic features, the cortex can also be divided into four vascular layers, which are delineated based on the structure and density of blood vessels (Duvernoy,

Delon, & Vannson, 1981). According to this alternative explanation, the peak fMRI signal at mid-cortical depth may be unrelated to differences in neuronal processing across cortical layers, but an artefact of a higher vascular density at mid-cortical depth. These two hypotheses are not mutually exclusive; i.e. a peak at mid-level grey matter could be the result of a combination of neuronal and vascular causes.

In this study, we investigated the contrast response properties of human V1 and V2 across cortical depths in an fMRI experiment at 7T, and applied spatial deconvolution based on the simulations by Markuerkiaga et al. (2016) in order to account for the ascending vein effect. We employed a visual stimulus with a parametrically-varied luminance contrast. The rationale of this approach is twofold: First, the processing of luminance contrast is probably the primary computational task carried out in early visual cortex. Altering the contrast of a stimulus is expected to be an effective way to reveal the profile of feedforward processing across the cortical depth in early visual cortex. Second, whereas the progression of contrast response properties has been studied along the hierarchy of visual areas in both monkeys (Albrecht & Hamilton, 1982; Tootell et al., 1988) and humans (Avidan et al., 2002; Boynton et al., 1999; Levitt et al., 1994; Sclar et al., 1990; Tootell et al., 1995), the responsiveness to contrast and the contrast sensitivity at different depths of early visual cortex has not been studied in humans so far. The only high-resolution fMRI study on contrast responses in humans has studied variations along the cortical surface, but has not investigated response properties at different cortical depths (Tootell & Nasr, 2017).

In the present study, we were able to extract cortical depth profiles of GE-fMRI signal changes in human V1 and V2 at 7T in response to a contrast stimulus and demonstrate that the shape of the depth profiles changes with spatial deconvolution. Only when accounting for the draining vein effect, both V1 and V2 show peak response amplitudes at mid-grey matter, as expected for feedforward processing of visual stimuli. In addition, the contrast sensitivity was found to be different between V1 and V2 in agreement with previous studies, but constant across cortical depth, both before and after spatial deconvolution. This study demonstrates the potential of high-resolution fMRI in humans at 7 T to investigate visual processing and perception, if vascular and MRI physics confounds are properly accounted for.

2.3 Methods

2.3.1 Experimental design

Healthy participants (n=11, age between 23 and 35 years, mean age 29 years, 7 females) gave informed consent before the experiment, and the study protocol was approved by the local ethics committee of the Faculty for Psychology & Neuroscience, Maastricht University. Subjects were presented visual grating stimuli at luminance contrasts of 2.5%, 6.1%, 16.3%, and 72.0% (Figure 2.1 A). The grating stimulus had the form of an annulus, with an inner radius of 1.5 degrees of visual angle and an outer radius of 4.0 degrees of visual angle. Within the annulus was a square wave grating with a spatial frequency of 2.0 degrees of visual angle. Stimuli were created with Psychopy (Peirce, 2007, 2008) and projected on a translucent screen mounted behind the MRI head coil, via a mirror mounted at the end of the scanner bore. The projection intensity was calibrated based on luminance measurements taken with a photometer. Stimuli were presented in a block design with stimulus block durations of 11.76 s and variable rest periods in random order (20.58 s, 23.52 s, or 26.46 s). Each run began with an initial rest period with a fixed duration of 23.52 s, and ended with a rest period of one of the three possible durations. Within each stimulus block, the luminance contrast of the stimulus was constant, and the stimulus orientation was altered between 0, 45, 90 and 135 degrees in a random order. Each orientation was presented for 1.68 s, interspersed with equally long inter-stimulus intervals (Figure 2.1 B). All lights in the scanner room were switched off during the experiment, and black cardboard was placed on the inside of the MRI transmit coil in order to minimise light reflection.

Throughout the experiment, participants were asked to fixate a central dot and to report randomly occurring changes in the dot's colour by button presses to retain the subjects' attention. These targets were presented for 300 ms, with a mean inter-trial interval of 16 s (range ±4 s). No targets occurred during the first and last 20 s of each run. The timing of the colour changes was arranged such that the predicted haemodynamic responses to the grating stimulus and to the colour changes have minimal correlation. First, a design vector representing the stimulus blocks and a design vector containing pseudo-randomly timed target events were separately convolved with a gamma function serving

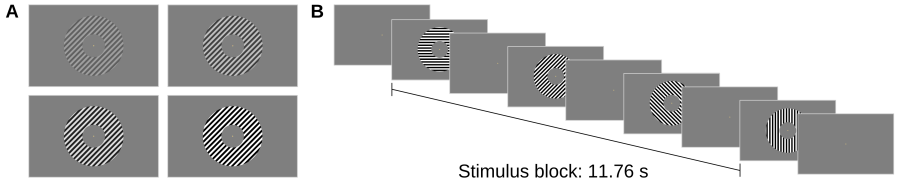

Figure 2.1: Stimuli used in the main experiment. (**A**) Grating stimuli were presented at four luminance contrast levels (2.5%, 6.1%, 16.3%, and 72.0%). (**B**) Within each stimulus block, the luminance contrast of the stimulus was constant, but the stimulus orientation was altered in random order.

as a model for the haemodynamic response. Second, the correlation between the predicted response to the stimulus blocks and to the target events was calculated. Third, if the correlation coefficient was above threshold (r>0.001), a new pseudo-random design matrix of target events was created, and the procedure was repeated. This procedure was repeated until the correlation was below threshold, separately for each run. Each subject completed six functional runs, with four repetitions of each luminance contrast level per run. The total duration of a run was 588 s. In an additional run, retinotopic mapping stimuli were presented for population receptive field estimation, allowing us to delineate early visual areas V1 and V2 on the cortical surface (Dumoulin & Wandell, 2008). The stimuli used for retinotopic mapping were oriented bars at four different orientations and eight different positions per orientation. Each of the resulting 32 stimulus configurations was presented 12 times for 2.94 s in random order.

2.3.2 Data acquisition & preprocessing

Functional MRI data were acquired on a 7 T scanner (Siemens Medical Systems, Erlangen, Germany) and a 32-channel phased-array head coil (Nova Medical, Wilmington, MA, USA) using a 3D GE EPI sequence (TR = 2.94 s, TE = 26 ms, nominal resolution 0.7 mm isotropic, 52 slices, coronal oblique slice orientation; Poser, Koopmans, Witzel, Wald, & Barth, 2010). We also acquired whole-brain structural T1 images using the MP2RAGE sequence (Marques et al., 2010) with 0.7 mm isotropic voxels, and EPI images with opposite phase encoding for distortion correction of the functional data (Andersson, Skare, &

Ashburner, 2003).

Motion correction was performed using SPM 12 (Friston, Williams, Howard, Frackowiak, & Turner, 1996), and the data were distortion corrected using FSL TOPUP (Andersson et al., 2003). More specifically, data were motion corrected within runs before estimating and correcting geometric distortions individually for each run. Afterwards, the distortion-corrected images were registered in order to correct for across-run head movement using SPM12's two pass procedure: images were first registered to the first image of the first run, and subsequently to the mean of all images after the first realignment. Standard statistical analyses were performed using FSL (Smith et al., 2004), fitting a general linear model (GLM) with separate predictors for the four stimulus conditions (luminance contrast levels) and a nuisance predictor for the target events of the fixation task. Highpass temporal filtering (cutoff value 100 s) was applied to both the model and the functional time series before GLM fitting. Population receptive field mapping (Dumoulin & Wandell, 2008) was performed using publicly available python code (Marquardt, Schneider, & Gulban, 2017) and standard scientific python packages (Numpy, Scipy, Matplotlib, Cython; Behnel et al., 2011; Millman & Aivazis, 2011; Oliphant, 2007; van der Walt, Colbert, & Varoquaux, 2011).

Each of the 11 subjects completed 6 functional runs of the main experiment. One subject completed two identical sessions on separate days. Cortical depth sampling requires a high level of spatial accuracy. However, the fMRI time series sometimes contained artefacts, such as unstable geometric distortions or strong, global image intensity fluctuations. These artefacts are presumably due to subject motion or field fluctuations due to scanner instability or physiological noise. In order to remove low-quality data based on a quantifiable and reproducible exclusion criterion, we calculated the spatial correlation between each functional volume and the mean EPI image of that session after the across-runs registration. If the mean correlation coefficient of the volumes in a run was lower than 0.93, that run was excluded from further analysis. The threshold ($r<0.93$) was chosen based on visual inspection of respective plots for all subjects (see Figure 2.10 in *Supplementary Material*), to discriminate low- and high-quality runs. Note that the value of 0.93 is conservative and may have lead to exclusion of valid data but made sure that only high-quality data was included in the final

results. For studies with low number of subjects and/or runs, a lower threshold can be chosen. The spatial correlation exclusion criterion resulted in the exclusion of 19 runs in total from 4 out of 11 subjects (for two subjects, all six runs were excluded; for four subjects, one run was excluded; and one subject had three runs removed). One additional run was excluded because the subject had detected less than 75% of targets, compared to an average performance of 95% across subjects. Thus, 20 runs were excluded in total. Because of hemispheric imbalances in temporal signal-to-noise ratio (tSNR), we limited the cortical-depth analysis to the left hemisphere in all subjects[1].

2.3.3 Segmentation & depth sampling

The anatomical MP2RAGE images were registered to the mean functional image of each subject using boundary-based registration (Greve & Fischl, 2009; Jenkinson, Bannister, Brady, & Smith, 2002; Jenkinson & Smith, 2001), and used for grey/white matter segmentation. We obtained an initial tissue type segmentation from FSL FAST (Zhang, Brady, & Smith, 2001). These initial segmentations were manually improved using publicly available python code (Gulban & Schneider, 2016) and ITK-SNAP (Yushkevich et al., 2006). Manual corrections of the automatic segmentations were based on the T1 image from the MP2RAGE sequence and aimed to remove mistakes in the definition of the white/grey matter boundary and at the pial surface. Particular care was taken to ensure that voxels outside the pial surface were correctly labelled as CSF. To this end, the T1 images were upsampled to a voxel size of 0.35 mm isotropic using trilinear interpolation, allowing for a more fine-grained delineation of tissue types.

[1] Functional data were acquired using a 3D EPI sequence with right-left phase encoding. The tSNR imbalance between hemispheres possibly is due to the asymmetric coil sensitivity profile and phase readout polarity. The asymmetry of the NOVA medical coil at 7T is a commonly observed issue and the result of the coil's design to improve the general homogeneity and reduce the sensitivity to head size and position within the coil. Because the stimulus was symmetric about the vertical meridian, it is not expected that the results qualitatively differ for the right hemisphere. Thus, we decided to focus our analysis on the hemisphere with the higher data quality. We tested this hypothesis on a subsample of subjects, which yielded very similar results for the right and left hemispheres (see Figure 2.16 in *Supplementary Material*).

Given the maximum spatial resolution currently achievable with fMRI, it is not yet possible to sample individual cortical layers. Therefore, cortical-depth specific fMRI studies need to increase the effective spatial resolution during post-processing, by upsampling (as in the present study), or by another super-resolution approach, such as spatial GLM (Kok, Bains, van Mourik, Norris, & de Lange, 2016). (See *Supplementary Material* for more details on spatial resolution and upsampling.) The final grey and white matter definitions were used to construct cortical depth profiles using volume-preserving parcellation implemented in CBS-tools (Bazin et al., 2007; Waehnert et al., 2014). CBS-tools represents information about cortical depth in distance maps, also known as level-set images. Based on these distance maps, the cortical grey matter was divided into 10 compartments, resulting in 11 depth-level images delineating the borders of these equi-volume compartments. The parameter estimates and z-scores from the GLM analysis, the population receptive field estimates, and the mean EPI images were up-sampled to the resolution of the segmentations (0.35 mm isotropic voxel size) using nearest-neighbour interpolation, and sampled along the previously established depth-levels using CBS-tools (Bazin et al., 2007; Waehnert et al., 2014). The depth-sampled data were then projected onto a surface mesh (Tosun et al., 2004), and visual areas V1 and V2 were delineated on the cortical surface based on the polar angle and eccentricity estimates from the pRF modelling using Paraview (Ahrens, Geveci, & Law, 2005; Ayachit, 2015). Note that the purpose of representing the data on a surface mesh was only to select our regions of interest (ROIs); the depth-sampling was performed in the previous step, and cortical fMRI profiles were obtained as described below. See Figure 2.2 and Figure 2.11 in *Supplementary Material* for a scheme of the preprocessing and analysis pipeline.

2.3.4 ROI selection

We defined the ROIs, on which all further analyses were performed, in a sequential procedure, designed to obtain an observer-independent, unbiased selection (see Figure 2.2). The first step of the ROI selection procedure was the retinotopic V1 and V2 definitions: Only 'columns' (i.e. grey matter segments covering all depths) that were located within V1 or V2 were selected (the procedure was carried out separately for V1 and

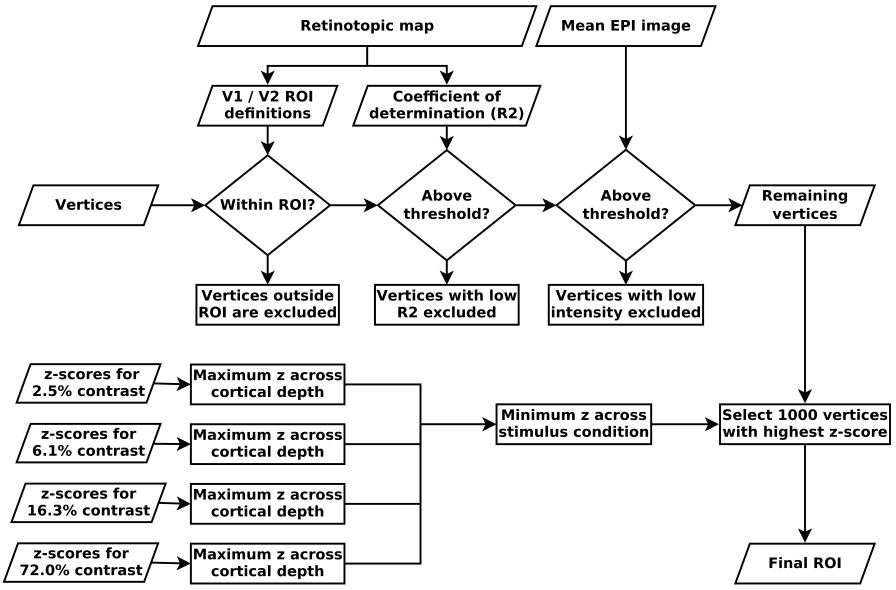

Figure 2.2: Overview of region of interest (ROI) selection. Vertices were selected based on a combination of criteria: retinotopic information, mean EPI image intensity, and z-scores from the GLM analysis. The selection procedure attempts to select vertices with a specific response to the stimulus while minimising subjective selection bias. This procedure was applied separately for V1 and V2. See *Methods* and Figure 2.11 in *Supplementary Material* for details.

V2). Secondly, 'columns' with a low population receptive field model fit at any depth level were excluded (minimum *R2* across cortical depth > 0.12). The purpose of this step was twofold: An unreasonably low pRF model fit indicates that the polar angle and eccentricity estimates may not be reliable, therefore calling into question the validity of the first selection criterion (i.e. V1 and V2 definitions). Furthermore, even in case of a cortical location that is certainly contained within V1 or V2 based on its anatomical location, a low pRF model fit is indicative of an unspecific visual response, which may be due to the presence of a large draining vein with a strong but unspecific signal change in response to visual stimulation. After these initial selection based on retinotopic information, the third selection criterion excluded 'columns' with a very low signal intensity at any cortical depth level in the mean EPI image, in order to avoid sampling from veins and low intensity regions around the transverse sinus, due to slight imprecisions in the registration and/or segmentation. Specifically, we excluded all 'columns' with EPI image intensity below 7000 at any cortical depth in the mean functional image, which has a mean intensity of about 10,000 for voxels contained within the brain.

The selection criteria described so far are based on anatomical and retinotopic information, irrespective of stimulus-induced signal changes in the main experiment. The final ROI selection was performed based on the responsiveness to the grating stimulus in the main experiment, as indicated by the GLM z-scores contrasting each of the four stimulus conditions against rest. For each 'column' that had passed all previous selection criteria, the maximum z-score across cortical depth levels was obtained separately for each of the four stimulus conditions. The minimum of these four z-values (one per stimulus condition) was determined, and from these the 'columns' containing the maximum 1000 z-values were selected. By first taking the minimum z-value across conditions, we aimed to select 'columns' that are responsive to all stimulus conditions, and not only to the highest luminance contrast. Note, however, selection based on minimum or mean across conditions did not produce significant differences in the main results (data not shown). The selection was based on z-values (and not on parameter estimates) because we expect the z-statistic to be less sensitive to pials veins (due to the high physiological noise caused by a large vein).

The ROI selection procedure was carried out separately for V1

and V2. Selection criteria were always applied to an entire 'column' – i.e. either the entire 'column' was included or excluded. The ROI selection described in this section, and all subsequent analysis steps were performed using standard scientific python packages (Numpy, Scipy, Matplotlib; Hunter, 2007; Millman & Aivazis, 2011; Oliphant, 2007; van der Walt et al., 2011).

2.3.5 Creation of cortical depth profiles

For each subject, we sampled the GLM parameter estimates corresponding to the four stimulus conditions within the final ROIs, separately for V1 and V2. The parameter estimates were then averaged within the cortical depth levels to obtain one depth profile of stimulus-induced activation for each subject. Because the fMRI signal amplitude of the stimulus-induced responses differed across subjects, we normalised the depth profiles of each subject before averaging across subjects. Normalisation was performed by dividing each subject's depth profile by the within-subject mean activation (given by the GLM parameter estimates) across depth levels and stimulus conditions. In this way, averaging across subjects does not bias the resulting group level profiles towards subjects with a strong level of activation.

2.3.6 Draining effect spatial deconvolution

As described above, cortical depth-specific BOLD fMRI using GE sequences is expected to result in depth-profiles with a signal increase towards the surface of the brain, due to the sensitivity to ascending draining veins (Koopmans et al., 2011; Markuerkiaga et al., 2016; see Uludağ & Blinder, 2018, for a review; Zhao, Wang, & Kim, 2004). That is, the fMRI signal at each cortical depth is not only influenced by the local neuronal activation but also by the draining of altered deoxyhemoglobin content and increased blood pressure from lower layers. As a result, the laminar-resolved, measured fMRI signal (S) is the sum of local fMRI activation (LA) and non-local fMRI signal changes (NL) due to ascending veins (assuming similar signal intensity S_0 at each layer). If we reasonably assume the flow direction from layer 6 (close to

white matter) to layer 1 (close to CSF), then we can formalize this as:

$$
\begin{aligned}
LA_6 &= S_6 \\
LA_5 &= S_5 - w_{6\to5} * LA_6 \\
LA_4 &= S_4 - w_{6\to4} * LA_6 - w_{5\to4} * LA_5
\end{aligned}
$$

and so on.

In other words, to obtain the fMRI signal due to local neuronal activation, the influence of the lower layers is subtracted from the measured signal with weighting factors $w_{(n+1)\to n}$. In laminar fMRI experiments, the weighting factors are usually not known. It may be, in the future, possible to derive these factors from resting-state or hypercapnia data, as suggested by Polimeni et al. (2010) and Guidi et al. (2016), or from laminar-specific dynamic fMRI signal models. In the current study, we used the model proposed by Markuerkiaga et al. (2016) to derive the weighting factors (from their Figure 3f, factors shown here in Table 2.1). In short, Markuerkiaga et al. (2016) developed a detailed microanatomical model of the vascular system of primate visual cortex, based on histological data, following the study by Boas et al. (2008). They combined this vascular model with the BOLD signal model proposed by Uludağ et al. (2009), and simulated the spread of fMRI signal changes across cortical layers. The simulations by Markuerkiaga et al. (2016) provided a specific estimate of the draining effect on the fMRI signal for each cortical layer, allowing differentiating between signal changes due to a local haemodynamic response, and signal changes due to the inflow of blood and deoxygenated haemoglobin from deeper layers. The model assumptions match our experimental parameters in terms of field strength, imaging parameters, and stimulus duration (Markuerkiaga et al., 2016). In order to account for the different relative thickness of the cortical layers in V1 and V2, and because the model by Markuerkiaga et al. (2016) is defined at five cortical layers (layers 2 and 3 are grouped together), we re-sampled our depth profiles to those five layers (de Sousa et al., 2010; Markuerkiaga et al., 2016; Waehnert et al., 2014).

The spatial deconvolution has, to the best of our knowledge, not been applied in an fMRI study before, and the model parameters have not yet been empirically validated. Therefore, before proceeding with

Table 2.1: Weighting factors for spatial deconvolution. Each row specifies the weighting factors w for the contribution of local fMRI activation (LA) and non-local fMRI signal changes (NL) to the total measured signal (S) at that depth level. For example, the measured signal S_6 is completely determined by the local activation LA_6, therefore $w_{6\to6} = 1.00$, and $\sum_{n=1}^{5} w_{(n\to6)} = 0$. In contrast, the measured signal S_5 is the sum of the local activation LA_5 and a fraction $w_{6\to5} = 0.32$ of the non-local signal NL_6, i.e. $S_5 = 1.00 * LA_5 + 0.32 * NL_6$ (weighting factors derived from Markuerkiaga et al., 2016, p. 495, their Figure 3f).

Depth level	1	2/3	4	5	6
1	1.00	0.41	0.59	0.20	0.26
2/3		1.00	0.59	0.20	0.26
4			1.00	0.20	0.32
5				1.00	0.32
6					1.00

the analysis of contrast response properties in V1 and V2, we need to assess the sensitivity of the BOLD signal profile after using the deconvolution method to changes in its model parameters. Whereas it is reasonable to assume that draining veins cause a unidirectional signal spread from deeper to more superficial cortical depth levels, the exact size of this draining effect is contingent on the model assumptions made by Markuerkiaga et al. (2016). In order to assess how our results would change with deviations in the draining model parameters, we multiplied the weighting factors $w_{(n+1)\to n}$ (see Table 2.1) with two different bias sources. First, the spatial deconvolution model is based on histological data on the structure of the vascular system. The respective histological monkey data may not be representative of our sample of human subjects, resulting in a systematic overestimation or underestimation of the extent of signal spread across cortical depth levels. Another source of systematic deviation may result from a bias in the model of the BOLD signal. We modelled such an over- and underestimation by using weighting factors that are 30% larger and smaller than the original weighting factors at all cortical depth levels.

Second, the histological data forming the basis of the deconvolution

model may be affected by random measurement error. We modelled such non-systematic error by multiplying the weighting factors with random Gaussian noise before applying the spatial deconvolution. More specifically, each weighting factor $w_{(n+1)\rightarrow n}$ was separately multiplied with a factor that was randomly sampled from a normal distribution with mean 1.0 and standard deviation 0.15. Thus, the average deviation of the perturbed model parameters was 15% with respect to the original model parameters. This procedure was repeated 10,000 times, each time sampling different random noise factors from the normal distribution. Because the random noise was distributed around 1.0, averaging across iterations results in mean depth profiles that are identical to the ones based on the original model parameters. The parameter of interest is therefore the spread of the resulting depth profiles.

2.3.7 Contrast response function

In order to characterise the response properties of V1 and V2 in more detail, we fitted a contrast response function to the depth profiles of stimulus induced signal changes, both before and after draining-effect spatial deconvolution, separately for all depth levels. Because our stimuli were well above the perceptual threshold, and due to the small number of stimulus contrast levels, we fitted a simple power function, which can approximate contrast responses under the given conditions reasonably well:

$$R_C = A * C^B$$

with C being the luminance contrast level, and A & B as free parameters (Albrecht & Hamilton, 1982). (Parameter A determines the overall response amplitude, and B specifies the slope of the function.) In order to determine the error of the fits, the contrast response function was fitted using a bootstrapping procedure. We randomly resampled the single-subject response profiles 10,000 times with replacement, and fitted the contrast response function to the across-subjects average profile of each bootstrapping iteration.

Based on the fitted contrast response function, we calculated the predicted response to a 50% contrast stimulus for each bootstrapping sample (i.e. $R_{0.5} = A * 0.5^B$). This 50% contrast response was obtained for both V1 and V2 for all cortical depth levels, both before and after

spatial deconvolution. The resulting response profiles are a summary of the overall responsiveness of a region/depth level to a contrast stimulus.

Furthermore, the semisaturation contrast was derived from the fitted contrast response function of each bootstrapping sample. The semisaturation contrast is the stimulus contrast necessary to create a half-maximum response and is used to describe the overall contrast sensitivity of neurons in the visual system (Albrecht & Hamilton, 1982; Sclar et al., 1990). Semisaturation contrast is insensitive to the overall response amplitude and relatively constant across spatial frequencies (Albrecht & Hamilton, 1982).

2.3.8 Peak identification

A peak identification algorithm was applied to quantify the shape of the cortical depth profiles. The depth profiles were up-sampled to 100 points, smoothed with a Gaussian kernel with a FWHM = 5% of the cortical depth, and peaks were defined as local maxima within a neighbourhood of ±10 points. If no such local maximum was present, the global maximum across cortical depths was defined as the peak of the respective depth profile. For instance, for a profile exhibiting a monotonic increase towards the pial surface, the peak is at the most superficial cortical depth level.

A permutation test was performed to test for statistical differences in peak positions in cortical depth profiles between V1 and V2. Specifically, we compared the difference in peak position obtained from across-subjects average depth profiles with a null distribution of the difference in peak position obtained by permuting the ROI labels (i.e. "V1" and "V2") within subjects. The null distribution comprised all possible resamples without replacement (k^n, where n is the number of subjects and k is the number of ROI labels, i.e. $2^{10} = 1,024$). This procedure was performed on depth profiles of the parameter estimates of all four stimulus conditions, before and after spatial deconvolution, as well as on the depth profiles of the predicted response to a 50% contrast stimulus, separately for V1 and V2.

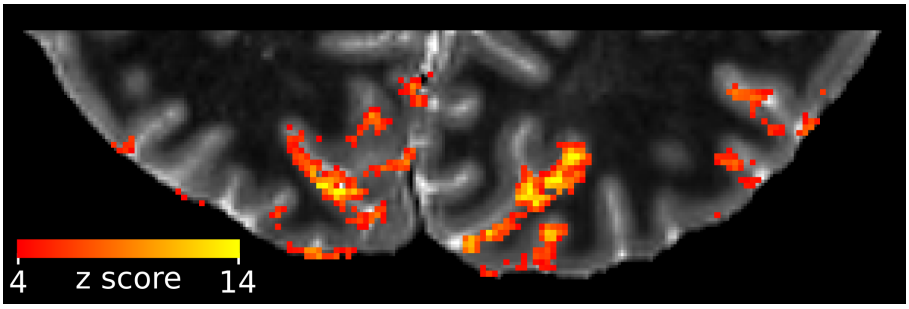

Figure 2.3: The visual grating stimulus caused strong fMRI signal changes across the visual cortex. Shown are the z-scores for the GLM contrast of the strongest contrast stimulus (72.0% contrast) against rest, overlaid on the quantitative T1 image, for a representative subject. The T1 image has been cropped to the approximate extent of the field-of-view of the functional images.

2.4 Results

The visual stimuli caused strong fMRI signal changes in early visual cortex (Figure 2.3). Not surprisingly, we observed a stronger response for higher luminance contrast levels irrespective of cortical depth (Figure 2.4). In the original depth-profiles (i.e. before spatial deconvolution), the response initially increased with distance from the white matter in V1, but levelled off at mid-cortical depth (Figure 2.4 A). The peak positions for the four stimulus conditions, from lowest to highest contrast, were located at ∼35%, ∼30%, ∼30%, and ∼35% of cortical depth from the pial surface, respectively. (Please note that these peak positions were determined from averaged and upsampled depth profiles.) The original depth-profiles for V2 showed a slightly more monotonic increase towards the pial surface (Figure 2.4 C; peak position at ∼0%, ∼0%, ∼5%, and ∼0% of cortical depth from the pial surface, respectively). The difference in the distribution of peak positions between V1 and V2 was not statistically significant, after correcting for multiple comparisons, for all but the lowest stimulus contrast condition ($p < 0.05$, $p > 0.05$, $p > 0.05$, $p > 0.05$, Bonferroni corrected, for the four stimulus conditions, from lowest to highest luminance contrast).

The spatial deconvolution dramatically changed this picture: After accounting for the draining effect, in V1, there was a local maximum at the middle of grey matter (Figure 2.4 B, at ∼55% of cortical depth

from the pial surface in all four stimulus conditions). In addition, there was another, even slightly higher, maximum at the lowest depth in V1. The deconvolved profile for V2 also showed a pronounced peak at mid grey matter, with a slight signal decrease towards the surface (Figure 2.4 D; peak position at ∼45% cortical depth from the pial surface for all four stimulus conditions).

Figure 2.5 shows the experimental fMRI response and the fitted contrast response functions exemplarily for three depth-levels for V1 and V2 after spatial deconvolution (see Figure 2.12 in *Supplementary Material* for the same data without spatial deconvolution). The fMRI responses were well approximated by a power function, and the resulting contrast response functions showed differences in shape and amplitude across areas and cortical depths. To characterise the contrast response properties in more detail, the predicted response at 50% contrast (Figure 2.6) and the semisaturation contrast (Figure 2.7) were obtained from the fitted contrast response functions.

Before spatial deconvolution, the peak of the response at 50% contrast was at ∼30% of cortical depth relative to the pial surface in V1 and at ∼0% of cortical depth in V2 (Figure 2.6 A). A permutation test revealed the difference in the distribution of peak positions between V1 and V2 to be statistically significant ($p < 0.05$). After accounting for the draining effect, the position of the mid grey matter peak in V1 was slightly deeper than in V2, at ∼55% and ∼45% of cortical depth relative to the pial surface for V1 and V2, respectively. Even though this difference in peak positions was statistically significant ($p < 0.05$), we caution against over-interpreting this effect. The peak positions of V1 and V2 are separated by a distance of ∼10% of the cortical depth. Given the limited spatial resolution of the data, different histological layering in V1 and V2, and possibly errors in the deconvolution parameters for the removal of the draining vein effect in V1 and V2, the certainty in determining the peaks may not be sufficient to relate this differences to the spatial profiles of neuronal activity.

We did not find statistical evidence for a difference in semisaturation contrast across cortical depths (Figure 2.7). However, as expected, the semisaturation contrast was much higher for V1 than for V2. These results were similar before and after spatial deconvolution (parametric bootstrap linear regression, 100,000 iterations; before & after spatial deconvolution: cortical depth level, $p > 0.05$; ROI (V1/V2), $p < 0.01$).

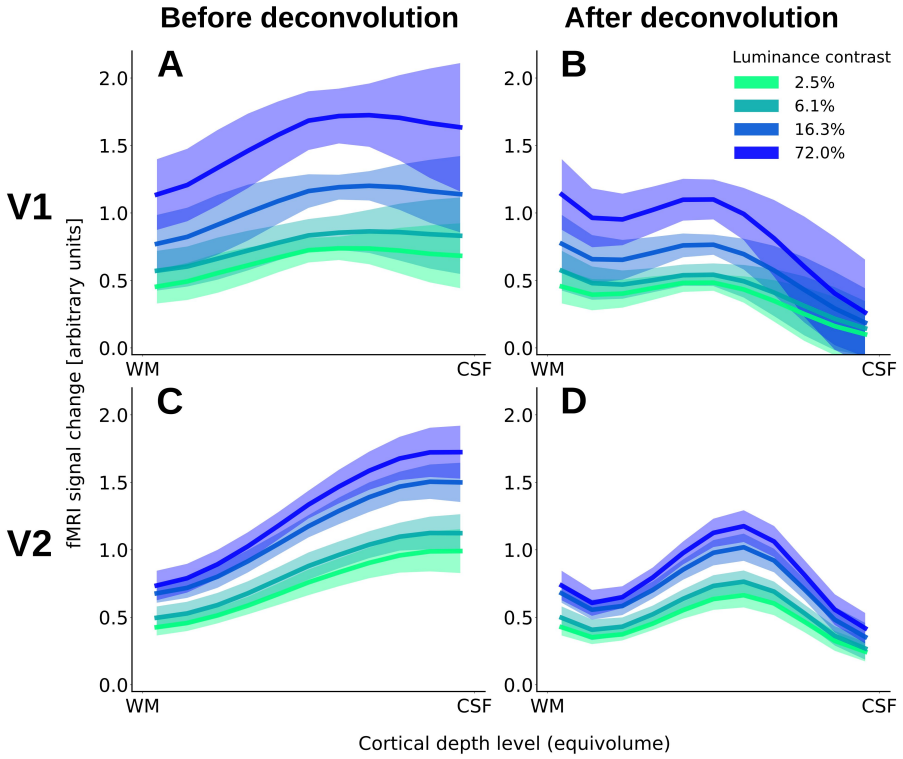

Figure 2.4: Cortical depth profiles for V1 (**A** & **B**) and V2 (**C** & **D**) before (**A** & **C**) and after (**B** & **D**) accounting for the draining effect. Shown are the mean GLM parameter estimates contrasting the response to the four different stimuli against rest, normalised and averaged across the left hemispheres of all subjects. The shading depicts the standard deviation (across subjects) of the mean.

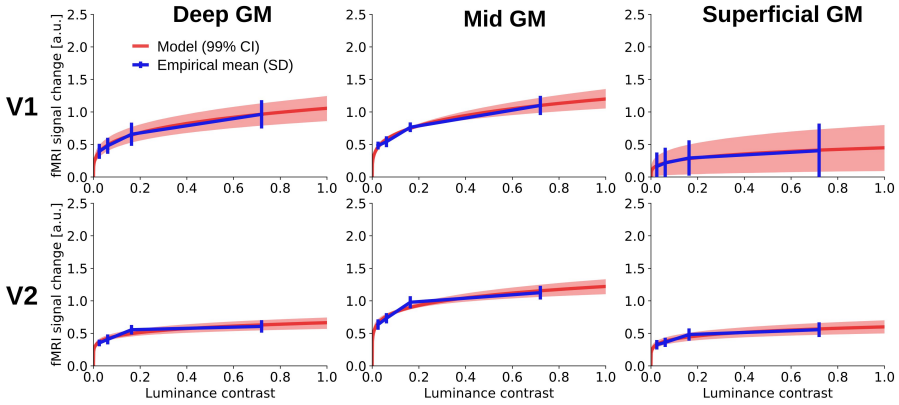

Figure 2.5: Contrast response function for V1 (upper row) and V2 (lower row) for three cortical depth levels (left: deep grey matter, middle: mid-grey matter, right: superficial grey matter). The blue line shows the experimental fMRI response after accounting for draining effects at the four stimulus contrast levels (2.5%, 6.1%, 16.3%, and 72.0%); the blue error bars represent the standard deviation of the mean across subjects. The red line indicates the median power function model fit across bootstrapping iterations, and the shaded region represents the corresponding 99% confidence interval. See Figure 2.12 in *Supplementary Material* for the same contrast response function fitted before spatial deconvolution.

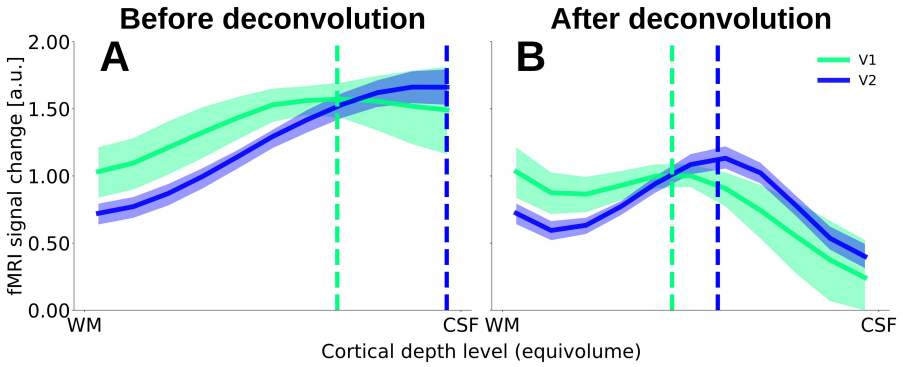

Figure 2.6: Response at 50% contrast across cortical depth, before (**A**) and after (**B**) spatial deconvolution. The solid lines indicate the median response for a stimulus with 50% luminance contrast, based on the bootstrapped contrast response function. Shaded regions indicate the 99% confidence interval of the median (percentile bootstrap). The dotted vertical lines indicate the median relative cortical depth of the peak.

Thus, we found the V2 response to saturate at a lower contrast than the response in V1, in line with a smaller dynamic range in V2.

Figure 2.8 plots the results of simulated deviations of the spatial deconvolution model parameters for the strongest luminance contrast level (75% luminance contrast). Systematic over- and underestimation of the weighting factors are represented by the two red lines, and the effect of random error is indicated by the blue error shading. The deepest cortical depth level, close to the white matter, is not affected by perturbing the model parameters, because no deconvolution is applied there. With increasing distance from the white matter, the effect of perturbing the model parameters becomes larger, both for systematic and random error. This is not surprising, since any deviation in the weighting factors affects the deconvolution at all subsequent (i.e. more superficial) depth levels. Importantly, although the range of the distribution becomes wider towards the cortical surface, the general shape of the profiles and the presence of the local maximum in mid-grey matter do not change.

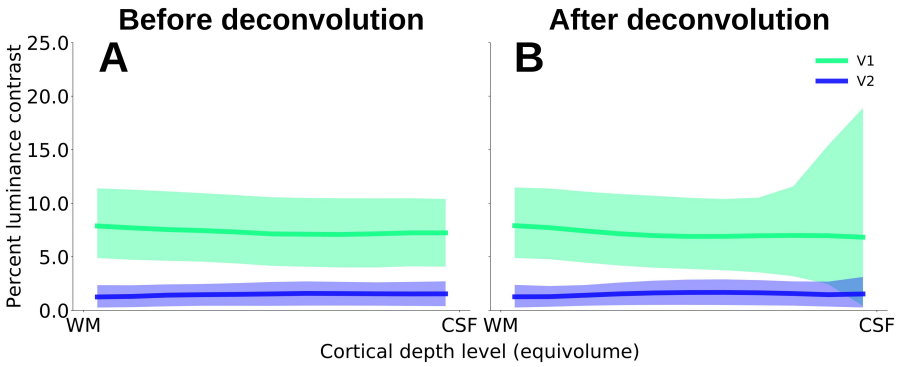

Figure 2.7: Semisaturation contrast across cortical depth in V1 and V2 (**A**) before and (**B**) after draining effect spatial deconvolution. Solid lines indicate the bootstrapped median semisaturation contrast, and the shading represents the respective 95% confidence interval. The semisaturation contrast is relatively constant across cortical depth, and is generally higher for V1 than for V2.

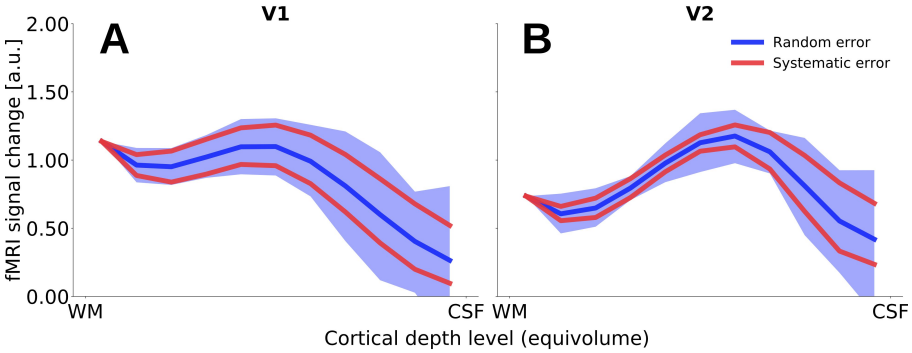

Figure 2.8: The effect of variance in the model assumptions on spatial deconvolution. We assessed the effect of two types of error: First, a systematic over- and underestimation of the extent of signal spread across cortical depth levels (represented by the red lines), and secondly, random error in the weighting factors used for spatial deconvolution (blue error shading represents the 0.5^{th} and 99.5^{th} percentile after applying random Gaussian noise to the deconvolution weighting factors over 10,000 iterations; see *Discussion* for details). With increasing distance from the white matter, the spread of the distribution becomes larger, reflecting a greater effect of changes in the model parameters towards the cortical surface. However, the general shape and peak positions are not affected. For better visibility, only the data for one stimulus condition (75% luminance contrast) are shown.

2.5 Discussion

Along the hierarchy of visual areas, neurons' preferred stimuli evolve from simple luminance contrasts to more complex visual features (Hochstein & Ahissar, 2002; Maunsell & Newsome, 1987; Vogels & Orban, 1996). Moreover, sensitivity to stimulus features varies between cortical layers, suggesting that cortical layers are interconnected but separate networks within the visual hierarchy (Alonso & Martinez, 1998; Gilbert, 1977; Hubel & Wiesel, 1968; Martinez & Alonso, 2003). Whereas the progression of response properties between visual areas in humans has been studied in detail (e.g. Hochstein & Ahissar, 2002), less is known about the specific role of human cortical layers in visual feature processing. To address this issue, we investigated the contrast response properties of human V1 and V2 across cortical depths in an fMRI experiment at 7T at high spatial resolution.

2.5.1 Contrast response properties over cortical depth

We fitted a contrast response function (Albrecht & Hamilton, 1982) to the stimulus-induced fMRI responses at different cortical depths, and determined the predicted response at 50% luminance contrast as a measure of the amplitude of the stimulus-induced response, and contrast sensitivity as a measure how much this response was modulated by varying luminance contrast levels. We did not observe an effect of cortical depth on contrast sensitivity (Figure 2.7). Hence, our results are not indicative of a contrast sensitivity gradient between the proposed two stages of feedforward processing in the middle and superficial layers of human V1 (Callaway, 1998). Differences in contrast sensitivity between layers have been reported in monkeys (Tootell et al., 1988), and we cannot exclude the possibility that the absence of such an effect may be due to a lower sensitivity and/or specificity of depth-dependent fMRI compared to invasive methods.

With respect to the stimulus-induced response amplitude, our results after spatial deconvolution (see below for discussion) indicate a signal peak at mid-grey matter in V1 and V2 (Figure 2.6 B). While there are, to the best of our knowledge, no previous studies on the cortical depth-dependence of contrast response properties in human

visual cortex, our results can be compared with studies in monkeys: Tootell et al. (1988) measured tracer uptake across cortical layers 3 to 6 in macaque V1 after prolonged exposure to grating stimuli at four different luminance contrasts. We applied the same contrast response function used to fit our fMRI data to their data (Tootell et al., 1988, p. 1602 their Figure 6), and found the cortical depth profiles of the normalised response amplitude in monkey V1 to be in close agreement with our data, with maxima in deep grey matter and at mid cortical depth (compare Figure 2.9 with Figure 2.6 B). This result is expected for feedforward stimuli. In fact, several high-resolution fMRI studies in animals (Chen, Wang, Gore, & Roe, 2013; Goense, Merkle, & Logothetis, 2012; Harel, Lin, Moeller, Ugurbil, & Yacoub, 2006; Jin & Kim, 2008; T. Kim & Kim, 2010; Lu et al., 2004; Yu et al., 2012; Yu, Qian, Chen, Dodd, & Koretsky, 2014; Zhao, Wang, Hendrich, Ugurbil, & Kim, 2006) and humans (Fracasso, Luijten, Dumoulin, & Petridou, 2017; Koopmans, Barth, & Norris, 2010; Koopmans et al., 2011) have also found a peak at intermediate depth levels in primary sensory cortex as a result of bottom-up stimulus modulation (see Uludağ & Blinder, 2018, for a review, including conflicting evidence), suggested to reflect direct thalamic input to V1, and cortico-cortical input from V1 to V2, respectively.

In addition to the expected local response maximum at mid cortical depth, we found an elevated signal in deep grey matter in V1, presumably originating from layers 5 and/or 6. This observation was somewhat surprising, as it is commonly assumed that the response to a simple feedforward stimulus is characterised by a peak mainly in thalamorecipient layer 4. Several electrophysiological studies in non-human primates found strong post-synaptic, stimulus-induced activity in layers 2, 3, and 4B of V1, but not in deep layers (Roberts et al., 2013; Xing, Yeh, Burns, & Shapley, 2012). Similarly, an fMRI study in rats reported evidence for a stimulus-induced activity increase in middle layers of primary visual cortex, but not in deep layers (Bissig & Berkowitz, 2009). In contrast, some fMRI experiments measuring BOLD signal and cerebral blood volume in anaesthetised macaque monkeys observed an elevated signal in deep layers (e.g. Goense, Zappe, & Logothetis, 2007 see their Figure 2B; Smirnakis et al., 2007 see their Figure 2D). Please note that most electrophysiological and fMRI studies presented drifting or flickering grating stimuli with a high temporal frequency. Self et al. (2017) point out that experiments using rapidly changing

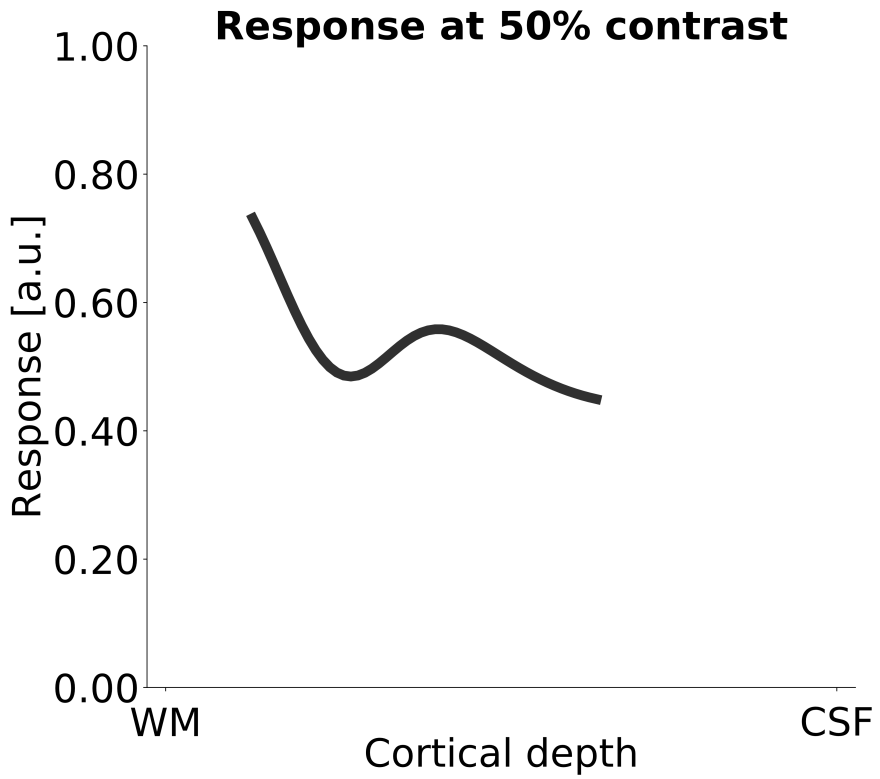

Figure 2.9: Tootell et al. (1988) measured tracer uptake across cortical layers in macaque V1 after prolonged exposure to grating stimuli at four different luminance contrasts. Shown is the predicted response at 50% luminance contrast after fitting their data with the same contrast response function that was used on our fMRI data. In order to facilitate the comparison with the fMRI results, Gaussian smoothing (SD = 20% of cortical depth) was applied to the histological data. Tracer uptake was reported for layers 3, 4A, 4B, 4Ca, 4Cb, 5, and 6 (Tootell et al., 1988).

visual stimuli are biasing the neuronal responses towards the feedforward modules. In contrast, stimuli at a lower temporal frequency are likely to result in a different relative response strength between feedforward and feedback modules. In line with this argument, a study, in which awake Macaque monkeys were presented with a uniform luminance stimulus for 1.5 s, found a broadband response in deep grey matter that lasted throughout the stimulus presentation, in addition to an onset response at mid-grey matter (Maier, Aura, & Leopold, 2011). Whereas the spatial properties of the stimulus used in that experiment were different to ours, the duration was very similar, and, in contrast to most invasive electrophysiological studies, the monkeys were awake. Similar to our experiment, the stimulus was not behaviourally relevant, and the monkeys' only task was to maintain fixation. Maier et al. (2011) propose three possible causes for their observed sustained, post-synaptic activity in deep layers: (1) direct thalamocortical sensory input from LGN, (2) indirect input from extrastriate visual cortex or from the pulvinar, or (3) intrinsic processing within V1, possibly due to recurrent activation within a cortical column. Based on the known connectivity pattern of the infragranular layers and the strengths of these connections, Maier et al. (2011) conclude that the third option, i.e. intrinsic cortical connections, is the most likely cause of the observed sustained activity within the deep layers of V1. Although speculative, their results, as well as our finding of an elevated responsiveness in deep grey matter in V1, may be the consequence of recurrent excitation caused by the prolonged presentation of a slowly changing stimulus.

In this context, it is worth noting that layer 6 receives collaterals of the feedforward projections originating in layer 4 (Callaway, 1998; Callaway & Wiser, 1996). Neurons in layer 6 of V1 presumably form a first-level feedback node that modulates the responses to incoming sensory information in layer 4C of V1, and in the LGN, according to behavioural needs (Callaway, 1998; J. Kim, Matney, Blankenship, Hestrin, & Brown, 2014; Olsen, Bortone, Adesnik, & Scanziani, 2012; Sherman, 2005; Thomson, 2010). Similarly, layer 5 of V1 constitutes a second-level feedback module (Adesnik & Scanziani, 2010; Callaway, 1998; Callaway & Wiser, 1996). In summary, the elevated response observed in mid grey matter in our study could be linked to the feedforward flow of transient information, whereas the peak in deep layers in V1 may be related to recurrent processing caused by the constant presence

of the stimulus. Note, however, that the response peak in deep layers has only been observed under particular stimulus conditions, and may not be present for all stimulus types and/or feedforward processing of transient stimuli. Therefore, a systematic comparison between laminar fMRI responses to various stimulus parameters will be needed to validate our findings and to identify the conditions under which a high response in deep layers is evoked.

Although the relationship between electrophysiological measures of neuronal activity and the fMRI signal is not completely understood (Logothetis, 2008), the fMRI signal, particularly in primary visual cortex, is more closely related to post-synaptic activity than to spiking (Goense & Logothetis, 2008; Logothetis, Pauls, Augath, Trinath, & Oeltermann, 2001; Viswanathan & Freeman, 2007). Hence, the most obvious explanation for a local response maximum is an increased metabolic demand due to post-synaptic activity caused either by afferent signals targeting layer 4 and 6 or by local processing. Alternatively, a higher vascular density at intermediate cortical depths may cause a peak in the fMRI signal (Uludağ & Blinder, 2018). However, after applying the spatial deconvolution, we observed a peak at mid-grey matter in both V1 and V2, but a higher local vascular density in middle layers has only been reported for V1, not for V2, in macaque monkeys (Weber et al., 2008). It is expected that human V1 and V2 exhibit a similar vascular volume distribution. Even though we cannot completely rule out the alternative, the electrophysiological evidence and relatively constant vascular volume across layers of V2 argue that the laminar fMRI signal profile after spatial deconvolution reflects the neuronal laminar profile.

2.5.2 Spatial deconvolution model assumptions

Our deconvolution results are contingent on the validity of the model proposed by Markuerkiaga et al. (2016). In order to assess the impact of deviations of the model predictions from the actual signal spread on the resulting cortical depth profiles, we modelled the effects of systematic and random error in the assumed signal spread on the resulting depth profiles (Figure 2.9), and found that the general shape of the profiles and the positions of local maxima remain intact despite strong perturbations of the model parameters. Therefore, our overall conclusions are relatively insensitive to the exact values of the weighting

factors that represent draining of deoxygenated haemoglobin and blood volume via ascending veins towards the cortical surface. In other words, the change of the *slope* of the fMRI response amplitude before spatial deconvolution as a function of cortical depth is a strong indicator of the underlying neuronal laminar profile. However, this may not be true for other experimental designs resulting in more subtle neuronal changes between layers. Thus, in vivo derivation or calibration of these weighting factors or invertible generative fMRI signal models may alleviate determination of underlying neuronal laminar profiles from experimental fMRI data.

It could be argued that the lowest cortical depth level (closest to white matter) has a particularly strong influence on the spatial deconvolution, in the sense that any measurement error at this level would affect the deconvolution at all higher depth levels. Partial volume effects at the white matter boundary may result in an underestimation of the stimulus-induced response in deep layers, because white matter tissue is presumably not responsive to the stimulus. We have simulated the effect of an underestimation of the response amplitude at the deepest cortical depth level, and found that while a strong underestimation alters the relative amplitude of the deep grey matter and mid grey matter peaks, the presence of those peaks is not affected (see Figure 2.13 in *Supplementary Material* for details).

At present, the model of signal spread between cortical depth levels developed by Markuerkiaga et al. (2016) is only defined for V1. Between-area variability, within-area variability, and between-subject variability in vascular structure may therefore lead to erroneous deconvolution results. When applying the deconvolution to V2, we accounted for the different relative thickness of cortical layers, but not for differences in vascular structure (Weber et al., 2008). However, simulations using systematically and random deviations from the model parameters did lead to similar depth profiles (Figure 2.8). To test the generalizability of our approach, we applied the deconvolution model to cortical depth profiles from primary motor cortex (M1), recently published by Huber et al. (2017). In that study, cortical blood volume (CBV) was measured using the VASO sequence, in addition to BOLD images acquired with a GE-EPI sequence. As CBV changes are assumed to be located in microvasculature (see Uludağ & Blinder, 2018, for a review), the CBV spatial profile is a non-linear proxy for the neuronal activity profile.

Cortical depth profiles were obtained for activation during a sensory-motor task. The GE-EPI BOLD data are, similar to our results, prone to vascular signal spread due to ascending veins. Because of differences in vascular structure and cortical thickness between V1 and M1, the spatial deconvolution model is not expected to provide an optimal solution in this context. However, when applying the spatial deconvolution with model parameters optimised for V1 to the data from M1, the BOLD fMRI profile becomes more similar to the CBV profile, and thus – presumably – more similar to the 'true' profile of local neuronal activity (Figure 2.14 in *Supplementary Material*). We take this as an indication that the optimal deconvolution parameters may not drastically differ between brain regions. Nevertheless, we recommend a sensitivity analysis of the weighting parameters in order to determine the dependence of the results on the exact values of the parameters.

Further research may measure cortical depth profiles of CBV or cerebral blood flow (CBF) in addition to the BOLD fMRI signal under identical stimulus conditions, and compare the cortical depth profiles of stimulus-induced signal change after spatial deconvolution with the CBV or CBF profiles. A close match between deconvolved BOLD fMRI profiles and CBV or CBF profiles would constitute converging evidence for the validity of the deconvolution approach and/or experimentally allow for subject- and brain area-specific estimation of the spatial weights.

We have applied spatial deconvolution in order to remove signal spread due to ascending veins. The resulting cortical depth profiles are expected to be 'closer' to the underlying neuronal activity than before the deconvolution. However, there are most likely other (possibly non-linear) transformations between neuronal activity and the BOLD signal, similarly as in low-resolution fMRI studies. Thus, in an additional step, an anatomically informed transfer function that models the relationship between neuronal activity and the hemodynamic response for each depth level, including a scaling factor related to capillary and venule CBV, has to be used to quantitatively deduce the underlying spatial neuronal activation profile. Nevertheless, the main experimental observations of the current study after spatial deconvolution, namely the decrease in the BOLD signal in V1 towards CSF and the pronounced peak in the middle layers in V2, are expected to remain valid even after such scaling.

While this study focused on the fMRI response to a modulation of 'bottom-up' stimulus properties, other studies have investigated the

neural correlates of 'top-down' perceptual processing (Kok et al., 2016; Muckli et al., 2015). Accounting for signal spread in the GE fMRI signal caused by draining veins may also benefit the deduction of other neuronal activity spatial profiles than in the current study and, thus, investigations of top-down effects.

2.5.3 Alternative approaches

In this study, we employed a model-based method to account for the effect of draining veins on the cortical depth profiles of the fMRI signal. Two alternative methods aim to deduce neuronal activity profiles from the fMRI signal rely on taking either a) the difference or b) the ratio of fMRI signal for two or more experimental conditions (Kashyap, Ivanov, Havlicek, Poser, & Uludağ, 2017). The rationale behind these methods is that any confounding vascular factors should affect different experimental conditions in the same way. The method of subtraction is used to remove nuisance signal components in fMRI studies at low spatial resolutions, as it is commonly applied in standard general linear model (GLM). However, in the case of high-resolution fMRI, subtracting the cortical depth profile of the response to a stimulus from that of a control condition is unlikely to remove the effect of ascending veins, and/or a possible blood volume bias, on cortical depth profiles, as such vascular effects are non-local and result in multiplicative factors of BOLD signal sensitivity, respectively (Kashyap et al., 2017). Second, the method of division can be useful in exploring non-linearities present in the data, most likely being neuronal in origin. That is, the division approach does not remove the ascending vein effect (but only the fMRI scaling factor proportional to baseline blood volume). Thus, it is rather an exploration tool to thoroughly characterize the properties of the data. In contrast, the method of the current study explicitly takes the ascending vein bias into account, albeit with some model assumptions. It remains to be tested whether these assumptions are generalizable to other brain areas and/or physiological states. Clearly, more work is required to reliably extract neuronal laminar profiles from high-resolution fMRI data.

Another proposed approach to deal with the spatial bias due to draining veins is to regress out time course contributions from other depth levels. Kok et al. (2016), separately for each depth level, removed the (neuronal and vascular) variance present at the other depth levels using

a regression model. The goal of this regression approach is to identify each depth level's unique contribution (i.e. to identify the differential neuronal activity of each layer). The advantage of this approach is that it does not require an explicit vascular model, in contrast to the model-based approach of the current study. However, the regression approach may inadvertently remove shared variance that is neuronal in origin, a) if some of the neuronal signal of interest is spread over more than one depth level, and b) because the draining vein effect leads to BOLD signal correlations between a neuronally active layer and the upstream layers. Finally, even though our approach needs spatial weights determined from a vascular model, for our specific experimental data, large deviations of these weights yield similar profiles. However, for more subtle neuronal changes in laminar profiles, this spatial deconvolution approach may not be sensitive enough, and subject- and brain area-specific weights may be necessary.

2.5.4 Limitations & directions for future research

T2-weighted sequences, such as GRASE (De Martino et al., 2013; Kemper et al., 2015; Kemper, De Martino, Yacoub, & Goebel, 2016), and sequences that are not based on the BOLD contrast, such as VASO (Huber et al., 2014, 2015, 2016; Huber, Uludağ, & Möller, 2017) and ASL (Huber, Uludağ, et al., 2017; Pfeuffer et al., 2002), are less affected by vascular biases and are therefore expected to yield a better estimation of local neuronal activity compared with GE sequences. However, this advantage comes at the price of a lower sensitivity and/or decreased coverage. The GE MRI sequence utilized in the current study achieves good coverage and sensitivity, but for cortical-depth-specific studies, the problem of reduced specificity due to signal spread along the ascending draining veins needs to be addressed. The spatial deconvolution model proposed by Markuerkiaga et al. (2016) may help to remove non-local signal contributions from cortical depth profiles. However, to be more generally applicable, the model needs to be extended to other brain areas with a different vascular structure, and to different experimental designs and imaging sequences. In particular, in its current state, the spatial deconvolution model is only applicable to the steady-state fMRI response to a block design. In order to investigate transient components of the fMRI signal, such as the initial overshoot or the post-stimulus

undershoot, at different cortical depths, a dynamic deconvolution model is needed. This may be achieved by a generative model of the temporal dynamics of the haemodynamic response across cortical depth. With the help of such dynamic deconvolution models, the disadvantages of GE acquisitions for cortical-depth-specific fMRI research may be addressed, while retaining its good sensitivity and coverage.

2.5.5 Summary

We have studied the contrast response properties of human V1 and V2 using fMRI at sub-millimetre resolution. After accounting for signal spread due to ascending draining veins, we found the stimulus-induced response to peak at mid cortical depths in V1 and V2, in addition to a response maximum in deep grey matter, which was more pronounced in V1. A response peak at middle depth levels is expected, as it is in agreement with electrophysiological evidence obtained in monkey V1 and V2. In contrast, a stimulus-induced response in deep layers has been observed in some (Goense et al., 2007; Maier et al., 2011; Smirnakis et al., 2007; Tootell et al., 1988), but not all (e.g. Bissig & Berkowitz, 2009; Roberts et al., 2013; Xing et al., 2012) relevant animal studies. A systematic investigation of the stimulus conditions under which a response in deep layers is evoked will be necessary to resolve this issue.

2.6 Supplementary Material

2.6.1 Spatial resolution & upsampling

At the currently achievable spatial resolution of fMRI, each voxel typically covers more than one cortical layer. Therefore, it is necessary for laminar fMRI studies to increase the effective spatial resolution via post-processing. This can be achieved by upsampling (as in the present study), or by another super-resolution approach, such as spatial GLM ("unmixing" Kok et al., 2016). Either of these approaches is based on two assumptions: a) the activity of each layer is similar across cortical locations within the ROI investigated, and b) the voxels included in the ROI sufficiently sample the layers with different spatial weights (i.e. the voxels differ in the partial volume contributions from the layers). The rationale behind upsampling or unmixing can be compared to the increase in effective temporal resolution achieved by jittering in event related designs, where a) would correspond to the assumption of a similar response across trials, and b) would be analogous to sampling enough trials at different (jittered) time points. To the best of our knowledge, assumption a) is common to all cortical depth specific fMRI studies but in principle requires validation for each stimulus type and ROI investigated (but see Kashyap et al. (2018) for a novel approach to directly measure laminar activation without the need for upsampling or unmixing). We think that for a simple contrast stimulus, as used in the current study, assumption a) is very likely to be true in V1 and V2. Assumption b) requires a minimum spatial extent of the ROI and quasi-random location of the voxels relative to the cortical layers, which should be fulfilled given the spatial dimensions and curvature of the V1 and V2 ROIs.

Given the need to upsample and interpolate, we tried to minimise its effect on our statistical results. To this end, we performed the GLM analysis on the original time series data in volume space, without upsampling, and with no interpolation except for motion correction and distortion correction. For the sole purpose of more fine-grained tissue type segmentations, we upsampled the T1 images using trilinear interpolation. The slight blurring introduced by trilinear interpolation is, in our experience, beneficial for anatomically plausible tissue type segmentation. In contrast to common practice in most low-resolution

fMRI studies, the anatomical T1 images were registered to the mean functional EPI image, thus avoiding the need to interpolate the statistical maps at this step. The mean functional EPI images and the statistical maps were upsampled to the same resolution as the T1 images and corresponding tissue type segmentations using nearest-neighbour interpolation (without this step, the mean EPI images and the statistical maps would have been at a different resolution than and the fine-grained tissue type segmentations, which would have complicated the analysis pipeline). The actual increase in effective spatial resolution was obtained during the subsequent cortical depth sampling. Cortical depth sampling was performed using nearest-neighbour interpolation, but very similar results were obtained using a linear interpolation algorithm.

Alternatively, one may perform cortical depth-sampling directly on the fMRI time series data, and perform GLM fitting on time courses averaged across the region of interest, separately at each depth level. However, the ROIs, within which the depth-sampling was performed, were selected based on the results of the GLM, in order to sample from regions of cortex that actually respond to the stimulus (see Figure 2.2). Thus, in our approach, the depth sampling necessarily has to be performed after the GLM fitting. Under the assumption of spatially homogeneous noise (within the ROI), no differences between the two alternative approaches are expected (i.e. GLM fitting on average ROI time courses, or averaging GLM parameter estimates within the ROI).

2.6.2 Relation to spatial GLM

Kok et al. (2016) employed a spatial regression to 'unmix' the fMRI time courses at three cortical depth levels. Their approach uses a general linear model to reconstruct the contribution of a cortical depth level to a measured voxel time course, where one voxel time course typically contains contributions from more than one depth level. The relative contributions of each cortical depth level are obtained from the beta weights of the general linear model. Our approach and the approach proposed by Kok et al. (2016) serve somewhat different purposes. Our approach tries to remove the non-local draining vein effect to obtain the spatial profile of local, layer-specific BOLD activation. In contrast, the approach by Kok et al. (2016) investigates the *differential* contribution of each layer by removing the common activation. These non-local

contributions can be of draining vein-origin (as accounted for in our approach), but also due to neuronal activation common over all other layers. That is, in the hypothetical case of statistically independent neuronal activities across all layers, the two approaches are expected to yield similar results. However, in case of neuronal activity that is correlated over layers, the approach of Kok et al. (2016) would remove neuronal signal contributions across depths, which may be relevant for the interpretation of neuronal activity profile.

2.6.3 tSNR imbalance

We observed a tSNR imbalance in our data that may be related to an asymmetry in the coil sensitivity profile, although we think that the phase readout polarity may also play a role (Figure 2.15). The asymmetry of the NOVA medical coil at 7T is a commonly observed issue and the result of the coil's design to improve the general homogeneity and reduce the sensitivity to head size and position within the coil. We acquired functional data using a 3D EPI sequence with right-left phase encoding. Thus, we decided to focus our analysis on the hemisphere with the higher data quality. Because segmentation quality is very important for cortical depth sampling, initial automatic segmentations were manually corrected. Although we limited manual corrections to occipital cortex, segmentation correction took >15 hours per hemisphere. Therefore, we decided not to segment the right hemispheres, given the lower tSNR and correspondingly lower data quality of the functional data in the right hemisphere. However, because the stimulus was symmetric about the vertical meridian, we do not expect the results to differ qualitatively for the right hemisphere, apart from higher noise/lower signal levels. For comparison, we have segmented and analysed three right hemispheres and have confirmed similarity of the results across hemispheres (Figure 2.16).

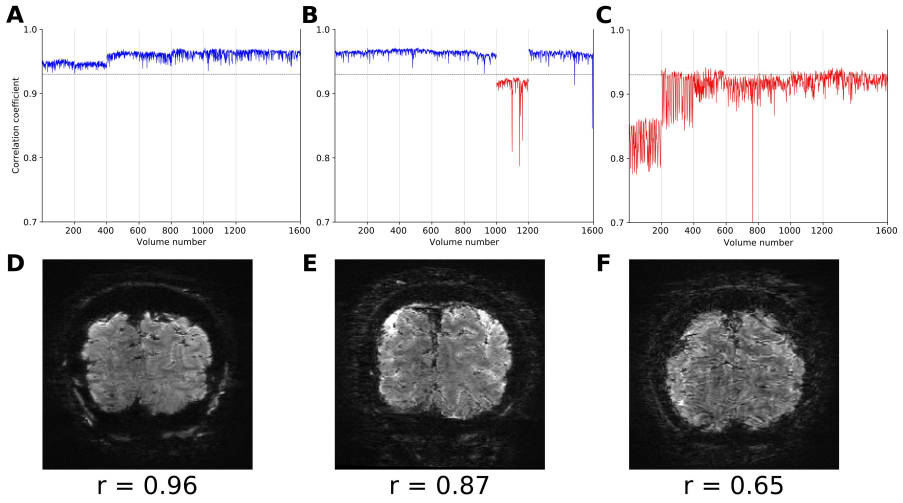

Figure 2.10: Quality control. In order to remove data affected by artefacts based on a quantitative criterion, the correlation of the voxel intensity between each EPI volume and the mean EPI image of the respective session was calculated. (**A**, **B**, **C**) Spatial correlation over time for three subjects. Runs with a mean correlation coefficient below criterion ($r < 0.93$) are plotted in red. The threshold was chosen to differentiate between data with a high and stable correlation (**A**), and runs with a low and unstable correlation (e.g. the second-last run in **B**, and all runs in **C**). Upon visual inspection, runs with a low correlation coefficient showed geometric distortions, ringing artefacts and intensity fluctuations, presumably due to subject head motion or physiological artefacts. (**A**) For this subject, no runs were excluded. (**B**) Only the second-last run was excluded for this subject. (**C**) All runs are below criterion, thus the entire session was excluded from analysis. (**D**, **E**, **F**) Example EPI slices illustrating the correspondence between image quality and spatial correlation. The images are taken from the subjects shown in **A**, **B**, and **C**, respectively. The lower data quality (i.e. distortions, ringing and blurring) in **E**, and especially in **F**, compared to **D** is reflected in a lower spatial correlation coefficient.

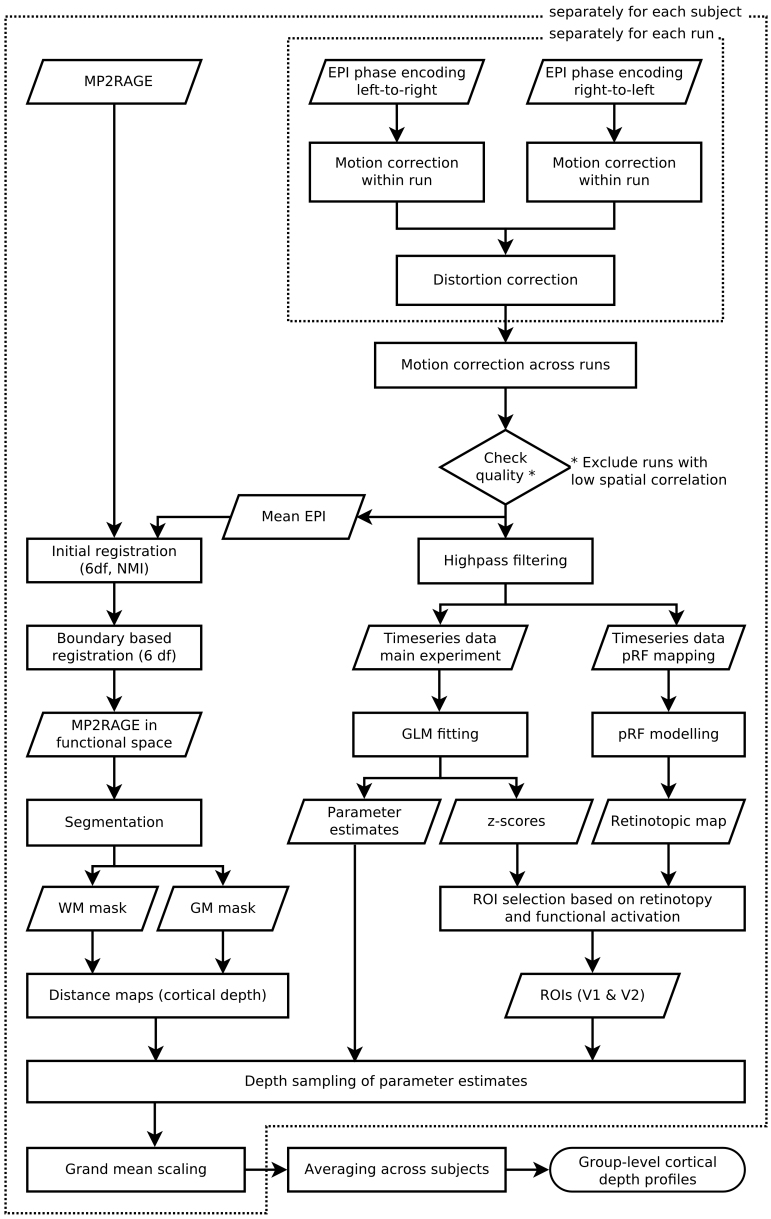

Figure 2.11: Details of the preprocessing and analysis pipeline.

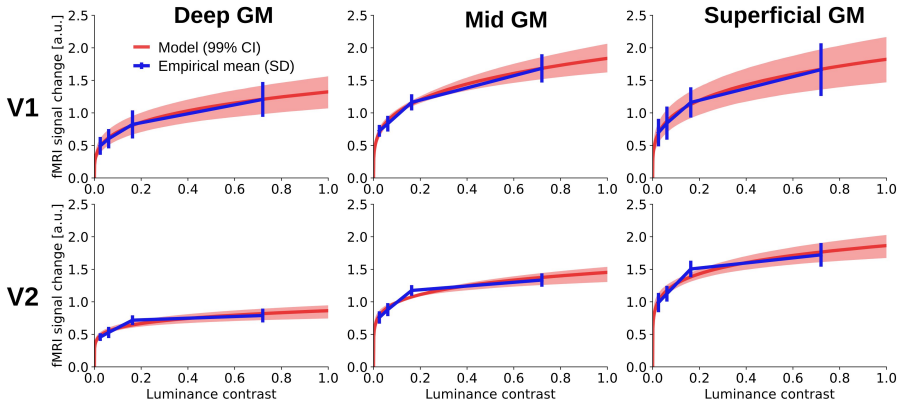

Figure 2.12: Same as Figure 2.5 in the main text, but without spatial deconvolution.

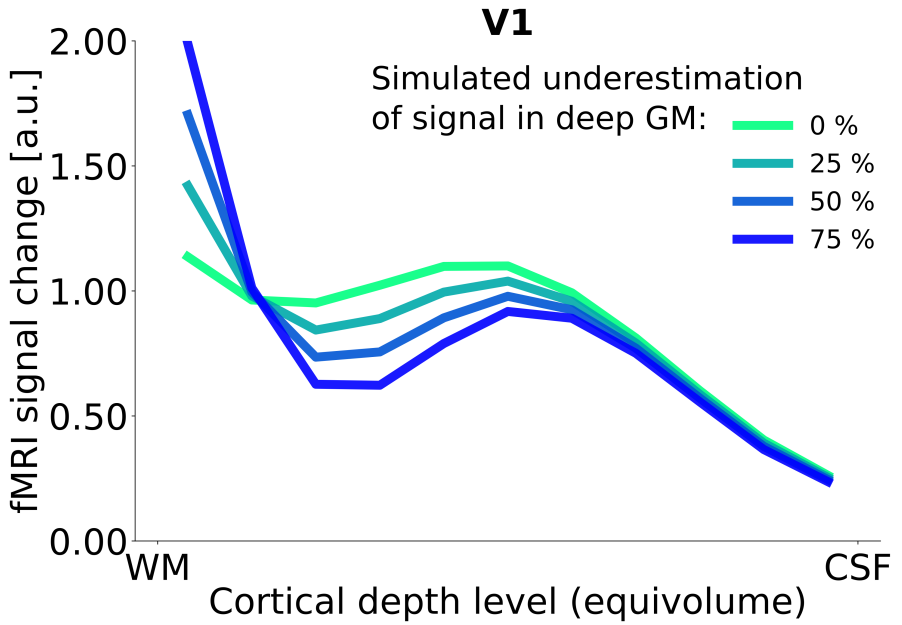

Figure 2.13: Simulation of an underestimation of the response amplitude at the deepest cortical depth level due to partial volume effects at the white matter/grey matter boundary. Although we have taken great care to not include white matter voxels in the grey matter segmentation, residual errors and partial volume effects may be present. Because white matter voxels are not expected to show a response to the visual stimulus, partial voluming with adjacent grey matter could result in an underestimation of the response amplitude in the deep grey matter. Here, we simulated the effect of underestimating the signal at the deepest cortical depth level (closest to white matter) by 25%, 50%, and 75%. The stimulus-induced response amplitude at the deepest cortical depth level was multiplied by the respective scaling factor (e.g. 1.25 for a 25% underestimation), to produce the hypothetical 'true' response amplitude for each scenario, and the deconvolution was applied. The line labelled '0%' corresponds to the depth profile in the main text (same as Figure 2.4 B). For better visibility, data are only plotted for one stimulus condition (72% luminance contrast). The general shape of the profile (i.e. presence of deep grey matter and mid grey matter peaks) is not affected. However, in case of an underestimated deep grey matter response, the mid grey matter peak is more pronounced, at a slightly lower amplitude.

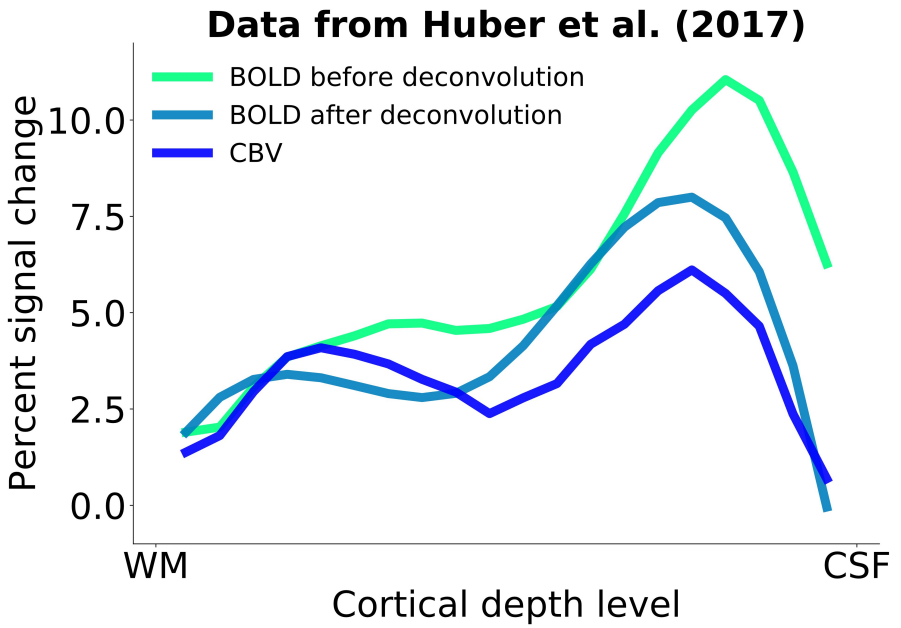

Figure 2.14: Spatial deconvolution applied to BOLD fMRI cortical depth profiles of task-induced activity in primary motor cortex (M1), and profile of cortical blood volume (CBV), from Huber et al. (2017). CBV was measured using the VASO sequence. Because CBV changes are thought to stem mostly from the microvasculature (see Uludağ & Blinder, 2018, for a review), the CBV profile is expected to more closely reflect underlying local neuronal activity. Even though the deconvolution model is not optimised for M1, the deconvolution brings the BOLD signal closer to the CBV profile.

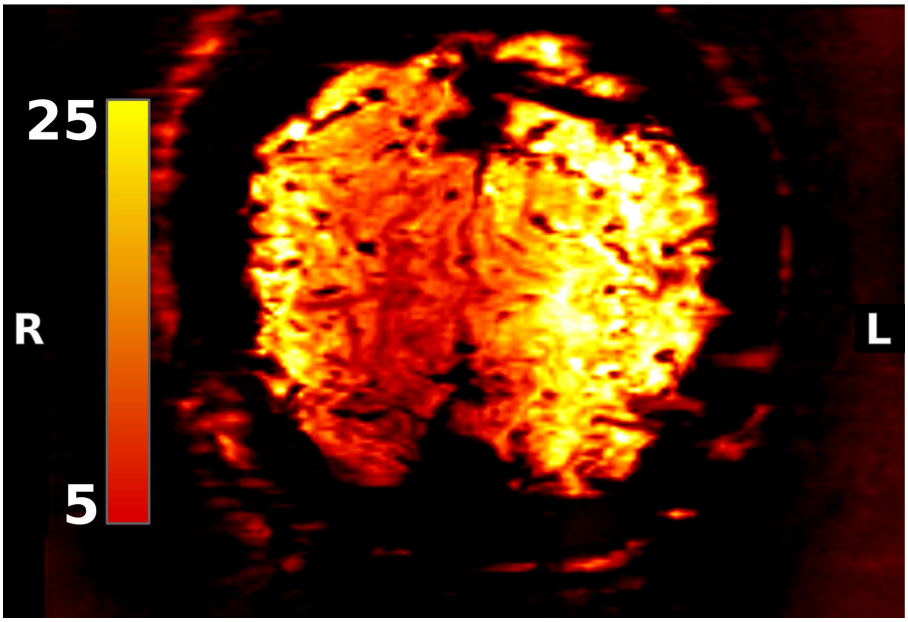

Figure 2.15: Temporal SNR image for one representative subject. The tSNR is higher in the left hemisphere (note that image is in radiological convention). The tSNR asymmetry is probably due to the coil sensitivity profile and phase encode polarity of the EPI sequence. We have not observed a tSNR imbalance in subsequent studies (Chapters 3 and 4) with a different coil of the same type.

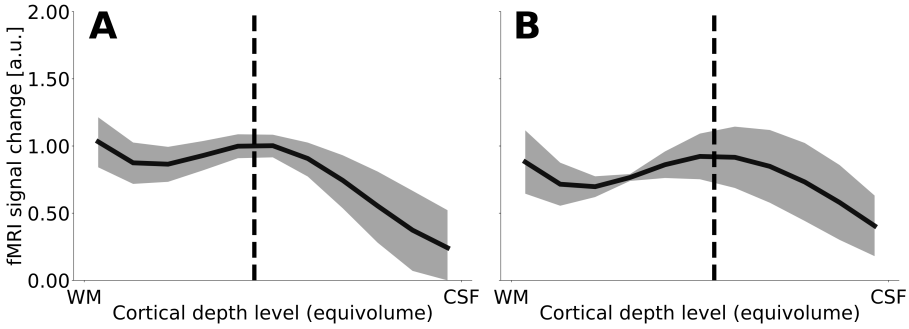

Figure 2.16: Response at 50% contrast across cortical depth in V1, for the left hemisphere (**A**) and three right hemispheres (**B**), after spatial deconvolution. (**A**) is identical to Figure 2.6 B. Since (**B**) is based on only three hemispheres, and resampling methods such as the percentile bootstrap (used in (**A**)) cannot meaningfully be applied at such a small sample size, the mean (solid line) and standard deviation (shading) across subjects is plotted in (**B**). The overall shape of the profiles is similar.

2.7 References

Adesnik, H., & Scanziani, M. (2010). Lateral competition for cortical space by layer-specific horizontal circuits. *Nature*, 464(7292), 1155–1160. https://doi.org/10.1038/nature08935

Ahrens, J., Geveci, B., & Law, C. (2005). ParaView: An End-User Tool for Large-Data Visualization. In C. D. Hansen & C. R. Johnson, *The Visualization Handbook* (pp. 717–731). Burlington: Elsevier Butterworth–Heinemann.

Albrecht, D. G., Geisler, W. S., Frazor, R. A., & Crane, A. M. (2002). Visual cortex neurons of monkeys and cats: temporal dynamics of the contrast response function. *Journal of Neurophysiology*, 88(2), 888–913.

Albrecht, D. G., & Hamilton, D. B. (1982). Striate cortex of monkey and cat: contrast response function. *Journal of Neurophysiology*, 48(1), 217–237.

Alonso, J. M., & Martinez, L. M. (1998). Functional connectivity between simple cells and complex cells in cat striate cortex. *Nature Neuroscience*, 1, 395–403.

Anderson, J. C., & Martin, K. A. C. (2009). The synaptic connections between cortical areas V1 and V2 in macaque monkey. *The Journal of Neuroscience: The Official Journal of the Society for Neuroscience*, 29(36), 11283–11293. https://doi.org/10.1523/JNEUROSCI.5757-08.2009

Andersson, J. L. R., Skare, S., & Ashburner, J. (2003). How to correct susceptibility distortions in spin-echo echo-planar images: application to diffusion tensor imaging. *NeuroImage*, 20(2), 870–888. https://doi.org/10.1016/S1053-8119(03)00336-7

Avidan, G., Harel, M., Hendler, T., Ben-Bashat, D., Zohary, E., & Malach, R. (2002). Contrast sensitivity in human visual areas and its relationship to object recognition. *Journal of Neurophysiology*, 87(6), 3102–3116.

Ayachit, U. (2015). The ParaView guide: updated for ParaView version 4.3 (Full color version; L. Avila, Ed.). Los Alamos: Kitware.

Bazin, P.-L., Cuzzocreo, J. L., Yassa, M. A., Gandler, W., McAuliffe, M. J., Bassett, S. S., & Pham, D. L. (2007). Volumetric neuroimage analysis extensions for the MIPAV software package. *Journal of Neuroscience Methods*, 165(1), 111–121. https://doi.org/10.1016/j.jneumeth.2007.05.024

Behnel, S., Bradshaw, R., Citro, C., Dalcin, L., Seljebotn, D. S., & Smith, K. (2011). Cython: The Best of Both Worlds. *Computing in Science & Engineering*, 13(2), 31–39. https://doi.org/10.1109/MCSE.2010.118

Bissig, D., & Berkowitz, B. A. (2009). Manganese-enhanced MRI of layer-specific activity in the visual cortex from awake and free-moving rats. *NeuroImage*, 44(3), 627–635. https://doi.org/10.1016/j.neuroimage.2008.10.013

Blasdel, G. G., & Lund, J. S. (1983). Termination of afferent axons in macaque striate cortex. *The Journal of Neuroscience: The Official Journal of the*

Society for Neuroscience, 3(7), 1389–1413.

Boas, D. A., Jones, S. R., Devor, A., Huppert, T. J., & Dale, A. M. (2008). A vascular anatomical network model of the spatio-temporal response to brain activation. *NeuroImage*, 40(3), 1116–1129. https://doi.org/10.1016/j.neuroimage.2007.12.061

Boynton, G. M., Demb, J. B., Glover, G. H., & Heeger, D. J. (1999). Neuronal basis of contrast discrimination. *Vision Research*, 39(2), 257–269.

Buracas, G. T., & Boynton, G. M. (2007). The effect of spatial attention on contrast response functions in human visual cortex. *The Journal of Neuroscience: The Official Journal of the Society for Neuroscience*, 27(1), 93–97. https://doi.org/10.1523/JNEUROSCI.3162-06.2007

Buracas, G. T., Fine, I., & Boynton, G. M. (2005). The relationship between task performance and functional magnetic resonance imaging response. *The Journal of Neuroscience: The Official Journal of the Society for Neuroscience*, 25(12), 3023–3031. https://doi.org/10.1523/JNEUROSCI.4476-04.2005

Callaway, E. M. (1998). Local circuits in primary visual cortex of the macaque monkey. *Annual Review of Neuroscience*, 21(1), 47–74. https://doi.org/10.1146/annurev.neuro.21.1.47

Callaway, E. M., & Wiser, A. K. (1996). Contributions of individual layer 2-5 spiny neurons to local circuits in macaque primary visual cortex. *Visual Neuroscience*, 13(5), 907–922.

Chen, G., Wang, F., Gore, J. C., & Roe, A. W. (2013). Layer-specific BOLD activation in awake monkey V1 revealed by ultra-high spatial resolution functional magnetic resonance imaging. *NeuroImage*, 64, 147–155. https://doi.org/10.1016/j.neuroimage.2012.08.060

De Martino, F., Yacoub, E., Kemper, V., Moerel, M., Uludag, K., De Weerd, P., ... Formisano, E. (2017). The impact of ultra-high field MRI on cognitive and computational neuroimaging. *NeuroImage*. https://doi.org/10.1016/j.neuroimage.2017.03.060

De Martino, F., Zimmermann, J., Muckli, L., Ugurbil, K., Yacoub, E., & Goebel, R. (2013). Cortical depth dependent functional responses in humans at 7T: improved specificity with 3D GRASE. *PloS One*, 8(3), e60514. https://doi.org/10.1371/journal.pone.0060514

de Sousa, A. A., Sherwood, C. C., Schleicher, A., Amunts, K., MacLeod, C. E., Hof, P. R., & Zilles, K. (2010). Comparative Cytoarchitectural Analyses of Striate and Extrastriate Areas in Hominoids. *Cerebral Cortex*, 20(4), 966–981. https://doi.org/10.1093/cercor/bhp158

Douglas, R. J., & Martin, K. A. C. (2004). Neuronal circuits of the neocortex. *Annual Review of Neuroscience*, 27, 419–451. https://doi.org/10.1146/annurev.neuro.27.070203.144152

Dumoulin, S. O., Fracasso, A., van der Zwaag, W., Siero, J. C. W., & Petridou, N. (2017). Ultra-high field MRI: Advancing systems neuroscience towards mesoscopic human brain function. *NeuroImage*. https://doi.org/10.1016/j.neuroimage.2017.01.028

Dumoulin, S. O., & Wandell, B. A. (2008). Population receptive field estimates in human visual cortex. *NeuroImage*, 39(2), 647–660. https://doi.org/10.1016/j.neuroimage.2007.09.034

Duvernoy, H. M., Delon, S., & Vannson, J. L. (1981). Cortical blood vessels of the human brain. *Brain Research Bulletin*, 7(5), 519–579.

Felleman, D. J., & Van Essen, D. C. (1991). Distributed hierarchical processing in the primate cerebral cortex. *Cerebral Cortex* (New York, N.Y.: 1991), 1(1), 1–47.

Fitzpatrick, D., Itoh, K., & Diamond, I. T. (1983). The laminar organization of the lateral geniculate body and the striate cortex in the squirrel monkey (Saimiri sciureus). *The Journal of Neuroscience: The Official Journal of the Society for Neuroscience*, 3(4), 673–702.

Fracasso, A., Luijten, P. R., Dumoulin, S. O., & Petridou, N. (2017). Laminar imaging of positive and negative BOLD in human visual cortex at 7T. *NeuroImage*. https://doi.org/10.1016/j.neuroimage.2017.02.038

Friston, K. J., Williams, S., Howard, R., Frackowiak, R. S., & Turner, R. (1996). Movement-related effects in fMRI time-series. *Magnetic Resonance in Medicine*, 35(3), 346–355.

Gilbert, C. D. (1977). Laminar differences in receptive field properties of cells in cat primary visual cortex. *The Journal of Physiology*, 268(2), 391–421. https://doi.org/10.1113/jphysiol.1977.sp011863

Goense, J. B. M., & Logothetis, N. K. (2008). Neurophysiology of the BOLD fMRI signal in awake monkeys. *Current Biology*: CB, 18(9), 631–640. https://doi.org/10.1016/j.cub.2008.03.054

Goense, J. B. M., Merkle, H., & Logothetis, N. K. (2012). High-resolution fMRI reveals laminar differences in neurovascular coupling between positive and negative BOLD responses. *Neuron*, 76(3), 629–639. https://doi.org/10.1016/j.neuron.2012.09.019

Goense, J. B. M., Zappe, A.-C., & Logothetis, N. K. (2007). High-resolution fMRI of macaque V1. *Magnetic Resonance Imaging*, 25(6), 740–747. https://doi.org/10.1016/j.mri.2007.02.013

Greve, D. N., & Fischl, B. (2009). Accurate and robust brain image alignment using boundary-based registration. *NeuroImage*, 48(1), 63–72. https://doi.org/10.1016/j.neuroimage.2009.06.060

Guidi, M., Huber, L., Lampe, L., Gauthier, C. J., & Möller, H. E. (2016). Lamina-dependent calibrated BOLD response in human primary motor cortex. *NeuroImage*, 141, 250–261. https://doi.org/10.1016/j.neuroimage.2016.06.030

Gulban, O. F., & Schneider, M. (2016). Segmentator: V1.1.0. https://doi.org/10.5281/zenodo.157996

Harel, N., Lin, J., Moeller, S., Ugurbil, K., & Yacoub, E. (2006). Combined imaging-histological study of cortical laminar specificity of fMRI signals. *NeuroImage*, 29(3), 879–887. https://doi.org/10.1016/j.neuroimage.2005.08.016

Henderickson, A. E., Wilson, J. R., & Ogren, M. P. (1978). The neurological organization of pathways between the dorsal lateral geniculate nucleus and visual cortex in old world and new world primates. *The Journal of Comparative Neurology*, 182(1), 123–136. https://doi.org/10.1002/cne.901820108

Hochstein, S., & Ahissar, M. (2002). View from the top: hierarchies and reverse hierarchies in the visual system. *Neuron*, 36(5), 791–804.

Hubel, D. H., & Livingstone, M. S. (1990). Color and contrast sensitivity in the lateral geniculate body and primary visual cortex of the macaque monkey. *The Journal of Neuroscience: The Official Journal of the Society for Neuroscience*, 10(7), 2223–2237.

Hubel, D. H., & Wiesel, T. N. (1968). Receptive fields and functional architecture of monkey striate cortex. *The Journal of Physiology*, 195(1), 215–243. https://doi.org/10.1113/jphysiol.1968.sp008455

Hubel, D. H., & Wiesel, T. N. (1972). Laminar and columnar distribution of geniculo-cortical fibers in the macaque monkey. *The Journal of Comparative Neurology*, 146(4), 421–450. https://doi.org/10.1002/cne.901460402

Huber, L., Goense, J. B. M., Kennerley, A. J., Ivanov, D., Krieger, S. N., Lepsien, J., … Möller, H. E. (2014). Investigation of the neurovascular coupling in positive and negative BOLD responses in human brain at 7 T. *NeuroImage*, 97, 349–362. https://doi.org/10.1016/j.neuroimage.2014.04.022

Huber, L., Goense, J. B. M., Kennerley, A. J., Trampel, R., Guidi, M., Reimer, E., … Möller, H. E. (2015). Cortical lamina-dependent blood volume changes in human brain at 7 T. *NeuroImage*, 107, 23–33. https://doi.org/10.1016/j.neuroimage.2014.11.046

Huber, L., Handwerker, D. A., Jangraw, D. C., Chen, G., Hall, A., Stüber, C., … Bandettini, P. A. (2017). High-Resolution CBV-fMRI Allows Mapping of Laminar Activity and Connectivity of Cortical Input and Output in Human M1. *Neuron*. https://doi.org/10.1016/j.neuron.2017.11.005

Huber, L., Ivanov, D., Guidi, M., Turner, R., Uludağ, K., Möller, H. E., & Poser, B. A. (2016). Functional cerebral blood volume mapping with simultaneous multi-slice acquisition. *NeuroImage*, 125, 1159–1168. https://doi.org/10.1016/j.neuroimage.2015.10.082

Huber, L., Uludağ, K., & Möller, H. E. (2017). Non-BOLD contrast for laminar fMRI in humans: CBF, CBV, and CMR02. *NeuroImage*. https://doi.org/10.1016/j.neuroimage.2017.07.041

Hunter, J. D. (2007). Matplotlib: A 2D Graphics Environment. *Computing in Science & Engineering*, 9(3), 90–95. https://doi.org/10.1109/MCSE.2007.55

Jenkinson, M., Bannister, P., Brady, M., & Smith, S. (2002). Improved optimization for the robust and accurate linear registration and motion correction of brain images. *NeuroImage*, 17(2), 825–841.

Jenkinson, M., & Smith, S. (2001). A global optimisation method for robust affine registration of brain images. *Medical Image Analysis*, 5(2), 143–156.

Jin, T., & Kim, S.-G. (2008). Cortical layer-dependent dynamic blood oxygenation, cerebral blood flow and cerebral blood volume responses during visual stimulation. *NeuroImage*, 43(1), 1–9. https://doi.org/10.1016/j.neuroimage.2008.06.029

Kashyap, S., Ivanov, D., Havlicek, M., Poser, B. A., & Uludağ, K. (2017). Impact of acquisition and analysis strategies on cortical depth-dependent fMRI. *NeuroImage*. https://doi.org/10.1016/j.neuroimage.2017.05.022

Kashyap, S., Ivanov, D., Havlicek, M., Sengupta, S., Poser, B. A., & Uludağ, K. (2018). Resolving laminar activation in human V1 using ultra-high spatial resolution fMRI at 7T. *Scientific Reports*, 8(1), 17063. https://doi.org/10.1038/s41598-018-35333-3

Kemper, V. G., De Martino, F., Vu, A. T., Poser, B. A., Feinberg, D. A., Goebel, R., & Yacoub, E. (2015). Sub-millimeter T2 weighted fMRI at 7 T: comparison of 3D-GRASE and 2D SE-EPI. *Frontiers in Neuroscience*, 9, 163. https://doi.org/10.3389/fnins.2015.00163

Kemper, V. G., De Martino, F., Yacoub, E., & Goebel, R. (2016). Variable flip angle 3D-GRASE for high resolution fMRI at 7 tesla. *Magnetic Resonance in Medicine*, 76(3), 897–904. https://doi.org/10.1002/mrm.25979

Kim, J., Matney, C. J., Blankenship, A., Hestrin, S., & Brown, S. P. (2014). Layer 6 corticothalamic neurons activate a cortical output layer, layer 5a. *The Journal of Neuroscience: The Official Journal of the Society for Neuroscience*, 34(29), 9656–9664. https://doi.org/10.1523/JNEUROSCI.1325-14.2014

Kim, T., & Kim, S.-G. (2010). Cortical layer-dependent arterial blood volume changes: improved spatial specificity relative to BOLD fMRI. *NeuroImage*, 49(2), 1340–1349. https://doi.org/10.1016/j.neuroimage.2009.09.061

Kleinnijenhuis, M., Zerbi, V., Küsters, B., Slump, C. H., Barth, M., & van Cappellen van Walsum, A.-M. (2013). Layer-specific diffusion weighted imaging in human primary visual cortex in vitro. *Cortex*, 49(9), 2569–2582. https://doi.org/10.1016/j.cortex.2012.11.015

Kok, P., Bains, L. J., van Mourik, T., Norris, D. G., & de Lange, F. P. (2016). Selective Activation of the Deep Layers of the Human Primary Visual Cortex by Top-Down Feedback. *Current Biology*, 26(3), 371–376. https://doi.org/10.1016/j.cub.2015.12.038

Koopmans, P. J., Barth, M., & Norris, D. G. (2010). Layer-specific BOLD activation in human V1. *Human Brain Mapping*, 31(9), 1297–1304. https://doi.org/10.1002/hbm.20936

Koopmans, P. J., Barth, M., Orzada, S., & Norris, D. G. (2011). Multi-echo fMRI of the cortical laminae in humans at 7T. *NeuroImage*, 56(3), 1276–1285. https://doi.org/10.1016/j.neuroimage.2011.02.042

Lamme, V. A., & Roelfsema, P. R. (2000). The distinct modes of vision offered by feedforward and recurrent processing. *Trends in Neurosciences*, 23(11), 571–579.

Legge, G. E. (1981). A power law for contrast discrimination. *Vision Research*, 21(4), 457–467.

Levitt, J. B., Kiper, D. C., & Movshon, J. A. (1994). Receptive fields and functional architecture of macaque V2. *Journal of Neurophysiology*, 71(6), 2517–2542.

Logothetis, N. K. (2008). What we can do and what we cannot do with fMRI. *Nature*, 453(7197), 869–878. https://doi.org/10.1038/nature06976

Logothetis, N. K., Pauls, J., Augath, M., Trinath, T., & Oeltermann, A. (2001). Neurophysiological investigation of the basis of the fMRI signal. *Nature*, 412(6843), 150–157. https://doi.org/10.1038/35084005

Lu, H., Patel, S., Luo, F., Li, S.-J., Hillard, C. J., Ward, B. D., & Hyde, J. S. (2004). Spatial correlations of laminar BOLD and CBV responses to rat whisker stimulation with neuronal activity localized by Fos expression. *Magnetic Resonance in Medicine*, 52(5), 1060–1068. https://doi.org/10.1002/mrm.20265

Lund, J. S. (1973). Organization of neurons in the visual cortex, area 17, of the monkey (Macaca mulatta). *The Journal of Comparative Neurology*, 147(4), 455–495. https://doi.org/10.1002/cne.901470404

Lund, J. S. (1988). Anatomical Organization of Macaque Monkey Striate Visual Cortex. *Annual Review of Neuroscience*, 11(1), 253–288. https://doi.org/10.1146/annurev.ne.11.030188.001345

Maier, A., Aura, C. J., & Leopold, D. A. (2011). Infragranular sources of sustained local field potential responses in macaque primary visual cortex. *The Journal of Neuroscience: The Official Journal of the Society for Neuroscience*, 31(6), 1971–1980. https://doi.org/10.1523/JNEUROSCI.5300-09.2011

Markuerkiaga, I., Barth, M., & Norris, D. G. (2016). A cortical vascular model for examining the specificity of the laminar BOLD signal. *NeuroImage*, 132, 491–498. https://doi.org/10.1016/j.neuroimage.2016.02.073

Marquardt, I., Schneider, M., & Gulban, O. F. (2017). py_pRF_mapping: A free & open python tool for population receptive field analysis. Retrieved from https://doi.org/10.5281/zenodo.835162

Marques, J. P., Kober, T., Krueger, G., van der Zwaag, W., Van de Moortele, P.-F., & Gruetter, R. (2010). MP2RAGE, a self bias-field corrected sequence for improved segmentation and T1-mapping at high field. *NeuroImage*, 49(2), 1271–1281. https://doi.org/10.1016/j.neuroimage.2009.10.002

Martinez, L. M., & Alonso, J.-M. (2003). Complex Receptive Fields in Primary Visual Cortex. *The Neuroscientist*, 9(5), 317–331. https://doi.org/10.1177/1073858403252732

Maunsell, J. H., & Newsome, W. T. (1987). Visual processing in monkey extrastriate cortex. *Annual Review of Neuroscience*, 10, 363–401. https://doi.org/10.1146/annurev.ne.10.030187.002051

Millman, K. J., & Aivazis, M. (2011). Python for Scientists and Engineers. *Computing in Science & Engineering*, 13(2), 9–12. https://doi.org/10.1109/MCSE.2011.36

Muckli, L., De Martino, F., Vizioli, L., Petro, L. S., Smith, F. W., Ugurbil, K., … Yacoub, E. (2015). Contextual Feedback to Superficial Layers of V1. *Current Biology*: CB, 25(20), 2690–2695. https://doi.org/10.1016/j.cub.2015.08.057

Oliphant, T. E. (2007). Python for Scientific Computing. *Computing in Science & Engineering*, 9(3), 10–20. https://doi.org/10.1109/MCSE.2007.58

Olsen, S. R., Bortone, D. S., Adesnik, H., & Scanziani, M. (2012). Gain control by layer six in cortical circuits of vision. *Nature*, 483(7387), 47–52. https://doi.org/10.1038/nature10835

Peirce, J. W. (2007). PsychoPy–Psychophysics software in Python. *Journal of Neuroscience Methods*, 162(1–2), 8–13. https://doi.org/10.1016/j.jneumeth.2006.11.017

Peirce, J. W. (2008). Generating stimuli for neuroscience using PsychoPy. *Frontiers in Neuroinformatics*, 2. https://doi.org/10.3389/neuro.11.010.2008

Pfeuffer, J., Adriany, G., Shmuel, A., Yacoub, E., Van De Moortele, P.-F., Hu, X., & Ugurbil, K. (2002). Perfusion-based high-resolution functional imaging in the human brain at 7 Tesla. *Magnetic Resonance in Medicine*, 47(5), 903–911. https://doi.org/10.1002/mrm.10154

Polimeni, J. R., Renvall, V., Zaretskaya, N., & Fischl, B. (2017). Analysis strategies for high-resolution UHF-fMRI data. *NeuroImage*. https://doi.org/10.1016/j.neuroimage.2017.04.053

Polimeni, J. R., Witzel, T., Fischl, B., Greve, D. N., & Wald, L. L. (2010). Identifying common-source driven correlations in resting-state fMRI via laminar-specific analysis in the human visual cortex. *Proc. Intl. Soc. Mag. Reson. Med.*, 18, 353.

Poser, B. A., Koopmans, P. J., Witzel, T., Wald, L. L., & Barth, M. (2010). Three dimensional echo-planar imaging at 7 Tesla. *NeuroImage*, 51(1), 261–266. https://doi.org/10.1016/j.neuroimage.2010.01.108

Roberts, M. J., Lowet, E., Brunet, N. M., Ter Wal, M., Tiesinga, P., Fries, P., & De Weerd, P. (2013). Robust gamma coherence between macaque V1 and V2 by dynamic frequency matching. *Neuron*, 78(3), 523–536. https://doi.org/10.1016/j.neuron.2013.03.003

Rockland, K. S., & Pandya, D. N. (1979). Laminar origins and terminations of cortical connections of the occipital lobe in the rhesus monkey. *Brain Research*, 179(1), 3–20. https://doi.org/10.1016/0006-8993(79)90485-2

Rockland, K. S., & Virga, A. (1989). Terminal arbors of individual 'feedback' axons projecting from area V2 to V1 in the macaque monkey: a study using immunohistochemistry of anterogradely transported Phaseolus vulgaris-leucoagglutinin. *The Journal of Comparative Neurology*, 285(1), 54–72. https://doi.org/10.1002/cne.902850106

Sclar, G., Maunsell, J. H., & Lennie, P. (1990). Coding of image contrast in central visual pathways of the macaque monkey. *Vision Research*, 30(1), 1–10.

Self, M. W., van Kerkoerle, T., Goebel, R., & Roelfsema, P. R. (2017). Benchmarking laminar fMRI: Neuronal spiking and synaptic activity during top-down and bottom-up processing in the different layers of cortex. *NeuroImage*. https://doi.org/10.1016/j.neuroimage.2017.06.045

Sherman, S. M. (2005). Thalamic relays and cortical functioning. *Progress in Brain Research*, 149, 107–126. https://doi.org/10.1016/S0079-6123(05)49009-3

Smirnakis, S. M., Schmid, M. C., Weber, B., Tolias, A. S., Augath, M., & Logothetis, N. K. (2007). Spatial specificity of BOLD versus cerebral blood volume fMRI for mapping cortical organization. *Journal of Cerebral Blood Flow and Metabolism: Official Journal of the International Society of Cerebral Blood Flow and Metabolism*, 27(6), 1248–1261. https://doi.org/10.1038/sj.jcbfm.9600434

Smith, S. M., Jenkinson, M., Woolrich, M. W., Beckmann, C. F., Behrens, T. E. J., Johansen-Berg, H., ... Matthews, P. M. (2004). Advances in functional and structural MR image analysis and implementation as FSL. *NeuroImage*, 23, S208–S219. https://doi.org/10.1016/j.neuroimage.2004.07.051

Thomson, A. M. (2010). Neocortical layer 6, a review. *Frontiers in Neuroanatomy*, 4, 13. https://doi.org/10.3389/fnana.2010.00013

Tootell, R. B., Hamilton, S. L., & Switkes, E. (1988). Functional anatomy of macaque striate cortex. IV. Contrast and magno-parvo streams. *The Journal of Neuroscience: The Official Journal of the Society for Neuroscience*, 8(5), 1594–1609.

Tootell, R. B., & Nasr, S. (2017). Columnar Segregation of Magnocellular and Parvocellular Streams in Human Extrastriate Cortex. *The Journal of Neuroscience: The Official Journal of the Society for Neuroscience*.

https://doi.org/10.1523/JNEUROSCI.0690-17.2017
Tootell, R. B., Reppas, J. B., Kwong, K. K., Malach, R., Born, R. T., Brady, T. J., ... Belliveau, J. W. (1995). Functional analysis of human MT and related visual cortical areas using magnetic resonance imaging. *The Journal of Neuroscience: The Official Journal of the Society for Neuroscience*, 15(4), 3215–3230.
Tosun, D., Rettmann, M. E., Han, X., Tao, X., Xu, C., Resnick, S. M., ... Prince, J. L. (2004). Cortical surface segmentation and mapping. *NeuroImage*, 23, S108–S118. https://doi.org/10.1016/j.neuroimage.2004.07.042
Uludağ, K., & Blinder, P. (2018). Linking brain vascular physiology to hemodynamic response in ultra-high field MRI. *NeuroImage*, 168, 279–295. https://doi.org/10.1016/j.neuroimage.2017.02.063
Uludağ, K., Müller-Bierl, B., & Uğurbil, K. (2009). An integrative model for neuronal activity-induced signal changes for gradient and spin echo functional imaging. *NeuroImage*, 48(1), 150–165. https://doi.org/10.1016/j.neuroimage.2009.05.051
van der Walt, S., Colbert, S. C., & Varoquaux, G. (2011). The NumPy Array: A Structure for Efficient Numerical Computation. *Computing in Science & Engineering*, 13(2), 22–30. https://doi.org/10.1109/MCSE.2011.37
Viswanathan, A., & Freeman, R. D. (2007). Neurometabolic coupling in cerebral cortex reflects synaptic more than spiking activity. *Nature Neuroscience*, 10(10), 1308–1312. https://doi.org/10.1038/nn1977
Vogels, R., & Orban, G. A. (1996). Coding of stimulus invariances by inferior temporal neurons. *Progress in Brain Research*, 112, 195–211.
Waehnert, M. D., Dinse, J., Weiss, M., Streicher, M. N., Waehnert, P., Geyer, S., ... Bazin, P.-L. (2014). Anatomically motivated modeling of cortical laminae. *NeuroImage*, 93, 210–220. https://doi.org/10.1016/j.neuroimage.2013.03.078
Weber, B., Keller, A. L., Reichold, J., & Logothetis, N. K. (2008). The microvascular system of the striate and extrastriate visual cortex of the macaque. *Cerebral Cortex* (New York, N.Y.: 1991), 18(10), 2318–2330. https://doi.org/10.1093/cercor/bhm259
Xing, D., Yeh, C.-I., Burns, S., & Shapley, R. M. (2012). Laminar analysis of visually evoked activity in the primary visual cortex. *Proceedings of the National Academy of Sciences*, 109(34), 13871–13876. https://doi.org/10.1073/pnas.1201478109
Yan, T., Wang, B., Geng, Y., Yan, Y., Mu, N., Wu, J., ... Peng, Y. (2014). Contrast response functions with wide-view stimuli in the human visual cortex. *Perception*, 43(7), 677–693. https://doi.org/10.1068/p7640
Yu, X., Glen, D., Wang, S., Dodd, S., Hirano, Y., Saad, Z., ... Koretsky, A. P. (2012). Direct imaging of macrovascular and microvascular contributions

to BOLD fMRI in layers IV-V of the rat whisker-barrel cortex. *NeuroImage*, 59(2), 1451–1460. https://doi.org/10.1016/j.neuroimage.2011.08.001

Yu, X., Qian, C., Chen, D., Dodd, S. J., & Koretsky, A. P. (2014). Deciphering laminar-specific neural inputs with line-scanning fMRI. *Nature Methods*, 11(1), 55–58. https://doi.org/10.1038/nmeth.2730

Yushkevich, P. A., Piven, J., Hazlett, H. C., Smith, R. G., Ho, S., Gee, J. C., & Gerig, G. (2006). User-guided 3D active contour segmentation of anatomical structures: Significantly improved efficiency and reliability. *NeuroImage*, 31(3), 1116–1128. https://doi.org/10.1016/j.neuroimage.2006.01.015

Zhang, Y., Brady, M., & Smith, S. (2001). Segmentation of brain MR images through a hidden Markov random field model and the expectation-maximization algorithm. *IEEE Transactions on Medical Imaging*, 20(1), 45–57. https://doi.org/10.1109/42.906424

Zhao, F., Wang, P., Hendrich, K., Ugurbil, K., & Kim, S.-G. (2006). Cortical layer-dependent BOLD and CBV responses measured by spin-echo and gradient-echo fMRI: insights into hemodynamic regulation. *NeuroImage*, 30(4), 1149–1160. https://doi.org/10.1016/j.neuroimage.2005.11.013

Zhao, F., Wang, P., & Kim, S.-G. (2004). Cortical depth-dependent gradient-echo and spin-echo BOLD fMRI at 9.4T. *Magnetic Resonance in Medicine*, 51(3), 518–524. https://doi.org/10.1002/mrm.10720

3

Surface perception and layer-specific feedback effects in human early visual cortex

Corresponding publication:

Marquardt, I., De Weerd, P., Schneider, M., Gulban, O. F., Ivanov, D., & Uludağ, K. (*2019*). Depth-resolved ultra-high field fMRI reveals feedback contributions to surface motion perception. https://doi.org/10.1101/653626

3.1 Abstract

Research on the early visual system has predominantly focused on the neuronal responses to contours. However, continuous surfaces constitute another ecologically relevant type of stimulus. Here, we presented human participants with uniform surfaces that were physically identical in the left visual hemifield, but varied in their global perceptual qualities. The stimulus-induced responses in early visual areas were measured with fMRI at sub-millimetre spatial resolution. We investigated the cortical depth-profiles of top-down feedback in early visual cortex, by focusing our analysis on the cortical hemisphere representing the physically constant visual hemifield. We observed a top-down effect that was most pronounced at mid-cortical depths in V2 and V3, and slightly more superficial in V1. A possible explanation for the observed pattern of activation could be that feedback from a higher cortical area re-enters at the level of V1, with a feedforward sweep through V2 and V3. However, alternative interpretations are possible, such as an indirect, cortico-thalamic-cortical feedback effect. Moreover, we observed a strongly negative, delayed response at the cortical representation of the surface stimulus. Interestingly, this negative response was accompanied by a faster, transient, positive response at the edges of the stimulus. In a control experiment, we discovered that the negative surface response depends on the type of background the stimulus is presented on, regardless of the shape of the stimulus.

3.2 Introduction

The neural correlates of surface perception have been studied using a variety of visual illusions. In this study, we investigated the neural correlates of surface motion in a centrally fixated luminance-defined disk from which a sector was removed, so that by rotating the sector back-and-forth, the whole surface was perceived as moving (Figure 3.1). Using ultra-high field 7T fMRI, we assessed whether there was more activity in retinotopic areas to the same luminance-defined surface when it was perceived as moving rather than static. In addition, we aimed to test whether there is a cortical layer-specific pattern of activity compatible with a contribution of feedback during the perception of the surface as moving.

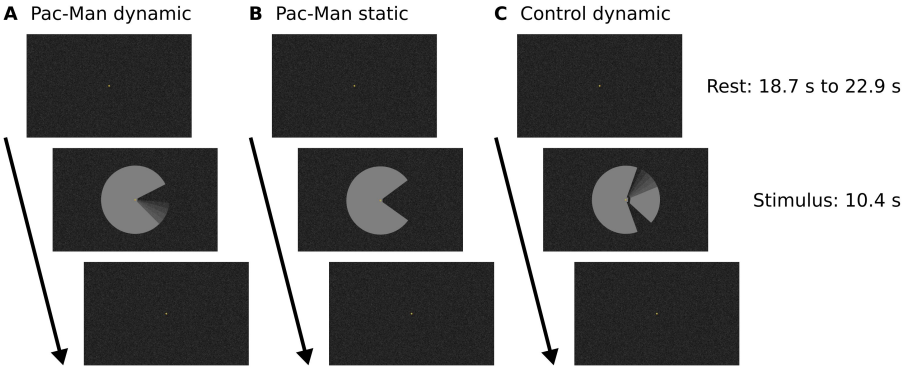

Figure 3.1: Experimental design. Stimuli were presented in a block design with rest blocks of variable duration. A central fixation dot and a static random texture background pattern were present throughout the duration of each run. (**A**) A 'Pac-Man' figure rotating about its centre served as the main experimental stimulus. At the beginning of each stimulus block, the 'mouth' was centred on the horizontal meridian (i.e. mirror-symmetric about the horizontal meridian). The 'mouth' had a circular arc of 70° (±35° from the right horizontal meridian), and rotated clockwise and anticlockwise by ±35° (with respect to the right horizontal meridian), at a rate of 0.85 cycles per second. This experimental condition is referred to as 'Pac-Man Dynamic'. (**B**) In the first of two control conditions, the same Pac-Man figure as in (**A**) was presented statically, i.e. without rotating about its centre. This condition is referred to as 'Pac-Man static'. (**C**) In the second control condition, a figure consisting of a stationary wedge on its left side, and a smaller, rotating wedge on its right side was presented. The movement of the right-hand wedge was similar to that of the 'mouth' of Pac-Man dynamic; i.e. it started centred on the horizontal meridian, and rotated with the same frequency and angular displacement as the 'mouth' of Pac-Man dynamic. The rotating, right-hand wedge had a circular arc of 65°, and the stationary, left-hand wedge had a circular arc of 220°. This condition is referred to as 'control dynamic'. All three stimuli had a diameter of 7.5° visual angle. In (**A**) and (**C**), the angular position of the 'mouth' and the wedge were modulated sinusoidally, to create the impression of a smooth, natural movement. Importantly, the Pac-Man dynamic stimulus is perceived to rotate as a whole, whereas the control dynamic stimulus creates the impression of a rotating wedge on the right, and a stationary wedge on the left. At the same time, the retinal image of all three stimuli is identical in the left visual field. All stimuli were presented on a static, textured random noise background to enhance figure-ground segmentation. The stimuli, including the texture background, were adapted from Akin et al. (2014). Videos of the stimuli are available online (https://doi.org/10.5281/zenodo.2583017).

The question, whether the perception of surface features is associated with activity in retinotopic cortical areas, has been a topic of debate. Some fMRI studies (Cornelissen, Wade, Vladusich, Dougherty, & Wandell, 2006; Perna, Tosetti, Montanaro, & Morrone, 2005) did not observe a response to surfaces in early visual cortex. By contrast, other fMRI studies (Hsieh & Tse, 2010; Kok & de Lange, 2014; Mendola, Dale, Fischl, Liu, & Tootell, 1999; Pereverzeva & Murray, 2008; Sasaki & Watanabe, 2004) as well as cat (Rossi & Paradiso, 1999; Rossi, Rittenhouse, & Paradiso, 1996) and monkey recording studies (De Weerd, Gattass, Desimone, & Ungerleider, 1995; Komatsu, Kinoshita, & Murakami, 2000; and in Komatsu et al., 2000; Lamme, 1995; Lamme, Rodriguez-Rodriguez, & Spekreijse, 1999; reviewed in Lamme & Roelfsema, 2000; Lu & Roe, 2007; Roe, Lu, & Hung, 2005; Zipser, Lamme, & Schiller, 1996) have found neuronal activation associated with the perception of surface brightness, colour, or texture.

Activity in early visual areas during the perception of various surface features may reflect neural interpolation mechanisms within early visual areas, as suggested by some human psychophysical (De Weerd, Desimone, & Ungerleider, 1998; Dresp & Bonnet, 1991; Paradiso & Nakayama, 1991) and monkey neurophysiological data (De Weerd et al., 1995; Huang & Paradiso, 2008). Diffusion-like mechanisms in a surface feature system, where spread of surface-related activation is contained within proper retinotopic bounds by local inhibition delivered by boundary representations, have been central in computational models of surface perception (Grossberg, 1987a, 1987b; see also Keil, Cristóbal, Hansen, & Neumann, 2005).

A contribution of feedback in the perception of surfaces was borne out by distinct superficial and deep cortical layer contributions in laminar recordings in monkeys (Self, van Kerkoerle, Supèr, & Roelfsema, 2013). Self et al. (2013) studied the laminar profile of figure-ground segregation in monkey V1. They observed neuronal activity related to feedforward, horizontal, and feedback mechanisms, supposedly related to the processing of stimulus texture, borders, and figure-ground segregation, respectively. The feedback signals were strongest in superficial and deep layers (Self et al., 2013), in accordance with projection patterns observed in anatomical studies (Anderson & Martin, 2009; Rockland & Pandya, 1979; Rockland & Virga, 1989).

While the tools to perform layer-specific recordings have been

available in invasive neurophysiology in animals for decades, the analysis of depth-specific activity in humans has only recently become within reach thanks to ultra-high field fMRI (Guidi, Huber, Lampe, Gauthier, & Möller, 2016; Huber et al., 2015; Klein et al., 2018; Koopmans, Barth, & Norris, 2010; Koopmans, Barth, Orzada, & Norris, 2011; Muckli et al., 2015; Olman et al., 2012; Polimeni, Fischl, Greve, & Wald, 2010; Ress, Glover, Liu, & Wandell, 2007). In the only depth-specific human fMRI study on surface perception to date, Kok et al. (2016) presented participants with Kanizsa stimuli containing illusory surfaces and contours. The illusory stimuli caused a response at deep cortical depths in V1, presumably due to feedback from higher cortical areas. Although the attribution of the activity in deep layers to feedback is plausible, the feedback could be related to the illusory contour or to the illusory surface, because the region of interest was centred on the edge of the Kanizsa stimulus.

Earlier studies in monkeys found neuronal activity caused by illusory contours in V2 (von der Heydt, Peterhans, & Baumgartner, 1984) and in V1 (Grosof, Shapley, & Hawken, 1993), but attributed this effect to horizontal connections, and not to top-down feedback. A later electrophysiological study confirmed responses to illusory contours in V1 and V2 (Lee & Nguyen, 2001). Because the response to illusory contours in V2 preceded that in V1, feedback mechanisms are a more convincing explanation for the observed response (rather than horizontal interactions) (Lee & Nguyen, 2001). Further evidence for a role of feedback to early visual cortex in the perception of illusory contours comes from a TMS study (Wokke, Vandenbroucke, Scholte, & Lamme, 2013), in which the involvement of V1/V2 in the perceptual completion of a Kanizsa-type figure succeeded that of higher-order visual cortex. To the best of our knowledge, the laminar profile of real and illusory surface perception has not been studied in humans so far.

Remarkably, research on the coding of surface properties has predominantly involved illusory figures, whereas real, static surfaces have received less attention. In studies focusing on motion interpolation, responses were most likely driven by contours rather than surfaces (Meng, Remus, & Tong, 2005; Muckli, Kohler, Kriegeskorte, & Singer, 2005), or by local elements in a non-uniform surface (Muckli, Singer, Zanella, & Goebel, 2002). More specifically, previous studies presented moving random dots (Muckli et al., 2002), moving gratings (Meng et al., 2005),

or the so-called motion quartet stimulus (Muckli et al., 2005). In primary visual cortex, a response was observed along the trace of the resulting illusory motion percept, i.e. without any local change in retinotopic input. This effect is thought to be caused by feedback originating in motion-sensitive area hMT (Meng et al., 2005; Muckli et al., 2005).

In the current study, instead of investigating a form of interpolation in an illusory display, we used ultra-high field 7T fMRI to determine whether the perceived motion of a luminance-defined surface was associated with enhanced activity in early visual cortex. The stimulus design (see Akin et al., 2014) and analysis methods (Marquardt, Schneider, Gulban, Ivanov, & Uludağ, 2018) were optimised to separate signal due to the figure surface from signal due to local discontinuities or boundaries. The stimulus consisted of a luminance-defined disk that was centrally fixated (Figure 3.1). The movement of the removed sector was limited to the right hemifield, so that fMRI activity related to the surface in the left hemifield could be unambiguously related to surface perception. Control stimuli without motion perception were physically identical in the left hemifield. In other words, the lack of local contrast variations or texture elements inside the surface ensured that a specific distribution of activity over cortical depth could be related unambiguously to perceived motion of the surface. Because the retinal image of all three stimuli was identical in the left hemifield, and because transcallosal connections are restricted to the vertical meridian in primate early visual cortex (Clarke & Miklossy, 1990; Essen & Zeki, 1978; Glickstein & Whitteridge, 1976; Houzel & Milleret, 1999; Van Essen, Newsome, & Bixby, 1982; Wong-Riley, 1974), any difference between stimulus conditions can be attributed to top-down feedback effects. Moreover, the stimulus was large enough so that contributions to fMRI signal from the surface were separable from contributions from the contour.

We employed a spatial deconvolution to remove signal spread caused by draining veins from the cortical depth profiles of stimulus-induced activation (Markuerkiaga, Barth, & Norris, 2016; Marquardt, Schneider, Gulban, et al., 2018). The combination of stimulus design and the recently developed spatial deconvolution approach maximized sensitivity for a first sub-millimetre fMRI investigation into contributions of feedback to the perception of surface motion in human V1, V2 and V3.

3.3 Methods

3.3.1 Experimental design

Healthy participants (n=9, age between 18 and 44 years, mean (SD) age 27.6 (7.3) years) gave informed consent before the experiment, and the study protocol was approved by the local ethics committee of the Faculty for Psychology & Neuroscience, Maastricht University. Subjects were presented three visual stimuli that differed in global perceptual quality, while being locally identical in the left half of the visual field. The main experimental stimulus was a 'Pac-Man' figure rotating around its centre (Figure 3.1 A). There were two control conditions: First, the same Pac-Man figure as in the main condition was presented statically, i.e. without rotating around its centre (Figure 3.1 B). Second, a stimulus consisting of a large, stationary wedge on the left side, and a smaller, rotating wedge on the right side (at the same location as the 'mouth' of the Pac-Man; Figure 3.1 C) was presented. We will henceforth refer to these three conditions as 'Pac-Man dynamic', 'Pac-Man static', and 'control dynamic', respectively.

All three stimuli had a diameter of 7.5° visual angle. The 'mouth' of the Pac-Man had a circular arc of 70° (±35° from the right horizontal meridian). In the Pac-Man dynamic condition, the 'mouth' of the Pac-Man rotated clockwise and anticlockwise by ±35°, at a rate of 0.85 cycles per second. The angular position of the 'mouth' was modulated sinusoidally in order to create the impression of a smooth, natural movement. In the control dynamic condition, the right-hand wedge rotated with the same frequency and angular displacement as the 'mouth' of the Pac-Man. The rotating, right-hand wedge had a circular arc of 65°, and the stationary, left-hand wedge had a circular arc of 220°. As a result, the Pac-Man dynamic stimulus is perceived to rotate as a whole, whereas the control dynamic stimulus creates the impression of a rotating wedge on the right and a stationary wedge on the left. Importantly, the retinal image of all three stimuli is identical in the left visual field. All stimuli were presented on a textured random noise background in order to enhance figure-ground segregation. The stimuli, including the texture background, were adapted from Akin et al. (2014). The texture pattern was created by randomly drawing pixel intensity values from a Gaussian distribution, and filtering the resulting image with a uniform

kernel (kernel size 6 x 6 pixel). The mean luminance of the texture background was 8 cd/m^2, and the figures had a uniform luminance of 163 cd/m^2.

Stimuli were created with Psychopy (Peirce, 2007, 2008) and projected onto a translucent screen mounted behind the MRI head coil, via a mirror mounted at the end of the scanner bore. The three stimulus conditions were presented in separate runs and in random order. Stimuli were presented in a block design with block durations of 10.4 s and variable rest periods in random order (18.7 s, 20.8 s, or 22.9 s). Each run began with an initial rest period with a fixed duration of 20.8 s, and ended with a rest period of one of the three possible durations. All lights in the scanner room were switched off during the experiment, and black cardboard was placed on the inside of the MRI transmit coil in order to minimise light reflection. Each subject completed six functional runs (two for each stimulus condition; with the exception of one subject, who completed three repetitions each of the Pac-Man dynamic and control dynamic conditions, and two for Pac-Man static). The total duration of a run was 520 s.

Participants were asked to fixate a central dot throughout the experiment and to report pseudo-randomly occurring changes in the dot's colour by button press. These targets were presented for 800 ms, with a mean inter-trial interval of 30 s (range ±10 s). No targets appeared during the first and last 15 s of each run. The timing of the colour changes was arranged such that the predicted haemodynamic responses to the experimental stimulus and to the colour changes are uncorrelated. To this end, a design vector representing the stimulus blocks and a design vector containing pseudo-randomly timed target events were separately convolved with a gamma function serving as model for the haemodynamic responses. The correlation between the predicted responses to the stimulus blocks and to the target events was calculated, and if the correlation coefficient was above threshold (r>0.001), a new pseudo-random design matrix of target events was created. This procedure was repeated until the correlation was below threshold, separately for each run.

In an additional run, retinotopic mapping stimuli were presented for population receptive field estimation, allowing us to delineate early visual areas V1, V2, and V3 on the cortical surface (Dumoulin & Wandell, 2008). Stimuli used for population receptive field mapping were

oriented bars at four different orientations and eight different positions per orientation, containing a black and white chequerboard pattern. The bars had a width of 1.25° visual angle, and the carrier pattern within the bar had a spatial frequency of 1.2 cycles/deg. The luminance of the black and white sectors of the carrier pattern was 2 cd/m^2 and 1390 cd/m^2, respectively, resulting in a luminance contrast of ∼1. The polarity of the chequerboard pattern was reversed at a frequency of 4 Hz, and the bar changed its position every 2.079 s (in synchrony with the volume TR). Each of the 32 stimulus configurations (four orientations, eight positions per orientation) was presented 12 times in random order. The duration of the population receptive field mapping run was 832 s (400 volumes). Similar to the main experiment, subjects were instructed to perform a central fixation task during the retinotopic mapping experiment. The python code used to create the experimental stimuli and videos of the stimuli (Marquardt, Schneider, & Gulban, 2018) and software for the presentation of the retinotopic mapping stimuli are publicly available (Marquardt, Gulban, & Schneider, 2018).

To better distinguish between sustained and transient responses (Horiguchi, Nakadomari, Misaki, & Wandell, 2009; Uludağ, 2008), we acquired an additional experimental run for the Pac-Man dynamic condition with longer block durations in a subset of subjects (n=5). The additional run had a duration of 424 s, during which the dynamic Pac-Man stimulus was presented five times for 25 s, interspersed between rest blocks of 50 s. As in the main experiment, subjects performed a central fixation task.

3.3.2 Data acquisition & preprocessing

Functional MRI data were acquired on a 7 T scanner (Siemens Medical Systems, Erlangen, Germany) and a 32-channel phased-array head coil (Nova Medical, Wilmington, MA, USA) using a 3D gradient echo (GE) EPI sequence (TR = 2.079 s, TE = 26 ms, nominal resolution 0.8 mm isotropic, 40 slices, coronal oblique slice orientation, phase encode direction right-to-left, phase partial Fourier 6/8; GRAPPA acceleration factor 3; Poser, Koopmans, Witzel, Wald, & Barth, 2010). We also acquired whole-brain structural T1 images using the MP2RAGE sequence (Marques et al., 2010) with 0.7 mm isotropic voxels, and a pair of five SE EPI images with opposite phase encoding for distortion correction of

the functional data (TR = 4.0 s, TE 41 = ms; position, orientation, and resolution same as for the GE sequence Feinberg et al., 2010; Moeller et al., 2010; Setsompop et al., 2012).

Motion correction was performed using SPM 12 (Friston, Williams, Howard, Frackowiak, & Turner, 1996), and the data were distortion corrected using FSL TOPUP (Andersson, Skare, & Ashburner, 2003). Standard statistical analyses were performed using FSL (Smith et al., 2004), fitting a general linear model (GLM) with separate predictors for the three stimulus conditions and a nuisance predictor for the target events of the fixation task. To account for both sustained and transient responses, each of the three stimulus conditions was modelled with two predictors: one based on a 'boxcar function' over the entire stimulus duration, and the other based on a delta function at stimulus onset and offset. (Only one predictor was used for the short target events.) All GLM predictors were convolved with a double-gamma haemodynamic response function. Highpass temporal filtering (cutoff = 35 s) was applied to the model and to the functional time series before GLM fitting. The parameter estimates obtained from the GLM were converted into percent signal change with respect to the initial pre-stimulus baseline (i.e. the first 20.8 s of each run). Population receptive field mapping (Dumoulin & Wandell, 2008) was performed using publicly available python code (Marquardt, Gulban, & Schneider, 2018) and standard scientific python packages (Numpy, Scipy, Matplotlib, Cython; Behnel et al., 2011; Millman & Aivazis, 2011; Oliphant, 2007; van der Walt, Colbert, & Varoquaux, 2011). To facilitate reproducibility, the complete analysis pipeline was containerised within docker images (Halchenko & Hanke, 2012; Kaczmarzyk et al., 2017).

Cortical depth sampling requires a high level of spatial accuracy. To detect and remove low-quality data based on a quantifiable and reproducible exclusion criterion, we calculated the spatial correlation between each functional volume and the mean EPI image of that session after motion correction and distortion correction (see Marquardt, Schneider, Gulban, et al., 2018 for details). If the mean correlation coefficient of the volumes in a run was below threshold ($r < 0.95$), that run would have been excluded from further analysis. However, no runs were excluded based on the spatial correlation criterion. Moreover, it was important for subjects to be awake and to maintain fixation throughout the experiment. Therefore, runs in which subjects had detected less

than 70% of targets were excluded from the analysis. This led to the exclusion of all runs from one subject. All other subjects had detected more than 70% of targets on all runs (mean hit rate for all subjects = 93%, standard deviation = 18%; mean hit rate after exclusion criterion = 98%, standard deviation = 5%).

3.3.3 Segmentation & cortical depth sampling

Separately for each subject, the anatomical MP2RAGE images were registered to the mean functional image. The nominal resolution of the MP2RAGE images was 0.7 mm isotropic, whereas that of the functional images was 0.8 mm isotropic[1]. To avoid downsampling of the anatomical images during registration, the mean functional image of each subject was upsampled to a resolution of 0.4 mm isotropic before registration (using trilinear interpolation). Thus, during registration of the anatomical images to the upsampled mean functional image, the anatomical images were indirectly upsampled (from 0.7 mm to 0.4 mm isotropic). This upsampling of anatomical images is beneficial for fine-grained tissue type segmentation, because it allows for better separation of adjacent sulci (avoiding erroneous grey matter 'bridges'). The anatomical images were roughly aligned in a first registration step based on normalized mutual information, followed by boundary-based registration (Greve & Fischl, 2009; Jenkinson, Bannister, Brady, & Smith, 2002; Jenkinson & Smith, 2001). The registered MP2RAGE images were used for grey/white matter segmentation. An initial tissue type segmentation was created with FSL FAST (Zhang, Brady, & Smith, 2001). These initial segmentations were semi-automatically improved using the Segmentator software (Gulban & Schneider, 2018; Gulban, Schneider, Marquardt, Haast, & De Martino, 2018) and ITK-SNAP (Yushkevich et al., 2006). These corrections of the segmentations obtained from FSL FAST were based on the T1 image from the MP2RAGE sequence, and aimed to remove mistakes in the definition of the white/grey matter

[1] We chose a resolution of 0.8^3 mm^3 for the functional acquisitions as a compromise between a high enough resolution for cortical depth sampling and sufficiently high temporal signal-to-noise ratio to be able to detect activation. We did not match the resolution of the anatomical MP2RAGE sequence to our functional images, because we expected that doing so would not have resulted in any significant advantages with respect to acquisition time or contrast-to-noise ratio (since the TR is limited by the relatively slow T1 decay).

boundary and at the pial surface.

The final grey and white matter definitions were used to construct cortical depth profiles, employing the volume-preserving parcellation implemented in CBS-tools (Bazin et al., 2007; Waehnert et al., 2014). Specifically, the cortical grey matter was divided into 10 compartments, resulting in 11 depth-level images delineating the borders of these equi-volume compartments. The results from the GLM analysis, the population receptive field estimates, and event-related fMRI time courses were up-sampled to the resolution of the segmentations (0.4 mm isotropic voxel size) using trilinear interpolation, and sampled along the previously established depth-levels using CBS-tools (Bazin et al., 2007; Waehnert et al., 2014). The depth-sampled data were projected onto a surface mesh (Tosun et al., 2004).

3.3.4 ROI selection

We aimed to define regions-of-interest (ROIs) in an observer-independent, quantifiable way. Only the first step of the ROI selection, i.e. the delineation of cortical areas V1, V2, and V3, was performed manually. The visual areas V1, V2, and V3 of the left hemisphere were delineated on the inflated cortical surface based on the polar angle estimates from the pRF modelling using Paraview (Ahrens, Geveci, & Law, 2005; Ayachit, 2015). Subsequently, three selection criteria were applied for each location on the cortical surface for all cortical depths (i.e. each segment) contained within V1, V2, or V3. First, only segments with good population receptive field model fits were included ($R2$>0.15, median across cortical depth levels), excluding regions that are not reliably activated (e.g. possibly due to unspecific responses). Second, segments with low signal intensity in the mean EPI image were excluded, to avoid sampling from veins and low intensity regions around the transverse sinus, which may be present due to slight imprecisions in the registration and/or segmentation. Specifically, segments with a mean EPI image intensity below 7000 at any cortical depth (i.e. minimum over cortical depths) were excluded. (The mean EPI image intensity was ∼10,000 for voxels within the brain.) Third, separate regions of interest were defined for the centre of the stimulus, with eccentricities between 1.0° to 3.0° visual angle, and for the edge of the stimulus, at eccentricities between 3.5° and 4.0° visual angle. The eccentricity of a

segment was defined as the median eccentricity over cortical depths. The lower bound of the ROI corresponding to the stimulus centre was set to 1.0° (and not to 0.0°) to avoid the cortical representation of the fixation dot. Selection criteria were always applied to all cortical depths in a segment – i.e. either the entire segment was included or excluded. The ROI selection described in this section, and all subsequent analysis steps were performed using standard scientific python packages (Numpy, Scipy, Matplotlib; Hunter, 2007; Millman & Aivazis, 2011; Oliphant, 2007; van der Walt et al., 2011). Percent signal change values were averaged over the ROI, separately for each cortical depth level.

3.3.5 Draining effect spatial deconvolution

Cortical depth-specific fMRI using GE sequences is affected by a venous bias caused by ascending draining veins, resulting in an unspecific haemodynamic signal increase towards the cortical surface (Koopmans et al., 2011; Markuerkiaga et al., 2016; see Uludağ & Blinder, 2017 for a review; Zhao, Wang, & Kim, 2004). To remove the effect of ascending veins from the cortical depth fMRI profiles, we employed leakage weights proposed by Markuerkiaga, et al. (2016), described in detail in Chapter 2. In brief, for each cortical depth level, we subtracted the estimated contribution of all deeper depth levels to obtain an estimate of the 'true' local signal change at that depth level.

3.3.6 Visual field projection

While it is instructive to examine the spatial extent of activation on the inflated cortical surface, the exact relationship between the visual stimulus and the surface activation map is difficult to interpret: Cortical magnification and differences in receptive field size across the cortex complicate the mapping from visual space to the cortical surface. Therefore, we projected the activation maps into the visual field, based on population receptive field estimates. The resulting visual field projections reveal the spatial pattern of activation with respect to the stimulus-space. Population receptive field mapping (Dumoulin & Wandell, 2008; Marquardt, Gulban, & Schneider, 2018) provides three parameters per vertex: x-position, y-position, and size of the Gaussian population receptive field model. For each vertex contained in the ROI, the 2D

Gaussian population receptive field model was multiplied with the percent signal change for that vertex. The resulting scaled 2D Gaussian were summed over vertices. The result (a 2D array) was normalised by the population receptive field density at each visual field location (i.e. divided by the sum of 2D Gaussian over vertices).

More formally, let $\boldsymbol{M}_{i,j,k}$ be a 3D tensor containing the population receptive field model for visual field positions i, j for vertices k. The population receptive field model at each visual field location is a 2D Gaussian function:

$$\boldsymbol{M}_{i,j,k} = g(x_k, y_k, w_k)$$

Where x_k, y_k, w_k are the x-position, y-position, and width (standard deviation) of the 2D Gaussian for vertex k, respectively. Furhter, let $\boldsymbol{p}_k$ be a vector with percent signal change values for n vertices contained in the ROI. The visual field projection of percent signal change values $\boldsymbol{p}_k$ was calculated as:

$$\boldsymbol{V}_{i,j} = \frac{\sum_{k=1}^{n} \boldsymbol{M}_{i,j,k} \odot \boldsymbol{p}_k}{\sum_{k=1}^{n} \boldsymbol{M}_{i,j,k}}$$

Where the multiplication and division operations are element-wise. The visual field projection $\boldsymbol{V}_{i,j}$ was calculated separately for each ROI and cortical depth level, but together for all subjects (by concatenating all subjects' population receptive field models, $\boldsymbol{M}_{i,j,k}$, and percent signal change vectors, $\boldsymbol{p}_k$). In this way, all subjects' activation maps can be projected into a single visual space; this is essentially a simple form of 'hyperalignment'. (The procedure is similar to that employed by Kok et al. (2016), with the difference that we did not apply any smoothing to the visual field projection.)

3.3.7 Hypothesis testing

Differences in stimulus-induced activation were investigated by means of a linear mixed effects model. First, we assessed whether the stimuli differentially activated brain areas V1, V2, and V3. (In other words, did activation differ between ROIs as a function of condition?)

Second, we tested whether the activation profiles across cortical depth differed between brain areas. Both tests were implemented by means of a mixed effects model including the fixed factors ROI, stimulus condition, and cortical depth, and a random slope for subjects. The autocorrelation structure of cortical depth (within subjects) was modelled as continuous autoregressive of order one. For the first test, a model with all possible two-way interactions was compared with a null model from which the stimulus condition by ROI interaction had been omitted (because this interaction reflects a differential effect of stimulus condition on brain areas). The second test compared a model with all possible two-way interactions with a null model without the cortical depth by ROI interaction (reflecting differences in cortical depth profiles between areas). The mixed effects models were fitted based on the percent signal change estimate of the sustained and transient predictors (for the stimulus centre and edge, respectively) obtained from the GLM. Comparisons of the respective pairs of models were conducted with a likelihood ratio tests. Models were created and compared using R and the nlme package (Pinheiro, Bates, DebRoy, Sarkar, & R Core Team, 2017; R Core Team, 2017).

3.3.8 Control experiment

A control experiment was conducted to investigate the role of the stimulus shape and of the background in the processing of a surface stimulus. Two uniform surface stimuli were presented: A central disk from which a sector was removed (i.e. a 'Pac-Man' figure, same as in the main experiment), and a central square. Both stimuli were identical in luminance and area. The disk (Pac-Man) had a diameter of 7.5° visual angle, and the omitted sector (the 'mouth' of the Pac-Man) had a circular arc of 70° (±35° from the right horizontal meridian). The square had a side length of 6.65° visual angle. Both stimuli were presented under two background conditions; either on a uniform, dark grey background, or on a random texture background (same as in the main experiment). The two background conditions (uniform/texture) were presented in separate experimental runs, whereas the two stimulus shapes (Pac-Man/square) were presented in random order within runs. The timing of the stimuli, including the fixation task, was identical to the main experiment (i.e. stimulus blocks of 12.4 s with variable rest blocks of 22.9 s, 25.0 s, or

27.0 s). The uniform background and the random texture pattern had a luminance of 8 cd/m^2, and the surface stimuli (Pac-Man & square) had a luminance of 163 cd/m^2. (The stimulus condition 'Pac-Man' on random texture background was identical to the 'Pac-Man static' condition in the main experiment). Two subjects completed six experimental runs each (three with uniform background, three with texture background). As in the main experiment, retinotopic mapping runs were acquired in the same session.

3.4 Results

The experimental stimuli caused widespread negative signal change in early visual cortex, particularly in the right hemisphere (Figure 3.2). A band of positive activation was observed at the cortical representation of the stimulus edge (Figure 3.3 C). Since the experimental manipulation (yielding perceptual differences in a locally identical stimulus) concerns the left visual field, the focus of the analysis was on the right hemisphere. The stimulus input to the right hemisphere was identical in experimental and control conditions, suggesting that differences in activity between the experimental and the control conditions are due to feedback.

At the cortical representation of the stimulus centre, the stimuli differentially activated brain areas V1, V2, and V3 (likelihood ratio (df) of ROI by condition interaction 39.6 (4), $p<0.0001$). Moreover, cortical depth profiles were significantly different between brain areas (likelihood ratio (df) of model comparison with/without cortical depth by ROI interaction 30.2 (2), $p<0.0001$). Similarly, the stimulus conditions caused differential activation at the cortical representation of the stimulus edge (likelihood ratio (df) of model comparison with/without ROI by condition interaction 22.8 (4), $p<0.0001$). However, with respect to the stimulus edge, there was no evidence for a differences in cortical depth profiles between brain areas (likelihood ratio (df) of model comparison with/without cortical depth by condition interaction 1.6 (2), $p=0.46$). Figure 3.4 shows the cortical depth profile of the condition contrast corresponding to the apparent motion effect for the cortical representation of the stimulus centre (see Figure 3.10 in *Supplementary Material* for cortical depth profiles of all possible condition contrasts; see Figure 3.11 in *Supplementary Material* for cortical depth profiles of the apparent motion effect at the stimulus edge). The peak of the

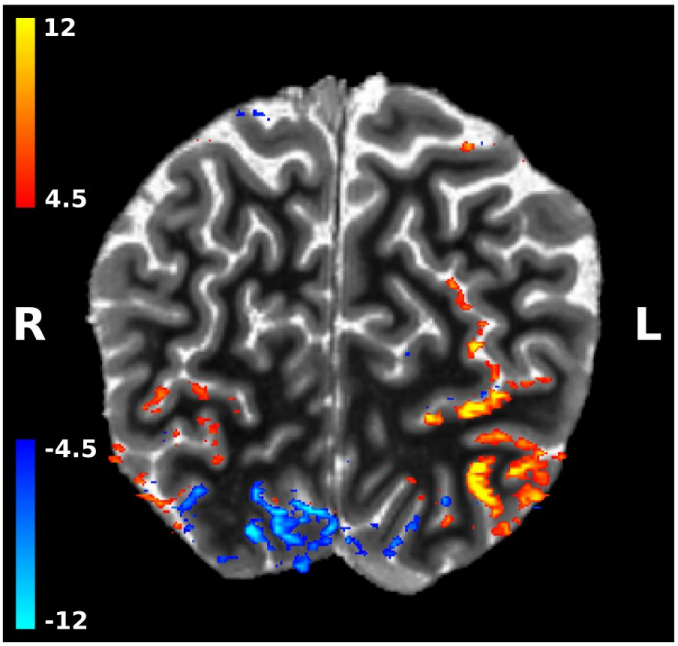

Figure 3.2: The Pac-Man stimulus caused positive and negative fMRI signal changes across visual cortex. Shown are the z-scores for the GLM contrast Pac-Man dynamic (sustained response) against rest, overlaid on a brain-masked T1 image, for a representative subject. Negative signal changes are particularly pronounced in early visual cortex of the right hemisphere, i.e. the hemisphere that 'sees' the left side of the Pac-Man. (Image is in radiological convention.)

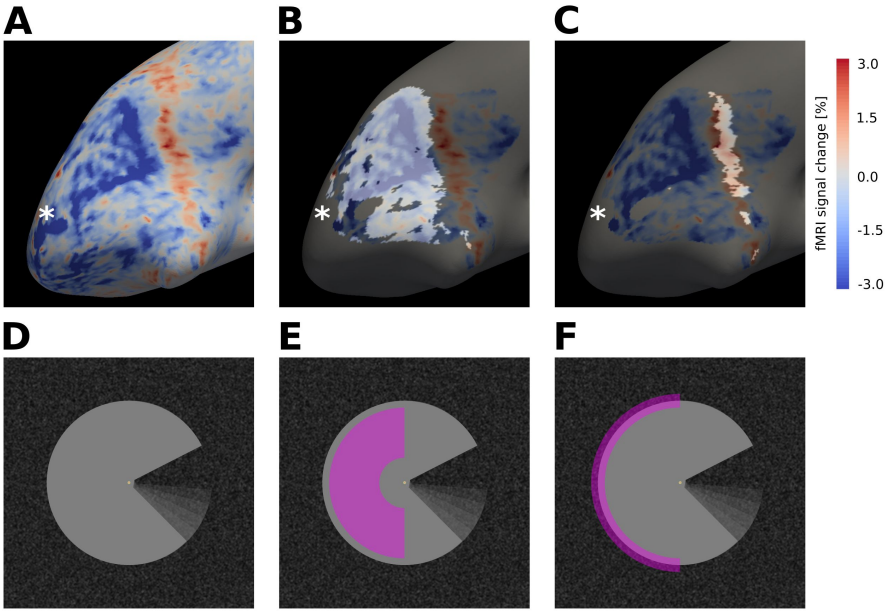

Figure 3.3: (**A**) Activation map for Pac-Man dynamic condition (stimulus shown in (**D**)), projected on the inflated cortical surface, for a representative subject (GLM parameter estimates for sustained response). An extended region of negative signal change (blue) is surrounded by a band of positive signal change (red). (**B**) The activation map from (**A**) is masked for V1, and the cortical area that retinotopically corresponds to the centre of the Pac-Man stimulus (**E**) is highlighted. (**C**) Same as (**B**), but the cortical area that contains the retinotopic representation of the edge of the Pac-Man stimulus (**F**) is highlighted. The band of positive signal change corresponds to the retinotopic representation of the edge of the Pac-Man stimulus. The areas highlighted in (**B**) and (**C**) were selected as ROIs for the simulus centre and edge, respectively. Discontinuities in the ROIs are due to thresholding of the retinotopic map ($R2$>0.15). The asterisk marks the approximate location of the cortical representation of the fovea (**A**, **B**, **C**).

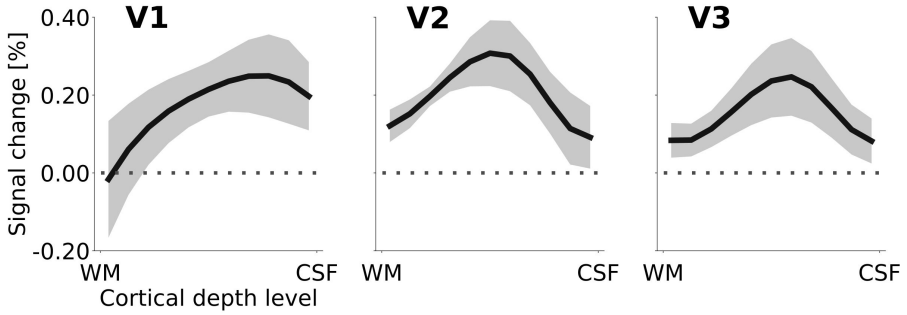

Figure 3.4: Cortical depth profiles of the apparent motion effect for the cortical representation of the stimulus centre (see Figure 3.3 E). The apparent motion effect was defined as the relative signal change associated with the condition contrast 'Pac-Man dynamic' (Figure 3.1 A) minus 'control dynamic' (Figure 3.1 C). Shading represents the standard error of the mean (across subjects). See Figure 3.10 in *Supplementary Material* for the same results for all experimental conditions, and Figure 3.11 in *Supplementary Material* for the cortical depth profile of the apparent motion effect at the representation of the stimulus edge.

apparent motion effect was located at ∼25% in V1, ∼50% in V2, and ∼40% in V3, relative to the pial surface (where 100% cortical depth would correspond to the white matter – grey matter boundary).

3.4.1 Temporal response pattern

To investigate the temporal dynamics of the negative and positive responses, we extracted event-related time courses separately corresponding to the centre and to the edge of the stimulus for areas V1, V2 and V3. In all three areas, the central region of interest exhibited a sustained negative response, whereas the edge region responded with a transient positive signal change at stimulus onset and offset (Figure 3.5). Separately for the sustained and transient responses, we determined response onset time as the first time point at which the signal was significantly different from zero (one-sample t-test, $p<0.05$, Bonferroni corrected). Surprisingly, this revealed that the onset of the transient response at the cortical representation of the stimulus edge preceded that of the sustained response at the stimulus centre by one time point (i.e. ∼2s; Figure 3.5). The pattern of positive transient and negative sustained

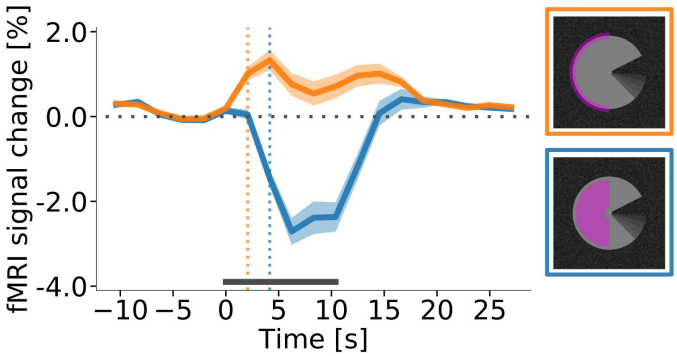

Figure 3.5: Response onset times in V1. Event-related fMRI timecourses for regions of interest corresponding to the stimulus centre (blue line) and the edge of the stimulus (orange line). The dotted vertical lines indicate the response onset, defined as the first time point at which the signal was significantly different from zero (one-sample t-test, $p<0.05$, Bonferroni corrected). The positive response at the stimulus edge precedes the negative response at the stimulus centre by one volume (i.e. by ∼2 s), suggesting that the negative response is not caused by the onset of the stimulus, but by its prolonged presentation. The response is shown for area V1 of the right hemisphere, averaged (mean) over subjects, stimulus conditions, and cortical depth levels. The horizontal grey bar marks the duration of the stimulus block. Error shading represents the standard error of the mean (across subjects). (See Figure 3.12 in *Supplementary Material* for same results separately for all areas and conditions.)

responses at the stimulus edge and centre, respectively, was consistent across areas and conditions (Figure 3.12 in *Supplementary Material*). An additional control experiment was performed to investigate whether the temporal dynamics of the responses were similar for a longer stimulus duration (Figure 3.13 in *Supplementary Material*). The results indicate that this was indeed the case, and that the negative response to the centre of the PacMan surface was sustained over long stimulus durations (25 s, compared to ∼10 s in the main experiment).

3.4.2 Spatial response pattern

The BOLD response to the figure's surface was strongly negative (Figures 3.3 & 3.5), and hence the increased activity related to the induced motion percept in experimental compared to control condition

reflected an increase from a very negative BOLD signal to a slightly less negative BOLD signal. At the same time, we observed a positive BOLD response to the edge (Figures 3.3 & 3.5). The spatial distribution of positive and negative signal change is directly visible in the visual field projections (Figure 3.6). Unsurprisingly, the dynamic parts of the stimulus (i.e. the rotating 'mouth' of the Pac-Man, and the rotating wedge of the dynamic control stimulus) caused a positive signal change in their cortical representations in V1, V2, and V3 (Figure 3.6 A, C, D, F, G, I). More surprisingly, but consistent with a previous report using the same stimuli (Akin et al., 2014), the surface region of all three stimuli in the left visual hemifield caused a negative signal change in the right hemisphere in all regions of interest (Figure 3.6 A–I). The band of positive signal change seen on the inflated brain (Figure 3.3 C) is also apparent in the visual field projections (particularly in Figure 3.6 D, E, F). Especially for the static Pac-Man stimulus, the shape of the stimulus is visible in the visual field projections (Figure 3.6 E & H).

The spatial extent of the negative signal change was similar across conditions, but differed across regions; from V1 over V2 to V3, the visual field projections became more blurred, likely due to the increasing receptive field size in higher-order areas.

3.4.3 Background effect

A control experiment was conducted to investigate the effect of the background and of the stimulus shape on the processing of a surface stimulus. The control experiment revealed that the directionality and temporal shape of the response is heavily affected by the type of background, but not by the shape of the stimulus (Figures 3.7 & 3.8). More specifically, in V1 the response to both the interior of the surface and to its edges is positive and sustained in case of a uniform background, as opposed to a transient positive response at the edges and a sustained, delayed, negative response at the surface interior in case of a texture background (Figure 3.8).

The response to the centre of the stimulus was very similar in V1 and V2 (Figure 3.8 A & D). It was positive and sustained when the background was uniform, but negative and sustained in the texture pattern background condition. This pattern was observed irrespective of the stimulus shape (square or 'Pac-Man'). Interestingly, at the

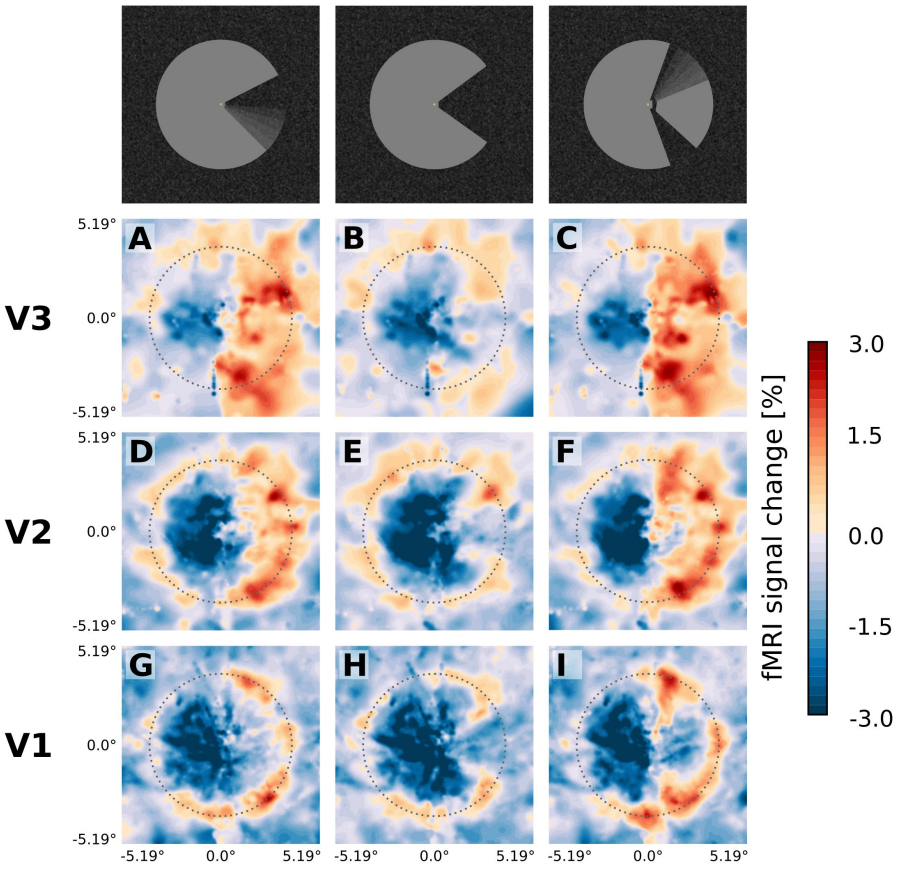

Figure 3.6: Projection of GLM parameters into visual space. The parameter estimates for the three stimulus conditions (Pac-Man dynamic (**A**, **D**, **G**), Pac-Man static (**B**, **E**, **H**), and control dynamic (**C**, **F**, **I**)) were projected into a model of the visual space based on their retinotopic location, and the size of their respective population receptive fields. The thin dashed circles correspond to an eccentricity of 3.75°, i.e. the radius of the Pac-Man stimulus. In all three stimulus conditions, there is a negative response to the left half of the stimulus. Visual field projections are averaged over cortical depth levels (mean).

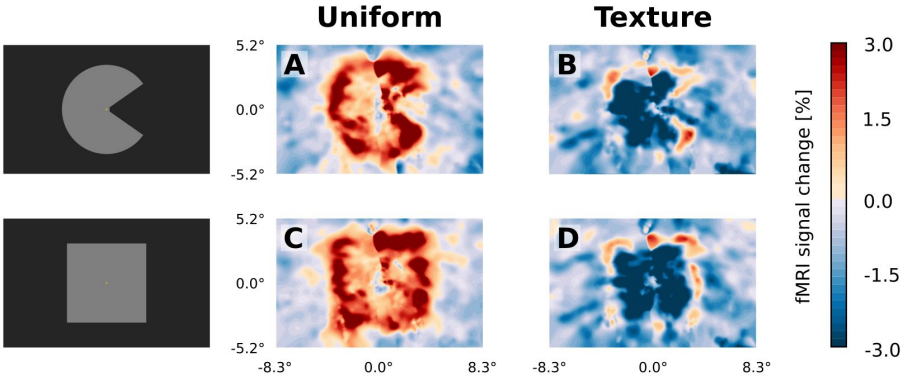

Figure 3.7: Visual field projections of GLM parameter estimates from control experiment with texture background and uniform background. A 'Pac-Man' figure and a square were presented either on a uniform background (**A** & **C**) or on a random texture background (**B** & **D**). When presented on a uniform background, the stimuli caused a positive response, especially at the retinotopic representation of the edges (**A** & **C**). In stark contrast, the response to the interior of the stimuli was negative when presented on a random texture background (**B** & **D**). At the edges of the stimuli, a small band of positive activity can still be observed (**B** & **D**).

interior of the surface, the positive response (in the uniform background condition) had a shorter latency than the negative response (in the texture background condition; Figure 3.8 A & D).

At the cortical retinotopic representation of the stimulus edges, the response was positive under all conditions (Figure 3.8 B & E). However, especially in V1, the shape of the response changed as a function of the background condition. The response was sustained in the uniform background condition, but transient in case of the texture background (Figure 3.8 B). A similar trend was found in V2, but the difference in the temporal shape was less clear (Figure 3.8 E).

A response was also observed in the peripheral ROI, although the retinotopic input from the respective section of the visual field was constant, and the stimuli were at a distance of 2.25° visual angle to the border of the ROI (Figure 3.8 C & F). There was a trend towards a modulation of the peripheral response by the background condition. Specifically, a trend towards a transient response at stimulus onset and offset was observed in the uniform background condition in V1 (Figure 3.8 C, orange & red lines), whereas the response was negative and sustained in case of the texture background (Figure 3.8 C, green & blue lines). In V2, a peripheral negative response slowly built up throughout the duration of the stimulus block, only reaching its minimum at the very end of the stimulus presentation, irrespective of the background condition (Figure 3.8 F).

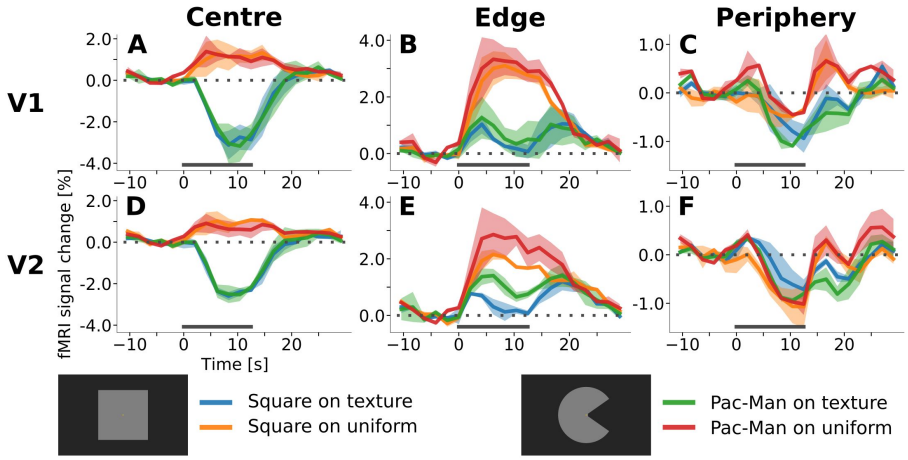

Figure 3.8: Event-related time courses from control experiment with texture background and uniform background, separately for regions of interest corresponding to the retinotopic representation of the centre of the stimulus (**A** & **D**), to its edges (**B** & **E**), and to the peripheral left and right edges of the screen (**C** & **F**). Irrespective of the shape of the stimulus (square or 'Pac-Man'), there was a positive response to the centre of the stimulus when the background was uniform (**A** & **D**, red & orange lines), and a negative response when the stimuli were presented on a random texture pattern (**A** & **D**, green & blue lines). Interestingly, the positive response had a shorter latency than the negative response. The response to the edges of the stimuli was positive under all conditions (**B** & **E**). However, the response amplitude was much stronger when the stimuli were presented on a uniform background (**B** & **E**). Especially in V1, the temporal dynamics changed as a function of the background; the response was sustained when the background was uniform (**B**, orange & red lines), but transient for the texture background (**B**, green and blue lines). A similar trend can be observed in V2, but the difference in the temporal dynamics is less pronounced (**E**). The retinotopic input from the peripheral left and right edges of the screen was constant throughout an experimental run. Nevertheless, a response can be observed in the peripheral region of interest in all stimulus conditions (**C** & **F**). There was a trend towards a transient positive response under the uniform background condition in V1 at stimulus onset and offset (**C**, orange and red lines), whereas the response was negative, and built up slowly over the duration of the stimulus presentation in case of the texture background (**C**, green and blues lines). The latter – i.e. a slowly evolving negative response – can be observed under all experimental conditions in V2 (**F**). The horizontal grey bar marks the duration of the stimulus. Please note that the scale of the y-axes is identical within columns, but differs between columns. Error shading represents the standard error of the mean (across subjects).

3.5 Discussion

In this study, we have investigated the cortical responses to static and moving uniform surfaces. Surprisingly, both static and moving surfaces resulted in widespread, negative responses in cortical areas V1, V2, and V3 (Figure 3.6). The negative response was located at the cortical retinotopic representation of the interior of the surface stimulus, and was sustained throughout the presentation period (Figure 3.5, and Figures 3.12 & 3.13 in *Supplementary Material*). The sustained negative response was accompanied by a transient, positive response at the retinotopic location corresponding to the edge of the stimulus (Figure 3.5). Interestingly, the edge response clearly preceded that of the surface by about 2 seconds (Figure 3.5).

The stimuli used in this study were physically identical in the left visual field, but differed in the right visual field, resulting in global perceptual differences (Figure 3.1). Because the retinotopic input from the left visual field is identical between stimulus conditions, any response difference in the early visual cortex of the right hemisphere can only be due to top-down feedback effects from areas that integrate information from both visual hemifields. After accounting for signal spread due to ascending veins (Markuerkiaga et al., 2016; Marquardt, Schneider, Gulban, et al., 2018), the top-down effect was strongest at mid-cortical depths in V2 and V3, and somewhat more superficial in V1 (Figure 3.4).

3.5.1 Negative response

Both the negative and the positive responses were observed in all three stimulus conditions (Pac-Man dynamic, Pac-Man static, control dynamic). Intuitively, it is unexpected that a surface with a luminance higher than the background causes negative signal change in early visual cortex. Luminance has been found to modulate neural activity in the visual cortex of cats (Dai & Wang, 2012; Wang et al., 2015) and humans (Haynes, Lotto, & Rees, 2004). In humans, both luminance increments and decrements evoke a positive, transient response in V1, V2, and V3 (Haynes et al., 2004). Thus, luminance is unlikely to be a major contributing factor for the observed negative response. Even though the negative response is unexpected, it is in accordance with previous findings: Akin et al. used stimuli very similar to ours and found negative

signal change in response to the dynamic Pac-Man stimulus and to the dynamic control stimulus in V1, V2, and V3 (2014).

To investigate the conditions under which a negative surface response is evoked, we conducted a control experiment in which we replaced the random texture background with a homogenous background with the same luminance. Additionally, we presented a square with the same luminance and area as the Pac-Man stimulus, to test whether the specific shape of the stimulus contributed to the negative response. The results clearly indicate that the negative surface response is only observed when the stimuli are presented on a texture background, irrespective of the stimulus shape (Figure 3.7). When presented on a homogenous background, the interior of the surface and its edges evoke a positive, sustained response (Figure 3.8). Thus, relative to the response in the homogenous background condition, the texture produces a delayed inhibition, both at the edges and at the interior of the surface.

What could have caused this inhibition, and why does it only occur under the texture background condition? An obvious possibility is that the texture causes a high baseline level of activation. Because of less than perfect fixation, the texture may continuously induce slight changes in local retinotopic input, and thereby drive contrast sensitive neurons in early visual cortex. After the onset of the uniform surface stimulus, the local retinotopic input at the cortical representation of the interior of the stimulus becomes constant, and activity is reduced. However, this explanation cannot completely account for the observed results.

First, the response at the stimulus centre had an amplitude in excess of –2% (Figures 3.5 & 3.8). In the uniform background condition (control experiment), the corresponding positive response had a magnitude of about 1.5% (Figure 3.8 A). Thus, if the negative surface response in the texture background condition was to be explained solely by an elevated baseline activation caused by the texture pattern, the effect of the texture pattern would have to be around 3.5% signal change, and this effect would have to be sustained throughout the entire experimental run. Although further research will be necessary to investigate the effect and temporal dynamics of a texture pattern relative to a homogenous background, it seems unlikely that a relatively subtle, static texture pattern would result in such a strong and sustained response.

Second, if the negative response was only driven by local changes

in retinotopic input, it is not clear why it would be delayed relative to the positive response at the edge (Figure 3.5) and at the interior of the surface in the homogenous background condition (Figure 3.8 A). At the cortical representation of the interior of the surface, a reduction in activity due to the disappearance of the texture and a positive, transient response caused by the onset of the stimulus might cancel out each other, and thus effectively delay the negative response. However, this explanation is not in line with the observation that the positive surface response in the homogenous background condition is sustained (Figure 3.8 A). Furthermore, the explanation cannot account for the temporal dynamics observed at the stimulus edge, where the response is always fast and positive, irrespective of the background condition, and sustained or transient, depending on the background condition (Figure 3.8 B). A higher baseline activation in the texture background condition could explain an overall lower response to the stimulus (relative to the uniform background condition). But it is not clear how the distinct temporal shape of the edge response in the texture background condition (i.e. a transient, positive onset and offset response) could be explained by an elevated baseline activation. Rather, the results suggest a contribution of top-down feedback or lateral projections. Inhibitory feedback may also explain the transient, positive offset response at the stimulus edge (Figure 3.8 B). Namely, the offset response may be the result of a release from inhibition. Yet, at the stimulus centre, a positive offset response was not observed, raising the question why the effect of disinhibition would be different for the interior and the edge. Further research will be needed to identify the factors that contribute to the occurrence of the negative surface response, and to its temporal shape. Future studies could, for example, contrast a full-field texture pattern against a uniform background in a block design with very long stimulus blocks, to investigate the possibility of elevated background activity caused by the static texture. Moreover, the uniform stimulus surface could be replaced by a texture pattern (i.e. a light grey textured square on a dark grey textured background). In this way, it could be tested whether the negative surface effect is related to figure-ground segregation, or a consequence of local, low-level effects of the stimulus surface.

Electrophysiological experiments typically measure responses over a time window of only a few hundred milliseconds after stimulus onset, and often use stimuli with a high temporal frequency. Results based on

experimental designs similar to the one used in the present study have, to the best of our knowledge, not been reported. It would be interesting to test whether the strong and sustained negative response during the prolonged presentation of a static, behaviourally irrelevant stimulus on a static texture background is accompanied by increased inhibition, or decreased excitation. In the only electrophysiological study known to us with a stimulus design roughly similar to ours, de Weerd, et al. (1995) presented monkeys with a uniform surface stimulus placed on a rapidly flickering texture pattern. The stimulus duration was similar to the one in the present study. Neurons in V1 were shown to be excited by the background texture pattern, well beyond the cells' classical receptive field (see Figure 3 A in De Weerd et al., 1995). The excitatory response was very fast and transient, was followed by a sharp fall-off (it subsided to baseline in less than a second), and, subsequently, by a slow increase in firing over a period of several seconds. Although it is difficult to directly relate these findings to the results of the present study, they indicate that lateral and/or top-down feedback effects play a role in the processing of surface stimuli.

3.5.2 Figure-ground segregation

Figure-ground segregation has been found to be accompanied by an enhanced response to the stimulus, and a suppression of the background (Poort, Self, van Vugt, Malkki, & Roelfsema, 2016; Self et al., 2013). While the positive, sustained surface response in the homogenous background condition (Figure 3.8 A) is in accordance with figure enhancement as a result of figure-ground segregation, the negative response at the representation of the centre of a stimulus cannot easily be reconciled with mechanisms underlying figure-ground segregation. Although we did not test this formally, perceptual figure-ground segregation is, if anything, enhanced by the texture background. Hence, reduced perceptual figure-ground segregation is not a plausible explanation for the present results.

3.5.3 Top-down feedback

The experimental stimuli were 'physically' identical in the left visual field, while the global perceptual quality of the stimulus depended

on the right half of the stimuli (Figure 3.1). This stimulus design offers two advantages. First, anatomical investigations have shown that transcallosal, interhemispheric connections are restricted to the proximity of the vertical meridian in primate early visual cortex (Clarke & Miklossy, 1990; Essen & Zeki, 1978; Glickstein & Whitteridge, 1976; Houzel & Milleret, 1999; Van Essen et al., 1982; Wong-Riley, 1974). Therefore, any differences observed in early visual cortex of the right hemisphere are very likely caused by top-down feedback effects from higher areas, and not by horizontal interactions. Second, the cortical region that retinotopically represents the constant left side of the stimulus and the one which induces the motion percept (i.e. the 'mouth' of the Pac-Man) were anatomically well apart. Thus, it is very unlikely that imprecisions in the retinotopic maps could confound our results.

The term 'apparent motion' is usually used for stimuli that induce the percept of motion along a trajectory between two flickering stimuli (Chong, Familiar, & Shim, 2016; Muckli et al., 2005; Sterzer, Haynes, & Rees, 2006). In the present study, we use the term 'apparent motion' to refer to the fact that the left side of a stimulus is perceived as rotating, although there is no local change in retinal input. Although this distinguishes our stimuli from those used in some previous studies, the decisive aspect of apparent motion – i.e. perceived motion in the absence of local changes in retinotopic input – is maintained. Apparent motion-related responses have been demonstrated in human V1 (Chong et al., 2016; Muckli et al., 2005; Sterzer et al., 2006). Moreover, it was shown that the apparent-motion effect in V1 was associated with enhanced functional connectivity between motion sensitive area V5 and area V1 (Sterzer et al., 2006). Further support for the notion that apparent motion involves top-down feedback comes from a study in ferrets (Ahmed et al., 2008), in which an apparent-motion stimulus induced a feedback signal from higher cortical areas to primary visual cortex. In humans, direct evidence for the functional significance of feedback from V5 to early visual cortex in the perception of motion comes from TMS studies (Laycock, Crewther, Fitzgerald, & Crewther, 2007; Pascual-Leone & Walsh, 2001).

The cortical depth profiles of the apparent motion effect in V1, V2, and V3 (Figure 3.4) suggests that top-down feedback may have re-entered at superficial layers in V1. This re-entrant information may have propagated to V2 and V3 via feedforward pathways. Even though

our data do not permit a direct test of the directionality and precise temporal dynamics of information flow, we deem re-entrant feedback at the level of V1 as a possible interpretation of the present results.

Alternatively, the apparent-motion effect at mid-cortical depth in V2 and V3 might have been caused by top-down effects acting via an indirect pathway through the pulvinar (Standage & Benevento, 1983; Trojanowski & Jacobson, 1977). The middle layers of extrastriate cortex are the target of projections from the pulvinar (Benevento & Rezak, 1976; Benevento, Rezak, & Bos, 1975; Ogren & Hendrickson, 1977; Rezak & Benevento, 1979), a structure that is sometimes referred to as a 'higher-order relay' because of its role in cortico-cortical communication (Sherman & Guillery, 2002). The pulvinar has been shown to regulate cortico-cortical communication in the visual system based on attentional demands (Saalmann, Pinsk, Wang, Li, & Kastner, 2012). Experiments in humans (M. Y. Villeneuve, Thompson, Hess, & Casanova, 2012; Martin Y. Villeneuve, Kupers, Gjedde, Ptito, & Casanova, 2005) and cats (Merabet, Desautels, Minville, & Casanova, 1998) have demonstrated a role of the pulvinar in higher-order motion processing (i.e. coherent motion of entire objects, as opposed to local motion). In line with this, Shimono et al. (2012) have found evidence for an involvement of the pulvinar in the interhemispheric integration of motion information. The two possible interpretations of the present results involving either re-entrant feedback in V1 or indirect top-down effects via the pulvinar are illustrated in Figure 3.9.

3.5.4 Limitations & outlook

Previous fMRI studies using different stimulus designs have found feedback effects to be associated with deep (Kok et al., 2016) and superficial (Muckli et al., 2015) layers in human primary visual cortex. Further research will be needed to identify factors in stimulus design and analysis strategy that caused these differences in results. With respect to stimulus design, the anatomical pathway that is invoked by the stimuli/task (e.g. cortical-cortical vs. cortical-subcortical-cortical) and the range of connections (short range vs. long range) may be contributing factors.

Regarding the analysis strategy, whether or not the effect of ascending draining veins is accounted for could play a role (see Chapter 2).

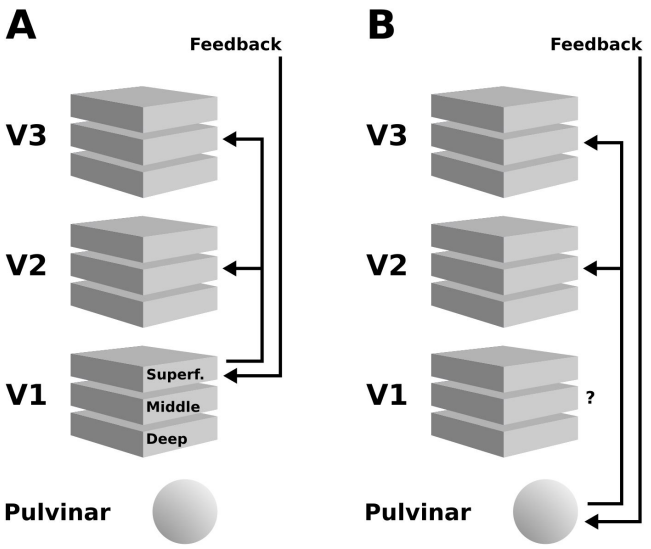

Figure 3.9: Schematic illustration of two possible interpretations of the present results. (**A**) Higher cortical areas may integrate the global motion percept across hemispheres, and send feedback projections to superficial layers of V1. Subsequently, this re-entrant feedback would be sent to V2 and V3 via feedforward connections. (**B**) Alternatively, the pulvinar may act as a 'higher-order relay', and send feedback from higher cortical areas to V2 and V3. See discussion section for details.

We have employed a spatial deconvolution to remove signal spread due to ascending veins (Markuerkiaga et al., 2016). Even though the exact parameters of the spatial deconvolution may be suboptimal, simulations have shown that the spatial deconvolution is relatively robust against deviations in its model parameters (see Figure 2.8). Thus, although the exact shape of the resulting cortical depth profiles is contingent on the model parameters of the spatial deconvolution, we do not expect the results to differ qualitatively in case of different model parameters.

When stimuli were presented on a texture background, we observed sustained, delayed negative signal change at the cortical representation of the surface of the stimuli, and a transient, positive response at the stimulus edge (Figure 3.5). Interestingly, the response both to the interior of the stimulus and to its edge changed dramatically when presented on a homogenous background; in that case, the response was fast, positive, and sustained (Figure 3.8). Further research will be needed to identify the factors that determine the direction and temporal shape of the surface response.

3.6 Supplementary Material

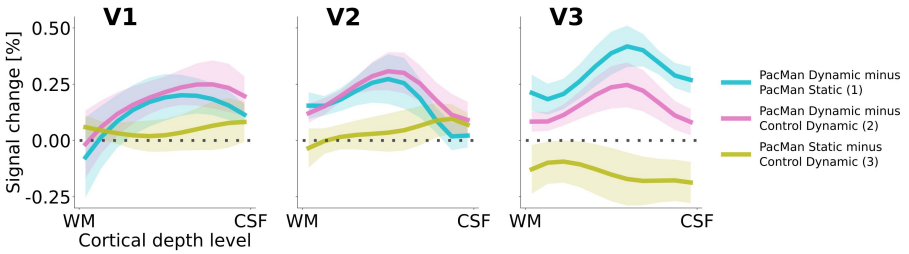

Figure 3.10: Cortical depth profiles of condition differences. There are three possible condition contrasts: (1) PacMan dynamic vs. PacMan static (blue line), (2) PacMan dynamic vs. control dynamic (magenta line), and (3) PacMan static vs. control dynamic (yellow line). Shading represents the standard error of the mean (across subjects). The spatial deconvolution for removal of signal spread due to draining veins was applied to the individual condition depth profiles separately for each subject.

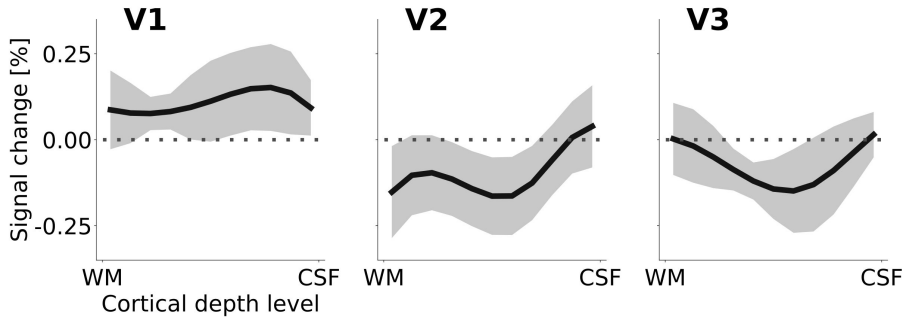

Figure 3.11: Cortical depth profiles of the apparent motion effect for the cortical representation of the stimulus edge (see Figure 3.3 C & F). The apparent motion effect was defined as the relative signal change associated with the condition contrast 'Pac-Man dynamic' (Figure 3.1 A) minus 'control dynamic' (Figure 3.1 C). Shading represents the standard error of the mean (across subjects).

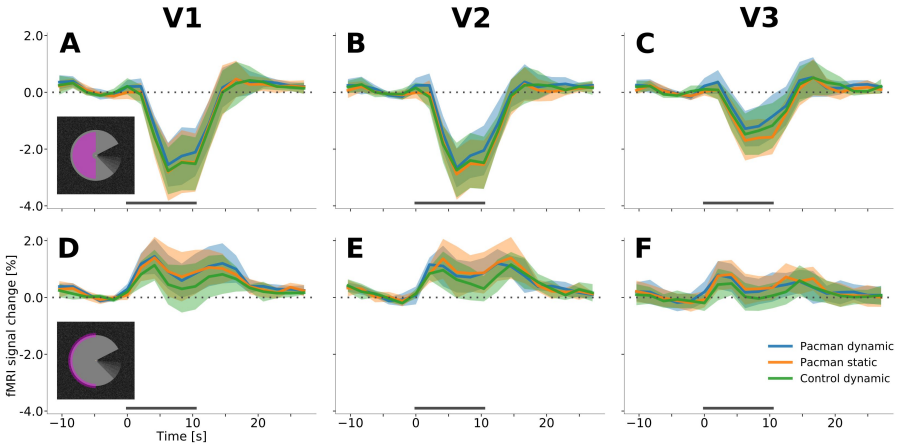

Figure 3.12: Event-related fMRI timecourses for region of interest corresponding to the stimulus centre (**A**, **B**, **C**) and the edge of the stimulus (**D**, **E**, **F**) in the right hemisphere. The horizontal grey bar marks the duration of the stimulus block. All three stimulus conditions (represented by separate lines) evoked a sustained negative response in V1, V2, and V3 in cortex that retinotopically represents the stimulus centre. In contrast, the cortex that represents the stimulus edge exhibits a transient, positive response at stimulus onset and stimulus offset. Interestingly, the positive response at the stimulus edge precedes the negative response at the stimulus centre (see also Figure 3.5 in the main text). Error shading represents the standard error of the mean (across subjects). The scale of the axes is identical in all subplots.

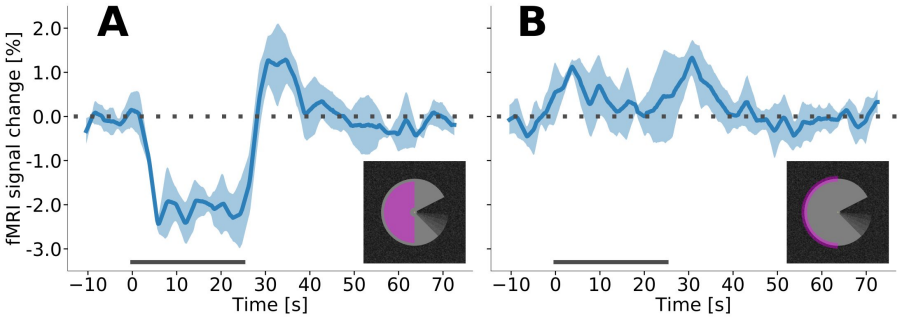

Figure 3.13: Event-related fMRI timecourses from an additional run with longer stimulus blocks, for V1 in the right hemisphere. In order to further investigate the temporal dynamics of the stimulus-evoked response, we acquired and additional run during which the dynamic Pac-Man stimulus was presented with longer block durations (in a subset of subjects, n=5). Stimulus duration was 25 s, with rest blocks of 50 s. (**A**) The region of interest that corresponds to the stimulus centre shows a sustained, negative response that resembles the 'canonical' haemodynamic response function. (**B**) The response to the stimulus edge is transient and positive.

3.7 References

Ahmed, B., Hanazawa, A., Undeman, C., Eriksson, D., Valentiniene, S., & Roland, P. E. (2008). Cortical dynamics subserving visual apparent motion. *Cerebral Cortex* (New York, N.Y.: 1991), 18(12), 2796–2810. https://doi.org/10.1093/cercor/bhn038

Ahrens, J., Geveci, B., & Law, C. (2005). ParaView: An End-User Tool for Large-Data Visualization. In C. D. Hansen & C. R. Johnson, *The Visualization Handbook* (pp. 717–731). Burlington: Elsevier Butterworth–Heinemann.

Akin, B., Ozdem, C., Eroglu, S., Keskin, D. T., Fang, F., Doerschner, K., … Boyaci, H. (2014). Attention modulates neuronal correlates of interhemispheric integration and global motion perception. *Journal of Vision*, 14(12). https://doi.org/10.1167/14.12.30

Anderson, J. C., & Martin, K. A. C. (2009). The synaptic connections between cortical areas V1 and V2 in macaque monkey. *The Journal of Neuroscience: The Official Journal of the Society for Neuroscience*, 29(36), 11283–11293. https://doi.org/10.1523/JNEUROSCI.5757-08.2009

Andersson, J. L. R., Skare, S., & Ashburner, J. (2003). How to correct susceptibility distortions in spin-echo echo-planar images: application to diffusion tensor imaging. *NeuroImage*, 20(2), 870–888.

https://doi.org/10.1016/S1053-8119(03)00336-7
Ayachit, U. (2015). The ParaView guide: updated for ParaView version 4.3 (Full color version; L. Avila, ed.). Los Alamos: Kitware.
Bazin, P.-L., Cuzzocreo, J. L., Yassa, M. A., Gandler, W., McAuliffe, M. J., Bassett, S. S., & Pham, D. L. (2007). Volumetric neuroimage analysis extensions for the MIPAV software package. *Journal of Neuroscience Methods*, 165(1), 111–121. https://doi.org/10.1016/j.jneumeth.2007.05.024
Behnel, S., Bradshaw, R., Citro, C., Dalcin, L., Seljebotn, D. S., & Smith, K. (2011). Cython: The Best of Both Worlds. *Computing in Science & Engineering*, 13(2), 31–39. https://doi.org/10.1109/MCSE.2010.118
Benevento, L. A., & Rezak, M. (1976). The cortical projections of the inferior pulvinar and adjacent lateral pulvinar in the rhesus monkey (Macaca mulatta): an autoradiographic study. *Brain Research*, 108(1), 1–24.
Benevento, L. A., Rezak, M., & Bos, J. (1975). Extrageniculate projections to layers VI and I of striate cortex (area 17) in the rhesus monkey (Macaca mulatta). *Brain Research*, 96(1), 51–55.
Chong, E., Familiar, A. M., & Shim, W. M. (2016). Reconstructing representations of dynamic visual objects in early visual cortex. *Proceedings of the National Academy of Sciences of the United States of America*, 113(5), 1453–1458. https://doi.org/10.1073/pnas.1512144113
Clarke, S., & Miklossy, J. (1990). Occipital cortex in man: organization of callosal connections, related myelo- and cytoarchitecture, and putative boundaries of functional visual areas. *The Journal of Comparative Neurology*, 298(2), 188–214. https://doi.org/10.1002/cne.902980205
Cornelissen, F. W., Wade, A. R., Vladusich, T., Dougherty, R. F., & Wandell, B. A. (2006). No functional magnetic resonance imaging evidence for brightness and color filling-in in early human visual cortex. *The Journal of Neuroscience: The Official Journal of the Society for Neuroscience*, 26(14), 3634–3641. https://doi.org/10.1523/JNEUROSCI.4382-05.2006
Dai, J., & Wang, Y. (2012). Representation of surface luminance and contrast in primary visual cortex. *Cerebral Cortex* (New York, N.Y.: 1991), 22(4), 776–787. https://doi.org/10.1093/cercor/bhr133
De Weerd, P., Desimone, R., & Ungerleider, L. G. (1998). Perceptual filling-in: a parametric study. *Vision Research*, 38(18), 2721–2734.
De Weerd, P., Gattass, R., Desimone, R., & Ungerleider, L. G. (1995). Responses of cells in monkey visual cortex during perceptual filling-in of an artificial scotoma. *Nature*, 377(6551), 731–734. https://doi.org/10.1038/377731a0
Dresp, B., & Bonnet, C. (1991). Psychophysical evidence for low-level processing of illusory contours and surfaces in the Kanizsa square. *Vision Research*, 31(10), 1813–1817.
Dumoulin, S. O., & Wandell, B. A. (2008). Population receptive field

estimates in human visual cortex. *NeuroImage*, 39(2), 647–660. https://doi.org/10.1016/j.neuroimage.2007.09.034

Essen, D. C., & Zeki, S. M. (1978). The topographic organization of rhesus monkey prestriate cortex. *The Journal of Physiology*, 277, 193–226.

Feinberg, D. A., Moeller, S., Smith, S. M., Auerbach, E., Ramanna, S., Gunther, M., … Yacoub, E. (2010). Multiplexed echo planar imaging for sub-second whole brain FMRI and fast diffusion imaging. *PloS One*, 5(12), e15710. https://doi.org/10.1371/journal.pone.0015710

Friston, K. J., Williams, S., Howard, R., Frackowiak, R. S., & Turner, R. (1996). Movement-related effects in fMRI time-series. *Magnetic Resonance in Medicine*, 35(3), 346–355.

Glickstein, M., & Whitteridge, D. (1976). Degeneration of layer III pyramidal cells in area 18 following destruction of callosal input. *Brain Research*, 104(1), 148–151.

Greve, D. N., & Fischl, B. (2009). Accurate and robust brain image alignment using boundary-based registration. *NeuroImage*, 48(1), 63–72. https://doi.org/10.1016/j.neuroimage.2009.06.060

Grosof, D. H., Shapley, R. M., & Hawken, M. J. (1993). Macaque V1 neurons can signal 'illusory' contours. *Nature*, 365(6446), 550–552. https://doi.org/10.1038/365550a0

Grossberg, S. (1987a). Cortical dynamics of three-dimensional form, color, and brightness perception: I. Monocular theory. *Perception & Psychophysics*, 41(2), 87–116.

Grossberg, S. (1987b). Cortical dynamics of three-dimensional form, color, and brightness perception: II. Binocular theory. *Perception & Psychophysics*, 41(2), 117–158.

Guidi, M., Huber, L., Lampe, L., Gauthier, C. J., & Möller, H. E. (2016). Lamina-dependent calibrated BOLD response in human primary motor cortex. *NeuroImage*, 141, 250–261. https://doi.org/10.1016/j.neuroimage.2016.06.030

Gulban, O. F., & Schneider, M. (2018, June 7). Segmentator V1.5.2. https://doi.org/10.5281/zenodo.595780

Gulban, O. F., Schneider, M., Marquardt, I., Haast, R. A. M., & De Martino, F. (2018). A scalable method to improve gray matter segmentation at ultra high field MRI. *PloS One*, 13(6), e0198335. https://doi.org/10.1371/journal.pone.0198335

Halchenko, Y. O., & Hanke, M. (2012). Open is Not Enough. Let's Take the Next Step: An Integrated, Community-Driven Computing Platform for Neuroscience. *Frontiers in Neuroinformatics*, 6, 22. https://doi.org/10.3389/fninf.2012.00022

Haynes, J.-D., Lotto, R. B., & Rees, G. (2004). Responses of human visual cortex to uniform surfaces. *Proceedings of the National Academy*

of Sciences of the United States of America, 101(12), 4286–4291. https://doi.org/10.1073/pnas.0307948101

Horiguchi, H., Nakadomari, S., Misaki, M., & Wandell, B. A. (2009). Two temporal channels in human V1 identified using fMRI. *NeuroImage*, 47(1), 273–280. https://doi.org/10.1016/j.neuroimage.2009.03.078

Houzel, J. C., & Milleret, C. (1999). Visual inter-hemispheric processing: constraints and potentialities set by axonal morphology. *Journal of Physiology*, Paris, 93(4), 271–284.

Hsieh, P.-J., & Tse, P. U. (2010). 'Brain-reading' of perceived colors reveals a feature mixing mechanism underlying perceptual filling-in in cortical area V1. *Human Brain Mapping*, 31(9), 1395–1407. https://doi.org/10.1002/hbm.20946

Huang, X., & Paradiso, M. A. (2008). V1 response timing and surface filling-in. *Journal of Neurophysiology*, 100(1), 539–547. https://doi.org/10.1152/jn.00997.2007

Huber, L., Goense, J. B. M., Kennerley, A. J., Trampel, R., Guidi, M., Reimer, E., ... Möller, H. E. (2015). Cortical lamina-dependent blood volume changes in human brain at 7 T. *NeuroImage*, 107, 23–33. https://doi.org/10.1016/j.neuroimage.2014.11.046

Hunter, J. D. (2007). Matplotlib: A 2D Graphics Environment. *Computing in Science & Engineering*, 9(3), 90–95. https://doi.org/10.1109/MCSE.2007.55

Jenkinson, M., Bannister, P., Brady, M., & Smith, S. (2002). Improved optimization for the robust and accurate linear registration and motion correction of brain images. *NeuroImage*, 17(2), 825–841.

Jenkinson, M., & Smith, S. (2001). A global optimisation method for robust affine registration of brain images. *Medical Image Analysis*, 5(2), 143–156.

Kaczmarzyk, J., Goncalves, M., Halchenko, Y., Mitchell, R., Nielson, D., Jarecka, D., ... Rokem, A. (2017, November 18). Kaczmarj/Neurodocker: Version 0.3.2. https://doi.org/10.5281/zenodo.1058998

Keil, M. S., Cristóbal, G., Hansen, T., & Neumann, H. (2005). Recovering real-world images from single-scale boundaries with a novel filling-in architecture. *Neural Networks: The Official Journal of the International Neural Network Society*, 18(10), 1319–1331. https://doi.org/10.1016/j.neunet.2005.04.003

Klein, B. P., Fracasso, A., van Dijk, J. A., Paffen, C. L. E., Te Pas, S. F., & Dumoulin, S. O. (2018). Cortical depth dependent population receptive field attraction by spatial attention in human V1. *NeuroImage*, 176, 301–312. https://doi.org/10.1016/j.neuroimage.2018.04.055

Kok, P., Bains, L. J., van Mourik, T., Norris, D. G., & de Lange, F. P. (2016). Selective Activation of the Deep Layers of the Human Primary

Visual Cortex by Top-Down Feedback. *Current Biology*, 26(3), 371–376. https://doi.org/10.1016/j.cub.2015.12.038

Kok, P., & de Lange, F. P. (2014). Shape perception simultaneously up- and downregulates neural activity in the primary visual cortex. *Current Biology*: CB, 24(13), 1531–1535. https://doi.org/10.1016/j.cub.2014.05.042

Komatsu, H., Kinoshita, M., & Murakami, I. (2000). Neural responses in the retinotopic representation of the blind spot in the macaque V1 to stimuli for perceptual filling-in. *The Journal of Neuroscience: The Official Journal of the Society for Neuroscience*, 20(24), 9310–9319.

Koopmans, P. J., Barth, M., & Norris, D. G. (2010). Layer-specific BOLD activation in human V1. *Human Brain Mapping*, 31(9), 1297–1304. https://doi.org/10.1002/hbm.20936

Koopmans, P. J., Barth, M., Orzada, S., & Norris, D. G. (2011). Multi-echo fMRI of the cortical laminae in humans at 7T. *NeuroImage*, 56(3), 1276–1285. https://doi.org/10.1016/j.neuroimage.2011.02.042

Lamme, V. A. (1995). The neurophysiology of figure-ground segregation in primary visual cortex. *The Journal of Neuroscience: The Official Journal of the Society for Neuroscience*, 15(2), 1605–1615.

Lamme, V. A., Rodriguez-Rodriguez, V., & Spekreijse, H. (1999). Separate processing dynamics for texture elements, boundaries and surfaces in primary visual cortex of the macaque monkey. *Cerebral Cortex* (New York, N.Y.: 1991), 9(4), 406–413.

Lamme, V. A., & Roelfsema, P. R. (2000). The distinct modes of vision offered by feedforward and recurrent processing. *Trends in Neurosciences*, 23(11), 571–579.

Laycock, R., Crewther, D. P., Fitzgerald, P. B., & Crewther, S. G. (2007). Evidence for fast signals and later processing in human V1/V2 and V5/MT+: A TMS study of motion perception. *Journal of Neurophysiology*, 98(3), 1253–1262. https://doi.org/10.1152/jn.00416.2007

Lee, T. S., & Nguyen, M. (2001). Dynamics of subjective contour formation in the early visual cortex. *Proceedings of the National Academy of Sciences of the United States of America*, 98(4), 1907–1911. https://doi.org/10.1073/pnas.031579998

Lu, H. D., & Roe, A. W. (2007). Optical imaging of contrast response in Macaque monkey V1 and V2. *Cerebral Cortex* (New York, N.Y.: 1991), 17(11), 2675–2695. https://doi.org/10.1093/cercor/bhl177

Markuerkiaga, I., Barth, M., & Norris, D. G. (2016). A cortical vascular model for examining the specificity of the laminar BOLD signal. *NeuroImage*, 132, 491–498. https://doi.org/10.1016/j.neuroimage.2016.02.073

Marquardt, I., Gulban, O. F., & Schneider, M. (2018, April 18). pyprf - A free & open source python package for population receptive field (pRF) analysis. https://doi.org/10.5281/zenodo.1220207

Marquardt, I., Schneider, M., & Gulban, O. F. (2018, August 21). Visual stimuli used in fMRI study on top-down feedback across cortical depths. https://doi.org/10.5281/zenodo.2583017

Marquardt, I., Schneider, M., Gulban, O. F., Ivanov, D., & Uludağ, K. (2018). Cortical depth profiles of luminance contrast responses in human V1 and V2 using 7 T fMRI. *Human Brain Mapping*. https://doi.org/10.1002/hbm.24042

Marques, J. P., Kober, T., Krueger, G., van der Zwaag, W., Van de Moortele, P.-F., & Gruetter, R. (2010). MP2RAGE, a self bias-field corrected sequence for improved segmentation and T1-mapping at high field. *NeuroImage*, 49(2), 1271–1281. https://doi.org/10.1016/j.neuroimage.2009.10.002

Mendola, J. D., Dale, A. M., Fischl, B., Liu, A. K., & Tootell, R. B. (1999). The representation of illusory and real contours in human cortical visual areas revealed by functional magnetic resonance imaging. *The Journal of Neuroscience: The Official Journal of the Society for Neuroscience*, 19(19), 8560–8572.

Meng, M., Remus, D. A., & Tong, F. (2005). Filling-in of visual phantoms in the human brain. *Nature Neuroscience*, 8(9), 1248–1254. https://doi.org/10.1038/nn1518

Merabet, L., Desautels, A., Minville, K., & Casanova, C. (1998). Motion integration in a thalamic visual nucleus. *Nature*, 396(6708), 265–268. https://doi.org/10.1038/24382

Millman, K. J., & Aivazis, M. (2011). Python for Scientists and Engineers. *Computing in Science & Engineering*, 13(2), 9–12. https://doi.org/10.1109/MCSE.2011.36

Moeller, S., Yacoub, E., Olman, C. A., Auerbach, E., Strupp, J., Harel, N., & Uğurbil, K. (2010). Multiband multislice GE-EPI at 7 tesla, with 16-fold acceleration using partial parallel imaging with application to high spatial and temporal whole-brain fMRI. *Magnetic Resonance in Medicine*, 63(5), 1144–1153. https://doi.org/10.1002/mrm.22361

Muckli, L., De Martino, F., Vizioli, L., Petro, L. S., Smith, F. W., Ugurbil, K., … Yacoub, E. (2015). Contextual Feedback to Superficial Layers of V1. *Current Biology*: CB, 25(20), 2690–2695. https://doi.org/10.1016/j.cub.2015.08.057

Muckli, L., Kohler, A., Kriegeskorte, N., & Singer, W. (2005). Primary visual cortex activity along the apparent-motion trace reflects illusory perception. *PLoS Biology*, 3(8), e265. https://doi.org/10.1371/journal.pbio.0030265

Muckli, L., Singer, W., Zanella, F. E., & Goebel, R. (2002). Integration of multiple motion vectors over space: an fMRI study of transparent motion perception. *NeuroImage*, 16(4), 843–856.

Ogren, M. P., & Hendrickson, A. E. (1977). The distribution of pulvinar

terminals in visual areas 17 and 18 of the monkey. *Brain Research*, 137(2), 343–350.

Oliphant, T. E. (2007). Python for Scientific Computing. *Computing in Science & Engineering*, 9(3), 10–20. https://doi.org/10.1109/MCSE.2007.58

Olman, C. A., Harel, N., Feinberg, D. A., He, S., Zhang, P., Ugurbil, K., & Yacoub, E. (2012). Layer-specific fMRI reflects different neuronal computations at different depths in human V1. *PloS One*, 7(3), e32536. https://doi.org/10.1371/journal.pone.0032536

Paradiso, M. A., & Nakayama, K. (1991). Brightness perception and filling-in. *Vision Research*, 31(7–8), 1221–1236.

Pascual-Leone, A., & Walsh, V. (2001). Fast backprojections from the motion to the primary visual area necessary for visual awareness. *Science* (New York, N.Y.), 292(5516), 510–512. https://doi.org/10.1126/science.1057099

Peirce, J. W. (2007). PsychoPy–Psychophysics software in Python. *Journal of Neuroscience Methods*, 162(1–2), 8–13. https://doi.org/10.1016/j.jneumeth.2006.11.017

Peirce, J. W. (2008). Generating stimuli for neuroscience using PsychoPy. *Frontiers in Neuroinformatics*, 2. https://doi.org/10.3389/neuro.11.010.2008

Pereverzeva, M., & Murray, S. O. (2008). Neural activity in human V1 correlates with dynamic lightness induction. *Journal of Vision*, 8(15), 8.1-10. https://doi.org/10.1167/8.15.8

Perna, A., Tosetti, M., Montanaro, D., & Morrone, M. C. (2005). *Neuron*al mechanisms for illusory brightness perception in humans. *Neuron*, 47(5), 645–651. https://doi.org/10.1016/j.neuron.2005.07.012

Pinheiro, J., Bates, D., DebRoy, S., Sarkar, D., & R Core Team. (2017). nlme: Linear and Nonlinear Mixed Effects Models. Retrieved from https://CRAN.R-project.org/package=nlme

Polimeni, J. R., Fischl, B., Greve, D. N., & Wald, L. L. (2010). Laminar analysis of 7T BOLD using an imposed spatial activation pattern in human V1. *NeuroImage*, 52(4), 1334–1346. https://doi.org/10.1016/j.neuroimage.2010.05.005

Poort, J., Self, M. W., van Vugt, B., Malkki, H., & Roelfsema, P. R. (2016). Texture Segregation Causes Early Figure Enhancement and Later Ground Suppression in Areas V1 and V4 of Visual Cortex. *Cerebral Cortex* (New York, N.Y.: 1991), 26(10), 3964–3976. https://doi.org/10.1093/cercor/bhw235

Poser, B. A., Koopmans, P. J., Witzel, T., Wald, L. L., & Barth, M. (2010). Three dimensional echo-planar imaging at 7 Tesla. *NeuroImage*, 51(1), 261–266. https://doi.org/10.1016/j.neuroimage.2010.01.108

R Core Team. (2017). R: A Language and Environment for Statistical Computing. Retrieved from https://www.R-project.org

Ress, D., Glover, G. H., Liu, J., & Wandell, B. (2007). Laminar profiles of functional activity in the human brain. *NeuroImage*, 34(1), 74–84. https://doi.org/10.1016/j.neuroimage.2006.08.020

Rezak, M., & Benevento, L. A. (1979). A comparison of the organization of the projections of the dorsal lateral geniculate nucleus, the inferior pulvinar and adjacent lateral pulvinar to primary visual cortex (area 17) in the macaque monkey. *Brain Research*, 167(1), 19–40.

Rockland, K. S., & Pandya, D. N. (1979). Laminar origins and terminations of cortical connections of the occipital lobe in the rhesus monkey. *Brain Research*, 179(1), 3–20. https://doi.org/10.1016/0006-8993(79)90485-2

Rockland, K. S., & Virga, A. (1989). Terminal arbors of individual 'feedback' axons projecting from area V2 to V1 in the macaque monkey: a study using immunohistochemistry of anterogradely transported Phaseolus vulgaris-leucoagglutinin. *The Journal of Comparative Neurology*, 285(1), 54–72. https://doi.org/10.1002/cne.902850106

Roe, A. W., Lu, H. D., & Hung, C. P. (2005). Cortical processing of a brightness illusion. *Proceedings of the National Academy of Sciences of the United States of America*, 102(10), 3869–3874. https://doi.org/10.1073/pnas.0500097102

Rossi, A. F., & Paradiso, M. A. (1999). Neural correlates of perceived brightness in the retina, lateral geniculate nucleus, and striate cortex. *The Journal of Neuroscience: The Official Journal of the Society for Neuroscience*, 19(14), 6145–6156.

Rossi, A. F., Rittenhouse, C. D., & Paradiso, M. A. (1996). The representation of brightness in primary visual cortex. *Science* (New York, N.Y.), 273(5278), 1104–1107.

Saalmann, Y. B., Pinsk, M. A., Wang, L., Li, X., & Kastner, S. (2012). The pulvinar regulates information transmission between cortical areas based on attention demands. *Science* (New York, N.Y.), 337(6095), 753–756. https://doi.org/10.1126/science.1223082

Sasaki, Y., & Watanabe, T. (2004). The primary visual cortex fills in color. *Proceedings of the National Academy of Sciences of the United States of America*, 101(52), 18251–18256. https://doi.org/10.1073/pnas.0406293102

Self, M. W., van Kerkoerle, T., Supèr, H., & Roelfsema, P. R. (2013). Distinct roles of the cortical layers of area V1 in figure-ground segregation. *Current Biology*: CB, 23(21), 2121–2129. https://doi.org/10.1016/j.cub.2013.09.013

Setsompop, K., Gagoski, B. A., Polimeni, J. R., Witzel, T., Wedeen, V. J., & Wald, L. L. (2012). Blipped-controlled aliasing in parallel imaging for simultaneous multislice echo planar imaging with reduced g-factor penalty. *Magnetic Resonance in Medicine*, 67(5), 1210–1224.

https://doi.org/10.1002/mrm.23097

Sherman, S. M., & Guillery, R. W. (2002). The role of the thalamus in the flow of information to the cortex. *Philosophical Transactions of the Royal Society of London. Series B, Biological Sciences*, 357(1428), 1695–1708. https://doi.org/10.1098/rstb.2002.1161

Shimono, M., Mano, H., & Niki, K. (2012). The brain structural hub of interhemispheric information integration for visual motion perception. *Cerebral Cortex* (New York, N.Y.: 1991), 22(2), 337–344. https://doi.org/10.1093/cercor/bhr108

Smith, S. M., Jenkinson, M., Woolrich, M. W., Beckmann, C. F., Behrens, T. E. J., Johansen-Berg, H., ... Matthews, P. M. (2004). Advances in functional and structural MR image analysis and implementation as FSL. *NeuroImage*, 23, S208–S219. https://doi.org/10.1016/j.neuroimage.2004.07.051

Standage, G. P., & Benevento, L. A. (1983). The organization of connections between the pulvinar and visual area MT in the macaque monkey. *Brain Research*, 262(2), 288–294.

Sterzer, P., Haynes, J.-D., & Rees, G. (2006). Primary visual cortex activation on the path of apparent motion is mediated by feedback from hMT+/V5. *NeuroImage*, 32(3), 1308–1316. https://doi.org/10.1016/j.neuroimage.2006.05.029

Tosun, D., Rettmann, M. E., Han, X., Tao, X., Xu, C., Resnick, S. M., ... Prince, J. L. (2004). Cortical surface segmentation and mapping. *NeuroImage*, 23, S108–S118. https://doi.org/10.1016/j.neuroimage.2004.07.042

Trojanowski, J. Q., & Jacobson, S. (1977). The morphology and laminar distribution of cortico-pulvinar neurons in the rhesus monkey. *Experimental Brain Research*, 28(1–2), 51–62.

Uludağ, K. (2008). Transient and sustained BOLD responses to sustained visual stimulation. *Magnetic Resonance Imaging*, 26(7), 863–869. https://doi.org/10.1016/j.mri.2008.01.049

Uludağ, K., & Blinder, P. (2017). Linking brain vascular physiology to hemodynamic response in ultra-high field MRI. *NeuroImage*. https://doi.org/10.1016/j.neuroimage.2017.02.063

van der Walt, S., Colbert, S. C., & Varoquaux, G. (2011). The NumPy Array: A Structure for Efficient Numerical Computation. *Computing in Science & Engineering*, 13(2), 22–30. https://doi.org/10.1109/MCSE.2011.37

Van Essen, D. C., Newsome, W. T., & Bixby, J. L. (1982). The pattern of interhemispheric connections and its relationship to extrastriate visual areas in the macaque monkey. *The Journal of Neuroscience: The Official Journal of the Society for Neuroscience*, 2(3), 265–283.

Villeneuve, M. Y., Thompson, B., Hess, R. F., & Casanova, C. (2012).

Pattern-motion selective responses in MT, MST and the pulvinar of humans. *The European Journal of Neuroscience*, 36(6), 2849–2858. https://doi.org/10.1111/j.1460-9568.2012.08205.x

Villeneuve, Martin Y., Kupers, R., Gjedde, A., Ptito, M., & Casanova, C. (2005). Pattern-motion selectivity in the human pulvinar. *NeuroImage*, 28(2), 474–480. https://doi.org/10.1016/j.neuroimage.2005.06.015

von der Heydt, R., Peterhans, E., & Baumgartner, G. (1984). Illusory contours and cortical neuron responses. *Science* (New York, N.Y.), 224(4654), 1260–1262.

Waehnert, M. D., Dinse, J., Weiss, M., Streicher, M. N., Waehnert, P., Geyer, S., ... Bazin, P.-L. (2014). Anatomically motivated modeling of cortical laminae. *NeuroImage*, 93, 210–220. https://doi.org/10.1016/j.neuroimage.2013.03.078

Wang, W.-L., Li, R., Ding, J., Tao, L., Li, D.-P., & Wang, Y. (2015). V1 neurons respond to luminance changes faster than contrast changes. *Scientific Reports*, 5(1). https://doi.org/10.1038/srep17173

Wokke, M. E., Vandenbroucke, A. R. E., Scholte, H. S., & Lamme, V. A. F. (2013). Confuse your illusion: feedback to early visual cortex contributes to perceptual completion. *Psychological Science*, 24(1), 63–71. https://doi.org/10.1177/0956797612449175

Wong-Riley, M. T. (1974). Demonstration of geniculocortical and callosal projection neurons in the squirrel monkey by means of retrograde axonal transport of horseradish peroxidase. *Brain Research*, 79(2), 267–272.

Yushkevich, P. A., Piven, J., Hazlett, H. C., Smith, R. G., Ho, S., Gee, J. C., & Gerig, G. (2006). User-guided 3D active contour segmentation of anatomical structures: Significantly improved efficiency and reliability. *NeuroImage*, 31(3), 1116–1128. https://doi.org/10.1016/j.neuroimage.2006.01.015

Zhang, Y., Brady, M., & Smith, S. (2001). Segmentation of brain MR images through a hidden Markov random field model and the expectation-maximization algorithm. *IEEE Transactions on Medical Imaging*, 20(1), 45–57. https://doi.org/10.1109/42.906424

Zhao, F., Wang, P., & Kim, S.-G. (2004). Cortical depth-dependent gradient-echo and spin-echo BOLD fMRI at 9.4T. *Magnetic Resonance in Medicine*, 51(3), 518–524. https://doi.org/10.1002/mrm.10720

Zipser, K., Lamme, V. A., & Schiller, P. H. (1996). Contextual modulation in primary visual cortex. *The Journal of Neuroscience: The Official Journal of the Society for Neuroscience*, 16(22), 7376–7389.

4

Estimation of the point spread function of sub-millimetre fMRI at 7T

Corresponding publication:

Marquardt, I., & Uludağ, K. (*in preparation*). Estimation of the point spread function of sub-millimetre fMRI at 7T.

4.1 Abstract

The point spread function (PSF) is a hypothetical concept that describes the mapping of a point source with an imaging system. The PSF is relevant for researchers because it gives an indication of the level of spatial detail that can be resolved with a particular imaging and analysis approach. In the context of fMRI, the PSF is influenced by technical characteristics of the scanner and the pulse sequence, by brain physiology, and by data processing. In the present study, we estimated the PSF of a sub-millimetre fMRI acquisition and analysis approach. The data used here have been previously presented with a focus on neuroscientific findings (Chapter 3). Here, we derived a cortical depth independent PSF for V1, V2 and V3, based on a spatial stimulus template, and a cortical depth dependent PSF for a gradient-echo MRI sequence at 7T with 0.8 mm isotropic acquisition. Both PSF parameters rely on the retinotopic organisation of the early visual cortex, and take into account the size of population receptive fields. In V1, we found the cortical depth-independent PSF to have a width (standard deviation) of approximately 0.9 mm. In agreement with previous reports, the width of the cortical depth-dependent PSF increased towards the cortical surface. Our results lend further support to the observation that while the fMRI signal amplitude tends to increase towards the cortical surface, the spatial specificity at which neuronal activity can be resolved may be highest in deep grey matter, close to the white matter boundary.

4.2 Introduction

Neuroimaging studies typically report the spatial resolution of their measurements in terms of the nominal voxel size. With advances in hardware and pulse sequences, isotropic voxel sizes of 0.7^3 mm^3 can now be reached with fMRI (Klein et al., 2018; e.g. Koopmans, Barth, Orzada, & Norris, 2011; Marquardt, Schneider, Gulban, Ivanov, & Uludağ, 2018). The voxel size describes the distance between sampling points in an image; it is a technical parameter that depends on the matrix size of the image and on the field of view. However, the voxel size does not completely characterise the spatial relationship between the sample (i.e. the brain) and the resulting image. First, the *imaging* point spread function (PSF) can be conceptualised as a sinc function (which only

approaches zero in the limit) for typical slice selction RF pulses (Buxton, 2009). By convention, MRI data is displayed such that the size of a data point in the image is matched to the nominal voxel size, but the resulting impression of MRI voxels as a discrete, cubical objects is artefactual, and somewhat misleading (Buxton, 2009). Even in an idealised scenario without physiological and thermal noise, the signal from a hypothetical point source would spread slightly further than one voxel.

Second, in addition to the imaging PSF, the specificity and spatial spread of the fMRI signal is dependent on the underlying brain physiology. Factors that contribute to the *functional* PSF are the spatial specificity of the haemodynamic response, the level of control for hyperaemia and the flow of venous blood originating from a neuronally active tissue (Uludağ & Blinder, 2017).

Third, fMRI data requires complex processing. Steps taken during image processing, such as motion correction, distortion correction, and spatial registrations, require spatial interpolation and may thus further impact the PSF. In the context of laminar fMRI, additional analysis steps are needed to map voxels to higher-resolution cortical depths. One may refer to this factor as the *analysis* PSF.

The width of the PSF is relevant because it informs neuroscientists at what level of detail they can expect to resolve neuronal activity with fMRI. However, the PSF is a theoretical concept – the hypothetical point source, on which it relies, does not exist in practise. Moreover, whereas in case of anatomical imaging an artificial object (e.g. a phantom) with a known structure can be tested, there is no ideal 'ground truth' against which functional images could be compared. In order to directly measure the PSF of fMRI, the 'true' pattern of neuronal activity would need to be known as a reference. Because there is no tool that can non-invasively measure activity in the human brain at a higher level of detail than fMRI, all attempts at estimating the PSF of fMRI have to rely on indirect measures.

The PSF of fMRI is especially relevant for contemporary high-resolution studies. With the availability of sub-millimetre acquisition methods at field strengths of 7T and above, the prospect of resolving cortical layers and columns becomes more promising. Kemper et al. (2015) compared the *imaging* PSF of two fMRI pulse sequences (3D GRASE and 2D SE EPI) at sub-millimetre resolution. Their approach served to evaluate the spatial signal spread due to technical properties

of the pulse sequence, and did not take into consideration the signal spread of functional activation originating from physiological processes. In contrast, Shmuel et al. (2007) and Polimeni et al. (2010) estimated the PSF by relating empirical activation maps to expected activation patterns based on prior information. Because of the known retinotopic organisation of primary visual cortex (Dumoulin & Wandell, 2008; Engel, Glover, & Wandell, 1997), fMRI activation maps can be compared against stimulus templates. In this way, an overall PSF, which includes contributions from the imaging, functional, and analysis PSF, can be estimated.

In a recent study, Chaimow et al. (2018) attempted to determine the PSF of fMRI without the use of an explicit retinotopic stimulus template. They argue that previous attempts – which relied on retinotopic stimulus templates – overestimated the PSF, because of a failure to take into consideration the size of receptive fields, and because of 'scatter' of receptive fields. To circumvent this problem, they developed an anatomical model of ocular dominance columns in human primary visual cortex, and a transfer function. The transfer function simulates fMRI activation maps based on the anatomical model. One of the free parameters of the transfer function is the width of the PSF. Empirical fMRI activation maps from a previous study (Yacoub, Shmuel, Logothetis, & Uğurbil, 2007) were compared against the simulated maps generated by the transfer function, to select a transfer function that has a high likelihood given the empirical fMRI data. In this way, the PSF was estimated indirectly, as part of the transfer function.

In the present study, we estimated the PSF directly from an empirically measured pattern of activation. Hence, our approach is similar, but not identical, to previous investigations of the PSF at 7T (Polimeni et al., 2010; Shmuel et al., 2007). Based on data presented previously (Chapter 3), we estimated two different PSFs. First, a PSF was estimated based on an explicit spatial model of the stimulus, by matching the model with the empirically observed pattern of activation. Importantly, we did not match the empirical activation pattern and the stimulus model in brain space, but in a two-dimensional model of the visual field based on population receptive field maps, thereby taking into account subjects' individual retinotopic layout. Second, following the observation by Polimeni et al. (2010) that fMRI activation patterns are sharpest in deep cortical layers, we assessed the blurring of retinotopic

stimulus representations across cortical depths, with respect to the activation pattern at the deepest cortical depth level (close to white matter). We refer to these two aspects as the cortical depth *independent* PSF and the cortical depth *dependent* PSF.

4.3 Methods

4.3.1 Experimental design

The data used in the current report have been presented previously, and the experimental design has been described in detail (Chapter 3). In brief, fMRI data were acquired from healthy participants (n=9), while centrally fixated stimuli were presented in a block design. Throughout the experiment, participants were performing a central fixation task. Functional MRI data were acquired on a 7 T scanner (Siemens Medical Systems, Erlangen, Germany) using a 32-channel phased-array head coil (Nova Medical, Wilmington, MA, USA) and a 3D gradient echo (GE) EPI sequence (TR = 2.079 s, TE = 26 ms, nominal resolution 0.8 mm isotropic, 40 slices, coronal oblique slice orientation, phase encode direction right-to-left, phase partial Fourier 6/8; GRAPPA acceleration factor 3; Poser, Koopmans, Witzel, Wald, & Barth, 2010).

Data were motion corrected using SPM 12 (Friston, Williams, Howard, Frackowiak, & Turner, 1996), and distortion correction was applied with FSL TOPUP (Andersson, Skare, & Ashburner, 2003). Parameter estimates of stimulus-induced activation were obtained from a GLM analysis performed using FSL (Smith et al., 2004). The retinotopic structure of early visual cortex was delineated by means of the population receptive field mapping method (Dumoulin & Wandell, 2008), using publicly available python code (Marquardt, Gulban, & Schneider, 2018) and standard scientific python packages (Numpy, Scipy, Matplotlib, Cython; Behnel et al., 2011; Millman & Aivazis, 2011; Oliphant, 2007; van der Walt, Colbert, & Varoquaux, 2011). Activation estimates from the GLM were projected into a model of the visual field based on the population receptive field estimates (see Chapter 3 for details).

4.3.2 Cortical depth-dependent and –independent point spread functions

The pattern of signal change in the visual field projections can be parametrised to compare the 'sharpness' of the visual field projection across areas or cortical depths (Figure 4.1). We assumed that the spatial smoothness of the stimulus representation at a given cortical depth and brain area can be factorized as two independent Gaussian filters.

First, in order to compare the 'sharpness' of the visual field projections across V1, V2, and V3, we fitted a model of the visual stimulus to the empirically observed projections (Figure 4.1 A). Specifically, we employed a spatial model of the stimulus consisting of three mutually exclusive sectors (stimulus centre, stimulus edge, and periphery) coded as 2D binary masks (i.e. arrays consisting of ones and zeros). Each of these stimulus compartments was multiplied with a scalar to account for the BOLD signal amplitude, the three compartments were added up, and the resulting 2D array was filtered with a Gaussian function. Separately for V1, V2, and V3, we determined the least squares fit for the four free parameters of the stimulus model (i.e. the scaling factors for the three compartments, and the width of the Gaussian filter) with respect to the empirical visual field projection at the deepest cortical depth level.

More formally, let $\boldsymbol{V}_{i,j}$ be a 2D tensor containing the visual field projection of GLM parameters for a particular region of interest (V1, V2, or V3), at the deepest cortical depth level (i.e. closest to the white matter boundary). Each element in $\boldsymbol{V}_{i,j}$ represents the amplitude of the stimulus-induced response at location i, j of the visual field, where i corresponds to the horizontal axis, and j indexes the vertical axis. The empirical visual field projection $\boldsymbol{V}_{i,j}$ is approximated by

$$\boldsymbol{V}_{i,j} = g(\boldsymbol{C}_{i,j} \cdot a + \boldsymbol{E}_{i,j} \cdot b + \boldsymbol{B}_{i,j} \cdot c) \tag{4.1}$$

Where $\boldsymbol{C}_{i,j}$, $\boldsymbol{E}_{i,j}$, and $\boldsymbol{B}_{i,j}$ are 2D tensors containing binary masks of the regions of the visual field corresponding to the centre of the stimulus, the stimulus edge, and the background, respectively (see Figure 4.1 A), and a, b, c are scalars. The cortical depth independent PSF is estimated by solving (1) for a, b, c, and for σ, the standard deviation of the Gaussian function g. The factors a, b, c account for the signal amplitude at the

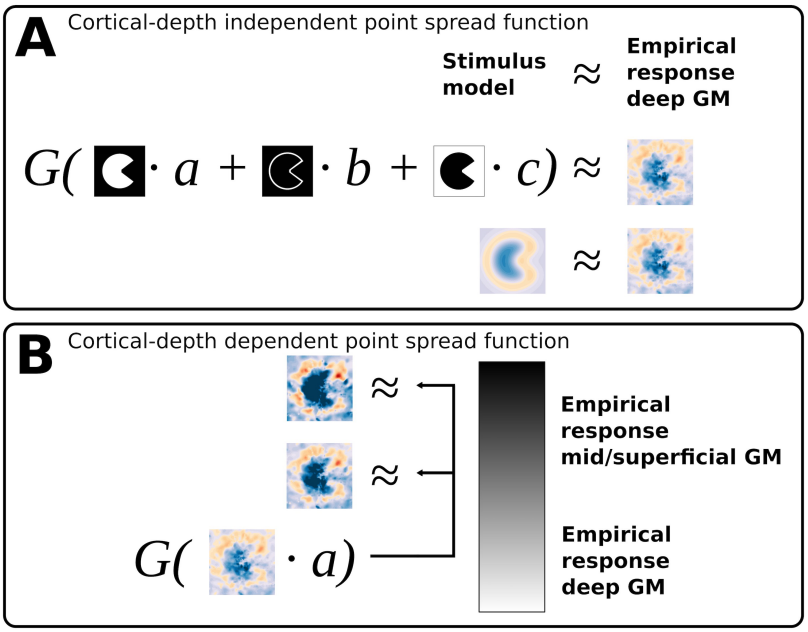

Figure 4.1: The visual field projections were parametrised in order to compare the 'sharpness' between cortical areas (**A**) and between cortical depth levels within an area (**B**). (**A**) For the comparison between cortical areas, a spatial model of the visual stimulus was fitted to the empirically observed projections. The stimulus model consisted of three mutually exclusive binary masks (for the stimulus centre, stimulus edge, and the periphery). The stimulus model was fitted to the empirical visual field projections by separately scaling each of the binary masks, adding the scaled masks, and convolving the sum with a Gaussian function. Thus, there were four free parameters: the three scaling factors, and the width of the Gaussian kernel. The width of the Gaussian was taken as an indicator of the 'sharpness' of the visual field projection. (**B**) A similar approach was employed to quantify differences in the visual field projections between cortical depth levels within an area, separately for each region of interest (V1, V2, V3). The visual field projection of the deepest cortical depth level (closest to white matter) served as a reference. This reference visual field projection was separately fitted to the visual field projections of all other cortical depth levels, by means of a scaling and a Gaussian convolution. Again, the width of the Gaussian filter was used as a measure of the relative 'sharpness' of the visual field projections.

respective sectors of the visual field, and σ corresponds to the width of the PSF.

The deepest cortical depth level (i.e. closest to white matter) was chosen as a reference for the comparison between cortical areas because, in our data, this is where the stimulus representation is least blurred (see Figure 4.3) and because the GE EPI fMRI signal is supposedly least affected by vascular artefacts at this depth level (Polimeni et al., 2010). The fitted width of the Gaussian filter served as an indicator of the 'sharpness' of the visual field projection, and we assume this parameter to be dependent on the size of the population receptive fields. Because the spatial stimulus model used here is static, we limited the fitting of the width of the Gaussian PSF to a static stimulus (there were three different visual stimuli, one of which was static; see Figure 4.3). In contrast, the cortical depth dependent PSF (see next paragraph) was estimated based on all three stimulus conditions, including dynamic stimuli.

Second, we used a similar procedure to quantify differences in the visual field projections between cortical depth levels (within an area; Figure 4.1 B). To this end, we used the visual field projection at the deepest cortical depth level (closest to white matter) as a reference, and determined the least squares fit between this reference and all other cortical depth levels. The least squares fit was obtained by a multiplication and the application of a Gaussian filter. Thus, the fitting procedure accounts for differences in signal amplitude and differences in 'sharpness' between visual field projections of different cortical depth levels.

With respect to the cortical depth dependent PSF, let $\boldsymbol{V}_{i,j,k}$ be a 2D tensor containing the visual field projection of GLM parameter estimates for a particular region of interest (V1, V2, or V3). Similar to equation (1), each element in $\boldsymbol{V}_{i,j,k}$ represents the amplitude of the stimulus-induced response at location i, j of the visual field, where i corresponds to the horizontal axis, and j indexes the vertical axis. Different to equation (1), there is one visual field projection for each cortical depth level k. The cortical depth dependent PSF is parametrised by solving, in the least squares sense,

$$\boldsymbol{V}_{i,j,k=0} = g(\boldsymbol{V}_{i,j,k>0} \cdot a) \tag{4.2}$$

where $k = 0$ refers to the deepest cortical depth level (closest to white matter), and $k > 0$ corresponds to all other, more superficial cortical depth levels. The factor a accounts for differences in signal amplitude between cortical depth levels, and the standard deviation σ of the Gaussian function g represents the width of the PSF.

4.4 Results

The projection of activation maps into a model of the visual field reveals a negative response at the cortical representation of the stimulus centre, and a positive response at the stimulus edges (Figure 4.2). Especially in V1 and V2, the shape of the stimulus can be recognised in the visual field projections (Figure 4.2 B & C). The width of the PSF was found to increase along the visual hierarchy (Figure 4.2 D). Based on the visual field projection of the activation at deep grey matter in V1, we found the PSF to have a width (standard deviation) of ∼0.26° visual angle (Figure 4.2 D; the units are in degrees of visual angle because the calculation is based on the visual field projections). The cortical magnification factor at the edge of the Pac-Man stimulus (i.e. at an eccentricity of 3.75°) is on average ∼3.5 mm/deg (Harvey & Dumoulin, 2011). Thus, the cortical depth-independent PSF at this position can be estimated to have a width (standard deviation) of ∼0.9 mm.

Separate visual field projections of stimulus-induced signal change at deep, middle, and superficial grey matter (Figure 4.3) reveal an increase of signal amplitude towards the cortical surface, accompanied by a blurring of the visual field projections. In other words, in addition to a larger signal amplitude, the spatial extent of the fMRI signal change expands towards the surface of the cortex. In particular, the strongly negative response at the cortical representation of the stimulus centre spreads further towards the location of the stimulus edge, making the positive response at the edge less visible at some locations. The level of blurring is similar across brain areas (Figure 4.4). The cortical depth-dependent PSF was found to be ∼0.5° at mid-cortical depth in V1 (Figure 4.4), which corresponds to ∼1.75 mm cortex (at the eccentricity of the edge of the stimulus).

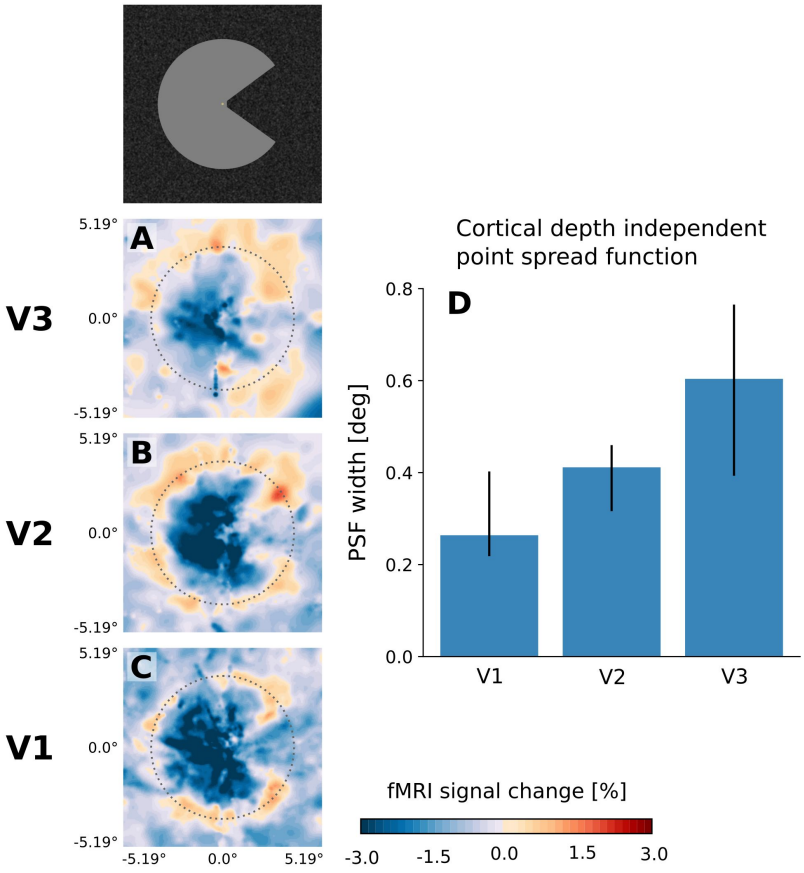

Figure 4.2: Cortical depth independent point spread function (PSF). The PSF was estimated based on the projection of GLM parameters of a stimulus ('Pac-Man') into the visual space (**A**, **B**, **C**). The thin dashed circles correspond to an eccentricity of 3.75°, i.e. the radius of the Pac-Man stimulus. (**D**) PSF width in deep grey matter in V1, V2, and V3. Because the spatial stimulus model used for the estimation of the PSF is static (see Figure 4.1 A), the analysis was restricted to a static stimulus condition. Error bars represent 90% bootstrap confidence interval.

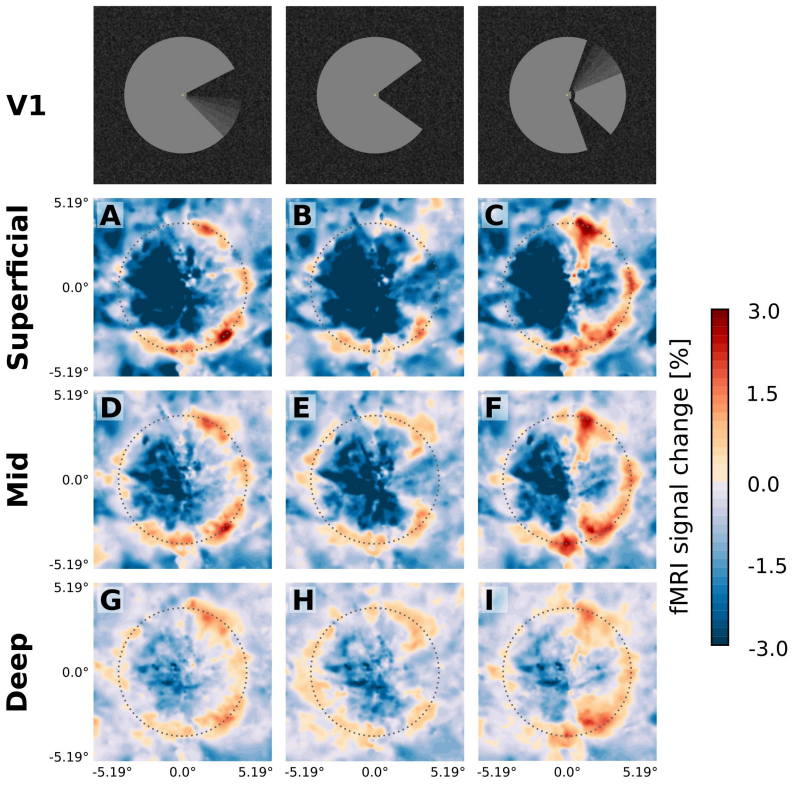

Figure 4.3: Visual field projections of GLM parameter estimates from three stimulus conditions, separately for superficial (**A**, **B**, **C**), middle (**D**, **E**, **F**), and deep (**G**, **H**, **I**) cortical depth levels in V1. The cortical depth dependent point spread function (PSF) was estimated based on the visual field projections from the deepest cortical depth level (see Figures 4.1 & 4.4). The dashed circles correspond to an eccentricity of 3.75°, i.e. the radius of the Pac-Man stimulus.

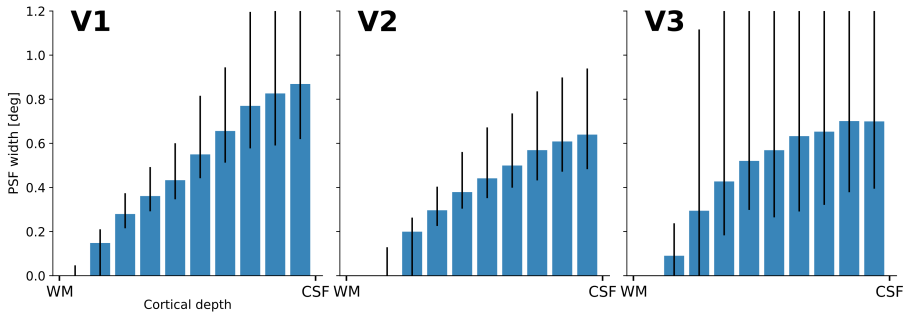

Figure 4.4: Width of the cortical depth dependent point spread function (PSF), separately for areas V1, V2, and V3. The cortical depth-dependent point spread function is based on the visual field projections of all three stimulus conditions (mean over stimulus conditions). The deepest cortical depth level (closest to white matter) serves as a reference; consequently it has a PSF width of zero. Error bars represent 90% bootstrap confidence interval.

4.5 Discussion

4.5.1 Cortical depth independent PSF

In one of the first cortical depth dependent fMRI studies in humans, Polimeni et al. have shown that while the stimulus-induced response increases in amplitude towards the cortical surface, it also becomes less spatially specific (2010). The suspected reason for this is the increased draining territory of cortical ascending veins towards the pial surface (Uludağ & Blinder, 2017). To investigate the spatial fidelity of the response pattern, we parametrised the visual field projections, and derived two point spread functions (PSFs). One PSF is independent of cortical depth, and was obtained by comparing the visual field projections of V1, V2 and V3 at the deepest cortical depth level with a spatial model of the stimulus (Figure 4.1 A). The cortical depth independent PSF is related to the tangential PSF proposed by Polimeni et al. (2010) and corresponds to the well-known receptive field extension of early visual areas. We estimated the cortical depth independent PSF to have a width (standard deviation) of ∼0.9 mm in V1 (Figure 4.2 based on a cortical magnification factor of ∼3.5 mm/deg (Harvey & Dumoulin, 2011). As this value has been determined by the edge response, it is likely to represent an upper value of the cortical depth independent PSF,

as the receptive fields closer to the fovea are narrower. This result is in agreement with previous results by Shmuel et al. (2007). Shmuel et al. (2007) reported the point spread function to have a FWHM of 2.34 mm, which corresponds to a standard deviation of 0.99 mm.

We found the depth independent PSF to become wider when ascending the visual hierarchy from V1 via V2 to V3 (Figure 4.2 D). This trend is also visible in the visual field projections, which are least sharp for V3 (Figure 4.2 A). This finding is probably largely due to the increasing receptive field size along the visual hierarchy (the population receptive field size directly affects the visual field projections, based on which the point spread function was estimated). In our data, the PSF had a width (standard deviation) of ∼0.26° visual angle in V1, ∼0.4° in V2, and ∼0.6° in V3 (Figure 4.2 D), which is roughly proportional to the mean population receptive field sizes in our data (at the eccentricity corresponding to the edge of the stimulus, i.e. 3.75°, we found population receptive field sizes of ∼0.6° in V1, ∼0.8° in V2, ∼1.1° in V3). A previous study has reported larger population receptive field sizes of 1.0° in V1, 1.2° in V2, and 1.8° in V3 for human visual cortex (Harvey & Dumoulin, 2011 Figure 4A). This difference may be attributed to differences in voxel size (2.5 mm isotropic in Harvey and Dumoulin (2011), vs. 0.8 mm isotropic in the present study), and differences in stimulus design (drifting bars in Harvey and Dumoulin (2011) vs. bars at pseudo-random positions in the present study). Indeed, Fracasso et al. (2016) found population receptive field centre sizes of ∼0.8° at mid-cortical depth in V1 based on fMRI data acquired at a voxel size of 0.7 mm isotropic. (See Senden, Reithler, Gijsen, & Goebel, 2014 for a detailed discussion of stimulus designs for retinotopic mapping.)

4.5.2 Cortical depth dependent PSF

The second PSF is dependent on cortical depth, and uses the visual field projection at the deepest cortical depth level within an area as a reference (Figure 4.1 B). The width of the cortical depth dependent PSF was estimated based on the blurring of the visual field projections across cortical depths. It can be compared to the concept of a radial PSF introduced by Polimeni et al. (2010). Using a method different from ours, Polimeni et al. (2010) found a blurring of 35% when comparing the activation patterns at the white matter boundary and at the pial surface,

based on a template of expected activation. A direct, quantitative comparison between the present results and the observations reported by Polimeni et al. (Polimeni et al., 2010) is hindered by differences in methodology. Their approach is based on the correlation between an empirically observed activation pattern and a template reflecting the shape of the stimulus. However, instead of assessing the correspondence between the stimulus template (in case of the cortical depth *independent* PSF) or the deep-grey-matter activation (in case of the cortical depth *dependent* PSF) and the empirical activation pattern by means of a correlation, we explicitly modelled the PSF as a Gaussian function.

The 35% decrease in correlation between deep and superficial layers reported by Polimeni et al. (2010) is based on a differential contrast between two stimulus conditions, whereas we relied on single-condition activation maps (relative to a rest condition; see discussion on single conditions vs. differential contrasts below). Polimeni et al. also reported corresponding results for a single-condition activity pattern (2010 see their Figure 9 B); in this case they observed an almost constant correlation across cortical depth levels. Our single-condition data are qualitatively in accordance with the results based on a differential contrast by Polimeni et al. (2010), as we also found the visual field projections to become more blurred towards the cortical surface (Figure 4.4). A possible explanation for the fact that we observed a monotonic increase in the width of the PSF even in single-condition data could be that an analysis based on retinotopically informed, subject-specific visual field projections, and the use of an explicit model of the PSF, might have increased sensitivity compared with previous attempts.

Differences in (population) receptive field size across cortical depth levels have been reported (Fracasso et al., 2016; Self, van Kerkoerle, Goebel, & Roelfsema, 2017; Self, van Kerkoerle, Supèr, & Roelfsema, 2013 see their Supplemental Figure S1 E), and may play a role in our results. However, (population) receptive field sizes were found to be smallest at mid-cortical depth. If the cortical depth dependent point spread function was mainly influenced by receptive field size, a U-shaped distribution would be expected for its width. Because we observed a monotonic increase towards the cortical surface, we assume vascular effects to be the main contributing factor. Please note that we assumed a constant population receptive field size for the visual field projections (mean over cortical depth levels), so as not to confound the results.

Thus, differences in PSF width are driven by differences in the activation pattern to the experimental stimuli across cortical depths, and not by differences in the population receptive field size estimates. Theoretically, an interaction between the width of the cortical depth dependent PSF and population receptive field size estimates would be expected.

4.5.3 Limitations & outlook

Knowing the PSF of an fMRI acquisition and data processing approach is relevant because it informs the researcher on the level of spatial detail that can be resolved. The quantification of the PSF is hindered by the fact that there is no 'ground truth' against which fMRI activation profiles could be compared. Thus, any assessment of the PSF of fMRI has to rely on indirect approximations. Previous investigations (Polimeni et al., 2010; Shmuel et al., 2007) have based their estimations on the retinotopic layout of early visual cortex. In the present study, we have also made use of the retinotopic structure of early visual cortex, but with the difference that we employed a population receptive field model that accounts for the position and width of population receptive fields.

Cheng (2016) argued that a narrower PSF can be expected for differential contrasts, as compared with single-condition data relative to a rest condition. For example, ocular dominance columns may not be visible in activation maps of monocular stimulation compared with a rest condition (without stimulation), but may become apparent when contrasting monocular left eye vs. right eye stimulus conditions due to selective reduction of BOLD signal activity of non-specific draining and pial veins (Cheng, 2016). Our PSF estimates are based on single-condition activation maps (with respect to a rest condition without stimulation). Thus, our PSF estimates are possibly wider than those for a differential contrast. However, activation profiles in response to a single stimulus condition can be neuroscientifically relevant, for example if there is doubt as to what would constitute a 'clean' control condition in a differential contrast. Depending on the research question and experimental design, the differential or the single-condition PSF of fMRI are of interest.

Shmuel et al. (2007) reported a PSF width (standard deviation) of 0.99 mm, using a GE EPI sequence at a voxel size of 1 mm $\times$ 1

mm × 3mm. The fact that our PSF estimate is only slightly narrower (∼0.9 mm in V1), despite a much smaller voxel size (0.8^3 mm^3), may be explained by the fact that Shmuel et al. (2007) based their estimates on maps of differential activation.

Chaimow et al. (2018) approximated the PSF of GE and SE pulse sequences at 7T indirectly, by means of an anatomical model of ocular dominance columns and a transfer function relating the model to simulated fMRI data. Their estimate of a Gaussian PSF for a GE sequence had a width (standard deviation) of 0.42 mm[1]. Again, their estimates are based on a differential condition contrast (left eye vs. right eye stimulation), which may explain their narrower PSF compared with the present, single-condition results.

Chaimow et al. (2018) argue that previous attempts overestimated the fMRI PSF, because the non-zero width of population receptive fields had not been taken into account. Our approach utilises a model of the visual space based on population receptive fields, whose width is explicitly modelled. Thus, our approach takes into consideration the individual retinotopic layout of early visual cortex, including population receptive field sizes. However, in order to obtain robust population receptive field models, we assumed a single set of position and width parameters for each location on the cortical surface (i.e. constant parameters across cortical depths). Substantially more data would be needed to estimate the population receptive field parameters independently at each cortical depth level. Moreover, the cortical depth specific population receptive field estimates may in turn be confounded by differences in the PSF width across cortical depths. Further research will be needed to assess the interaction between population receptive field sizes and the cortical depth dependent PSF of fMRI. In addition, the PSF due to ascending and pial veins may be brain area specific, as vascular density and architecture varies over the cortex, and is distinctly different in subcortical structures.

4.6 References

Andersson, J. L. R., Skare, S., & Ashburner, J. (2003). How to correct susceptibility distortions in spin-echo echo-planar images: application to diffusion tensor imaging. *NeuroImage*, 20(2), 870–888.

[1]They reported the PSF width in terms of FWHM, which was 0.99 mm for the GE sequence and 0.86 mm for the SE sequence.

https://doi.org/10.1016/S1053-8119(03)00336-7

Behnel, S., Bradshaw, R., Citro, C., Dalcin, L., Seljebotn, D. S., & Smith, K. (2011). Cython: The Best of Both Worlds. *Computing in Science & Engineering*, 13(2), 31–39. https://doi.org/10.1109/MCSE.2010.118

Buxton, R. B. (2009). *Introduction to Functional Magnetic Resonance Imaging: Principles and Techniques* (2nd Edition). Cambridge, New York: Cambridge University Press.

Chaimow, D., Yacoub, E., Uğurbil, K., & Shmuel, A. (2018). Spatial specificity of the functional MRI blood oxygenation response relative to neuronal activity. *NeuroImage*, 164, 32–47. https://doi.org/10.1016/j.neuroimage.2017.08.077

Cheng, K. (2016). What We Have Learned about Human Primary Visual Cortex from High Resolution Functional Magnetic Resonance Imaging. Magnetic Resonance in Medical Sciences: MRMS: An Official Journal of Japan Society of *Magnetic Resonance in Medicine*, 15(1), 1–10. https://doi.org/10.2463/mrms.2015-0008

Dumoulin, S. O., & Wandell, B. A. (2008). Population receptive field estimates in human visual cortex. *NeuroImage*, 39(2), 647–660. https://doi.org/10.1016/j.neuroimage.2007.09.034

Engel, S. A., Glover, G. H., & Wandell, B. A. (1997). Retinotopic organization in human visual cortex and the spatial precision of functional MRI. *Cerebral Cortex* (New York, N.Y.: 1991), 7(2), 181–192.

Fracasso, A., Petridou, N., & Dumoulin, S. O. (2016). Systematic variation of population receptive field properties across cortical depth in human visual cortex. *NeuroImage*, 139, 427–438. https://doi.org/10.1016/j.neuroimage.2016.06.048

Friston, K. J., Williams, S., Howard, R., Frackowiak, R. S., & Turner, R. (1996). Movement-related effects in fMRI time-series. *Magnetic Resonance in Medicine*, 35(3), 346–355.

Harvey, B. M., & Dumoulin, S. O. (2011). The relationship between cortical magnification factor and population receptive field size in human visual cortex: constancies in cortical architecture. *The Journal of Neuroscience: The Official Journal of the Society for Neuroscience*, 31(38), 13604–13612. https://doi.org/10.1523/JNEUROSCI.2572-11.2011

Kemper, V. G., De Martino, F., Vu, A. T., Poser, B. A., Feinberg, D. A., Goebel, R., & Yacoub, E. (2015). Sub-millimeter T2 weighted fMRI at 7 T: comparison of 3D-GRASE and 2D SE-EPI. *Frontiers in Neuroscience*, 9, 163. https://doi.org/10.3389/fnins.2015.00163

Klein, B. P., Fracasso, A., van Dijk, J. A., Paffen, C. L. E., Te Pas, S. F., & Dumoulin, S. O. (2018). Cortical depth dependent population receptive field attraction by spatial attention in human V1. *NeuroImage*, 176, 301–312. https://doi.org/10.1016/j.neuroimage.2018.04.055

Koopmans, P. J., Barth, M., Orzada, S., & Norris, D. G. (2011). Multi-echo fMRI of the cortical laminae in humans at 7T. *NeuroImage*, 56(3), 1276–1285. https://doi.org/10.1016/j.neuroimage.2011.02.042

Marquardt, I., Gulban, O. F., & Schneider, M. (2018, April 18). pyprf - A free & open source python package for population receptive field (pRF) analysis. https://doi.org/10.5281/zenodo.1220207

Marquardt, I., Schneider, M., Gulban, O. F., Ivanov, D., & Uludağ, K. (2018). Cortical depth profiles of luminance contrast responses in human V1 and V2 using 7 T fMRI. *Human Brain Mapping*. https://doi.org/10.1002/hbm.24042

Millman, K. J., & Aivazis, M. (2011). Python for Scientists and Engineers. *Computing in Science & Engineering*, 13(2), 9–12. https://doi.org/10.1109/MCSE.2011.36

Oliphant, T. E. (2007). Python for Scientific Computing. *Computing in Science & Engineering*, 9(3), 10–20. https://doi.org/10.1109/MCSE.2007.58

Polimeni, J. R., Fischl, B., Greve, D. N., & Wald, L. L. (2010). Laminar analysis of 7T BOLD using an imposed spatial activation pattern in human V1. *NeuroImage*, 52(4), 1334–1346. https://doi.org/10.1016/j.neuroimage.2010.05.005

Poser, B. A., Koopmans, P. J., Witzel, T., Wald, L. L., & Barth, M. (2010). Three dimensional echo-planar imaging at 7 Tesla. *NeuroImage*, 51(1), 261–266. https://doi.org/10.1016/j.neuroimage.2010.01.108

Self, M. W., van Kerkoerle, T., Goebel, R., & Roelfsema, P. R. (2017). Benchmarking laminar fMRI: Neuronal spiking and synaptic activity during top-down and bottom-up processing in the different layers of cortex. *NeuroImage*. https://doi.org/10.1016/j.neuroimage.2017.06.045

Self, M. W., van Kerkoerle, T., Supèr, H., & Roelfsema, P. R. (2013). Distinct roles of the cortical layers of area V1 in figure-ground segregation. *Current Biology*: CB, 23(21), 2121–2129. https://doi.org/10.1016/j.cub.2013.09.013

Senden, M., Reithler, J., Gijsen, S., & Goebel, R. (2014). Evaluating population receptive field estimation frameworks in terms of robustness and reproducibility. *PloS One*, 9(12), e114054. https://doi.org/10.1371/journal.pone.0114054

Shmuel, A., Yacoub, E., Chaimow, D., Logothetis, N. K., & Ugurbil, K. (2007). Spatio-temporal point-spread function of fMRI signal in human gray matter at 7 Tesla. *NeuroImage*, 35(2), 539–552. https://doi.org/10.1016/j.neuroimage.2006.12.030

Smith, S. M., Jenkinson, M., Woolrich, M. W., Beckmann, C. F., Behrens, T. E. J., Johansen-Berg, H., ... Matthews, P. M. (2004). Advances in functional and structural MR image analysis and implementation as FSL. *NeuroImage*, 23, S208–S219.

https://doi.org/10.1016/j.neuroimage.2004.07.051

Uludağ, K., & Blinder, P. (2017). Linking brain vascular physiology to hemodynamic response in ultra-high field MRI. *NeuroImage*. https://doi.org/10.1016/j.neuroimage.2017.02.063

van der Walt, S., Colbert, S. C., & Varoquaux, G. (2011). The NumPy Array: A Structure for Efficient Numerical Computation. *Computing in Science & Engineering*, 13(2), 22–30. https://doi.org/10.1109/MCSE.2011.37

Yacoub, E., Shmuel, A., Logothetis, N., & Uğurbil, K. (2007). Robust detection of ocular dominance columns in humans using Hahn Spin Echo BOLD functional MRI at 7 Tesla. *NeuroImage*, 37(4), 1161–1177. https://doi.org/10.1016/j.neuroimage.2007.05.020

5

Background suppression in human early visual cortex during the perception of real and illusory surfaces

Corresponding publication:

Marquardt, I., De Weerd, P., Schneider, M., Ivanov, D., & Uludağ, K. (*in preparation*). Background suppression in human early visual cortex during the perception of real and illusory surfaces.

5.1 Abstract

To perceive a visual scene, the visual system needs to identify contours between objects. Moreover, continuous surfaces need to be identified for object identification. In Kanizsa-type visual displays, illusory contours enclosing an illusory surface are perceived in the absence of local contrast variations. Here, we studied the spatial and temporal dynamics of responses to real and illusory contours and surfaces in human early visual cortex by means of sub-millimetre fMRI. Especially in V2, a trend towards a negative response at the retinotopic representation of the illusory surface relative to rest was observed. However, peripheral regions of visual cortex that did not receive direct bottom-up stimulus input also showed a negative response. Thus, the evidence does not directly support a cortical response specific to the processing of an illusory surface in V1 and V2. Rather, the most parsimonious explanation for the observed pattern of activation is a general background suppression during the presentation of both the Kanizsa inducers and the control stimuli.

5.2 Introduction

To perceive a visual scene, objects need to be identified and distinguished from each other. Segments of the retinal input that belong to the same object need to be grouped, and those that belong to distinct objects or to the background need to be segregated. Luminance contours are an important cue for the visual system to accomplish this task, in particular for the detection of object boundaries. Early vision research has focused on the cortical response to contrast edges, and the primary visual cortex was found to be very sensitive to these (Albrecht & Hamilton, 1982; Hubel & Wiesel, 1968). On the other hand, to group segments of the retinal input into coherent objects, continuous surfaces need to be identified. Whereas the perception of surfaces defined by texture has been studied extensively (Kastner, De Weerd, & Ungerleider, 2000; Lamme, 1995; Lamme, Rodriguez-Rodriguez, & Spekreijse, 1999; Lamme, Zipser, & Spekreijse, 1998; Lamme & Spekreijse, 1998; Self, van Kerkoerle, Supèr, & Roelfsema, 2013; van Kerkoerle et al., 2014), the processing of static, uniform surfaces has received less attention but, for experiments employing briefly presented uniform surface stimuli, see (Huang & Paradiso, 2008; Kinoshita & Komatsu, 2001; Zurawel,

Ayzenshtat, Zweig, Shapley, & Slovin, 2014). This is quite remarkable, since especially human-made environments contain an abundance of uniform surfaces (such as an empty table, a painted wall, a blank screen, etc.).

One of the few available studies investigated the cortical response to uniform surfaces in anaesthetised cats (MacEvoy, Kim, & Paradiso, 1998). Neurons in cat primary visual cortex were found to be excited when a uniformly luminous disk was placed on their receptive field, in the absence of local luminance contrast. In other words, the cells were active even though the edges of the surface stimulus were well outside their receptive field. The authors concluded that the functional properties of neurons in primary visual cortex cannot be fully characterised by probing their responses with grating stimuli or contrast edges, as is commonly done, and that a significant percentage of cells encodes information about surfaces (MacEvoy et al., 1998).

A study in behaving Macaque monkeys measured the spiking response to static, uniform surfaces presented on a uniform background (Kinoshita & Komatsu, 2001). Surfaces that were darker and surfaces that were brighter than the background were tested. Both types of surfaces evoked transient onset and offset responses. Only surfaces that were bright relative to the background also elicited a sustained response that lasted throughout the stimulus presentation, in addition to transient onset and offset peaks. Thus, the neural response was overall stronger for brighter surfaces (Kinoshita & Komatsu, 2001). Conversely, an optical imaging study reported a stronger response to black surfaces than to white surface in primary visual cortex of awake monkeys (Zurawel et al., 2014). The stimuli used in the two apparently conflicting studies were spatially similar (static, uniform black and white squares presented on a uniform grey background), but differed in duration (1 s vs 300 ms). The latter study (Zurawel et al., 2014) also compared the responses at the cortical representation of the edge and at the centre of the stimulus surfaces, and found the activation at the stimulus edge to be faster (with a time to peak difference in the order of tens of milliseconds Zurawel et al., 2014 see their Figure 2).

The processing of luminance has been studied in humans with fMRI. Haynes et al. (2004) found both increments and decrements in luminance to cause a transient, positive activation in human early visual cortex. They presented luminance stimuli at short (1.3 s) and long (15

s) durations, and observed no sustained response component for the longer stimulus duration, suggesting that the luminance response in early visual cortex is entirely transient (Haynes et al., 2004). Other studies in humans have focused on the processing of Kanizsa-type illusory surfaces. An early fMRI study reported an increase in the responsiveness to illusory surfaces along the hierarchy of visual areas (Mendola, Dale, Fischl, Liu, & Tootell, 1999). More recent experiments profited from higher spatial resolutions and more sophisticated retinotopic mapping techniques, and found a positive response to illusory surfaces presented at a relatively high temporal frequency (Kok, Bains, van Mourik, Norris, & de Lange, 2016; at a presentation rate of 1 Hz Kok & de Lange, 2014). In a previous study (Chapter 3), we observed a strongly negative, delayed response to static, uniform surfaces in early visual cortex (Figure 5.1). A control experiment revealed that the surface response was only negative if the background contained a texture pattern (Figure 3.7). In case of a uniform surface on a uniform background, the response to the surface interior and to its edges was positive and sustained, consistent with some, but not all, of the studies mentioned above (Figure 3.8; in contrast Haynes et al., 2004, reported an exclusively transient response to a full-field luminance stimulus with a duration comparable to ours; our previous results are in line with Kinoshita & Komatsu, 2001; and Zurawel et al., 2014, although it should be noted that our stimulus duration was much longer).

Comparisons between invasive recording studies in monkeys and fMRI experiments in humans are hindered by differences in the sampling rate of the measurements and the presentation rate of the stimuli, in addition to the sensitivity to different physiological processes (i.e. neuronal vs vascular). In animal studies, the neuronal response can be sampled at a very high rate, and stimulus durations are often short (Huang & Paradiso, 2008, p. 550 ms; Kinoshita & Komatsu, 2001, pp. 500 to 2000 ms, "typically" 1000 ms; Zurawel et al., 2014, p. 300 ms). Consequently, transient and sustained responses are observed on a very short timescale. For example, Kinoshita and Komatsu (2001) reported a transient response to a surface stimulus that subsided in less than 100 ms, and a sustained response lasting approximately 1 s. In contrast, we have previously observed transient responses that lasted several seconds (Figure 5.1, see also Figures 3.8 & 3.12) and sustained responses lasting for up 25 s (Figure 3.13, see also Uludağ, 2008). Thus, what is often

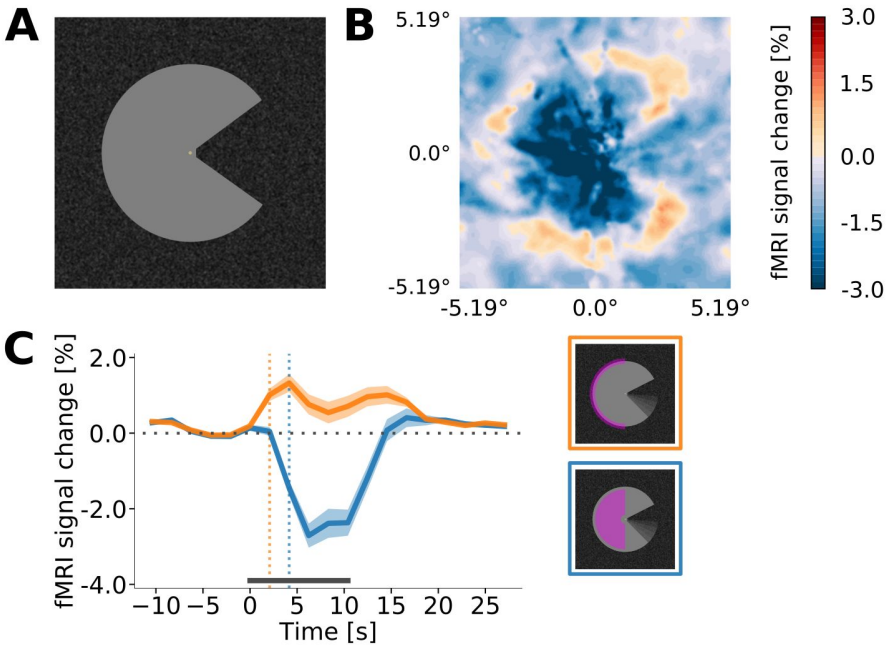

Figure 5.1: Negative surface response. (**A**) In a previous fMRI experiment (Chapter 3), participants were presented a uniform grey stimulus ('Pac-Man') on a dark random texture background. (**B**) Projection of the response in primary visual cortex into a model of the visual field reveals a strongly negative response at the centre of the Pac-Man figure, whereas the response at the edge of the stimulus was positive. (**C**) The temporal dynamics of the stimulus-induced response differ considerably across visual space. The positive response at the edge is transient, and precedes the sustained negative response at the stimulus centre. The aim of the current study was to further investigate responses to real and illusory surface in early visual cortex at a similar spatio-temporal scale.

considered a sustained response in electrophysiology may be classified as transient in an fMRI study.

The purpose of the present study was to further investigate the processing of illusory and real surfaces, enabling comparison with earlier experiments on illusory surfaces (Kok et al., 2016; Kok & de Lange, 2014) and our own previous results (Chapter 3). In brief, we did not replicated earlier reports of a positive response to illusory surfaces (Kok et al., 2016; Kok & de Lange, 2014). On the contrary, we found a slight trend towards a negative response to an illusory surface relative to rest (which is not statistically significant at the present sample size). Because this response was also present in a control condition without an illusory surface, it might have been caused by a general background suppression. In line with this interpretation, peripheral regions of V2 that did not receive direct bottom-up stimulus input exhibited background suppression under a variety of stimulus conditions. A more complex response profile occurred in V1, where either transient responses or background suppression were observed depending on the experimental condition. More data will be needed before definite conclusions can be drawn.

5.3 Methods

5.3.1 Experimental design – main experiment

Healthy participants (n=4, age between 25 and 30 years, mean (SD) age 27.0 (2.1) years) gave informed consent before the experiment, and the study protocol was approved by the local ethics committee of the Faculty for Psychology & Neuroscience, Maastricht University[1]. Subjects were presented three visual stimuli interspersed with rest blocks (Figure 5.2). One experimental condition was a version of the 'Kanizsa illusion' (Figure 5.3 A). Four 'Pac-Man' inducers were arranged, so as to induce the percept of an illusory surface at the centre of the screen. In a control condition, the 'Pac-Man' inducer stimuli were oriented differently, so as not to cause the perception of a surface (Figure 5.3 B). In both conditions, the dark grey inducer stimuli were presented on a uniform light grey background. In a third condition, a light grey square was

[1]Work in progress – final sample size is intended to be n=10.

presented on a dark grey background (Figure 5.3 C). The position and size of the light grey square was congruent with the induced illusory square. In the following, we will refer to these three stimulus conditions as 'Kanizsa square', 'Kanizsa rotated', and 'real square', respectively. The luminance of the bright grey surface areas was 246 cd/m^2 (i.e. the background in the Kanizsa conditions, and the real square), and that of the dark areas was 0.43 cd/m^2 (i.e. the Kanizsa inducers, and the dark frame around the real square). These luminance intensities matched those in an earlier study by Kok & de Lange (2014). At all times, a fixation dot with a diameter of 0.18° visual angle was present at the centre of the screen. The Kanizsa inducers ('Pac-Man') were discs, from which a sector spanning 90° was removed. They had a diameter of 3.0° visual angle, and their centre was displaced by 3.0° visual angle in the vertical and horizontal direction, relative to the centre of the screen (i.e. the distance between the fixation dot and the centre of the inducer stimuli was 4.24° visual angle).

The three stimulus conditions were presented in pseudo-random order (with the constraint that the same event does not occur twice in succession). Stimulus blocks had a duration of 12.4 s, and were interspersed with rest periods of variable duration (22.9 s, 25.0 s, or 27.0 s, in random order). The first rest block at the beginning of each run had a fixed duration of 25 s. Each run included twelve stimulus blocks (four repetitions per condition). Each subject completed six functional runs. The total duration of a run was 474 s.

Participants were instructed to fixate a central dot throughout the experiment and to report pseudo-randomly occurring changes in the dot's colour by button press. Targets were presented for 0.6 s, and the mean inter-trial interval between targets was 20 s (range ±10 s). No targets were shown during the first and last 15 s of each run. The timing of target events was arranged such that the predicted haemodynamic responses to the targets and to the experimental stimulus are uncorrelated (see Chapter 2, *Methods*, for details).

Stimuli were created with Psychopy (Peirce, 2007, 2008) and projected onto a translucent screen mounted behind the MRI head coil, via a mirror mounted at the end of the scanner bore. During the experiment all lights in the scanner room were switched off, and black cardboard was placed on the inside of the MRI transmit coil in order to minimise light reflection. The python code used to create

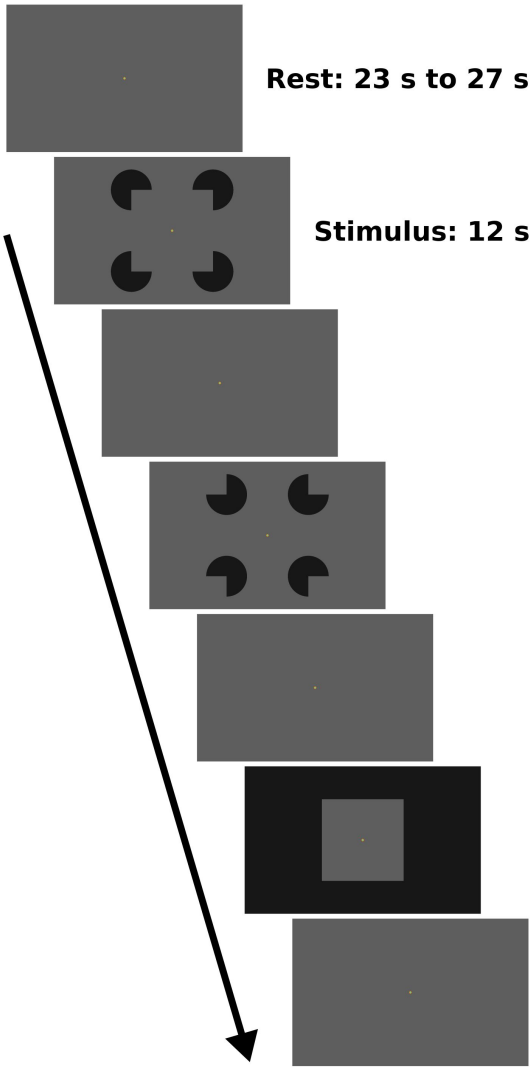

Figure 5.2: Experimental design. Stimuli were presented in pseudo-random order in a block design. Rest blocks lasted 23 s, 25 s, or 27 s (pseudo-random order), and stimulus blocks always lasted 12 s. There were three experimental conditions: (1) A configuration of inducer stimuli that resulted in the perception of an illusory surface, referred to as 'Kanizsa square' in the following; (2) the same stimuli were rotated so as not to induce an illusory surface, referred to as 'Kanizsa rotated'; (3) a light grey square on a dark background, referred to as 'real square'. Throughout the experiment, subjects were fixating a central dot. The luminance of the central area of the screen, around the fixation dot, was identical in all conditions.

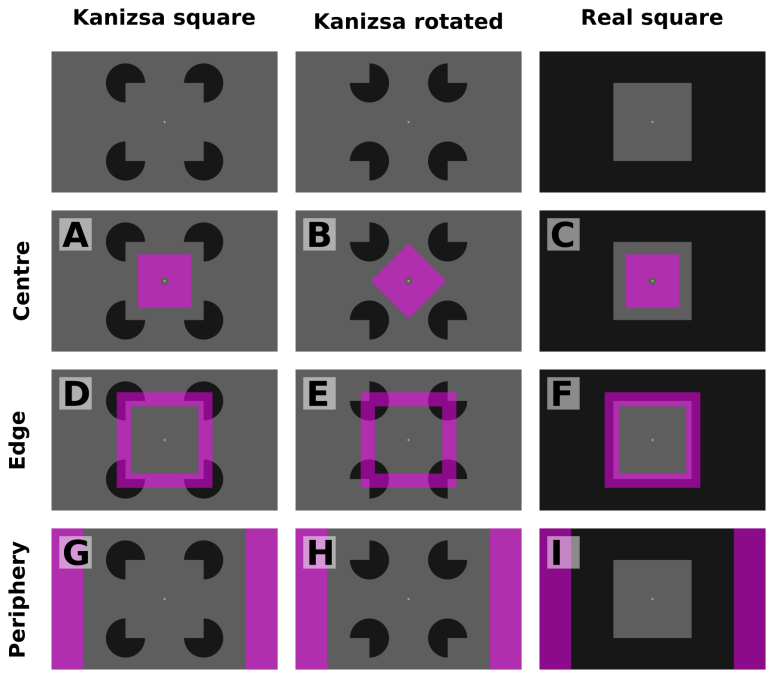

Figure 5.3: Regions of interest. Based on retinotopic maps, the visual space was divided into three regions of interest (ROIs), corresponding to the centre of the stimulus (**A**, **B**, **C**), its edges (**D**, **E**, **F**), and a control region at the periphery of the stimulated visual field (**G**, **H**, **I**). The central ROI (**A**, **B**, **C**) was a square with a side length of 4° visual angle, centred on the fixation dot. A central, circular region with a diameter of 0.5° visual angle was omitted from the central ROI in order to avoid the fixation dot (the fixation dot had a diameter of 0.18° visual angle). In the 'Kanizsa square' condition (**A**), the distance between the border of the central ROI and the induced illusory contours was 1° visual angle. In order to maintain a similar distance between the central ROI and the inducer stimuli in the 'Kanizsa rotated' condition (**B**), the central ROI was rotated by 45°, resulting in a diamond shape with the same area as in (**A**), and a minimum distance to the inducer stimulus of 0.75° visual angle. The edge ROI (**D**, **E**, **F**) covered the illusory border (**D**) or the real contour (**F**), spanning a width of 1° visual angle. Finally, the peripheral ROI (**G**, **H**, **I**) covered the left and right edges of the stimulated visual field. Its width was 2.3° visual angle. The minimum distance between the border of the peripheral ROI and the Kanizsa inducer stimuli was 1.5° visual angle (**G**, **H**), and its distance to the 'real square' (**I**) was 3° visual angle.

the experimental stimuli (Marquardt, 2019a; Marquardt, Gulban, & Schneider, 2018) and videos of the stimuli (Marquardt, 2019b) are publicly available.

5.3.2 Retinotopic mapping

In addition to the six functional runs of the main experiment, each subject completed three runs of retinotopic mapping, allowing us to delineate early visual areas V1, V2, and V3 on the cortical surface. Retinotopic mapping was performed following the population receptive field mapping framework (Dumoulin & Wandell, 2008), using a previously described implementation (see Chapter 3, Methods). In brief, stimuli used for population receptive field mapping were bars containing a black and white chequerboard pattern. There were 14 possible bar positions along the width of the screen (vertical orientation) and along the diagonals (for oblique orientations), and 9 along the height of the screen (horizontal orientation). Throughout the retinotopic mapping experiment, participants were instructed to fixate a central dot, surrounded by a thin fixation grid, and report changes in the colour of the fixation dot via button press. Targets were presented at random for 0.3 s, with a mean inter-trial interval of 15 s. One retinotopy run lasted ∼472 s (227 volumes).

5.3.3 Data acquisition & preprocessing

The experiments were conducted on a 7 T scanner (Siemens Medical Systems, Erlangen, Germany), using a 32-channel phased-array head coil (Nova Medical, Wilmington, MA, USA). Functional data were acquired with a 3D gradient echo (GE) EPI sequence (TR = 2.079 s, TE = 26 ms, nominal resolution 0.8 mm isotropic, 40 slices, coronal oblique slice orientation, phase encode direction right-to-left, phase partial Fourier 6/8; GRAPPA acceleration factor 3; Poser, Koopmans, Witzel, Wald, & Barth, 2010). A pair of five SE EPI images with opposite phase encoding (right-left and left-right) was obtained for distortion correction of the functional data (TR = 4.0 s, TE 41 = ms; position, orientation, and resolution same as for the GE sequence; Feinberg et al., 2010; Moeller et al., 2010; Setsompop et al., 2012). For anatomical contrast, a whole-brain T1 image was acquired using the MP2RAGE

sequence (Marques et al., 2010) with 0.7 mm isotropic voxels.

The analysis procedure has been described previously (Chapter 3). Data were motion corrected with SPM 12 (Friston, Williams, Howard, Frackowiak, & Turner, 1996), and distortion corrected using FSL TOPUP (Andersson, Skare, & Ashburner, 2003). A general linear model (GLM) with separate predictors for the three stimulus conditions and a nuisance predictor for the target events of the fixation task was fitted using FSL FEAT (Smith et al., 2004). Sustained and transient responses were modelled using two separate predictors for each of the three stimulus conditions. The predictor for the sustained response consisted of a 'boxcar function' over the entire stimulus duration, and the predictor for the transient response was based on a delta function at stimulus onset and offset. (Only one predictor was used for the short target events.) All predictors were convolved with a double-gamma function to model the temporal dynamics of the haemodynamic response. Before fitting the model, high-pass temporal filtering (cutoff = 40 s) was applied to the functional data as well as to the convolved design matrix. Percent signal change values (relative to the initial pre-stimulus baseline, i.e. the first 25 s of each run) were calculated based on parameter estimates of stimulus-induced activation from the GLM analysis, by applying a scaling that takes into account the height of the predictors in the design matrix (Mumford, 2007; Poldrack, Mumford, & Nichols, 2011). The resulting percent signal change values were used for the cortical depth profiles and the visual field projections.

Event-related timecourses were extracted from the fMRI time series, and were used to visualise the temporal dynamics of the response (see Figures 5.7 and 5.8) and for statistical tests (see section *Hypothesis testing*). The event-related timecourses were normalised to the three volumes preceding the stimulus onset, separately for each trial, before averaging.

Retinotopic maps were derived using the population receptive field mapping framework (Dumoulin & Wandell, 2008). The population receptive field analysis is implemented in a publicly available python package (pyprf Marquardt, Gulban, et al., 2018), using standard scientific python packages (Numpy, Scipy, Matplotlib, Cython; Behnel et al., 2011; Millman & Aivazis, 2011; Oliphant, 2007; van der Walt, Colbert, & Varoquaux, 2011). In order to facilitate reproducibility, the complete analysis pipeline (including preprocessing, statistical analysis, population

receptive field mapping, and depth sampling) is containerised within docker images (Halchenko & Hanke, 2012; Kaczmarzyk et al., 2017).

For quality assurance, in addition to visual inspection of the data, we calculated the spatial correlation between each functional volume and the mean EPI image of that session after motion correction and distortion correction (see Marquardt, Schneider, Gulban, Ivanov, & Uludağ, 2018 for details). Runs with a mean correlation coefficient below threshold ($r < 0.9$) would have been excluded from further analysis, but no runs were excluded based on this spatial correlation criterion. A central fixation task was used to ensure that subjects were awake and maintained fixation throughout the experiment. Runs with a target detection performance of below 95% would have been excluded from the analysis. Again, no runs were excluded based on this criterion (mean performance across subject = 99%, standard deviation = 0.9%).

5.3.4 Segmentation & cortical depth sampling

For each subject, the mean functional image was calculated after motion correction and distortion correction. The T1 image from the MP2RAGE sequence was registered to the mean functional image. Before registration, the mean functional image was upsampled (using trilinear interpolation) from a resolution of 0.8 mm isotropic to 0.4 mm isotropic, so as to avoid downsampling of the anatomical image during registration (the MP2RAGE images were acquired at a nominal resolution of 0.7 mm isotropic). We find that conducting tissue type segmentation in a high-resolution image space facilitates anatomically plausible, fine-grained segmentation (especially with respect to separating adjacent sulci). Using SPM12, the anatomical images were bias-field corrected and aligned to the mean functional image based on the normalized mutual information cost function. This initial registration was followed by boundary-based registration with FSL (Greve & Fischl, 2009; Jenkinson, Bannister, Brady, & Smith, 2002; Jenkinson & Smith, 2001).

An initial grey/white matter segmentation was obtained with FSL FAST based on the registered MP2RAGE images (Zhang, Brady, & Smith, 2001). Semi-automatic error correction of tissue-type classification errors was performed using the Segmentator software (Gulban & Schneider, 2018; Gulban, Schneider, Marquardt, Haast, & De Martino, 2018) and ITK-SNAP (Yushkevich et al., 2006).

Cortical depth profiles were created based on the grey and white matter tissue type segmentations, using volume-preserving parcellation implemented in CBS-tools (Bazin et al., 2007; Waehnert et al., 2014). The retinotopic maps, activation maps from the GLM analysis, and event-related fMRI time courses were up-sampled, so as to match the resolution of the tissue type segmentations (0.4 mm isotropic voxel size) using trilinear interpolation. Subsequently, the data were sampled along the cortical depth profiles using CBS-tools (Bazin et al., 2007; Waehnert et al., 2014), and projected onto an inflated surface mesh (Tosun et al., 2004).

5.3.5 ROI selection

Visual areas V1, V2, and V3 were delineated based on retinotopic maps that had been projected onto the inflated cortical surface. Specifically, the borders between early visual areas were identified from polar angle maps using Paraview (Ahrens, Geveci, & Law, 2005; Ayachit, 2015). Apart from the manual delineation of areal borders, all further region of interest (ROI) selection criteria were applied automatically. The final ROIs were defined based on three selection criteria; these selection criteria were applied at each location on the cortical surface for all cortical depth levels ('column') at once: First, only locations that showed a reliable response during the retinotopic mapping experiment were included, as defined by the coefficient of determination from the population receptive field analysis ($R2$>0.15, median across cortical depth levels). Second, in order to avoid sampling from regions affected by the presence of large veins, locations with low signal intensity in the mean EPI image were excluded (as a safeguard against slight imprecisions in the registration and/or segmentation). Locations were excluded if the image intensity of the mean EPI image was below 7000 at any cortical depth (compared to a mean image intensity of ∼10.000 for voxels within the brain.) Third, the ROIs passing the previous two criteria were subdivided into three distinct retinotopic regions, corresponding to the centre of the stimulus, its edges, and a control region at the periphery of the stimulated visual field (Figure 5.3).

The central ROI (Figure 5.3 A, B, C) was defined as a square with a side length of 4° visual angle, centred on the fixation dot. A circular sector with a diameter of 0.5° visual angle was omitted in order

to avoid the fixation dot (which had a diameter of 0.18° visual angle). The distance between the fixation dot and the edge of the inducer stimuli ('Pac-Man') was different for the 'Kanizsa square' condition compared to the 'Kanizsa rotated' condition, because the open sectors of the inducer discs (i.e. the 'mouth') was pointing inward or outward, respectively (Figure 5.3 A & B). In order to maintain a similar distance between the central ROI and the inducer stimuli in both conditions, while preserving the area of the ROI, the central ROI was rotated by 45°. Consequently, the minimum distance between the central ROI and the inducer stimuli was 1° visual angle in the 'Kanizsa square' condition, and 0.75° visual angle in the 'Kanizsa rotated' condition. (Please note that keeping the distance exactly the same would have required to change the size of the ROI.)

A second ROI was constructed along the edge of the illusory surface (Figure 5.3 D) and the real contour (Figure 5.3 F), covering a width of 1° visual angle. Finally, the left and right edges of the stimulated visual field were encompassed in a peripheral ROI, spanning a width of 2.3° visual angle (Figure 5.3 G, H, I). This peripheral ROI was separated from the Kanizsa inducer stimuli by 1.5° visual angle (Figure 5.3 G, H), and by 3° visual angle relative to the 'real square' (Figure 5.3 I). Standard scientific python packages were used for the selection of the ROIs, as well as for all subsequent analyses (Numpy, Scipy, Matplotlib; Hunter, 2007; Millman & Aivazis, 2011; Oliphant, 2007; van der Walt et al., 2011).

5.3.6 Draining effect spatial deconvolution

Ascending veins cause an unspecific fMRI signal increase towards the cortical surface, especially when using gradient-echo pulse sequences (Koopmans, Barth, Orzada, & Norris, 2011; Markuerkiaga, Barth, & Norris, 2016; Zhao, Wang, & Kim, 2004; see Uludağ & Blinder, 2018, for a review). We applied a spatial deconvolution to all cortical depth profiles in order to remove the effect of ascending veins, and the parameters for the deconvolution were derived based on simulations by Markuerkiaga, et al. (2016). The spatial deconvolution approach is described in detail in Chapter 2. In short, the estimated contribution of all deeper depth levels was iteratively subtracted from each cortical depth level, resulting in an estimate of the local signal change at each depth level (Marquardt,

Schneider, et al., 2018).

5.3.7 Visual field projection

Percent signal change estimates from the GLM analysis were projected into a model of the visual field, in order to visualise the spatial extent of activation relative to the stimuli. This visual field projection technique has been previously described in detail (Chapter 3, and Kok & de Lange, 2014). In summary, the percent signal change of each location on the cortical surface was projected into a 2D model of the visual space, based on the position and size of the population receptive field for that location. In addition to providing an intuitive visualisation of the stimulus-induced activation, this procedure allows to align the activation maps of all subjects in a reference frame that abstracts away from individual brain anatomy. (Our procedure for visual field projection is similar to that originally proposed by Kok et al. (2016), the difference being that no spatial smoothing was applied on the visual field projections in our implementation.)

5.3.8 Hypothesis testing

Differences in stimulus-induced activation were investigated by means of a linear mixed effects model, using a procedure similar to that described previously (Chapter 3, Methods). In brief, we tested for condition differences in the event-related timecourses and in the cortical depth profiles. In case of the event-related timecourses, the temporal autocorrelation structure was modelled as continuous autoregressive of order one. The time segment used for this analysis comprised eleven time points, starting at the first volume of the stimulus presentation (so as to capture the entire stimulus-induced response, including the late phase of the response at stimulus offset). In the separate analysis of the cortical depth profiles, the autocorrelation structure of cortical depth was likewise modelled as continuous AR(1). Tests were conducted by comparing a full model with a null model, from which the effect of interest had been removed, using a likelihood ratio tests. Models were created and compared using R and the nlme package (Pinheiro, Bates, DebRoy, Sarkar, & R Core Team, 2017; R Core Team, 2017).

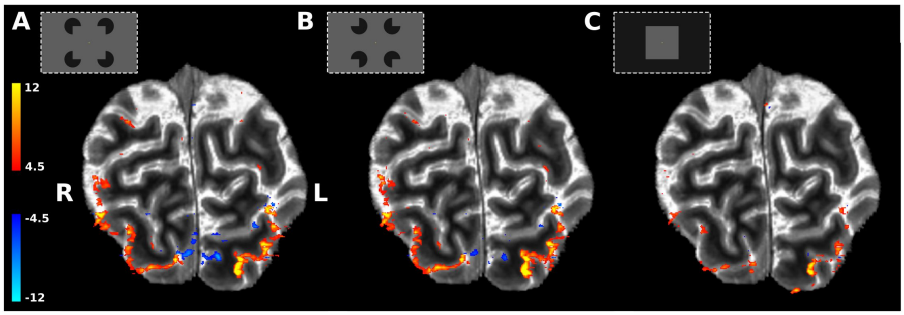

Figure 5.4: The visual stimuli caused positive and negative fMRI signal changes in visual cortex. Responses to (**A**) the illusory surface stimulus ('Kanizsa square'), (**B**) the control condition ('Kanizsa rotated'), and (**C**) the 'real surface' stimulus. Shown are the z-scores from the GLM contrast stimulus against rest, overlaid on a brain-masked T1 image, for a representative subject. Images are in radiological convention.

5.4 Results

5.4.1 Spatial response pattern

The experimental stimuli caused bilateral positive and negative responses in visual cortex (Figure 5.4). Activation maps were projected into a model of the visual field to visualise the spatial distribution of the response. In the following, the spatial pattern of the stimulus responses is described qualitatively; see subsequent sections (*Temporal response pattern* and *Cortical depth profiles*) for a statistical assessment.

A positive response was observed at the cortical representation of the inducer stimuli in the 'Kanizsa square' condition (illusory square; Figure 5.5 A & B), and in the 'Kanizsa rotated' condition (Figure 5.5 C & D). In the foveal area between the inducer stimuli, the response was slightly negative, both in the 'Kanizsa square' condition (Figure 5.5 A & B) and in the 'Kanizsa rotated' condition (Figure 5.5 C & D). The response to the figure background at the edges of the visual field was also negative (Figure 5.5 A–D). This response pattern was similar in V1 and V2, with the difference that the visual field projections are more sharp in V1, which is to be expected based on the smaller receptive field sizes in V1 compared with V2 (Harvey & Dumoulin, 2011). Unsurprisingly, the 'real square' caused a positive response at the location of its edges

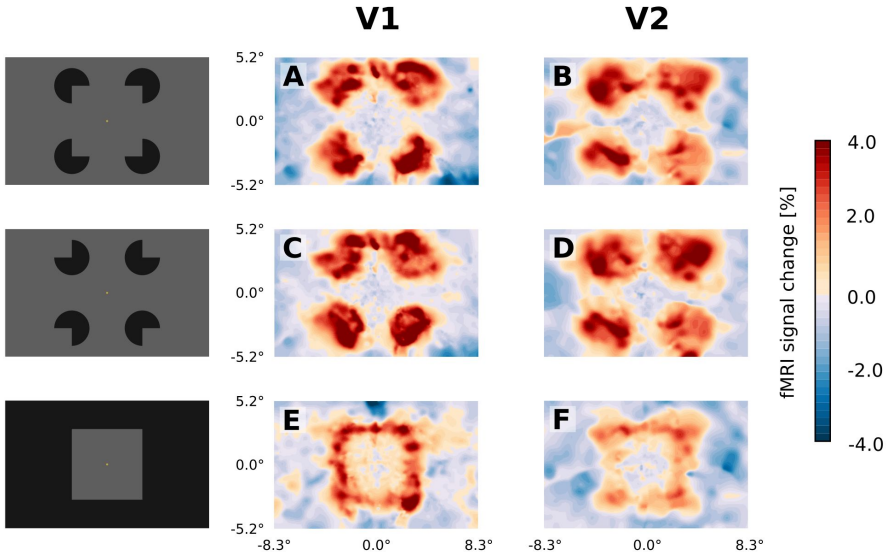

Figure 5.5: Visual field projections. Parameter estimates from the GLM analysis were projected into a model of the visual field based on a population receptive analysis. Both in the Kanizsa square condition (illusory square; **A**, **B**) and in the condition with rotated inducer stimuli (**C**, **D**), the inducer stimuli caused a positive response at their respective locations in the visual field. There is a tendency for a negative response both within the illusory surface (**A**, **B**) and generally across the entire background area (**A**, **B**, **C**, **D**). In the 'real square' condition (**E**, **F**), there is a positive response at the cortical representation of the edge of the stimulus. There is a slightly positive response at the centre of the square in V1 (but more data will be needed to establish this effect). In V2, the response to the dark background surrounding the square is negative (**F**).

(Figure 5.5 E & F). The response at the centre of the 'real square' was slightly positive in V1 (Figure 5.5 E), but this effect was small and more data will be needed to establish whether this is a reliable effect. In V2, the response amplitude at the edges of the 'real square' was lower than in V1, and there was no positive response inside the square (Figure 5.5 F). In V2, the response to the dark background surrounding the 'real square' was negative (Figure 5.5 F).

Differences in the response to a real vs. an illusory surface were visualised by subtracting the visual field projections of the 'Kanizsa square' condition from that of the 'real square' condition (Figure 5.6

A & B). As would be expected, the inducer stimuli ('Pac-Man') are clearly visible in the condition contrast as negative clusters, both in V1 and V2. Between the inducer stimuli, the area corresponding to the real and illusory contours shows pronounced positive clusters, indicating that real contours caused stronger activation than illusory contours in V1 (Figure 5.6 A). Interestingly, this preference for real contours is less pronounced in V2 (Figure 5.6 B). Conversely, the differential response at the interior of the real/illusory surface does not exhibit any obvious difference between V1 and V2. In both cases, the response was slightly stronger for the real surface.

No clear pattern emerges from contrasting the conditions 'Kanizsa square' and 'Kanizsa rotated' (Figure 5.6 C & D). In V1, the only clear structure is that of adjacent positive and negative clusters at the location of the inducer stimuli (indicating high accuracy of our intersubject visual field projection algorithm), most likely evoked by the local disparity in the area covered by the differentially oriented inducer stimuli in the two conditions (i.e. the 'mouths' of the four small 'Pac-Man' inducers). The more interesting aspect of the condition contrast between 'Kanizsa square' and 'Kanizsa rotated' concerns the central region between the inducers, corresponding to the difference between the presence of an illusory square, and its absence. No differential activity can be observed, neither in V1 nor in V2 (Figure 5.6 C & D).

5.4.2 Temporal response pattern

The temporal dynamics of the response to the three stimulus conditions were investigated by extracting event-related time courses, separately for the retinotopic regions corresponding to the centre and to the edge of the stimuli, and to the background (Figure 5.7). The response in the central ROI was much lower in amplitude than that in the other two ROIs (Figure 5.7). A tendency can be observed towards a slightly positive response at the centre of the 'real square' in V1 (Figure 5.7 A, blue line), and a small negative central response in the Kanizsa square condition (Figure 5.7 A, orange line). A model comparison revealed that the three experimental stimuli differentially activated brain areas V1 and V2 at the cortical representation of the stimulus centre (likelihood ratio (df) of time by condition interaction 14.7 (2), p=0.0006).

At the stimulus edges, the response was sustained and positive in

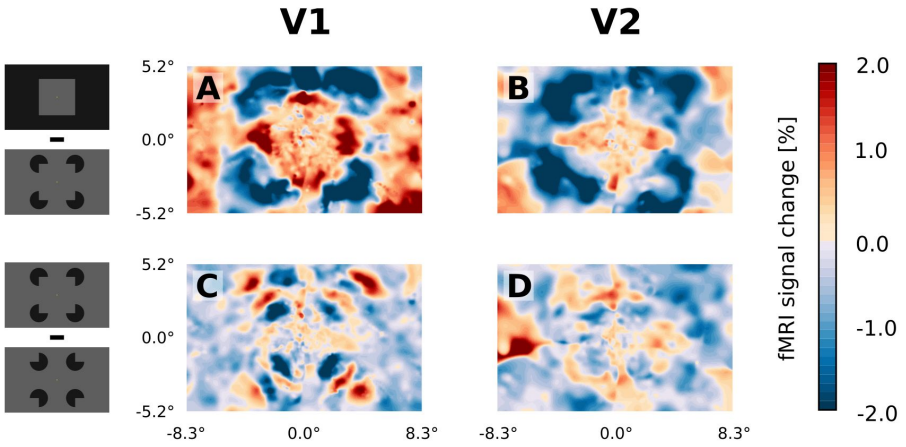

Figure 5.6: Visual field projections of condition contrasts. (**A** & **B**) Difference of stimulus-induced response to the 'real square' minus the illusory 'Kanizsa square' for V1 (**A**) and V2 (**B**). Unsurprisingly, the locations of the inducer stimuli ('Pac-Man') show less activation in the 'real square' condition than in the 'Kanizsa square' condition. In V1 (**A**), real contours cause much stronger activation than illusory contours, as evidenced by the four strongly positive (red) regions between the inducer stimuli. Interestingly, this preference for real contours is weaker in V2 (**B**). There is no obvious difference in the response to the inducer stimuli between V1 and V2. Both in V1 and in V2 (**A** & **B**), the response to the interior of the surface (at the centre of the visual field) is stronger for the 'real square' than for the 'Kanizsa square'. (**C** & **D**) Differences between response to 'Kanizsa square' and 'Kanizsa rotated'. In V1 (**C**), a pattern of positive and negative clusters at the location of the inducer stimuli can be observed, probably corresponding to the spatial difference between the inducer stimuli in the two conditions. In particular, the location of the left-out segments of the inducer discs (the 'mouth') in the 'Kanizsa square' condition is visible as a region of negative activation (four central negative clusters). These negative clusters are flanked by more peripheral positive clusters, at the location of the left-out inducer segments ('mouths') in the 'Kanizsa roated' condition. Apart from these clusters of activity that can be attributed to the inducer stimuli, no coherent response pattern can de discerned at the location of the illusory contours, or at the interior of the illusory surface.

V1 and V2 (Figure 5.7 C & D). In the visual field projections, a tendency towards a stronger response amplitude for real contours (as opposed to illusory contours) can be observed in V1 (Figure 5.6 A). A corresponding trend is also visible in the event-related timecourses (Figure 5.7 C), but this trend towards a preference for real contours was not statistically significant (likelihood ratio (df) of ROI by condition interaction ∼0.0 (2), $p \approx 1.0$).

The dark background in the 'real square' condition evoked a transient positive response at stimulus onset and offset in the peripheral ROI in V1 (Figure 5.7 E, blue line). A negative undershoot followed the transient onset and offset responses. In V2, the response to the background of the 'real square' was negative (Figure 5.7 F, blue line). This negative response was very slow, only reaching its minimum at the end of the stimulus block. Contrary to the 'real square' condition, there was no change in retinotopic input to the peripheral ROI in the 'Kanizsa square' and 'Kanizsa rotated' conditions. Still, both the 'Kanizsa square' and 'Kanizsa rotated' conditions showed a negative response at the cortical representation of the background (Figure 5.7 E & F, orange & green lines), even though the border of the respective ROI and the outer edge of the inducer stimuli were separated by a distance of 1.5° visual angle. The differential activation of the peripheral ROI by the three stimulus conditions was statistically significant (likelihood ratio (df) of time by condition interaction 16.2 (2), p=0.0003). Interestingly, the responses at the stimulus edge was faster than that at the stimulus centre or at the background (Figure 5.8), in line with the pattern observed in our previous experiment (Figure 5.1).

5.4.3 Cortical depth profiles

The retinotopic input to the central ROI (Figure 5.3 A–C) was constant throughout all experimental conditions, whereas the perceptual quality of the respective area of the visual field differed considerably. The central ROI represents the foreground stimulus in the 'real square' condition, the illusory square in the 'Kanizsa square' condition, and the figure background in the 'Kanizsa rotated' condition. Yet, due to the constant bottom-up input, differences in activity within the central ROI are presumably due to top-down feedback effects. Figure 5.9 shows the cortical depth profiles of condition differences between all three possible

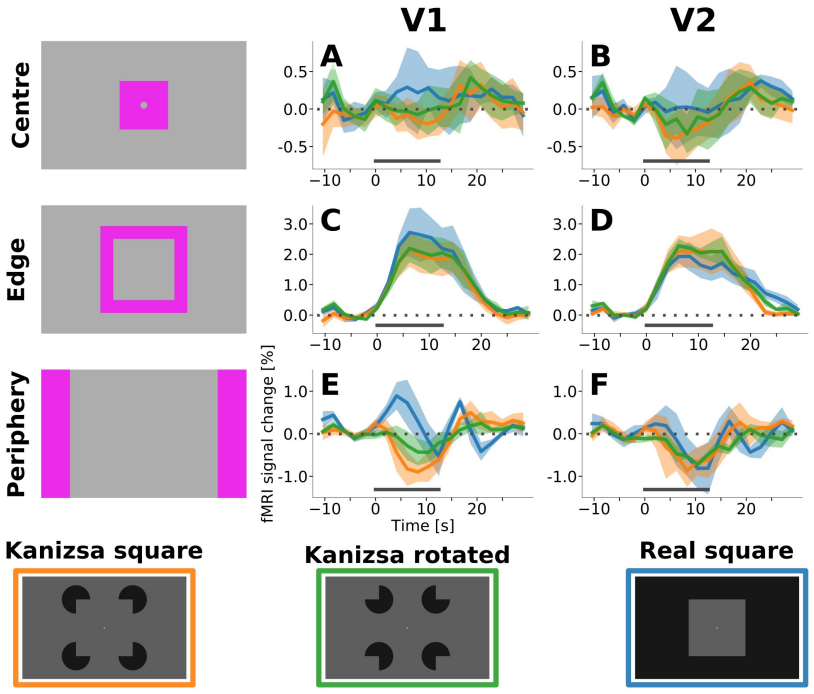

Figure 5.7: Event-related time courses. (**A** & **B**) There is a tendency for a slightly positive response to the centre of the 'real square' in V1, and a negative central response in the Kanizsa conditions, but clearly more data will be needed in order to establish the nature of this effect. The response to the stimulus edges is positive and sustained in V1 and V2 (**C** & **D**). Interestingly, there is a transient positive response to the dark background in the 'real square' condition at stimulus onset and offset in V1 (**E**, blue line). Both the onset and the offset response are followed by a negative undershoot. In V2, the shape of the response to the 'real square' is similar, but overall more negative (**F**, blue line). More data will be needed in order to establish whether the response in V2 is a weak positive transient response followed by a strong negative undershoot, or a delayed negative response. In V1 and V2, the cortical representation of the background responds negatively to the 'Kanizsa square' and 'Kanizsa rotated' conditions (**E** & **F**, orange and green lines), even though there is a distance of 1.5° visual angle between the border of the peripheral ROI and the outer edge of the inducer stimuli. Timecourses were normalised to be pre-stimulus baseline of each trial. The shading represents the standard error of the mean (across subjects), and the horizontal grey bar marks the duration of the stimulus. Please note that the scale of the y-axes is identical within rows (**A** & **B**, **C** & **D**, **E** & **F**), but differs between rows.

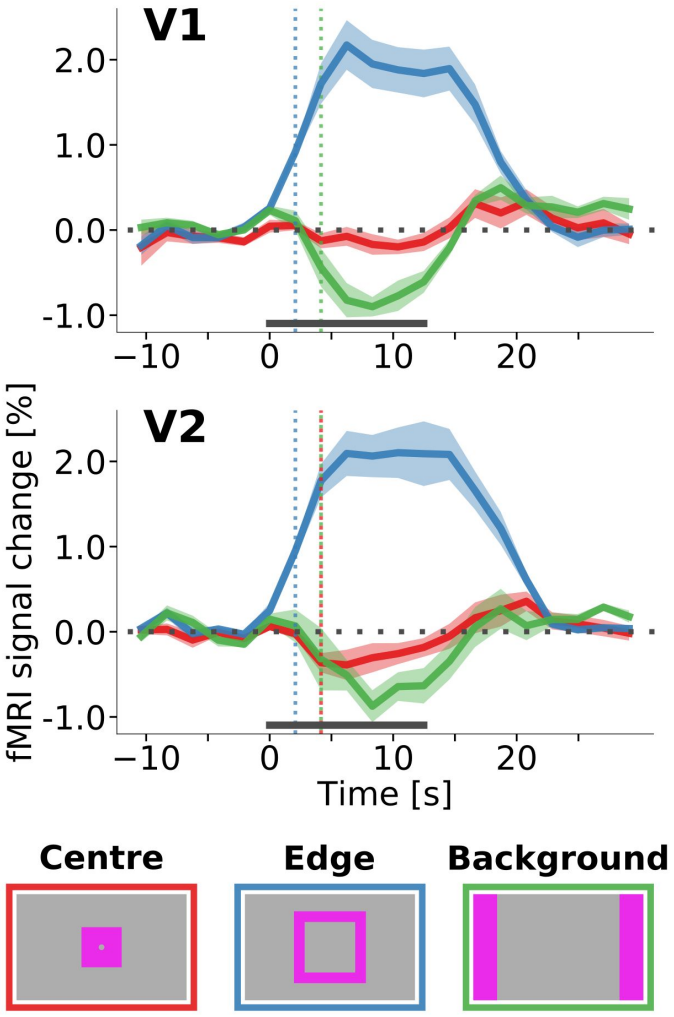

Figure 5.8: Onset time differences between regions of interest corresponding to the cortical retinotopic representation of the stimulus centre (red line), the stimulus edge (blue line), and the peripheral background (green line), for the 'Kanizsa square' stimulus. Onset time was defined as the time point after stimulus onset at which the absolute response exceeded 0.3% signal amplitude (vertical dotted lines). Data are the same as in Figure 5.7 (orange line), just arranged differently for visualisation purposes. Horizontal grey bar indicates duration of the stimulus. Shading represents standard error of the mean (across subjects).

condition contrasts for the central ROI. Especially in V1, there was a trend towards a stronger response to the 'real square' compared to either of the Kanizsa conditions (Figure 5.9 A)

The fact that there was no differential response to the 'Kanizsa square' as compared to the 'Kanizsa rotated' stimulus is reflected in a flat cortical depth profile with zero amplitude, both in V1 and in V2 (Figure 5.9 A & B). A comparison of the activation profiles of the 'Kanizsa' and 'Kanizsa rotated' conditions (omitting the 'real square' condition) confirms that there was no statistically significant differences between these two conditions (likelihood ratio (df) of condition effect 0.18 (1), p=0.67).

The differential contrast between the 'real square' condition and either of the Kanizsa conditions results in cortical depth profiles of very similar shape and amplitude, with a peak at superficial cortical depths. In other words, at superficial cortical depths there is a trend towards a preference for the 'real surface' (as compared to either the illusory surface or the background between the inducers in the 'Kanizsa rotated' control condition), but this effect was not statistically significant (likelihood ratio (df) of condition by depth interaction 1.9 (2), p=0.39).

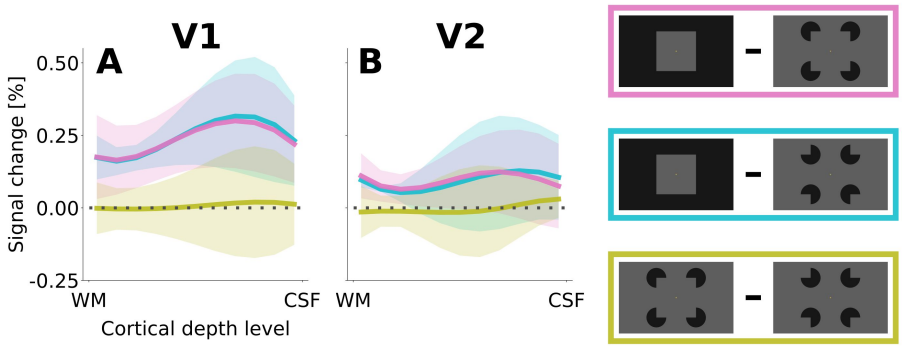

Figure 5.9: Cortical depth profiles of condition differences for the central region of interest. There are three possible comparisons between conditions: (1) 'Real square' vs. 'Kanizsa square' (purple line), (2) 'real square' vs. 'Kanizsa rotated' (blue line), and (3) 'Kanizsa square' vs. 'Kanizsa rotated' (yellow line). Because the cortical depth profiles are sampled from the central part of the visual field (see Figure 5.3 A, B, C), the retinotopic input is identical for all three stimulus conditions (uniform light grey). However, the perceptual quality of the visual field representations differs (uniform foreground stimulus in the 'real square' condition, illusory surface in the 'Kanizsa square' condition, uniform background in the 'Kanizsa rotated' condition). In V1 and V2, the response to 'real square' is positive compared to the illusory square (purple line) and to the background (blue line). Interestingly, there is no response difference between the illusory surface and the background (yellow line). Spatial deconvolution for removal of signal spread due to draining veins was applied to the individual condition depth profiles separately for each subject, before contrasting conditions. Shading represents standard error of the mean (across subjects).

5.5 Discussion

In this study, we have investigated the processing of real and illusory surfaces in early visual cortex with high-resolution fMRI. In a previous study (Chapter 3), we observed a strongly negative response to the interior of a luminance-defined surface stimulus, if the stimulus was presented on a texture background. This negative response was sustained and delayed, and was accompanied by an earlier, transient, positive response at the edge of the stimulus (Figure 5.1). The experimental design of the present study was chosen to enable comparison both with earlier studies on the processing of illusory surfaces (2016; Kok & de Lange, 2014), and with our previous results on the processing of real surfaces (Chapter 3). In particular, the 'Kanizsa square' condition was, with modifications, adapted from Kok et al. (2014).

5.5.1 Response to illusory surfaces

In earlier fMRI studies, Kok et al. (Kok et al., 2016; 2014) presented stimuli that induced the perception of an illusory triangle, and a control condition with rotated inducer stimuli in which no illusory shape was perceived. When contrasting the illusory condition with the control condition, they found a positive response to the illusory stimulus, and a negative response to the inducer stimuli. In other words, the response to the illusory surface was stronger than that to the background when no illusory figure was perceived, and the response to the inducer stimuli was (relatively) suppressed when they formed an illusory figure. Our present findings did not replicate any of these observations. We did find systematic positive and negative clusters of relative activation at the location of the inducer stimuli, depending on whether they were arranged so as to form an illusory stimulus or not (Figure 5.6 C). However, this relative activation seems to be a consequence of the difference in retinotopic area covered by the inducer stimuli, depending on their orientation. Moreover, we found no enhanced activity at the location of the illusory surface, or at its contour (Figure 5.6 C). On the contrary, we observed a slight trend towards a negative response at the retinotopic representation of the illusory surface relative to rest (Figure 5.7 A & B, orange lines). The decisive condition contrast between the 'Kanizsa square' condition and the 'Kanizsa rotated' control condition results in

flat cortical depth profile with approximately zero amplitude in V1 and V2 (Figure 5.9, yellow lines), indicating that there was no activation specific to the processing of an illusory surface.

Why do our results differ from those reported by Kok et al. (2016; 2014)? The stimuli were matched in luminance and similar in size. The spatial arrangement of the stimuli was different; in the earlier study the inducer stimuli were arranged so as to form an illusory triangle, whereas in the present study the illusory stimulus was a square. However, it does not seem plausible that the processing of illusory stimuli should differ fundamentally for simple geometric shapes. Rather, the discrepancy may be explained by differences in the temporal frequency of the stimulus presentation. In the present study, stimuli were presented at a low temporal frequency (stimulus blocks had a duration of 12.4 s, during which the stimuli were constant). The long stimulus duration enabled us to probe the temporal evolution of the response (Figure 5.7), and permits comparisons with our previous results (Chapter 3). In contrast, Kok et al. (2016; 2014) presented their stimuli at a much higher temporal frequency; the Kanizsa inducer stimuli were alternated with black discs (i.e. the 'mouth' of the inducer stimulus was filled) at a rate of 1 Hz. Thus, it is possible that the response to an illusory surface (and possibly to its contour) is only evoked at stimulus onset (and possibly offset), but that illusory surfaces do not cause any sustained response in early visual cortex. However, we also did not observe a positive response to the illusory surface at stimulus onset. On the contrary, there is a tendency for a negative response to the illusory surface (relative to rest), especially in V2 (Figure 5.7 B).

Alternatively, the discrepancy between the results presented by Kok et al. (2016; 2014) and our data may in part be explained by a suppression of the background. We constructed a peripheral region of interest, comprising the left and right edges of the stimulated visual field, to investigate the response to the background. This peripheral region of interest was chosen so as to maximise the retinotopic distance to the inducer stimuli, thereby reducing the risk of confounding from the central stimulus response. Both in the illusory 'Kanizsa square' condition and in the 'Kanizsa rotated' condition, there was a negative response in the peripheral region of interest – in other words, the background was suppressed (Figure 5.7 E & F, orange and green lines). In the 'Kanizsa rotated' condition, the central area between the inducer stimuli

perceptually belongs to the background (Figure 5.3 B). Contrasting the illusory surface/contour condition with a control condition in which background suppression occurs could give the impression of a positive response to the illusory stimulus, even if there was no positive response relative to rest. However, at least in V1, we found no evidence for background suppression in the central region of interest in the 'Kanizsa rotated' condition (Figure 5.7 A, green line), and a slight trend towards a negative illusory surface response (Figure 5.7 A, orange line), rendering this explanation less likely.

Kok et al. found the effect of the illusory surface and/or contour to be maximal at deep cortical layers, where an fMRI signal change of approximately 0.13% was observed when an illusory stimulus was perceived, and circa 0.02% signal change in the control condition without an illusory contour (2016 their Figure 2A). In contrast, the response to the inducer stimuli was maximal at superficial layers, with a signal change of about 0.95% if the inducer stimuli formed an illusory figure, and circa 1.05% if the inducers were rotated so as not to create an illusory figure (Kok et al., 2016 their Figure 3A). The discrepancy with our results is striking; our results do not only differ with respect to the sign of the response (i.e., a negative response to the illusory surface), but also in magnitude. Specifically, we observed a signal change of about –0.20% in V1, and circa –0.40% in V2, at the cortical representation of the illusory surface (Figure 5.7 A & B, orange line). Moreover, in the edge ROI, which comprises the inducer stimuli (Figure 5.3 D), we observed a signal amplitude of about 2.0% in V1 and in V2 (Figure 5.7 C & D, orange line). Finally, we observed a background suppression of almost 1.0% in V1 and V2 (Figure 5.7 E & F, orange line). In other words, the background suppression in our data, which occurred in the absence of any change in local bottom-up stimulus input, had an absolute amplitude similar to the response to the flickering inducer stimuli in the study by Kok et al. (2016).

Differences in the analysis may account for some, but not all of the differences between the reports by Kok et al. (2016; 2014) and the present results. With respect to the cortical depth profiles, Kok et al. (2016) have reciprocally regressed out the contribution of other cortical depth levels, whereas we have applied a spatial deconvolution to account for the effect of draining veins. Whereas this difference in methodology may explain some of the difference in the response amplitude, it seems

unlikely that the sign of the response would change in either approach. Regarding the visual field projections, Kok et al. (2016; 2014) have applied spatial smoothing, which we did not. Moreover, Kok et al. (2016; 2014) presented stimuli in many different spatial arrangements, and averaged over stimulus configurations after rotating the visual field projections into a common reference frame. In contrast, we only presented stimuli in two spatial arrangements, with the inducer stimuli either oriented so as to create the percept of an illusory square, or rotated outwards. We assume that these variations in experimental design and analysis may explain why the visual field projections reported by Kok et al. are relatively blurred (compare their Figure 1C with our Figure 5.5; Kok et al., 2016). However, these methodological difference cannot account for the differences in the direction of the response (positive vs. negative), and the presence or absence of background suppression. To the best of our knowledge, Kok et al. (2016; 2014) have not reported event-related timecourses, so that differences in the temporal evolution of the response cannot be assessed.

In summary, we observed a trend towards a negative response to the interior of a Kanizsa-type illusory surface relative to rest, and a suppression of the background. The discrepancy between our preliminary observations and earlier reports (Kok et al., 2016; Kok & de Lange, 2014) is remarkable, and although the difference in the presentation rate of the stimuli may play a role, we see no completely satisfactory explanation for the incongruence. We have conducted a follow-up experiment (in preparation), in which we presented a Kanizsa-type illusory stimulus, and a control condition with rotated inducer stimuli. The stimuli were positioned away from the fixation dot, and were presented in two different temporal conditions; statically (as in the present study) and flickering, at a temporal frequency of 1 Hz (and Kok et al., 2016; as in Kok & de Lange, 2014). We hope that this additional experiment will shed light on the presently inexplicable, considerable discrepancy between the present study and the reports by Kok et al. (2016; 2014).

5.5.2 Brightness induction

The interior of the real surface evoked a slightly positive response relative to the interior of the illusory surface (Figure 5.6 A & B, Figure 5.7 A & B). The preference for the interior of the real surface over the

illusory surface tended to be strongest at superficial cortical depth (even though this effect was not statistically significant; Figure 5.9, pink lines). However, contrasting the response to the real square with that of the 'Kanizsa rotated' control condition results in an almost identical depth profile, suggesting that this effect was not specific to the illusory surface (Figure 5.9, blue line). Moreover, the contrast between the illusory surface and the rotated inducer condition results in a flat cortical depth profile with approximately zero amplitude (Figure 5.9, yellow line). Thus, the differential effects in the cortical depth profiles are probably driven by the 'real square' condition. The effect may be explained by brightness induction, a phenomenon in which the perceived brightness of a surface is modulated by the luminance of the surround. Brightness induction has been shown to affect neuronal activity in primary visual cortex in cats (Rossi & Paradiso, 1999; Rossi, Rittenhouse, & Paradiso, 1996) and humans (Pereverzeva & Murray, 2008; van de Ven, Jans, Goebel, & De Weerd, 2012). It is possible that the slightly positive response to the 'real square' in V1 (Figure 5.7 A, blue line) was driven by brightness induction rather than by enhancement of the square as a foreground figure. Interestingly, there was no such trend in V2 (Figure 5.7 B, blue line). The possibility of brightness induction limits the suitability of the 'real square' condition as a control condition for comparison with an illusory surface.

5.5.3 Background suppression

In all stimulus conditions, the peripheral section of the visual field obtains background status at stimulus onset. In V2, there was a slowly evolving, negative peripheral response under all stimulus conditions (Figure 5.7 F, a similar phenomenon was also observed in a previous experiment, see Figure 3.8 F). Remarkably, this background suppression occurred irrespective of whether there was a local change in retinotopic input (in the 'real square' condition, Figure 5.7 F, blue line) or not (in all other conditions, Figure 5.7 F, orange and green lines). The background suppression in V2 had an amplitude of about one per cent, regardless of stimulus type, background condition, or change in local retinotopic input (Figure 5.7 F, see also Figure 3.8 F). Thus, V2 exhibits strong background suppression, possibly driven by top-down effects.

The results with respect to background suppression are less clear

for V1. In the present study, V1 only exhibited background suppression when there was no change in local retinotopic input (i.e. in the 'Kanizsa square' and 'Kanizsa rotated' conditions, Figure 5.7 E, orange & green lines). Conversely, in the 'real square' condition (in which the local retinotopic input changed from grey to black), there was a transient, positive response at stimulus onset and offset in V1. This transient, positive response might be driven by the local luminance change, which would be in accordance with previous reports (Haynes et al., 2004). However, the picture is complicated by a previous experiment, where background suppression in V1 was only clearly observed if the background consisted of a texture pattern (Figure 3.8 C, green & blue lines). When the stimuli were presented on a uniform background, V1 showed a trend towards a positive, transient peripheral response (Figure 3.8 C, orange & red lines), similar to the activation in the 'real square' condition in the present experiment (Figure 5.7 E, blue line). This suggests that the transient, positive background response in V1 was not related to a change in local retinotopic input (of which there was none in the previous experiment), but that it specifically occurs when a bright stimulus is presented on a dark, uniform background. If the background is bright relative to the stimuli (as in the Kanizsa conditions, Figure 5.7 E, orange & green lines), or if the background contains a texture pattern (Figure 3.8 C, green & blue lines), V1 responds with background suppression – as does V2 under all conditions.

It may be worth noting that the average global luminance (and the corresponding pupillary response) does not appear to be a relevant factor, because background suppression was observed under a decrease in global luminance (Kanizsa conditions, Figure 5.7 E, orange & green lines), and under an increase in global luminance (previous experiment, Figure 3.8 C, green & blue lines). Furthermore, a transient, positive response was observed under a concurrent local and global decrease in luminance ('real square' condition, Figure 5.7 E, blue line), and under an increase in global luminance (previous experiment, Figure 3.8 C, orange & red lines).

Interestingly, an effect of contrast polarity was also observed for the response to surface interiors in monkey studies, where the temporal shape and the amplitude of the response was found to depend on whether the surface was brighter or darker than the background (Kinoshita & Komatsu, 2001; Zurawel et al., 2014). Laminar recordings revealed that

the preference for luminance decrements probably arises at the level of V1 (Xing, Yeh, & Shapley, 2010; Yeh, Xing, & Shapley, 2009). Our preliminary finding of a differential *background response* depending on contrast polarity may add to these previous reports on a differential response to the *stimulus* itself. Psychophysical evidence on a lower detection threshold for luminance decrements as compared to increments suggests that effects of contrast polarity on neuronal activity are functionally significant (Bowen, Pokorny, & Smith, 1989; Dannemiller & Stephens, 2001; Short, 1966; Whittle, 1986).

In summary, V2 was found to exhibit strong and consistent background suppression under a variety of stimulus conditions. For V1, background suppression and a transient, positive background response can be observed. The brightness polarity of the background/stimulus, and whether the background is uniform or contains a texture pattern may play a role (see Chapter 3). Since these observations are based on a small sample (n=4 for the present study, n=2 for the previous control experiment with texture/uniform background, Chapter 3), any conclusions are preliminary, and further data will be needed.

5.5.4 Temporal delay

Invasive animal experiments typically display stimuli at a relatively high temporal frequency (Kinoshita & Komatsu, 2001; MacEvoy et al., 1998, 1998). A study on filling-in presented a uniform surface on a dynamic background, and measured a response that evolved over a time period of up to 12 seconds (De Weerd, Gattass, Desimone, & Ungerleider, 1995). Although direct comparisons are difficult due to the complexity of the haemodynamic response, we observed a negative surface response with a delay of more than two seconds (Figure 5.1 C, Figure 3.8, A & D), and a trend towards background suppression that slowly built up over approximately 8 to 12 seconds (Figure 5.7, E & F, Figure 3.8, C & F). Such high response latencies are exceptional even for the slow haemodynamic response. Although speculative, there is a possibility that the cortical processing of surfaces involves a slow component that is not revealed in experimental designs with stimulus durations of less than two seconds.

5.5.5 Limitations & outlook

The results from this ongoing research project are preliminary, and are to be interpreted with caution. In conclusion, we found no activation specific to the processing of an illusory surface in V1 and V2 in comparison with a control condition. Instead, we observed a slight trend towards a negative response at the retinotopic representation of the illusory surface relative to rest. However, this response was not specific to the illusory condition and may have been caused by background suppression. Strong background suppression occurred in peripheral regions of V2 that did not receive direct bottom-up stimulus input, under a variety of stimulus conditions. In contrast, V1 exhibited background suppression or a transient, positive background response, depending on the experimental condition. Finally, there was some evidence for brightness induction in V1, but not in V2.

Assuming that the trends visible at present will be confirmed by additional, already acquired data, several open questions remain. (1) Why did we not observe a positive response to the illusory surface, as reported by Kok et al. (2016; 2014), but a trend towards a negative response (relative to rest)? At present, the difference in the temporal frequency of the stimuli presents itself as a possible explanation. (2) Which factors determine whether V1 shows background suppression, or a positive, transient response to the background? (3) Why is the background suppression so slow? Further research will be needed to address these questions.

5.6 References

Ahrens, J., Geveci, B., & Law, C. (2005). ParaView: An End-User Tool for Large-Data Visualization. In C. D. Hansen & C. R. Johnson, *The Visualization Handbook* (pp. 717–731). Burlington: Elsevier Butterworth–Heinemann.

Albrecht, D. G., & Hamilton, D. B. (1982). Striate cortex of monkey and cat: contrast response function. *Journal of Neurophysiology*, 48(1), 217–237.

Andersson, J. L. R., Skare, S., & Ashburner, J. (2003). How to correct susceptibility distortions in spin-echo echo-planar images: application to diffusion tensor imaging. *NeuroImage*, 20(2), 870–888. https://doi.org/10.1016/S1053-8119(03)00336-7

Ayachit, U. (2015). The ParaView guide: updated for ParaView version 4.3

(Full color version; L. Avila, Ed.). Los Alamos: Kitware.

Bazin, P.-L., Cuzzocreo, J. L., Yassa, M. A., Gandler, W., McAuliffe, M. J., Bassett, S. S., & Pham, D. L. (2007). Volumetric neuroimage analysis extensions for the MIPAV software package. *Journal of Neuroscience Methods*, 165(1), 111–121. https://doi.org/10.1016/j.jneumeth.2007.05.024

Behnel, S., Bradshaw, R., Citro, C., Dalcin, L., Seljebotn, D. S., & Smith, K. (2011). Cython: The Best of Both Worlds. *Computing in Science & Engineering*, 13(2), 31–39. https://doi.org/10.1109/MCSE.2010.118

Bowen, R. W., Pokorny, J., & Smith, V. C. (1989). Sawtooth contrast sensitivity: decrements have the edge. *Vision Research*, 29(11), 1501–1509.

Dannemiller, J. L., & Stephens, B. R. (2001). Asymmetries in contrast polarity processing in young human infants. *Journal of Vision*, 1(2), 112–125. https://doi.org/10.1167/1.2.5

De Weerd, P., Gattass, R., Desimone, R., & Ungerleider, L. G. (1995). Responses of cells in monkey visual cortex during perceptual filling-in of an artificial scotoma. *Nature*, 377(6551), 731–734. https://doi.org/10.1038/377731a0

Dumoulin, S. O., & Wandell, B. A. (2008). Population receptive field estimates in human visual cortex. *NeuroImage*, 39(2), 647–660. https://doi.org/10.1016/j.neuroimage.2007.09.034

Feinberg, D. A., Moeller, S., Smith, S. M., Auerbach, E., Ramanna, S., Gunther, M., ... Yacoub, E. (2010). Multiplexed echo planar imaging for subsecond whole brain FMRI and fast diffusion imaging. *PloS One*, 5(12), e15710. https://doi.org/10.1371/journal.pone.0015710

Friston, K. J., Williams, S., Howard, R., Frackowiak, R. S., & Turner, R. (1996). Movement-related effects in fMRI time-series. *Magnetic Resonance in Medicine*, 35(3), 346–355.

Greve, D. N., & Fischl, B. (2009). Accurate and robust brain image alignment using boundary-based registration. *NeuroImage*, 48(1), 63–72. https://doi.org/10.1016/j.neuroimage.2009.06.060

Gulban, O. F., & Schneider, M. (2018, June 7). Segmentator V1.5.2. https://doi.org/10.5281/zenodo.595780

Gulban, O. F., Schneider, M., Marquardt, I., Haast, R. A. M., & De Martino, F. (2018). A scalable method to improve gray matter segmentation at ultra high field MRI. *PloS One*, 13(6), e0198335. https://doi.org/10.1371/journal.pone.0198335

Halchenko, Y. O., & Hanke, M. (2012). Open is Not Enough. Let's Take the Next Step: An Integrated, Community-Driven Computing Platform for Neuroscience. *Frontiers in Neuroinformatics*, 6, 22. https://doi.org/10.3389/fninf.2012.00022

Harvey, B. M., & Dumoulin, S. O. (2011). The relationship between cortical magnification factor and population receptive field size in human visual

cortex: constancies in cortical architecture. *The Journal of Neuroscience: The Official Journal of the Society for Neuroscience*, 31(38), 13604–13612. https://doi.org/10.1523/JNEUROSCI.2572-11.2011

Haynes, J.-D., Lotto, R. B., & Rees, G. (2004). Responses of human visual cortex to uniform surfaces. *Proceedings of the National Academy of Sciences of the United States of America*, 101(12), 4286–4291. https://doi.org/10.1073/pnas.0307948101

Huang, X., & Paradiso, M. A. (2008). V1 response timing and surface filling-in. *Journal of Neurophysiology*, 100(1), 539–547. https://doi.org/10.1152/jn.00997.2007

Hubel, D. H., & Wiesel, T. N. (1968). Receptive fields and functional architecture of monkey striate cortex. *The Journal of Physiology*, 195(1), 215–243. https://doi.org/10.1113/jphysiol.1968.sp008455

Hunter, J. D. (2007). Matplotlib: A 2D Graphics Environment. *Computing in Science & Engineering*, 9(3), 90–95. https://doi.org/10.1109/MCSE.2007.55

Jenkinson, M., Bannister, P., Brady, M., & Smith, S. (2002). Improved optimization for the robust and accurate linear registration and motion correction of brain images. *NeuroImage*, 17(2), 825–841.

Jenkinson, M., & Smith, S. (2001). A global optimisation method for robust affine registration of brain images. *Medical Image Analysis*, 5(2), 143–156.

Kaczmarzyk, J., Goncalves, M., Halchenko, Y., Mitchell, R., Nielson, D., Jarecka, D., ... Rokem, A. (2017, November 18). Kaczmarj/Neurodocker: Version 0.3.2. https://doi.org/10.5281/zenodo.1058998

Kastner, S., De Weerd, P., & Ungerleider, L. G. (2000). Texture segregation in the human visual cortex: A functional MRI study. *Journal of Neurophysiology*, 83(4), 2453–2457. https://doi.org/10.1152/jn.2000.83.4.2453

Kinoshita, M., & Komatsu, H. (2001). Neural representation of the luminance and brightness of a uniform surface in the macaque primary visual cortex. *Journal of Neurophysiology*, 86(5), 2559–2570. https://doi.org/10.1152/jn.2001.86.5.2559

Kok, P., Bains, L. J., van Mourik, T., Norris, D. G., & de Lange, F. P. (2016). Selective Activation of the Deep Layers of the Human Primary Visual Cortex by Top-Down Feedback. *Current Biology*, 26(3), 371–376. https://doi.org/10.1016/j.cub.2015.12.038

Kok, P., & de Lange, F. P. (2014). Shape perception simultaneously up- and downregulates neural activity in the primary visual cortex. *Current Biology*: CB, 24(13), 1531–1535. https://doi.org/10.1016/j.cub.2014.05.042

Koopmans, P. J., Barth, M., Orzada, S., & Norris, D. G. (2011). Multi-echo fMRI of the cortical laminae in humans at 7T. *NeuroImage*, 56(3), 1276–1285. https://doi.org/10.1016/j.neuroimage.2011.02.042

Lamme, V. A. (1995). The neurophysiology of figure-ground segregation in primary visual cortex. *The Journal of Neuroscience: The Official Journal of the Society for Neuroscience*, 15(2), 1605–1615.

Lamme, V. A., Rodriguez-Rodriguez, V., & Spekreijse, H. (1999). Separate processing dynamics for texture elements, boundaries and surfaces in primary visual cortex of the macaque monkey. *Cerebral Cortex* (New York, N.Y.: 1991), 9(4), 406–413.

Lamme, V. A., & Spekreijse, H. (1998). Neuronal synchrony does not represent texture segregation. *Nature*, 396(6709), 362–366. https://doi.org/10.1038/24608

Lamme, V. A., Zipser, K., & Spekreijse, H. (1998). Figure-ground activity in primary visual cortex is suppressed by anesthesia. *Proceedings of the National Academy of Sciences of the United States of America*, 95(6), 3263–3268.

MacEvoy, S. P., Kim, W., & Paradiso, M. A. (1998). Integration of surface information in primary visual cortex. *Nature Neuroscience*, 1(7), 616–620. https://doi.org/10.1038/2849

Markuerkiaga, I., Barth, M., & Norris, D. G. (2016). A cortical vascular model for examining the specificity of the laminar BOLD signal. *NeuroImage*, 132, 491–498. https://doi.org/10.1016/j.neuroimage.2016.02.073

Marquardt, I. (2019a). Stimuli & analysis pipeline for the surface perception project. Retrieved from https://github.com/ingo-m/surface

Marquardt, I. (2019b, March 4). Visual stimuli used in fMRI experiment on processing of real and illusory surfaces. https://doi.org/10.5281/zenodo.2583035

Marquardt, I., Gulban, O. F., & Schneider, M. (2018, April 18). pyprf - A free & open source python package for population receptive field (pRF) analysis. https://doi.org/10.5281/zenodo.1220207

Marquardt, I., Schneider, M., Gulban, O. F., Ivanov, D., & Uludağ, K. (2018). Cortical depth profiles of luminance contrast responses in human V1 and V2 using 7 T fMRI. *Human Brain Mapping*. https://doi.org/10.1002/hbm.24042

Marques, J. P., Kober, T., Krueger, G., van der Zwaag, W., Van de Moortele, P.-F., & Gruetter, R. (2010). MP2RAGE, a self bias-field corrected sequence for improved segmentation and T1-mapping at high field. *NeuroImage*, 49(2), 1271–1281. https://doi.org/10.1016/j.neuroimage.2009.10.002

Mendola, J. D., Dale, A. M., Fischl, B., Liu, A. K., & Tootell, R. B. (1999). The representation of illusory and real contours in human cortical visual areas revealed by functional magnetic resonance imaging. *The Journal of Neuroscience: The Official Journal of the Society for Neuroscience*, 19(19), 8560–8572.

Millman, K. J., & Aivazis, M. (2011). Python for Scientists and

Engineers. *Computing in Science & Engineering*, 13(2), 9–12. https://doi.org/10.1109/MCSE.2011.36

Moeller, S., Yacoub, E., Olman, C. A., Auerbach, E., Strupp, J., Harel, N., & Uğurbil, K. (2010). Multiband multislice GE-EPI at 7 tesla, with 16-fold acceleration using partial parallel imaging with application to high spatial and temporal whole-brain fMRI. *Magnetic Resonance in Medicine*, 63(5), 1144–1153. https://doi.org/10.1002/mrm.22361

Mumford, J. A. (2007). A guide to calculating percent change with featquery. Retrieved from http://mumford.fmripower.org/perchange_guide.pdf

Oliphant, T. E. (2007). Python for Scientific Computing. *Computing in Science & Engineering*, 9(3), 10–20. https://doi.org/10.1109/MCSE.2007.58

Peirce, J. W. (2007). PsychoPy–Psychophysics software in Python. *Journal of Neuroscience Methods*, 162(1–2), 8–13. https://doi.org/10.1016/j.jneumeth.2006.11.017

Peirce, J. W. (2008). Generating stimuli for neuroscience using PsychoPy. *Frontiers in Neuroinformatics*, 2. https://doi.org/10.3389/neuro.11.010.2008

Pereverzeva, M., & Murray, S. O. (2008). Neural activity in human V1 correlates with dynamic lightness induction. *Journal of Vision*, 8(15), 8.1-10. https://doi.org/10.1167/8.15.8

Pinheiro, J., Bates, D., DebRoy, S., Sarkar, D., & R Core Team. (2017). nlme: Linear and Nonlinear Mixed Effects Models. Retrieved from https://CRAN.R-project.org/package=nlme

Poldrack, R. A., Mumford, J. A., & Nichols, T. E. (2011). Handbook of functional MRI data analysis. Cambridge New York Melbourne Madrid: Cambridge University Press.

Poser, B. A., Koopmans, P. J., Witzel, T., Wald, L. L., & Barth, M. (2010). Three dimensional echo-planar imaging at 7 Tesla. *NeuroImage*, 51(1), 261–266. https://doi.org/10.1016/j.neuroimage.2010.01.108

R Core Team. (2017). R: A Language and Environment for Statistical Computing. Retrieved from https://www.R-project.org

Rossi, A. F., & Paradiso, M. A. (1999). Neural correlates of perceived brightness in the retina, lateral geniculate nucleus, and striate cortex. *The Journal of Neuroscience: The Official Journal of the Society for Neuroscience*, 19(14), 6145–6156.

Rossi, A. F., Rittenhouse, C. D., & Paradiso, M. A. (1996). The representation of brightness in primary visual cortex. *Science* (New York, N.Y.), 273(5278), 1104–1107.

Self, M. W., van Kerkoerle, T., Supèr, H., & Roelfsema, P. R. (2013). Distinct roles of the cortical layers of area V1 in figure-ground segregation. *Current Biology*: CB, 23(21), 2121–2129. https://doi.org/10.1016/j.cub.2013.09.013

Setsompop, K., Gagoski, B. A., Polimeni, J. R., Witzel, T., Wedeen, V. J.,

& Wald, L. L. (2012). Blipped-controlled aliasing in parallel imaging for simultaneous multislice echo planar imaging with reduced g-factor penalty. *Magnetic Resonance in Medicine*, 67(5), 1210–1224. https://doi.org/10.1002/mrm.23097

Short, A. D. (1966). Decremental and incremental visual thresholds. *The Journal of Physiology*, 185(3), 646–654.

Smith, S. M., Jenkinson, M., Woolrich, M. W., Beckmann, C. F., Behrens, T. E. J., Johansen-Berg, H., ... Matthews, P. M. (2004). Advances in functional and structural MR image analysis and implementation as FSL. *NeuroImage*, 23, S208–S219. https://doi.org/10.1016/j.neuroimage.2004.07.051

Tosun, D., Rettmann, M. E., Han, X., Tao, X., Xu, C., Resnick, S. M., ... Prince, J. L. (2004). Cortical surface segmentation and mapping. *NeuroImage*, 23, S108–S118. https://doi.org/10.1016/j.neuroimage.2004.07.042

Uludağ, K. (2008). Transient and sustained BOLD responses to sustained visual stimulation. *Magnetic Resonance Imaging*, 26(7), 863–869. https://doi.org/10.1016/j.mri.2008.01.049

Uludağ, K., & Blinder, P. (2018). Linking brain vascular physiology to hemodynamic response in ultra-high field MRI. *NeuroImage*, 168, 279–295. https://doi.org/10.1016/j.neuroimage.2017.02.063

van de Ven, V., Jans, B., Goebel, R., & De Weerd, P. (2012). Early human visual cortex encodes surface brightness induced by dynamic context. *Journal of Cognitive Neuroscience*, 24(2), 367–377. https://doi.org/10.1162/jocn_a_00126

van der Walt, S., Colbert, S. C., & Varoquaux, G. (2011). The NumPy Array: A Structure for Efficient Numerical Computation. *Computing in Science & Engineering*, 13(2), 22–30. https://doi.org/10.1109/MCSE.2011.37

van Kerkoerle, T., Self, M. W., Dagnino, B., Gariel-Mathis, M.-A., Poort, J., van der Togt, C., & Roelfsema, P. R. (2014). Alpha and gamma oscillations characterize feedback and feedforward processing in monkey visual cortex. *Proceedings of the National Academy of Sciences*, 111(40), 14332–14341. https://doi.org/10.1073/pnas.1402773111

Waehnert, M. D., Dinse, J., Weiss, M., Streicher, M. N., Waehnert, P., Geyer, S., ... Bazin, P.-L. (2014). Anatomically motivated modeling of cortical laminae. *NeuroImage*, 93, 210–220. https://doi.org/10.1016/j.neuroimage.2013.03.078

Whittle, P. (1986). Increments and decrements: luminance discrimination. *Vision Research*, 26(10), 1677–1691.

Xing, D., Yeh, C.-I., & Shapley, R. M. (2010). Generation of black-dominant responses in V1 cortex. *The Journal of Neuroscience: The Official Journal of the Society for Neuroscience*, 30(40), 13504–13512.

https://doi.org/10.1523/JNEUROSCI.2473-10.2010
Yeh, C.-I., Xing, D., & Shapley, R. M. (2009). 'Black' responses dominate macaque primary visual cortex v1. *The Journal of Neuroscience: The Official Journal of the Society for Neuroscience*, 29(38), 11753–11760. https://doi.org/10.1523/JNEUROSCI.1991-09.2009
Yushkevich, P. A., Piven, J., Hazlett, H. C., Smith, R. G., Ho, S., Gee, J. C., & Gerig, G. (2006). User-guided 3D active contour segmentation of anatomical structures: Significantly improved efficiency and reliability. *NeuroImage*, 31(3), 1116–1128. https://doi.org/10.1016/j.neuroimage.2006.01.015
Zhang, Y., Brady, M., & Smith, S. (2001). Segmentation of brain MR images through a hidden Markov random field model and the expectation-maximization algorithm. *IEEE Transactions on Medical Imaging*, 20(1), 45–57. https://doi.org/10.1109/42.906424
Zhao, F., Wang, P., & Kim, S.-G. (2004). Cortical depth-dependent gradient-echo and spin-echo BOLD fMRI at 9.4T. *Magnetic Resonance in Medicine*, 51(3), 518–524. https://doi.org/10.1002/mrm.10720
Zurawel, G., Ayzenshtat, I., Zweig, S., Shapley, R., & Slovin, H. (2014). A contrast and surface code explains complex responses to black and white stimuli in V1. *The Journal of Neuroscience: The Official Journal of the Society for Neuroscience*, 34(43), 14388–14402. https://doi.org/10.1523/JNEUROSCI.0848-14.2014

6
General discussion

6.1 Summary

This thesis presents investigations into the processing of visual stimuli in human early visual cortex with high-resolution fMRI. We conducted studies that probed stimulus-driven feedforward processing (Chapter 2), feedback signals related to global perceptual qualities of a locally invariant stimulus (Chapter 3), and a follow-up study on the neural correlates of surface perception (Chapter 5). We found distinct cortical depth profiles of activity in early visual cortex under stimulus conditions related to feedforward and feedback processing (Chapters 2 & 3). Additionally, we employed a novel analysis approach to estimate and remove the spatial bias in the cortical-depth dependent fMRI signal caused by draining veins (Chapters 2), and estimated the width of the fMRI point spread function (Chapter 4). While investigating the cortical depth profile of feedback processing, we observed a negative response to uniform surfaces (Chapter 3), in apparent contrast to previously reported luminance responses measured with fMRI (Haynes, Lotto, & Rees, 2004). Based on this, we conducted two experiments to improve our understanding of the processing of surface stimuli in early visual cortex. We found the cortical response to the edges and to the interior of uniform surfaces to be highly dependent on the surrounding background, with remarkable variations in the directionality and temporal profile of the response (Chapters 3 & 5). Finally, initial findings suggest a previously unknown pattern of activity in response to an illusory surface (Chapter 5). Although this work is still in progress, in comparison with earlier studies (Kok, Bains, van Mourik, Norris, & de Lange, 2016; Kok & de Lange, 2014), our preliminary results indicate that the response to an illusory surface may differ depending on the temporal frequency of the stimulus.

The early visual cortex is probably the best studied brain area in humans (as well as in other species). Yet, it has to be conceded that we are a long way from a mechanistic understanding of primary visual cortex, let alone visual perception as a whole. This is not to say that no progress has been made. The notion that perception is a constructive process arising from the interplay between bottom-up stimulus input and top-down expectations has not only become mainstream in cognitive science, but has also inspired much neuroscientific research. The idea can take several forms. For example, Cisek and Kalaska have put

forward the view that perception, cognition, and action are not separate, successive processes, but can be conceptualised more holistically (2010). A more well-known example is the predictive coding framework, in which perception and cognition are likewise not separable processes, as the brain is constantly performing predictive inference to consolidate top-down predictions and bottom-up stimulus input (Friston, 2005; Rao & Ballard, 1999). Irrespective of the particular theoretical framework one subscribes to, attempts to functionally map the interplay between bottom-up and top-down processing motivate much of the contemporary effort invested into layer specific fMRI. As laid out in the introduction to this thesis, the divide between cognitive and computational theory on the one hand, and empirical cognitive neuroscience is still huge. However, with the increase in spatial resolution achieved over the past decade, there is a prospect of resolving computationally relevant functional clusters at the laminar level *in vivo* with fMRI. The research presented in this thesis is part of this research project.

Although some of the first cortical depth specific fMRI studies have been published about ten years ago (Koopmans, Barth, & Norris, 2010; Polimeni, Fischl, Greve, & Wald, 2010; Ress, Glover, Liu, & Wandell, 2007), the field is – perhaps not in its infancy – but in its adolescence. From the perspective of a cognitive neuroscientist, an obvious target for further improvement concerns the image acquisition side. Pulse sequences with an even higher spatial resolution and signal to noise ratio, ideally with less geometric distortions, would enable more robust detection of layer-specific signals. While this task falls within the domain of the MRI physicists, there is also much work to be done on the side of the cognitive neuroscientists, with respect to experimental design, analysis, and interpretation. Thus, in the following, we will discuss methodological considerations pertaining to the previous chapters, adding further details to our choices regarding analysis and experimental design, and broach unresolved issues and directions for further research. In particular, we consider (1) strategies regarding experimental designs for high-resolution fMRI studies, (2) which statistical parameter to sample when constructing cortical depth profiles, (3) hypothesis testing on cortical depth profiles, and (4) the spatial deconvolution for the removal of the draining vein bias.

6.2 Experimental design

All three studies presented in this thesis employed a single-session, within-subject experimental design. In other words, all experimental conditions were tested in each subject, and each subject completed one experimental session. Although this type of experimental design is common in fMRI research, it is not without alternatives. For instance, contemporary electrophysiological studies in monkeys typically sample only two subjects (i.e. monkeys), with many measurements per subject (e.g. Bastos et al., 2015; Maier, Adams, Aura, & Leopold, 2010; Maier, Aura, & Leopold, 2011; Roberts et al., 2013; Self, van Kerkoerle, Supèr, & Roelfsema, 2013; van Kerkoerle, Self, & Roelfsema, 2017). This is in contrast to human psychological research, which often has a much higher number of participants. There are probably both practical and theoretical reasons for this discrepancy. Monkeys require extensive training and surgical preparation, which makes large sample sizes impractical. Moreover, unnecessarily large sample sizes can be considered unethical in case of invasive animal research. In comparison, for fMRI studies in healthy humans, universities provide a large pool of potential subjects to sample at a relatively low cost.

Besides these practical considerations, the research question constraints the choice of experimental design. When studying phenomena, for which a considerable between-subject variance is expected, it is necessary to sample from a large enough number of subjects, especially if inferences to the population level are intended. This is particularly true for complex, high-level phenomena, such as social cognition, emotion, personality, etc. In these contexts, between-subject variability may not only be large, but also meaningful with respect to the research questions. In contrast, for low-level phenomena, such as the processing of visual stimuli in early visual cortex, less between-subject variance is expected, at least in healthy individuals. To be sure, sufficiently large sample sizes are always necessary for population-level generalisations, also in fundamental neuroscience. However, in practice, the need for large amounts of data is rather driven by a low signal-to-noise ratio of the measurements than by the desire to generalise to the population level. In actual scientific practice, the generalisability of low-level neuroscientific phenomena is deemed high enough *a priori* to justify inference not only across individuals, but even across species – after all, many

visual neuroscience studies have been conducted in cats (Gilbert, 1977; Gray, König, Engel, & Singer, 1989; Hubel & Wiesel, 1962), monkeys (Hubel & Wiesel, 1968; Self et al., 2013; Tootell, Hamilton, & Switkes, 1988), rats (Constantinople & Bruno, 2013; Johnson & Burkhalter, 1997; Sloan et al., 2010), and mice (Adesnik, 2018; Adesnik & Scanziani, 2010; Olsen, Bortone, Adesnik, & Scanziani, 2012). Neuroscientific research in rodents is not motivated by an interest in the rodent brain per se, but by practical and ethical considerations, and by the assumption that the fundamental phenomena under investigation are conserved across species. This is exemplified by titles such as "Deep cortical layers are activated directly by thalamus" (and not "Rats' deep cortical layers are activated directly by thalamus"; Constantinople & Bruno, 2013).

It could be argued that fMRI studies of visual processing in early visual cortex, like the ones presented in this thesis, could follow the example of electrophysiological research and perform repeated measurements in a very small number of subjects. This might bring about several practical advantages. For example, fewer time-intense and error-prone tissue-type segmentations would need to be performed. With fewer subjects per study, (even) more time could be spend on each individual tissue-type segmentation, potentially reducing error due to tissue misclassification. Moreover, in a multi-session experiment with a small number of subjects, less time would be spent on acquiring auxiliary data, such as retinotopic maps and high-resolution anatomical images (since these only need to be acquired once per subject). Thus, scanner time – which is a scarce resource – could be used more efficiently, resulting in more powerful experimental designs.

The number of subjects required in fMRI studies is a matter of debate. Whereas some authors have stressed the importance of between-subject variability and the resulting need for a large number of subjects (Thirion et al., 2007), others have found substantial within-subject, between session variability (McGonigle et al., 2000) and have therefore recommended acquiring sufficient individual-level data (McGonigle et al., 2000; Nee, 2018). We suggest that generalised recommendations regarding sample size are not possible because of the profound differences in experimental design and analysis strategy. For example, low-resolution studies, in which subjects' brains are warped into a common anatomical space, will be affected differently by between-subject variance (e.g. due to anatomical variability) than high-resolution studies, in which direct

across-subjections registration to a common anatomical template is not performed.

Kolossa and Kopp (2018) have pointed out that the focus on sample size (i.e. number of subjects) and a disregard for the number of measurements per subject in cognitive neuroscience has historical roots. Specifically, they argue that the discipline has been dominated by a statistical mindset that puts emphasis on *sampling* error. That is to say, cognitive neuroscientists have followed the lead of what Cronbach (1957) referred to as 'experimental psychology', and have prioritised the variance between organisms (as opposed to the variance between measurements), with the goal of reducing the error inherent in a sample statistic relative to the underlying population parameters. In contrast, measurement theory, which stresses the role of *measurement* error, has received less attention (Kolossa & Kopp, 2018). High-resolution fMRI research on laminar and columnar structures is operating at the current technical limits with respect to spatial resolution. As a consequence, high measurement error – which cognitive neuroscientists typically refer to as a low signal-to-noise ratio – is a particularly pressing issue. Hence, it could be argued that, as long as the phenomenon under investigation is assumed to be reasonably consistent across individuals, high-resolution fMRI experiments should repeatedly sample a small number of subjects, to reduce the influence of measurement error.

Simulations support the value of 'small-N' experimental designs in general (P. L. Smith & Little, 2018), and a recent fMRI study demonstrated the value of high-precision mapping of individual brains (Gordon et al., 2017). Nevertheless, all studies presented in this thesis were single-session experiments. The reason for this is that the potential benefits of a multi-session experiment can, at present, not actually be leveraged because of limitations related to the image acquisition and analysis. Especially for high-resolution (i.e. sub-millimetre) fMRI pulse sequences using an EPI readout, across-sessions image registration is severely impeded by changing geometric distortions. Although others have successfully employed multi-session experimental designs at high resolutions for investigations into columnar structures (Nasr, Polimeni, & Tootell, 2016; Tootell & Nasr, 2017), we found across-sessions registration to be error prone for an analysis involving cortical depth sampling, and opted for a single-session experimental design. Our approach results in long experimental sessions (>2 hours) that are exhausting for the

subject and can only be successfully completed by experienced, motivated participants. These considerations may seem trivial, but they pose serious limitations on experimental design. Long, exhausting sessions and the resulting need for a behavioural task (to keep the subject engaged) make it difficult to control for attentional state. Furthermore, the inevitable fluctuations in attention over a long experimental session may increase the variance in the already noisy fMRI signal. In all studies presented in this thesis, we have aimed to sustain participant's attention with help of a simple fixation task that required a motor response, and have excluded data that was affected by poor behavioural performance (presumably due to a lack of attention, or the subject having fallen asleep). While this is a workable solution for the particular research questions addressed here, future sub-millimetre fMRI research could profit immensely from distortion-free pulse sequences that would allow more flexible experimental designs.

Single-session experimental designs require the alignment of data (e.g. activation maps) across subjects. For low resolution fMRI studies, volume-based non-linear warping can be used to register subjects' brains into a common reference space (Andersson, Jenkinson, & Smith, 2007). Alternatively, surface-based alignment can be used to register brains based on macroanatomical curvature, and has been shown to provide an improved registration compared to volume-based methods (Desai, Liebenthal, Possing, Waldron, & Binder, 2005; Fischl, Sereno, Tootell, & Dale, 1999). However, these methods cannot be expected to achieve the sub-millimetre accuracy that is required for cortical depth sampling. Thus, throughout the research presented in this thesis, we have pooled data across subjects in an abstract space that is not directly related to individuals' anatomy. In particular, we have defined regions of interest based on quantifiable criteria separately in each subject, and pooled cortical depth profiles across subjects. Furthermore, we have aligned subjects' activation maps in a model of the visual field based on population receptive field estimates (visual field projections). The latter approach is particularly useful, because it of its intuitive appeal and the potential to reveal unexpected activation patterns. Unfortunately, visual field projections require a well-defined and robust model of the stimulus space, such as the population receptive field. This limits the use of this method to early visual cortex. It is expected that future sub-millimetre fMRI research will attempt to investigate cognitive processes in high-order

cortical areas. To this end, new means of aligning data across subjects will have to be explored.

6.3 Choice of depth signal

The cerebral cortex is a layered structure, and different layers are involved in distinct aspects of information processing (Callaway, 1998; Felleman & Van Essen, 1991; Rockland & Pandya, 1979). By measuring the distribution of activity across cortical layers, inferences may be made about the role of feed-forward and feedback mechanisms in perception. Combining evidence on the laminar distribution of neuronal activity with information on microanatomical structure and connectivity might help to develop a deeper, more mechanistic understanding of brain function. When using high-resolution fMRI to test hypotheses about cortical-depth dependent differences in neuronal activity, researchers have to decide, which statistical parameters to sample across the depth of the grey matter. The researcher would like to sample some statistical parameter that truthfully reflects signal changes in response to the experimental manipulation (e.g. the presentation of a stimulus, or a task). The statistical parameter is sampled and plotted across the cortical depth, i.e. from white matter towards the pial surface[1]. Three possible parameters to be sampled are percent signal change, GLM parameter estimates, or z-scores from a GLM analysis. We will discuss these in turn.

[1] Electrophysiological studies in animals usually plot cortical depth on the y-axis, with the CSF border at the top (Briggs & Callaway, 2001; Dougherty, Cox, Ninomiya, Leopold, & Maier, 2017; Maier et al., 2010; van Kerkoerle et al., 2014). This form of presentation is probably inspired by photograpic depictions of histological slices, in which superficial layers are likewise at the upper end of the figure (Fitzpatrick, Itoh, & Diamond, 1983; Lund, 1973, 1988; Lund, Lund, Hendrickson, Bunt, & Fuchs, 1975). In contrast, most fMRI studies present layer profiles with cortical depth on the x-axis, and the white-grey matter border at the origin, i.e. on the left (Kashyap et al., 2018; Kok et al., 2016; Koopmans et al., 2010; Koopmans, Barth, Orzada, & Norris, 2011; Marquardt, Schneider, Gulban, Ivanov, & Uludağ, 2018; Muckli et al., 2015; Olman et al., 2012; Polimeni, Witzel, Fischl, Greve, & Wald, 2010; Ress et al., 2007). However, there are also some fMRI studies that present laminar profiles with the CSF border at the origin (Huber, Handwerker, et al., 2017; Huber, Uludağ, & Möller, 2017).

6.3.1 Percent signal change

Percent signal change is a seemingly straightforward parameter to perform depth sampling on. In an experiment with a rest condition and one or more activate conditions, one can split the fMRI time series into event-related segments, and calculate the signal change between each trial and the preceding rest block. This approach is perhaps the simplest way to perform fMRI data analysis, seemingly uncomplicated and free from modelling assumptions. Reporting percent signal change has the advantage that results can more easily be compared across studies (provided that similar pulse sequences are used), and that empirical results can more easily be related to physiological models. However, the decision, which time points to include in the baseline time period and in the active condition, relies on implicit assumptions about the temporal dynamics of the haemodynamic response. Differences in the onset latency or the time to peak between conditions or depth levels may confound the result. Visual inspection of event-related time courses may aid the decision, but in the end the decision, which time points to include, remains to some degree arbitrary, increasing the researcher degrees of freedom. Moreover, when calculating the percent signal change in this way, it is often assumed that the signal has returned to baseline, which is not given for insufficient rest durations due to the post-stimulus undershoot, which often lasts twice the stimulation duration. Not modelling the post-stimulus undershoot can be seen as an advantage if there are reasons to believe that the post-stimulus undershoot does not conform to the 'canonical' haemodynamic response model. However, it follows that very long rest periods are necessary between every stimulus presentation, so that the signal can completely recover to baseline. Sufficiently long rest periods are needed in every block design, but incomplete signal recovery can be modelled in the GLM (assuming the correct local estimate of the haemodynamic response function), for example in a fast event related design. This is not an option when the percent signal change is calculated 'manually'.

If there are short and variable rest periods, or if the stimulus events have variable duration, the percent signal change is not well defined (Mumford, 2007; Poldrack, Mumford, & Nichols, 2011). The reason for this is that, in case of short rest periods of variable duration, the fMRI signal has not completely returned back to baseline at the start of the

subsequent trial, and the degree of incomplete recovery depends on the duration of the rest period. Thus, it is not clear what exactly constitutes the rest period. Similarly, in case of stimulus events of variable duration, the average signal change is expected to differ depending on the duration of the stimulus event. As a consequence, there is no single percent signal change parameter in this case; the parameter would need to be defined with respect to some reference event (i.e. a stimulus event of a particular duration; Mumford, 2007; Poldrack et al., 2011).

Additionally, even in block designs with long rest periods, the term 'percent signal change' can be ambiguous, since some researchers prefer to take the temporal mean over all time points as a baseline, as opposed to the pre-stimulus interval (Poldrack et al., 2011). Finally, the perhaps most decisive drawback of 'manually' calculating the percent signal change is that this approach discards the time points that are not included when calculating the ratio between rest and active periods. Again, this may be seen as an advantage if some part of the response (e.g. the post-stimulus undershoot) cannot be modelled, but, in all other cases, disregarding the information present in the left-out time points effectively reduces statistical power.

6.3.2 GLM parameter estimates

Another approach is to perform cortical depth sampling on parameter estimates from a GLM analysis. The details of GLM analysis in the context of fMRI have been discussed extensively (e.g. Goebel, 2007; S. M. Smith, 2004). For each predictor in the GLM, a parameter estimate (also referred to as beta value) is obtained. It reflects the signal change between some baseline condition (e.g. rest periods) and an experimental condition, under the assumption that the temporal dynamics of the fMRI response follows a certain model, typically quantified by a double gamma function. In a block design with long enough rest blocks, the parameter estimates are very close to the 'manually' calculated percent signal change, given that the haemodynamic model provides a good fit, and the appropriate time points are chosen for the calculation of the percent signal change (Poldrack et al., 2011). The use of parameter estimates based on an explicit model of the haemodynamic response has the advantage that the entire time series is taken into consideration (Friston et al., 1998). Nevertheless, deviations from the haemodynamic

response model (Lindquist, Meng Loh, Atlas, & Wager, 2009), and possible differences in the shape of the response between cortical depth levels could lead to a biased result (Goense, Bohraus, & Logothetis, 2016). Fitting temporal derivatives of the predictor time courses or a set of basis functions may result in a better model fit under such circumstances, albeit complicating the interpretation of results (Lindquist & Wager, 2007; Steffener, Tabert, Reuben, & Stern, 2010).

In summary, GLM parameter estimates can make more efficient use of the information in the signal, but their magnitude is arbitrary (it depends on the height of the regressor). The amplitude of percent signal change values can more easily be compared across studies, and be related to physiological models. Therefore, in the research presented in this thesis, we have calculated percent signal change based on parameter estimates of stimulus-induced activation from a GLM analysis, by applying a scaling that takes into account the height of the predictors in the design matrix (Mumford, 2007; Poldrack et al., 2011). We have chosen this approach because we assume that in the case of a simple experimental design with long stimulus and rest blocks, the advantages of the well-established GLM analysis outweigh its limitations. Still, further research will be required to establish the validity of the GLM assumptions in the context of cortical-depth dependent analyses.

6.3.3 Z-statistics

In the context of low-resolution fMRI studies, where results are often depicted in form of volumetric activation maps, GLM parameter estimates are usually transformed into z- or t-statistics, so as to reflect the variance inherent in the response. In other words, z-statistics are plotted to illustrate how well the fMRI signal is characterised by a model time course reflecting the effect of the experimental manipulation in different brain regions (see, for example, Figure 2.3). Even if, on average, a condition is associated with a strong signal change, this may not result in a high z-statistic if there is a lot of variance in the response. This makes the z-statistic an unfavourable parameter for cortical depth profiles; because of the larger volume fraction of veins at the cortical surface, the signal-to-noise ratio and, correspondingly, the variance of parameter estimates increase towards the cortical surface (Koopmans et al., 2010, 2011). (See Figure 2.4 A for an example of increasing variance

of parameter estimates at the cortical surface.) In the hypothetical case of constant activation in all layers, we could expect a flat cortical depth profile of parameter estimates, with increasing variance towards the cortical surface. Thus, a corresponding depth profile of the z-statistic would decrease in the direction of the cortical surface.

We suggest that a sensible way to reflect the variance inherent in cortical depth profiles of fMRI signal change is to employ a bootstrapping procedure. By using a bootstrapping procedure to create confidence intervals for cortical depth profiles, one can incorporate information about the variance inherent in the response without biasing the shape of the average profile with respect to cortical depth, as would be the case when plotting the z-statistic. As another advantage, the bootstrapping confidence intervals can be asymmetric about the median if the bootstrapping distribution is skewed. A skewed distribution may otherwise remain unnoticed.

An example of a cortical depth profile with bootstrapped confidence intervals can be found in Figure 2.6. Although the percentile bootstrap method that we employed in this case has the advantages of not relying on possibly invalid assumptions about the underlying distribution and can identify skewed distributions, it is not without limitations. Most importantly, the percentile bootstrap can give poor estimates in case of small sample sizes (Good, 2005; Mooney & Duval, 1993). Other, more sophisticated methods have been proposed to overcome the limitations of the percentile bootstrap, such as the bias-corrected bootstrap and the percentile-t method. However, these alternatives are much more complex than the percentile bootstrap, and come with additional assumptions and open choices regarding their implementation (Mooney & Duval, 1993). It remains to be seen, whether resampling techniques will gain traction in the context of cortical depth analysis.

6.4 Hypothesis testing

The goal of high-resolution fMRI studies is to test hypotheses about neural processing. Once cortical depth profiles have been sampled, inference can be conducted to test for response differences between experimental conditions and/or cortical areas. Inference on cortical depth profiles poses some methodological challenges, and we think that the field of high-resolution fMRI is still at an early stage of development

with respect to statistical inference. In the research presented in this thesis, we have primarily conducted inference on cortical depth profiles by means of resampling methods. For instance, we have used permutation tests to assess differences in parameters relating to the shape of cortical depth profiles. In particular, we have tested for differences in the peak position of cortical depth profiles between cortical areas and experimental conditions. It has been argued that permutations tests are conceptually superior to more commonly used methods, such as the t-test in situations in which non-random samples are randomly assigned to experimental conditions (Ludbrook & Dudley, 1998). (In case of the within-subject designs employed in this thesis, each subject received all experimental conditions in random order.) Another advantage of permutations tests is that they do not rely on the assumption of a normal distribution (Good, 2005). Nevertheless, like any statistical method, they are not free from limitations. For instance, in case of unequal variances, a significant test statistic may erroneously be interpreted as evidence for a difference in means (the so-called Behrens-Fisher problem, see Neuhäuser & Manly, 2004). Furthermore, permutation tests assume the exchangeability of observations under the null hypothesis (Good, 2005; Hayes, 1996), and it is not completely clear what the effect of non-independence between samples is (Hayes, 1996). Overall, the scope of permutation tests in the context of cortical depth analysis is limited, and a more generalisable method would be preferable.

A typical cortical-depth dependent statistical analysis may involve four factors: (1) experimental condition, (2) brain area, (3) cortical depth, and (4) subject. Current layer fMRI studies mostly attempt to functionally map activation patterns in the healthy brain (Huber, Handwerker, et al., 2017; Kok et al., 2016; Koopmans et al., 2010, 2011; Muckli et al., 2015; Polimeni, Fischl, et al., 2010), and can therefore use more powerful within-subject designs (as opposed to treatment/control between-subjects designs in clinical studies; Charness, Gneezy, & Kuhn, 2012; Greenwald, 1976). The main challenge is the correlation structure of the third factor, i.e. cortical depth. Adjacent data points along the cortical depth are heavily autocorrelated for a variety of reasons. First, even if two adjacent data points originated from two separate voxels, their signals would be statistically dependent because the point-spread function of a voxel exceeds its nominal resolution (Buxton, 2009, p. 223ff). Second, two adjacent data points in the cortical depth profile

do not usually originate from separate voxels if the cortical layers are reconstructed at a resolution higher than the nominal voxel resolution, as is commonly done (Huntenburg, Steele, & Bazin, 2018; Waehnert et al., 2014). Third, even if the point spread function of the fMRI signal was perfectly sharp (i.e. not wider than the nominal resolution), and voxel signals were not mixed during the analysis, the layer fMRI signal would still be autocorrelated, simply because neuronal activity at two nearby points within the grey matter is not independent. Finally, even in the hypothetical case of neural activity that is decoupled between layers within a cortical column, the fMRI signal would be autocorrelated because of the drainage of deoxygenated haemoglobin along ascending draining veins (Markuerkiaga, Barth, & Norris, 2016; Weber, Keller, Reichold, & Logothetis, 2008). Thus, the autocorrelation structure of the layer fMRI signal has to be accounted for in the statistical analysis.

One possibility to model autocorrelation is to employ a repeated-measures ANOVA, which is commonly used in case of temporal autocorrelation between measurements in psychology or clinical studies (Gueorguieva & Krystal, 2004). However, the repeated measures ANOVA relies on rather restrictive assumptions, such as homogeneity of variances (homoscedastic) and sphericity. There are methods for correcting violations of assumptions, but these can affect the sensitivity of the test (Gueorguieva & Krystal, 2004; Quené & van den Bergh, 2004). Mixed-effects regression models have been recommended as an alternative to repeated measures ANOVA, because they come with less restrictive assumptions and offer more flexibility in modelling the covariance structure (Bagiella, Sloan, & Heitjan, 2000; Gueorguieva & Krystal, 2004; Keselman, Algina, & Kowalchuk, 2001; Quené & van den Bergh, 2004). In the context of layer fMRI, mixed models may be particularly beneficial for two reasons. First, the variance of the activation tends to increase towards the cortical surface (Koopmans et al., 2010, 2011), potentially leading to a violation of repeated measures ANOVA assumptions. Second, the hierarchical structure of layer fMRI data, with regions of interest and cortical depth levels nested within subjects, and subjects as a random effect, can be flexibly modelled in a mixed regression model. Moreover, this approach would allow to explicitly model the correlation structure of the cortical depth factor. Unfortunately, the implementation of mixed models is not straightforward (Bagiella et al., 2000; Gueorguieva & Krystal, 2004; Quené & van den Bergh, 2004). We

hope that future research will explore the potential of mixed models for inference on cortical depth profiles, and possibly bring about a more systematic and coherent methodology for layer fMRI data analysis.

6.5 Spatial deconvolution

A consistent finding from the earliest cortical depth specific fMRI studies in humans was an increase in response amplitude towards the cortical surface (Koopmans et al., 2010, 2011; Polimeni, Fischl, et al., 2010; Ress et al., 2007). This effect is thought to be caused by the unidirectional flow of venous blood through ascending veins towards the cortical surface (Koopmans et al., 2011; Markuerkiaga et al., 2016; Weber et al., 2008). Especially gradient-echo fMRI sequences are sensitive to signal originating from veins (Uludağ, Müller-Bierl, & Uğurbil, 2009). A stronger capillary weighting offered by alternative pulse sequences would be favourable for layer fMRI research, because of the potentially higher spatial specificity. However, at sub-millimetre voxel sizes (e.g. 0.7^3 mm^3 or 0.8^3 mm^3), the higher sensitivity of gradient echo sequences becomes paramount (Uludağ et al., 2009). The current alternatives to GE-acquisition, e.g. SE, VASO or ASL, suffer from lower SNR and/or reduced brain coverage (Norris, 2012, 2015), while their physiological PSF also does not guarantee a perfect specificity to neuronal activity. SE-EPI sequences are not free from T2*-weighting, so that sensitive to ascending vein effects cannot be avoided completely (Goense & Logothetis, 2006). In case of VASO, in spite of its weighting towards microvasculature (Huber et al., 2015), other factors (such as arterial and venous blood volume changes) can also contribute to the VASO contrast (Donahue et al., 2006). Therefore, leveraging the advantages of GE-EPI in combination with appropriate steps during data analysis to increasing its spatial specificity (e.g. the spatial deconvolution approach), promises to be a viable approach for many high-resolution fMRI studies investigating the mesoscopic architecture of the human brain.

Throughout the research presented in this thesis, we have used a spatial deconvolution to estimate and remove the signal spread due to ascending veins. Our approach was inspired by an anatomically motivated model of the vascular signal spread proposed by Markuerkiaga et al. (2016). The spatial deconvolution employs an explicit model of the laminar point spread function to approximate the underlying neuronal

activation profile from the fMRI signal. Two alternative approaches rely on taking the difference or the ratio of the cortical depth profiles from two experimental conditions.

The subtraction logic is generally used in conventional, low-resolution fMRI studies to contrast two experimental conditions (Poldrack, 2010). By subtracting the signal from two conditions, signal components that are common to both conditions can be removed, and unique signal contributions thus identified. A division between the cortical depth profiles from two experimental conditions could be useful to account for differences in the sensitivity of the fMRI signal across layers (Kashyap, Ivanov, Havlicek, Poser, & Uludağ, 2017; Uludağ & Blinder, 2018). Such a sensitivity difference can be due to a heterogeneous distribution of baseline cortical blood volume over voxels (Kashyap et al., 2017; Uludağ & Blinder, 2018); this aspect has inspired the normalisation of activation maps by a global, hypercapnia-induced BOLD signal (Bandettini & Wong, 1997; Cohen et al., 2004). However, while a divisive normalisation might partially account for differences in the baseline distribution of cortical blood volume, it is not intended to, and cannot, remove the effect of draining veins (see below). In the following, we will discuss the properties of the spatial deconvolution, normalisation by subtractions, and normalisation by division, with respect to the draining vein bias. Future research may aim for an integrated approach, possibly by applying the spatial deconvolution (to remove the draining vein bias), followed by a divisive normalisation (to account for heterogeneous sensitivity due to differences in baseline blood volume).

For comparison of the spatial deconvolution with the subtraction and division approach, we simulated cortical depth profiles for three scenarios (Figure 6.1). In each scenario, an experimental condition (Figure 6.1 A–C, blue line) was compared against a control condition (Figure 6.1 A–C, orange line). To simulate the draining vein effect, the activation profiles were convolved with a decaying exponential term (Figure 6.1 A–C). The purpose of this convolution was to approximate the general trend of unidirectional signal spread in the data; the 'true' laminar point spread function is likely more complex, with a varying slope at difference cortical depth levels.

As expected, subtracting the profile of the control condition from the experimental condition fails to remove the signal increase towards the

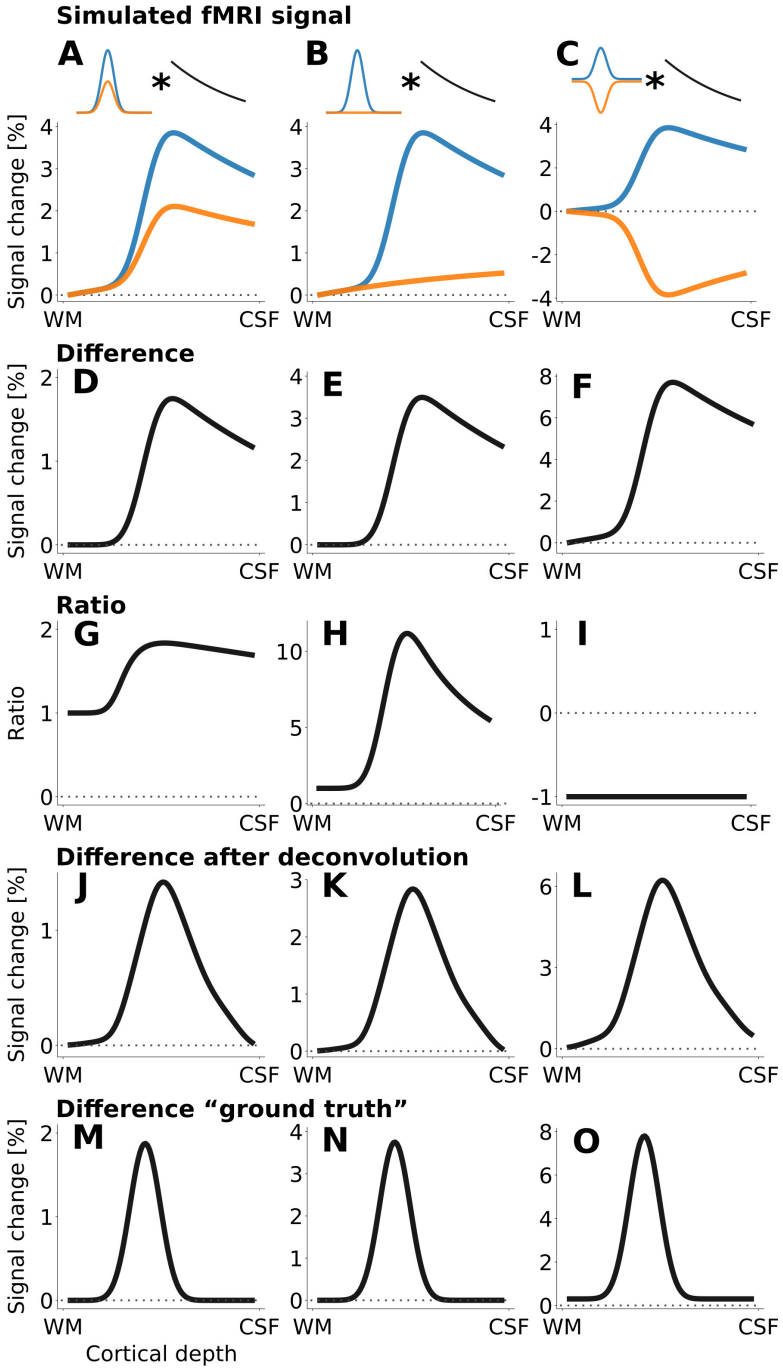
Simulated fMRI signal
A
B
C
Signal change [%]
WM
CSF
Difference
D
E
F
Ratio
G
H
I
Ratio
Difference after deconvolution
J
K
L
Difference "ground truth"
M
N
O
Cortical depth

Figure 6.1 *(previous page)*: Effect of subtractive and divisive normalisation on the draining vein bias in cortical depth profiles. Three scenarios were simulated. (**A**) First scenario; one stimulus condition evokes strong activation at middle layers (blue line), and a second condition causes weaker activation at the same location (orange line). To simulate the draining vein bias due to the unidirectional flow of venous blood, the activation profiles were convolved with a decaying exponential term (see small schematic in top row). (**B**) Second scenario; there is one condition with strong mid-layer activation (blue line), and a control condition with almost no activation (orange line). (**C**) Third scenario; there is strongly positive mid-layer activation in one condition (blue line), and strongly negative activation in the second condition (orange line). (**D, E, F**) Subtracting the depth profiles of the control condition (orange line) from the first condition (blue line) results in similarly shaped difference depth profiles for all scenarios (with varying amplitude). The draining vein bias is not removed in any of the scenarios. (**G, H, I**) Normalisation by division (blue line divided by orange line) results in very different ratio depth profiles for the three scenarios. The linear trend is only removed in the third scenario (**I**), where the absolute value of the activation is identical across the two conditions. (**J, K, L**) The spatial deconvolution removes most of the draining vein effect in all scenarios. Because the deconvolution model is currently only defined at five discrete depth levels, the resulting profiles loose spatial resolution, and the peaks are slightly shifted towards the cortical surface. (**M, N, O**) "Ground truth", derived by subtracting the original simulated activation profiles (without draining vein effect). Please note that the spatial deconvolution (**J, K, L**) is based on an anatomically motivated model (Markuerkiaga, et al., 2016), and that we approximated the draining effect with a generic exponential function (**A, B, C**).

cortical surface (Figure 6.1, D–F). In our three scenarios, the subtraction does identify the maximum condition difference at middle layers (slightly displaced towards CSF), but overestimates the condition difference at superficial layers in two scenarios (Figure 6.1, D & E). The ratio cannot remove the draining vein bias in two scenarios (Figure 6.1, G & H). Only in case of identical absolute signal amplitude can the bias be removed (Figure 6.1 I). Subtraction after applying the spatial deconvolution succeeds in removing the draining vein bias (Figure 6.1 J–L), resulting in profiles that are closer to the "ground truth" (Figure 6.1 M–O) than the other two approaches. Because the spatial deconvolution is currently only defined at five cortical depth levels (Markuerkiaga et al., 2016), the resulting difference profiles are less sharp than the "ground truth", and the peak difference is slightly displaced towards the CSF (as in the other two approaches). Future research may remedy this loss in sharpness by developing a continuously defined laminar point spread function.

Even though our simulation assumes a simplified exponential laminar point spread function, it highlights the shortcomings of approaches that do not employ an explicit model of the draining vein bias. Although further research will be required to establish and validate the exact parameters of the laminar point spread function, we believe that the spatial deconvolution is currently the "best guess" to approximate the underlying activity profile. We suggest that it is preferable to employ a model of the draining vein effect that is less than perfect, as opposed to ignoring the bias altogether. As more sophisticated deconvolution models become available, the bias may be removed with increasing accuracy.

The generalisability of the spatial deconvolution is restricted by assumptions regarding experimental design (stimulus duration), image acquisition (magnetic field strength, TE), and anatomy (primary visual cortex). However, we have simulated the effect of deviations in the model parameters (Figure 2.8) and partial volume effects at the white matter border (Figure 2.13), and have applied the model to cortical depth profiles from motor cortex (Figure 2.14). The results indicate that the model is relatively robust against deviations in the model parameters, and with respect to anatomical assumptions. Still, a more formal assessment of the validity of the spatial deconvolution is needed. In particular, cortical depth profiles from measurements that are not affected by the draining vein bias may be compared with deconvolved profiles based on gradient-echo, blood oxygenation level-dependent fMRI. Moreover,

further research could aim to develop a more comprehensive model that would make the spatial deconvolution explicitly applicable to a variety of brain areas, experimental designs, and acquisition parameters.

The model used here, as well as the two other (discouraged) normalisation approaches presented in Figure 6.1, are based on steady-state laminar activation profiles. In other words, the activation estimate represents the average signal over a time period (e.g. a stimulus block). This limits the flexibility of the method, and potentially disregards information inherent in the time domain. Thus, one potential direction for future research would be the development of a dynamic model that explicitly models the causal mechanisms between neural activity and the fMRI signal (Havlicek, Ivanov, Roebroeck, & Uludağ, 2017). In this way, prior knowledge on the characteristics of the haemodynamic coupling and the fMRI signal could be taken into account. Moreover, both the draining vein bias, and sensitivity differences across cortical depth due to the vascular structure could be integrated in one model. Finally, the effect of remote pial veins on the local layer fMRI signals (i.e. the so-called blooming effect) has to be taken into account to obtain unbiased laminar fMRI signals.

6.6 Concluding remarks

The goal of cognitive neuroscience is to develop a deeper, more mechanistic understanding of human cognition, and its physiological underpinning. It can be difficult to bridge cognitive and computational theory on the one hand, and neuroscientific observations on the other hand, because these often pertain to different levels of analysis and spatial scales. High-resolution fMRI allows to measure neuronal activity in the human brain at an unprecedented level of spatial detail and extent, and thus has the potential to lessen the gap between theory and data. We have contributed to this research project by studying the processing of visual stimuli in early visual cortex at sub-millimetre resolution. In particular, we have investigated aspects of bottom-up and top-down processing at different cortical depth levels. The field of cortical depth specific fMRI is still relatively young, and many open questions remain with respect to experimental design, analysis, and hypothesis testing. A particularly pressing issue for cortical depth specific fMRI is the draining vein bias, which we addressed by means of a spatial deconvolution.

Finally, even outside of the domain of sub-millimetre fMRI research on layers and columns, the study of early visual cortex is not at its end. After many decades of detailed electrophysiological investigations in cat and primate visual cortex, and more than two decades of fMRI research on human visual cortex, seemingly elementary aspects such as the processing of simple uniform surfaces can still produce unexpected results. The findings on the processing of real and illusory surfaces presented in this thesis leave several, quite basic, open questions, such as "What determines whether the response to a surface is positive or negative?", and "Which factors influence whether the response to a contour is transient or sustained?". As the saying goes, more research will be needed.

6.7 References

Adesnik, H. (2018). Layer-specific excitation/inhibition balances during neuronal synchronization in the visual cortex. *The Journal of Physiology*, 596(9), 1639–1657. https://doi.org/10.1113/JP274986

Adesnik, H., & Scanziani, M. (2010). Lateral competition for cortical space by layer-specific horizontal circuits. *Nature*, 464(7292), 1155–1160. https://doi.org/10.1038/nature08935

Andersson, J. L. R., Jenkinson, M., & Smith, S. (2007). Non-linear registration aka Spatial normalisation - FMRIB Technial Report TR07JA2. Retrieved from http://www.fmrib.ox.ac.uk/datasets/techrep/tr07ja2/tr07ja2.pdf

Bagiella, E., Sloan, R. P., & Heitjan, D. F. (2000). Mixed-effects models in psychophysiology. *Psychophysiology*, 37(1), 13–20.

Bandettini, P. A., & Wong, E. C. (1997). A hypercapnia-based normalization method for improved spatial localization of human brain activation with fMRI. NMR in Biomedicine, 10(4–5), 197–203.

Bastos, A. M., Vezoli, J., Bosman, C. A., Schoffelen, J.-M., Oostenveld, R., Dowdall, J. R., ... Fries, P. (2015). Visual Areas Exert Feedforward and Feedback Influences through Distinct Frequency Channels. *Neuron*, 85(2), 390–401. https://doi.org/10.1016/j.neuron.2014.12.018

Briggs, F., & Callaway, E. M. (2001). Layer-specific input to distinct cell types in layer 6 of monkey primary visual cortex. *The Journal of Neuroscience: The Official Journal of the Society for Neuroscience*, 21(10), 3600–3608.

Buxton, R. B. (2009). *Introduction to Functional Magnetic Resonance Imaging: Principles and Techniques* (2nd Edition). Cambridge, New York: Cambridge University Press.

Callaway, E. M. (1998). Local circuits in primary visual cortex of the macaque monkey. *Annual Review of Neuroscience*, 21(1), 47–74.

https://doi.org/10.1146/annurev.neuro.21.1.47
Charness, G., Gneezy, U., & Kuhn, M. A. (2012). Experimental methods: Between-subject and within-subject design. *Journal of Economic Behavior & Organization*, 81(1), 1–8. https://doi.org/10.1016/j.jebo.2011.08.009
Cisek, P., & Kalaska, J. F. (2010). Neural mechanisms for interacting with a world full of action choices. *Annual Review of Neuroscience*, 33, 269–298. https://doi.org/10.1146/annurev.neuro.051508.135409
Cohen, E. R., Rostrup, E., Sidaros, K., Lund, T. E., Paulson, O. B., Ugurbil, K., & Kim, S.-G. (2004). Hypercapnic normalization of BOLD fMRI: comparison across field strengths and pulse sequences. *NeuroImage*, 23(2), 613–624. https://doi.org/10.1016/j.neuroimage.2004.06.021
Constantinople, C. M., & Bruno, R. M. (2013). Deep cortical layers are activated directly by thalamus. *Science* (New York, N.Y.), 340(6140), 1591–1594. https://doi.org/10.1126/science.1236425
Cronbach, L. J. (1957). The two disciplines of scientific psychology. *American Psychologist*, 12(11), 671–684. https://doi.org/10.1037/h0043943
Desai, R., Liebenthal, E., Possing, E. T., Waldron, E., & Binder, J. R. (2005). Volumetric vs. surface-based alignment for localization of auditory cortex activation. *NeuroImage*, 26(4), 1019–1029. https://doi.org/10.1016/j.neuroimage.2005.03.024
Donahue, M. J., Lu, H., Jones, C. K., Edden, R. A. E., Pekar, J. J., & van Zijl, P. C. M. (2006). Theoretical and experimental investigation of the VASO contrast mechanism. *Magnetic Resonance in Medicine*, 56(6), 1261–1273. https://doi.org/10.1002/mrm.21072
Dougherty, K., Cox, M. A., Ninomiya, T., Leopold, D. A., & Maier, A. (2017). Ongoing Alpha Activity in V1 Regulates Visually Driven Spiking Responses. *Cerebral Cortex* (New York, N.Y.: 1991), 27(2), 1113–1124. https://doi.org/10.1093/cercor/bhv304
Felleman, D. J., & Van Essen, D. C. (1991). Distributed hierarchical processing in the primate cerebral cortex. *Cerebral Cortex* (New York, N.Y.: 1991), 1(1), 1–47.
Fischl, B., Sereno, M. I., Tootell, R. B., & Dale, A. M. (1999). High-resolution intersubject averaging and a coordinate system for the cortical surface. *Human Brain Mapping*, 8(4), 272–284.
Fitzpatrick, D., Itoh, K., & Diamond, I. T. (1983). The laminar organization of the lateral geniculate body and the striate cortex in the squirrel monkey (Saimiri sciureus). *The Journal of Neuroscience: The Official Journal of the Society for Neuroscience*, 3(4), 673–702.
Friston, K. J. (2005). A theory of cortical responses. *Philosophical Transactions of the Royal Society of London. Series B, Biological Sciences*, 360(1456), 815–836. https://doi.org/10.1098/rstb.2005.1622

Friston, K. J., Fletcher, P., Josephs, O., Holmes, A., Rugg, M. D., & Turner, R. (1998). Event-related fMRI: characterizing differential responses. *NeuroImage*, 7(1), 30–40. https://doi.org/10.1006/nimg.1997.0306

Gilbert, C. D. (1977). Laminar differences in receptive field properties of cells in cat primary visual cortex. *The Journal of Physiology*, 268(2), 391–421. https://doi.org/10.1113/jphysiol.1977.sp011863

Goebel, R. (2007). Localization of Brain Activity using Functional *Magnetic Resonance Imaging*. In C. Stippich (Ed.), Clinical Functional MRI (pp. 9–51). https://doi.org/10.1007/978-3-540-49976-3_2

Goense, J. B. M., Bohraus, Y., & Logothetis, N. K. (2016). fMRI at High Spatial Resolution: Implications for BOLD-Models. *Frontiers in Computational Neuroscience*, 10, 66. https://doi.org/10.3389/fncom.2016.00066

Goense, J. B. M., & Logothetis, N. K. (2006). Laminar specificity in monkey V1 using high-resolution SE-fMRI. *Magnetic Resonance Imaging*, 24(4), 381–392. https://doi.org/10.1016/j.mri.2005.12.032

Good, P. I. (2005). Permutation, parametric and bootstrap tests of hypotheses (3rd ed). New York: Springer.

Gordon, E. M., Laumann, T. O., Gilmore, A. W., Newbold, D. J., Greene, D. J., Berg, J. J., … Dosenbach, N. U. F. (2017). Precision Functional Mapping of Individual Human Brains. *Neuron*, 95(4), 791-807.e7. https://doi.org/10.1016/j.neuron.2017.07.011

Gray, C. M., König, P., Engel, A. K., & Singer, W. (1989). Oscillatory responses in cat visual cortex exhibit inter-columnar synchronization which reflects global stimulus properties. *Nature*, 338(6213), 334–337. https://doi.org/10.1038/338334a0

Greenwald, A. G. (1976). Within-subjects designs: To use or not to use? *Psychological Bulletin*, 83(2), 314–320. https://doi.org/10.1037/0033-2909.83.2.314

Gueorguieva, R., & Krystal, J. H. (2004). Move over ANOVA: progress in analyzing repeated-measures data and its reflection in papers published in the *Archives of General Psychiatry. Archives of General Psychiatry*, 61(3), 310–317. https://doi.org/10.1001/archpsyc.61.3.310

Havlicek, M., Ivanov, D., Roebroeck, A., & Uludağ, K. (2017). Determining Excitatory and Inhibitory Neuronal Activity from Multimodal fMRI Data Using a Generative Hemodynamic Model. *Frontiers in Neuroscience*, 11, 616. https://doi.org/10.3389/fnins.2017.00616

Hayes, A. F. (1996). Permutation test is not distribution-free: Testing H_0: ρ=0. *Psychological Methods*, 1(2), 184–198. https://doi.org/10.1037/1082-989X.1.2.184

Haynes, J.-D., Lotto, R. B., & Rees, G. (2004). Responses of human visual cortex to uniform surfaces. *Proceedings of the National Academy of Sciences of the United States of America*, 101(12), 4286–4291.

https://doi.org/10.1073/pnas.0307948101
Hubel, D. H., & Wiesel, T. N. (1962). Receptive fields, binocular interaction and functional architecture in the cat's visual cortex. *The Journal of Physiology*, 160, 106–154.
Hubel, D. H., & Wiesel, T. N. (1968). Receptive fields and functional architecture of monkey striate cortex. *The Journal of Physiology*, 195(1), 215–243. https://doi.org/10.1113/jphysiol.1968.sp008455
Huber, L., Goense, J. B. M., Kennerley, A. J., Trampel, R., Guidi, M., Reimer, E., ... Möller, H. E. (2015). Cortical lamina-dependent blood volume changes in human brain at 7 T. *NeuroImage*, 107, 23–33. https://doi.org/10.1016/j.neuroimage.2014.11.046
Huber, L., Handwerker, D. A., Jangraw, D. C., Chen, G., Hall, A., Stüber, C., ... Bandettini, P. A. (2017). High-Resolution CBV-fMRI Allows Mapping of Laminar Activity and Connectivity of Cortical Input and Output in Human M1. *Neuron*. https://doi.org/10.1016/j.neuron.2017.11.005
Huber, L., Uludağ, K., & Möller, H. E. (2017). Non-BOLD contrast for laminar fMRI in humans: CBF, CBV, and CMR02. *NeuroImage*. https://doi.org/10.1016/j.neuroimage.2017.07.041
Huntenburg, J. M., Steele, C. J., & Bazin, P.-L. (2018). Nighres: processing tools for high-resolution neuroimaging. *GigaScience*, 7(7). https://doi.org/10.1093/gigascience/giy082
Johnson, R. R., & Burkhalter, A. (1997). A polysynaptic feedback circuit in rat visual cortex. *The Journal of Neuroscience: The Official Journal of the Society for Neuroscience*, 17(18), 7129–7140.
Kashyap, S., Ivanov, D., Havlicek, M., Poser, B. A., & Uludağ, K. (2017). Impact of acquisition and analysis strategies on cortical depth-dependent fMRI. *NeuroImage*. https://doi.org/10.1016/j.neuroimage.2017.05.022
Kashyap, S., Ivanov, D., Havlicek, M., Sengupta, S., Poser, B. A., & Uludağ, K. (2018). Resolving laminar activation in human V1 using ultra-high spatial resolution fMRI at 7T. *Scientific Reports*, 8(1), 17063. https://doi.org/10.1038/s41598-018-35333-3
Keselman, H. J., Algina, J., & Kowalchuk, R. K. (2001). The analysis of repeated measures designs: a review. *The British Journal of Mathematical and Statistical Psychology*, 54(Pt 1), 1–20.
Kok, P., Bains, L. J., van Mourik, T., Norris, D. G., & de Lange, F. P. (2016). Selective Activation of the Deep Layers of the Human Primary Visual Cortex by Top-Down Feedback. *Current Biology*, 26(3), 371–376. https://doi.org/10.1016/j.cub.2015.12.038
Kok, P., & de Lange, F. P. (2014). Shape perception simultaneously up- and downregulates neural activity in the primary visual cortex. *Current Biology*: CB, 24(13), 1531–1535. https://doi.org/10.1016/j.cub.2014.05.042
Kolossa, A., & Kopp, B. (2018). Data quality over data quantity in

computational cognitive neuroscience. *NeuroImage*, 172, 775–785. https://doi.org/10.1016/j.neuroimage.2018.01.005

Koopmans, P. J., Barth, M., & Norris, D. G. (2010). Layer-specific BOLD activation in human V1. *Human Brain Mapping*, 31(9), 1297–1304. https://doi.org/10.1002/hbm.20936

Koopmans, P. J., Barth, M., Orzada, S., & Norris, D. G. (2011). Multi-echo fMRI of the cortical laminae in humans at 7T. *NeuroImage*, 56(3), 1276–1285. https://doi.org/10.1016/j.neuroimage.2011.02.042

Lindquist, M. A., Meng Loh, J., Atlas, L. Y., & Wager, T. D. (2009). Modeling the hemodynamic response function in fMRI: efficiency, bias and mis-modeling. *NeuroImage*, 45(1 Suppl), S187-198. https://doi.org/10.1016/j.neuroimage.2008.10.065

Lindquist, M. A., & Wager, T. D. (2007). Validity and power in hemodynamic response modeling: a comparison study and a new approach. *Human Brain Mapping*, 28(8), 764–784. https://doi.org/10.1002/hbm.20310

Ludbrook, J., & Dudley, H. (1998). Why Permutation Tests are Superior to t and F Tests in Biomedical Research. *The American Statistician*, 52(2), 127–132. https://doi.org/10.1080/00031305.1998.10480551

Lund, J. S. (1973). Organization of neurons in the visual cortex, area 17, of the monkey (Macaca mulatta). *The Journal of Comparative Neurology*, 147(4), 455–495. https://doi.org/10.1002/cne.901470404

Lund, J. S. (1988). Anatomical Organization of Macaque Monkey Striate Visual Cortex. *Annual Review of Neuroscience*, 11(1), 253–288. https://doi.org/10.1146/annurev.ne.11.030188.001345

Lund, J. S., Lund, R. D., Hendrickson, A. E., Bunt, A. H., & Fuchs, A. F. (1975). The origin of efferent pathways from the primary visual cortex, area 17, of the macaque monkey as shown by retrograde transport of horseradish peroxidase. *The Journal of Comparative Neurology*, 164(3), 287–303. https://doi.org/10.1002/cne.901640303

Maier, A., Adams, G. K., Aura, C., & Leopold, D. A. (2010). Distinct superficial and deep laminar domains of activity in the visual cortex during rest and stimulation. *Frontiers in Systems Neuroscience*, 4. https://doi.org/10.3389/fnsys.2010.00031

Maier, A., Aura, C. J., & Leopold, D. A. (2011). Infragranular sources of sustained local field potential responses in macaque primary visual cortex. *The Journal of Neuroscience: The Official Journal of the Society for Neuroscience*, 31(6), 1971–1980. https://doi.org/10.1523/JNEUROSCI.5300-09.2011

Markuerkiaga, I., Barth, M., & Norris, D. G. (2016). A cortical vascular model for examining the specificity of the laminar BOLD signal. *NeuroImage*, 132, 491–498. https://doi.org/10.1016/j.neuroimage.2016.02.073

Marquardt, I., Schneider, M., Gulban, O. F., Ivanov, D., & Uludağ, K.

(2018). Cortical depth profiles of luminance contrast responses in human V1 and V2 using 7 T fMRI. *Human Brain Mapping*. https://doi.org/10.1002/hbm.24042

McGonigle, D. J., Howseman, A. M., Athwal, B. S., Friston, K. J., Frackowiak, R. S., & Holmes, A. P. (2000). Variability in fMRI: an examination of intersession differences. *NeuroImage*, 11(6 Pt 1), 708–734. https://doi.org/10.1006/nimg.2000.0562

Mooney, C. Z., & Duval, R. D. (1993). Bootstrapping: a nonparametric approach to statistical inference. Newbury Park, Calif: Sage Publications.

Muckli, L., De Martino, F., Vizioli, L., Petro, L. S., Smith, F. W., Ugurbil, K., … Yacoub, E. (2015). Contextual Feedback to Superficial Layers of V1. *Current Biology*: CB, 25(20), 2690–2695. https://doi.org/10.1016/j.cub.2015.08.057

Mumford, J. A. (2007). A guide to calculating percent change with featquery. Retrieved from http://mumford.fmripower.org/perchange_guide.pdf

Nasr, S., Polimeni, J. R., & Tootell, R. B. H. (2016). Interdigitated Color- and Disparity-Selective Columns within Human Visual Cortical Areas V2 and V3. *The Journal of Neuroscience: The Official Journal of the Society for Neuroscience*, 36(6), 1841–1857. https://doi.org/10.1523/JNEUROSCI.3518-15.2016

Nee, D. E. (2018). fMRI replicability depends upon sufficient individual-level data. BioRxiv. https://doi.org/10.1101/352633

Neuhäuser, M., & Manly, B. F. J. (2004). The Fisher-Pitman permutation test when testing for differences in mean and variance. *Psychological Reports*, 94(1), 189–194. https://doi.org/10.2466/pr0.94.1.189-194

Norris, D. G. (2012). Spin-echo fMRI: The poor relation? *NeuroImage*, 62(2), 1109–1115. https://doi.org/10.1016/j.neuroimage.2012.01.003

Norris, D. G. (2015). Pulse Sequences for fMRI. In K. Uludag, K. Ugurbil, & L. Berliner (Eds.), *fMRI: From Nuclear Spins to Brain Functions* (Vol. 30, pp. 131–162). https://doi.org/10.1007/978-1-4899-7591-1_7

Olman, C. A., Harel, N., Feinberg, D. A., He, S., Zhang, P., Ugurbil, K., & Yacoub, E. (2012). Layer-specific fMRI reflects different neuronal computations at different depths in human V1. *PloS One*, 7(3), e32536. https://doi.org/10.1371/journal.pone.0032536

Olsen, S. R., Bortone, D. S., Adesnik, H., & Scanziani, M. (2012). Gain control by layer six in cortical circuits of vision. *Nature*, 483(7387), 47–52. https://doi.org/10.1038/nature10835

Poldrack, R. A. (2010). Subtraction and Beyond: The Logic of Experimental Designs for Neuroimaging. In S. J. Hanson & M. Bunzl (Eds.), *Foundational Issues in Human Brain Mapping* (pp. 147–160). https://doi.org/10.7551/mitpress/9780262014021.003.0014

Poldrack, R. A., Mumford, J. A., & Nichols, T. E. (2011). Handbook of

functional MRI data analysis. Cambridge New York Melbourne Madrid: Cambridge University Press.

Polimeni, J. R., Fischl, B., Greve, D. N., & Wald, L. L. (2010). Laminar analysis of 7T BOLD using an imposed spatial activation pattern in human V1. *NeuroImage*, 52(4), 1334–1346. https://doi.org/10.1016/j.neuroimage.2010.05.005

Polimeni, J. R., Witzel, T., Fischl, B., Greve, D. N., & Wald, L. L. (2010). Identifying common-source driven correlations in resting-state fMRI via laminar-specific analysis in the human visual cortex. *Proc. Intl. Soc. Mag. Reson. Med.*, 18, 353.

Quené, H., & van den Bergh, H. (2004). On multi-level modeling of data from repeated measures designs: a tutorial. *Speech Communication*, 43(1–2), 103–121. https://doi.org/10.1016/j.specom.2004.02.004

Rao, R. P., & Ballard, D. H. (1999). Predictive coding in the visual cortex: a functional interpretation of some extra-classical receptive-field effects. *Nature Neuroscience*, 2(1), 79–87. https://doi.org/10.1038/4580

Ress, D., Glover, G. H., Liu, J., & Wandell, B. (2007). Laminar profiles of functional activity in the human brain. *NeuroImage*, 34(1), 74–84. https://doi.org/10.1016/j.neuroimage.2006.08.020

Roberts, M. J., Lowet, E., Brunet, N. M., Ter Wal, M., Tiesinga, P., Fries, P., & De Weerd, P. (2013). Robust gamma coherence between macaque V1 and V2 by dynamic frequency matching. *Neuron*, 78(3), 523–536. https://doi.org/10.1016/j.neuron.2013.03.003

Rockland, K. S., & Pandya, D. N. (1979). Laminar origins and terminations of cortical connections of the occipital lobe in the rhesus monkey. *Brain Research*, 179(1), 3–20. https://doi.org/10.1016/0006-8993(79)90485-2

Self, M. W., van Kerkoerle, T., Supèr, H., & Roelfsema, P. R. (2013). Distinct roles of the cortical layers of area V1 in figure-ground segregation. *Current Biology*: CB, 23(21), 2121–2129. https://doi.org/10.1016/j.cub.2013.09.013

Sloan, H. L., Austin, V. C., Blamire, A. M., Schnupp, J. W. H., Lowe, A. S., Allers, K. A., … Sibson, N. R. (2010). Regional differences in neurovascular coupling in rat brain as determined by fMRI and electrophysiology. *NeuroImage*, 53(2), 399–411. https://doi.org/10.1016/j.neuroimage.2010.07.014

Smith, P. L., & Little, D. R. (2018). Small is beautiful: In defense of the small-N design. *Psychonomic Bulletin & Review*, 25(6), 2083–2101. https://doi.org/10.3758/s13423-018-1451-8

Smith, S. M. (2004). Overview of fMRI analysis. *The British Journal of Radiology*, 77(suppl_2), S167–S175. https://doi.org/10.1259/bjr/33553595

Steffener, J., Tabert, M., Reuben, A., & Stern, Y. (2010). Investigating hemodynamic response variability at the group

level using basis functions. *NeuroImage*, 49(3), 2113–2122. https://doi.org/10.1016/j.neuroimage.2009.11.014

Thirion, B., Pinel, P., Mériaux, S., Roche, A., Dehaene, S., & Poline, J.-B. (2007). Analysis of a large fMRI cohort: Statistical and methodological issues for group analyses. *NeuroImage*, 35(1), 105–120. https://doi.org/10.1016/j.neuroimage.2006.11.054

Tootell, R. B., Hamilton, S. L., & Switkes, E. (1988). Functional anatomy of macaque striate cortex. IV. Contrast and magno-parvo streams. *The Journal of Neuroscience: The Official Journal of the Society for Neuroscience*, 8(5), 1594–1609.

Tootell, R. B., & Nasr, S. (2017). Columnar Segregation of Magnocellular and Parvocellular Streams in Human Extrastriate Cortex. *The Journal of Neuroscience: The Official Journal of the Society for Neuroscience*. https://doi.org/10.1523/JNEUROSCI.0690-17.2017

Uludağ, K., & Blinder, P. (2018). Linking brain vascular physiology to hemodynamic response in ultra-high field MRI. *NeuroImage*, 168, 279–295. https://doi.org/10.1016/j.neuroimage.2017.02.063

Uludağ, K., Müller-Bierl, B., & Uğurbil, K. (2009). An integrative model for neuronal activity-induced signal changes for gradient and spin echo functional imaging. *NeuroImage*, 48(1), 150–165. https://doi.org/10.1016/j.neuroimage.2009.05.051

van Kerkoerle, T., Self, M. W., Dagnino, B., Gariel-Mathis, M.-A., Poort, J., van der Togt, C., & Roelfsema, P. R. (2014). Alpha and gamma oscillations characterize feedback and feedforward processing in monkey visual cortex. *Proceedings of the National Academy of Sciences*, 111(40), 14332–14341. https://doi.org/10.1073/pnas.1402773111

van Kerkoerle, T., Self, M. W., & Roelfsema, P. R. (2017). Layer-specificity in the effects of attention and working memory on activity in primary visual cortex. *Nature Communications*, 8, 13804. https://doi.org/10.1038/ncomms13804

Waehnert, M. D., Dinse, J., Weiss, M., Streicher, M. N., Waehnert, P., Geyer, S., … Bazin, P.-L. (2014). Anatomically motivated modeling of cortical laminae. *NeuroImage*, 93, 210–220. https://doi.org/10.1016/j.neuroimage.2013.03.078

Weber, B., Keller, A. L., Reichold, J., & Logothetis, N. K. (2008). The microvascular system of the striate and extrastriate visual cortex of the macaque. *Cerebral Cortex* (New York, N.Y.: 1991), 18(10), 2318–2330. https://doi.org/10.1093/cercor/bhm259

Summary

This thesis presents three empirical studies, all of which employed cutting-edge high-resolution functional magnetic resonance imaging (fMRI) at sub-millimetre resolution to study visual perception in the human brain. First, we studied bottom-up (i.e. sensory driven) processing in visual cortex (Chapter 2). In particular, we investigated how variations in simple physical properties of a visual stimulus affect neuronal activity in visual brain areas. The unprecedented high level of spatial detail in our studies enabled us to resolve activity at different cortical depths. Because cortical layers are thought to form distinct computational networks with specialised roles, a more fine-grained understanding of these neuronal networks has the potential to refine cognitive theories of visual perception.

A major challenge in the high-resolution mapping of cortical layers is a spatial bias in the measured fMRI signal caused by the flow of blood perpendicular to the cortical layers. We employed, for the first time in a human fMRI study, a spatial deconvolution model that allowed us to partially remove this bias. In this way, we were able to approximate the local neuronal contribution to the fMRI signal at different cortical layers. The field of high-resolution fMRI is still evolving, and we hope that our methodological contributions will benefit future research. Methodological aspects pertaining to the removal of the draining veins bias, and the spatial specificity of the fMRI signal at 7T, are extensively discussed in Chapters 2 and 4, respectively.

The first study on bottom-up processing (Chapter 2) was followed by a complementary study on top-down effects (Chapter 3). The term 'top-down' is used to describe aspects of perception and cognition that are not directly driven by physical properties of the sensory input, but by prior knowledge, expectations, attention, or other high-level mechanisms. We investigated the processing of a centrally fixated stimulus that is perceived to move as a whole, although the retinotopic input from one visual hemifield is constant. The cortical depth profile of top-down effects suggest a role of re-entrant feedback at the level of V1. However, other interpretations, such as indirect feedback, for example via the pulvinar, are possible.

We continued our investigation of visual perception with a study on the spatial and temporal dynamics of neuronal responses to illusory contours ('Kanizsa' type visual illusions; Chapter 5). This type of illusion is a popular test case in psychology and neuroscience, because it is a simple and powerful example of how top-down expectations shape visual perception. Although the analysis of the data is ongoing, our preliminary findings indicate a previously unknown pattern of activation in early visual cortex.

In summary, our projects comprise research into the detailed spatial profile of bottom-up and top-down processing in human early visual cortex. We have explored activation profiles of stimuli that were designed to preferentially engage bottom-up or top-down perceptual mechanisms, and have employed a new modelling technique to account for known biases in the high-resolution fMRI signal.

Knowledge valorisation

What is – or should be – the purpose of cognitive neuroscience? In the introduction of this thesis, I suggested an answer to this question, with a focus on the way how knowledge should be created. I argued that academic research should not be restricted to observation, but should aim for explanations and understanding. To achieve this goal, quantitative models that identify causal mechanisms and allow predictions about future observations are necessary. With respect to the studies presented in this thesis, I reasoned that high-resolution fMRI research might, in the long run, contribute to the development of mechanistic models of cognition by reducing the gap between data and theory in neuroscience and cognitive science.

The above argument presupposes that the purpose of cognitive neuroscience, like that of other academic disciplines, lies in the creation of knowledge. Conversely, the very term 'knowledge valorisation' challenges the inherent value of knowledge, and asks for additional value. According to a promotional website of the University of Amsterdam, "Knowledge valorisation refers to the utilisation of scientific knowledge in practice. Examples include developing a product or a medicine [...]" (University of Amsterdam, 2015). This may be interpreted from a Marxist perspective, where academia becomes a part of the production process[1], because "Money [...] forms the starting-point and the conclusion of every valorisation process" (Marx, Fowkes, & Fernbach, 1981, p. 255). In other words, money is necessary to commence a research project, and money is expected to be generated by the research project. In case of high-resolution fMRI research, the amount of money that is committed to the research process is indeed substantial. Just to give an indication, at the time of the research presented in this thesis, the hourly rate for usage of the 7T MRI scanner at Maastricht University was in excess of 700 euros, excluding taxes (although this is apparently a higher rate than at some other imaging centres). Moreover, one has to consider the costs of labour, and of additional equipment and materials (such as office space, high-performance computers, conference visits, etc.). It is

[1] Although, on a more conventional reading of Marx, academia would rather belong to the 'superstructure', and not to the base of society.

clear that these substantial investments will not be directly returned by the respective research outcomes in the short run.

It could be argued that an uncertain and – if at all – much delayed, indirect return of capital is a defining characteristic of fundamental research. A typical argument in its defence is that historically, fundamental research has sometimes resulted in completely unforeseen applications with enormous societal, medical, or economic implications. Although I agree with this view, I will not elaborate on it, because it is the very nature of unforeseen consequences that their anticipation amounts to pure speculation. Instead, I will discuss two aspects of 'knowledge valorisation' related to (1) the societal impact of research, and to (2) knowledge dissemination.

Let me start by pointing out that I absolutely agree with the notion that academic researchers should not be ignorant to the societal impact of their work. Researchers at public institutions are endowed with public money, and they consequently bear the responsibility to use their resources in a way that is likely to benefit society. It would be naive to entrust individual researchers with this task in the absence of any structural incentives. The obligation to discuss 'knowledge valorisation' of scientific work can be seen as such a structural incentive. However, although I strongly agree with the premise of 'knowledge valorisation', I take issue with an interpretation that narrowly focuses on "utilisation of scientific knowledge *in practice*" (University of Amsterdam, 2015, emphasis added by the author). It would be unethical for researchers to waste public resources through inefficiency or lack or scientific rigour, but the purpose of fundamental research cannot be solely derived from the creation of new products.

Consider the Apollo program, arguably one of the greatest scientific achievements of the 20$^{\text{th}}$ century. The Apollo program was very costly (CBO, 2004), but brought about technological developments that resulted in the improvement of existing, and the development of new products (Lowman, 1975; Schnee, 1977). Nevertheless, it has been argued that the importance of spin-offs resulting from the space program have been overrated (Alic, 1986), and that the costs of the Apollo program have been disproportionate relative to the returns generated by technological innovations (Gisler & Sornette, 2009). Arguably, the most important consequence of the Apollo program may have been its societal impact (Gisler & Sornette, 2009). Although it is hard to quantify the cultural

impact of science, it is safe to assume that the inherent fascination of human space exploration inspired many people. For example, the 'Blue Marble' photograph of the earth taken from an Apollo spacecraft is thought to have affected the public discourse regarding the value and fragility of our planet, and became an icon of the environmental movement (Darius, 1984; Geppert, 2018; Jasanoff, 2004).

Neuroimaging of the human brain may be less spectacular, and receives less public attention than space exploration did in the 1960s. Nevertheless, I expect the advances in the understanding of human brain function brought about by functional neuroimaging to have a lasting cultural impact, beyond the technical details of academic debates. Functional properties of visual neurons had been measured in animal brains before the advent of fMRI, just like the earth had been charted before the age of space flight. Yet, to know what is going on in human brains may, in subtle ways, change people's perception of themselves and their position in the world, just like a photograph of the earth gave people a new perspective on our planet. I do hope that fMRI research will generate new technological applications that will have a positive economic impact, but I think that the potential cultural significance of functionally mapping the human brain by far outweighs any vague hopes for direct return of capital.

The reference to space exploration can be extended to my second, more down-to-earth argument on knowledge dissemination. In 1969, the moon landing was broadcast worldwide, reaching maximum publicity (Gisler & Sornette, 2009). NASA does not only publish beautiful pictures of the earth and the stars, but also makes research data and computer code freely available (NASA, 2017, 2019a, 2019b). I am convinced that it is imperative for publicly funded research to be publicly accessible for three main reasons. First, research that was paid for by the public belongs to the public, and it is unethical to withhold it. Second, research that is not read is a waste of resources, and access restrictions limit the audience that can be reached with a publication. Third, public sharing of data and analysis tools incentivize scientific rigour, hinder questionable research practices and fraud, and can lead to new discoveries by enabling re-use. Furthermore, potential errors that would go unnoticed without public sharing may be discovered.

In my own research, I tried to facilitate knowledge dissemination as best as I could by following open science practices. As a first step, I

scripted my analyses in programming languages that are freely available under permissive licences, such as Python and GNU Bash. To enhance readability and facilitate potential re-use, I stringently commented my code, and tried to adhere to common style guidelines. A central element in the analysis pipelines of all projects presented in this thesis is the population receptive field mapping method (Dumoulin & Wandell, 2008). The Python implementation I developed for this is freely available through the Python Package Index, i.e. it can easily be installed by anyone (Marquardt, Gulban, & Schneider, 2018). Furthermore, a documentation is provided to enable potential users to install and use the software without having to contact the author (github.com/ingo-m/pyprf). A continuous integration service (travis-ci.org) automatically tests every modification of the code for potential bugs. In other words, after every modification, an analysis is performed on a small example dataset, and the result is compared with a template. Should the test result deviate from the template, an alarm is raised. This approach, which is common practice in the software industry, is very powerful at detecting errors, and therefore immensely beneficial in the context of data analysis and scientific programming.

Neuroimaging studies require a vast amount of preprocessing and analysis steps before meaningful results can be obtained. The reproducibility of neuroimaging results has been drawn into question by reports on the effect of operating system and software version on anatomical and functional maps (Glatard et al., 2015; Gronenschild et al., 2012). Such effects do not only affect reproducibility across research groups, but also make the individual researcher dependent on their particular workstation. Changes to the hardware or operating system during a study may confound results. One solution to increase reproducibility both across research groups and across time is the use of containerisation (Boettiger, 2015). In this way, analyses can be carried out in a controlled environment that is stable over time, and can easily be shared. Docker is a containerisation software that is particularly well suited for the needs of computationally intense scientific analyses, because of its negligible impact on computational speed (Di Tommaso et al., 2015; Felter, Ferreira, Rajamony, & Rubio, 2015). The analysis pipelines pertaining to Chapters 3 and 4 of this thesis were implemented within docker containers, and these resources will be made publicly available upon publication of the respective papers.

References

Alic, J. . (1986). The federal role in commercial technology development. *Technovation*, 4(4), 253–267. https://doi.org/10.1016/0166-4972(86)90029-5

Boettiger, C. (2015). An introduction to Docker for reproducible research, with examples from the R environment. *ACM SIGOPS Operating Systems Review*, 49(1), 71–79. https://doi.org/10.1145/2723872.2723882

CBO. (2004). A budgetary analysis of NASA's new vision for space exploration. Congress Of The United States Congressional Budget Office.

Darius, J. (1984). *Beyond vision.* Oxford: Oxford University Press.

Di Tommaso, P., Palumbo, E., Chatzou, M., Prieto, P., Heuer, M. L., & Notredame, C. (2015). The impact of Docker containers on the performance of genomic pipelines. *PeerJ*, 3, e1273. https://doi.org/10.7717/peerj.1273

Dumoulin, S. O., & Wandell, B. A. (2008). Population receptive field estimates in human visual cortex. *NeuroImage*, 39(2), 647–660. https://doi.org/10.1016/j.neuroimage.2007.09.034

Felter, W., Ferreira, A., Rajamony, R., & Rubio, J. (2015). An updated performance comparison of virtual machines and Linux containers. *2015 IEEE International Symposium on Performance Analysis of Systems and Software (ISPASS)*, 171–172. https://doi.org/10.1109/ISPASS.2015.7095802

Geppert, A. C. T. (2018). The Post-Apollo Paradox: Envisioning Limits During the Planetized 1970s. In A. C. T. Geppert (Ed.), *Limiting Outer Space* (pp. 3–26). https://doi.org/10.1057/978-1-137-36916-1_1

Gisler, M., & Sornette, D. (2009). Exuberant Innovations: The Apollo Program. *Society*, 46(1), 55–68. https://doi.org/10.1007/s12115-008-9163-8

Glatard, T., Lewis, L. B., Ferreira da Silva, R., Adalat, R., Beck, N., Lepage, C., … Evans, A. C. (2015). Reproducibility of neuroimaging analyses across operating systems. *Frontiers in Neuroinformatics*, 9, 12. https://doi.org/10.3389/fninf.2015.00012

Gronenschild, E. H. B. M., Habets, P., Jacobs, H. I. L., Mengelers, R., Rozendaal, N., van Os, J., & Marcelis, M. (2012). The effects of FreeSurfer version, workstation type, and Macintosh operating system version on anatomical volume and cortical thickness measurements. *PloS One*, 7(6), e38234. https://doi.org/10.1371/journal.pone.0038234

Jasanoff, S. (2004). Heaven and Earth: The Politics of Environmental Images. In S. Jasanoff & M. L. Martello (Eds.), *Earthly politics: local and global in environmental governance* (pp. 31–52). Cambridge, Mass: MIT Press.

Lowman, P. D. (1975). The Apollo Program: Was It Worth It? *World Resources: The Forensic Quarterly*, 49, 291–302.

Marquardt, I., Gulban, O. F., & Schneider, M. (2018, April 18). pyprf - A free & open source python package for population receptive field (pRF) analysis. https://doi.org/10.5281/zenodo.1220207

Marx, K., Fowkes, B., & Fernbach, D. (1981). *Capital: a critique of political economy*. In Penguin Classics. London: Penguin Books in association with New Left Review.

NASA. (2017). NASA Open Source Development. Retrieved from https://www.nasa.gov/open/open-source-development.html

NASA. (2019a). NASA Data Portal. Retrieved from https://data.nasa.gov/

NASA. (2019b). NASA Open Source Software Projects. Retrieved from https://software.nasa.gov/

Schnee, J. E. (1977). Space Program Impacts Revisited. *California Management Review*, 20(1), 62–73. https://doi.org/10.2307/41164739

University of Amsterdam. (2015). Knowledge valorisation. Retrieved from http://www.uva.nl/en/research/research-and-cooperation/knowledge-valorisation/outreach.html

Acknowledgments

First of all, I would of course like to thank **Kâmil** for being my supervisor. It was a pleasure to work with you. Even though our project faced some quite difficult scientific challenges in the first one or two years, I would not hesitate to work with you as a supervisor if I had to make the choice again. I particularly value the reliable style of supervision, the clear, straightforward feedback, and the freedom with respect to technicalities and implementation. The fact that I had freedom of choice at implementation gave me the chance to gather experience in data analysis and scientific programming. But most importantly, I appreciate your calm and sincere character.

During the first year of my master, I was not sure yet whether to pursue a PhD. I was a student in **Rainer**'s tutorial group, and he suggested that I consider applying for PhD funding. Thanks for encouraging me to take this path.

Dimo, thank you for teaching me how to operate the MRI scanner! Seeing that this entire thesis is based on fMRI research, the importance of your contribution should be quite self-evident...

The PhD time was quite a journey, and I thank my travel companions **Marian** and **Faruk**. We started this journey together, and as it seems we are about to reach our destination soon. This journey would have been less worthwhile without you two. Not only would it have been a lot less fun, but we would not have reached the point where we are now without each other. Many of the destinations we visited, and the skills and treasures we picked up on the way, we would not have found without each other's support. It is sad that the fellowship will have to part ways now, but we have places to go. May our paths cross again.

Yawen, thank you for being the best 7T participant of all times, for the mooncake, and for being a good friend. You're always welcome in Berlin. Same goes for **Geraldine** and **Linda**; I hope we

will find a place and time to continue our Saturday evening cocktail bar tradition.

Mario Archila, there are numerous things I could mention about philosophical and scientific discussions, but I will rather only say this – thanks for accompanying me on the most unexpectedly memorable night out in Maastricht.

Sri, in Germany, they call their supervisors 'Doctor father'; hence, you are my 'Doctor bro'. Thanks for that, and for compelling me to use SPM. May the motion correction be with you.

Franc, you are my favourite ukulele playing astrophysicist, and I would always want to have you with me on a night out. I wish you all the best for your future in Hamburg.

Roy, thanks for your valuable input regarding cortical depth sampling with CBS tools. This may sound like a small detail, but a great deal of the content that made it into this thesis actually relies on this very detail.

Peter, thanks for your scientific and personal support, and for being a great teacher of visual neuroscience. If there ever was an archetype of a scientist, it's you.

Federico and **Michelle**, thank you for numerous dinner invitations and the great Italian food. Federico, I appreciate your constant and unwavering willingness to always get into a good, heated discussion with me. How could I resist.

Thank you, **Ben**, for the 3D GE EPI sequence (after all, the backbone of my research), for your MRI-physics support, and for the occasional alcohol-infused, late evening conversation (→*country club*).

Thanks to **Andrew** (aka Tyler) for your moderating influence in various discussions. It cannot be denied that Faruk, Marian and I at times reinforce each other's tendency towards positions that may be perceived as outlandish by some; it is clearly beneficial to occasionally

be reminded of this[1].

Thomas, thanks for being an open science and free software role model. `from __future__ import data_science as skill`.

The Cognitive Neuroscience department wouldn't be what it is without the **Bandito** team – thank you! For the coffee, of course, but even more importantly for being a social hub and an essential source of information regarding Maastricht nightlife. The same goes for **Rahi**. Party tonight? Let's meet at Take Five first?

Ganz besonderer Dank gilt natürlich meinen Eltern **Martina** und **Hendrik**, sowie meiner Schwester **Sina**. Meinen Eltern danke ich dafür, dass sie mich und meine Schwester immer und mit grossem Einsatz gefördert haben. Nur durch eure emotionale und praktische Unterstützung war es uns möglich unseren Lebensweg einzuschlagen. Ebenfalls danke ich meinen Großeltern **Helmuth** und **Gerda** für unsere gemeinsame Zeit, und für die Unterstützung im Studium und darüber hinaus.

Finally, I thank my partner **Lea** for being with me all this time. Time goes so quickly; it feels like it was yesterday that we met at the end of our first year at university, and here we are, nearly ten years on. I am very glad for our time together, and for the experiences we shared. Having spent almost all our 20s together, may our 30s be just as bright.

[1] Even if our opinion doesn't change, we may at least reconsider our rhetoric :)

About the author

Ingo Marquardt was born on June 20th 1988 in Hildesheim, Germany. He received his secondary education at Gymnasium Alfeld, and obtained his high school diploma ('Abitur') in 2008. After graduating from high school, he performed a year of community service ('Zivildienst') at a therapy centre. In 2009, he began his university education at University College Maastricht. During his Bachelor studies, he completed courses in Neuroscience and Philosophy, among others. In 2011, he spent a semester abroad at the University of Waikato, New Zealand. He obtained a Bachelor in Liberal Arts and Science in 2012, and subsequently enrolled in a two-year Research Master programme in Cognitive Neuroscience at Maastricht University. In 2013, he was awarded a scholarship by the German Academic Scholarship Foundation ('Studienstiftung des deutschen Volkes'). From 2013 to 2014, he conducted a research internship at the FMRIB centre at the University of Oxford. Under supervision of Dr. Jacinta O'Shea, in the research group lead by Prof. Dr. Heidi Johansen-Berg, he designed and carried out a real-time fMRI neurofeedback study. After completion of his Master thesis in 2014, he began his PhD research with his supervisor Dr. Kâmil Uludağ at the Department of Cognitive Neuroscience at Maastricht University. The PhD research was funded by a prestigious 'Research Talent' grant awarded by the Netherlands Organisation for Scientific Research. Moreover, he was admitted into the Doctoral programme of the German Academic Scholarship Foundation in 2015.